High Resolution Spectroscopy of Small Molecules using Laser and Fourier Transform Techniques

by

Zulfikar Morbi

A thesis

presented to the University of Waterloo

in fulfilment of the

thesis requirement for the degree of

Doctor of Philosophy

in

Chemistry

Waterloo, Ontario, Canada, 1997

The University of Waterloo requires the signatures of all persons using or photocopying this thesis. Please sign below, and give address and date.

Abstract

The first part of this thesis is concerned with the electronic spectroscopy of the monovalent derivatives of the alkaline earth metals (Mg,Ca,Sr,Ba). The electronic transitions in these molecules arise from a predominantly metal–centered electron. Therefore, the low resolution spectra of these species show characteristic features (spin-orbit splittings, vibrational frequencies...) which changes little when the ligand is changed. The simple one-electron model usually used to describe diatomic alkaline earth halides (CaF,SrF...) will be shown to be applicable to the polyatomic derivatives. A general discussion of these spectral and structural similarities, as well as methods to produce and detect theses species will be presented. Then the high resolution spectrum of the $\tilde{C}\ ^2A_1$–$\tilde{X}\ ^2A_1$ transition of $CaNH_2$, generated in a laser ablation/molecular beam spectrometer, will be discussed. The simple pure precession model will be derived for polyatomic species and applied to predict the spin-rotation interactions in the $CaNH_2$ molecule.

The second part deals with the high resolution infrared emission spectra of metal-containing diatomic molecules, InF and the coinage (Cu,Ag,Au) metal hydrides. The high temperature Fourier transform infrared spectra of these molecules are recorded at high resolution to derive accurate molecular constants. The data analysis is carried out using standard procedures (Dunham model) and also by directly solving the radial Schödinger equation. In this way, an effective Born–Oppenheimer potential is determined by fitting many isotopomer data to an equation containing a parameterized potential function. The potentials derived in this manner are superior to standard methods for predicting various molecular properties.

Acknowledgements

It has taken many years for me to get this far. I could not have done with without the love and support of my parents and family. Although they think I don't appreciate them, I really do. Thanks Mom and Dad. To my little nieces, Marium and Shanez, I always have you close to my heart !

I'd really like to thank Peter Bernath for giving me the opportunity to work in his lab, for his patience and also his tolerance of my ignorance. I truly admire your knowledge and dedication of science.

Early on in my graduate career, I had the opportunity to work with and also learn from Mike Dulick. I thank him for his encouragement and unique teaching skills. I always loved the way you told your stories and I consider you my friend. I hope that we have a chance to meet again !

I'd like to thank my friends in London who helped me keep my sanity over the years! Mike Macleod, Santosh Pudupakkam, Kyla Esteves, Norm Yu and Glen Beasley. And to the new mates, Karl McCullagh and Joost Luiken. This past year would not have been any fun without you guys !! We go and we get it done !! To those people who have come and gone during my days at Waterloo, especially Brad White, who I should email more often, Dom Appadoo, Ed Keller and Lisa Prokopich. Thanks all. I also want to acknowledge some of the Beams group people, Pina Colarusso, Keqing Zhang, Ralph Schiell, and the new guys Gang Li, T. Hirao, and to Lisa Beauchamp, who taught me a few simple words, search for self knowledge not justifcation ! I especially want to thank James Martin, for listening to my stories and for telling me some of his (more than once !!) and for being a good friend. I'll miss all of you guys !

This last paragraph is one I wish I never had to write. To the memory of my good friend, Jeff Waller, the few months that you touched our lives are ones I will never forget. I will carry your friendship with me always. It is to him I wish to dedicate this thesis.

Contents

List of Figures

List of Tables

Chapter 1

Introduction

Free radicals have been studied for a relatively short time in the history of chemistry. In the past these molecules have proven difficult to characterize because they are unstable in normal room temperature environments. Free radicals are usually highly reactive, short–lived (transient) species that have unpaired electrons. Early work focused on small molecules, mostly diatomic, that were found in flames, arcs and electrical discharges, or other extreme environments. Due to their transient nature, it was not until fairly recently (last 50 years) that attempts to characterize free radicals became successful. This is in large part due to the developments in novel experimental techniques, beginning with flash photolysis [2] and and later with laser-based techniques. The pioneering work on the interpretation of molecular spectra by Herzberg [3], Mulliken, Barrow and others also played an important role. Lastly, the ability to study molecules in novel environments such as the interstellar medium [4], comets [5], and the earth's atmosphere [6] led to the identification of many free radicals [7] which were previously unknown.

The importance of free radicals is well known in atmospheric chemistry. The gas phase oxidation of hydrochloroflourocarbons (HCFC's) and hydrocarbons in the troposphere are known not to dependent on the O_2 or O_3 concentration in the atmosphere. Rather, this oxidation, which generates hydrocarbon free radicals, depends on the OH radical concentration. This is amazing because the tropospheric abundance of OH corresponds to a mole fraction of 10^{-14} [8] and it still remains a major player in ozone destruction.

The OH molecule was also the first radical to be identified in the interstellar medium. A transition between two Λ-doublet levels of the ground state ($^2\Pi_i$), first measured in the laboratory in the 1950's [9,10], was observed in absorption in 1963. This transition, known as the OH maser line occurring at a wavelength of 18 cm, was measured in the radio source Cassiopeia A [11]. It was not for another five years, in 1968, when the second molecule, NH_3 [12] was identified a by radio observation of Sagittarius A. Despite theoretical predictions to the contrary, it soon became obvious that both stable molecules and free radicals could survive the harsh environment of space [4]. The list of interstellar molecules contained about 20 members in 1972 and has grown to over 200 in the 1990's [13].

1.1 Alkaline Earth Molecules

There has been a recent resurgence of interest in spectroscopic studies of alkaline earth–containing polyatomic molecules. The linear molecules CaOH [14,15], SrOH [16–18], and CaCCH [19–22] have been studied using a high temperature source called a Broida oven [23]. CaOH [14,15,24–28] has been the most studied species

of this family of molecules (see Table 1.1). It was first observed in flames, when the greenish and reddish emission spectrum was observed by Herschel in 1823 [29]. The identity of the emitting species was not known at the time but it was believed the emissions came from a calcium–containing molecule. There was considerable speculation over the next 100 years about which molecule was responsible for the emission. In the early part of this century it was believed the calcium dimer (Ca_2) [30] or CaO [31] was responsible; however, it was not until 1955 that James and Sugden [32] suggested the emissions were from the alkaline earth (MOH, M=Ca, Sr, Ba) hydroxide species. Their assignment was based on similarities observed between the spectra of alkaline earth halide molecules and the hydroxides. It turned out that they were correct, but their insight was not fully appreciated until the electronic structure of the alkaline earth molecules became better understood (§ 1.3).

The CaOH molecule can be easily synthesized in the gas phase by a reaction of vaporized Ca atoms with H_2O or more simply, by spraying an aerosol of a calcium metal salt (i.e. $CaCO_3$) into a flame [33, 34]. Since CaOH is easily generated, it is predicted to be found in both atmospheric and astrophysical environments. The singly–ionized Ca atom has been detected in the upper atmosphere ($\geq$100 km) for nearly 40 years [35, 36]. The major naturally occurring source of these metals is from ablation of meteorites entering the earth's atmosphere [37, 38]. It has been postulated that the deliberate release of these metals (both alkali and alkaline earth) could reduce the environmental impact of hydrocarbons [37]. The HCFC's are important precursor molecules in ozone depletion and the presence of alkaline earth atoms in the gas phase has been shown to reduce the concentration

of OH radicals [37]. The formation of CaOH in an energetic environment [39] can readily occur although the direct gas phase reaction of calcium with water is endothermic (§ 1.4). Thus the $\tilde{B}^2\Sigma^+$–$\tilde{X}^2\Sigma^+$ and $\tilde{A}^2\Pi$ –$\tilde{X}^2\Sigma^+$ transitions of CaOH have both been observed in absorption of the stellar atmospheres of M–type dwarf stars [40, 41]. The only other alkaline earth molecule observed in an astrophysical source has been a radio observation of MgNC [42, 43] and its isomer MgCN [44] in the circumstellar envelope of the carbon star IRC+10216.

When alkaline earth metals are present as a fuel additive in an oxygen–hydrocarbon flame, it has been shown that there is a significant decrease in soot formation and in unburned hydrocarbons [45]. Although the mechanism causing this suppression is not well understood [46, 47], it is believed that a metal–induced decrease of OH concentration in the flame is responsible for the effect. Spatial distribution of the MOH and MOH^+ molecules (M=Ca,Sr,Ba) in the flame has shown that these species play the most significant role in soot suppression, with Ba>Sr>Ca in order of effectiveness [48]. The formation of soot particles in the combustion process is a very important consideration in the design of gas turbine and jet engines. Soot particles are a problem in locations where exhaust fumes from jet engines are prevalent (e.g. airports or military installations). Therefore, the fuel burned in these engines becomes an important consideration in the engine design. Health effects on human populations near such facilities need also to be considered [45]. It has therefore been suggested that the addition of alkaline earth metals to fuels could be an economical and convenient method to control soot formation in combustion processes. It is interesting to note that similar mechanisms (although not well un-

derstood) involving removal of OH radicals are believed to be important in both soot suppression in combustion processes and in the reduction of HCFC's impact on ozone depletion.

1.2 Nonlinear Molecules

The nonlinear alkaline earth–containing polyatomic molecules were first studied by Harris and co–workers [49] and then further extended by Bernath and co–workers [50]. These researchers used a Broida–type oven, which is a relatively high temperature (400-500K) molecular source that is convenient for Doppler–limited spectroscopic studies. In the course of experiments in the Bernath laboratory, an interesting aspect of the photochemistry of alkaline earth vapor reactions was discovered. It was found that if the atomic metal species was excited to the $^3P_1$ state, then the formation of product molecules was greatly enhanced [51]. This can be achieved by using a laser to drive the $^3P_1 \leftarrow ^1S_0$ transition of the metal atom with $\lambda = 6573, 6892, 7911$ Å for Ca, Sr and Ba, respectively. For example, the reaction of ground state Ca atoms with H_2O to make CaOH is endothermic by 1.17 eV (27 kcal/mol). The addition of 1.90 eV (44 kcal/mol) of energy from an external source (i.e. a laser) results in an exothermic reaction. The enhanced reactivity of excited alkaline earth atoms (M^*) became a very important discovery because it was soon realized that large polyatomic derivatives of Ca, Sr, and Ba could not be synthesized without laser excitation. The best example of this was the reaction of Ca^* atoms with cyclopentadiene (C_5H_6). The spectra of the resulting molecule, CaCp ($Cp = C_5H_5$), was not observed unless the laser exciting the Ca atoms was

present [52]. Using this method, the group led by Bernath was able to synthesize a wide variety of organometallic species such as the monomethyls (MCH_3, M=Ca or Sr) [53], monoalkoxides (MOR, R=CH_3,C_2H_5...) [51], monocarboxylates (MO_2CR) [54], monoalkylamides (MNHR) [55] and a host of others [56–62]. The use of a Broida oven severely limited the information derived from a spectrum particularly for the nonlinear polyatomic derivatives. This is because the spectra consisted of broad peaks from many overlapping lines which were a result of the relatively high temperature of the molecular source. Thus, rotational analysis was only possible in a few cases such as CaCCH [20], $CaCH_3$ [61] and SrNNN [57] using narrowband fluorescence techniques, while only a partial vibronic analysis was possible for most of the nonlinear polyatomic molecules [51–55, 63, 64].

Much of the recent work has been carried out with the supersonic molecular beam technique. This has allowed the study of nonlinear polyatomic molecules at high resolution. The low rotational (<10 K) and vibrational (< 300 K) temperatures allows detailed information on the fine structure, hyperfine structure, asymmetry splittings and dipole moments to be extracted from the spectra. The most novel and interesting examples of these free radicals are the ring bonding (η^5) alkaline earth half–sandwich molecules such as MCp ($Cp = C_5H_5$) and the isoelectronic MPy (Py=C_4H_4N). These are gas phase analogs of full sandwich molecules called metallocenes, the most celebrated of which is ferrocene ($FeCp_2$). The alkaline earth half–sandwich molecules were first synthesized by a laser–driven chemical reaction of excited M (^3P) atoms with cyclopentadiene in Broida oven [52]. The low resolution electronic spectrum of MCp was consistent with C_{5v} symmetry of a η^5–

coordinated complex. This assignment also led to the suggestion that MPy [56] also had a ring bonding geometry. These molecules were subsequently studied in great detail by the Miller group using a jet-cooled source [65–70]. Jet-cooled molecular spectroscopy facilitated an improved vibronic analysis on CaCp and showed weak Jahn–Teller induced bands that were not discernible in the high temperature spectrum [65]. The cold spectra eventually led to the first complete rotational analysis of an electronic transition of a half-sandwich molecule ($\tilde{A}^2E_1$–$\tilde{X}^2A_1$ transition of CaCp) [67]. The molecular beam experiments also found a misinterpretation in the electronic spectrum of CaPy which was assumed to have pseudo-C_{5v} symmetry [56]. That is, the replacement of CH in cyclopentadiene with N in pyrrole was not significant enough to change the electronic spectrum. Using this erroneous model, the first excited state of CaPy was assigned as a spin–orbit doublet, $\tilde{A}^2E_{1(1/2)}$ and $\tilde{A}^2E_{1(3/2)}$, because this splitting was of similar magnitude (68 cm^{-1}) to the CaCp spin–orbit splitting (56 cm^{-1}). The cold spectrum showed the vibrational progression of ν_{12}, the Ca–Py stretch, of the two "spin–orbit" components had different spacings, 248 cm^{-1} vs. 231 cm^{-1}. In CaCp, these modes have the same vibrational frequency of 329 cm^{-1}, indicating that the splitting in CaPy could not come from pure spin–orbit interactions. This interpretation was further supported by the jet-cooled spectra of the fully deuterated (d_4–CaPy) species. Therefore these bands were reassigned as two different electronic transitions, the $\tilde{A}^2A'$–$\tilde{X}^2A'$ and $\tilde{B}^2A''$–$\tilde{X}^2A'$ transitions of CaPy. The high resolution experiments illustrate the ability to extract a wealth of spectroscopic information from a cold spectrum. A vibronic band that typically has a full width at half-maximum (FWHM) of ~50 cm^{-1} in an Broida oven experiment

has a width of the order 1–2 cm^{-1} in a jet–cooled experiment.

Related studies include recent experiments on singly charged alkaline earth–containing complexes such as $Ca^+(H_2O)$ [71], $Mg^+(H_2O)$ [72] and their deuterated analogs. The molecules $Sr^+(H_2O)$, and $Sr^+(NH_3)_n$ (n=1–6) have also been studied [73, 74]. These species are analogous to the isoelectronic neutral Ca and Sr derivatives, $CaNH_2$, $SrNH_2$, $SrCH_3$. The binding energy (D_0 = 28 kcal/mol for $Ca^+(H_2O)$ [75]) between the metal and ligand in this case is predominately a long range electrostatic (ion–dipole) interaction. The perturbation of the metal atom orbitals by the bonding ligand is not as significant as the strong Coulombic interaction present in the Ca^+OH^- (D_0 = 95 kcal/mol [76]) or $Ca^+NH_2^-$ molecule. Therefore, the electronic transitions of the singly charged species lie close to the atomic ion resonance lines ($^2P \leftarrow ^2S$) which occur at much higher energies ($\geq$21500 cm^{-1}) than the transitions of the isoelectronic MOH and MNH_2 molecules.

1.3 Electronic Structure

The Broida oven work illustrated the close connection between the spectra of the polyatomic alkaline earth derivatives and the well–understood spectra of the alkaline earth monohalide molecules. It is well known that the electronic structure of the monohalide molecules is represented by a one–electron hydrogenic picture [50]. This leads to "simplicity" in the spectroscopy of these molecules, since we do not deal with high spin ($\vec{S}$) or high orbital ($\vec{L}$) angular momentum. The spectra of transition metal–containing molecules with high $\vec{S}$ and high $\vec{L}$ states can be difficult to interpret because of the high density of electronic states. Many of these

states are of relatively low energy ($\leq$10 000 cm^{-1}) [77, 78] and are populated at room temperature. The qualitative one–electron model applicable to the alkaline earth molecules allows for good predictions of many of the molecular properties in these systems. These predictions are in reasonable agreement with *ab initio* calculations [79], and also with the large amount of experimental data that is currently available [50, 80].

The basic properties of the alkaline earth monohalides (e.g. electronic origins, spin-orbit splittings, lifetimes, dipole moments, etc...) are well described by the ligand field model proposed by Rice, Martin and Field [81]. This model treats the ligand (X^-) as a point charge that influences the non–bonding valence electron on the metal (M^+) ion. For example, the Ca^+ ion is perturbed by the electrostatic field of the fluoride anion (F^-), with the Ca^+ ion modelled as a closed shell Ca^{2+} core with a single valence electron. The approach of the F^- ligand destroys the spherical symmetry of the $4s$ atomic orbital and gives rise to the X $^2\Sigma^+$ state of the CaF molecule. Figure 1.1 is a correlation diagram between the atomic orbitals of the Ca^+ ion and the electronic states of the isoelectronic CaF and $CaNH_2$ molecules. The Coulombic interaction of a polyatomic X^- ligand and an alkaline earth ion can give rise to surprisingly strong bonds ($D_{Ca\text{-}OH} = 4.11$ eV) for a transient free radical.

Electronic excitation of the molecule can be considered as a transition of the $4s$ electron to a predominately $4p$ orbital "belonging" to the Ca^+ ion. The doubly degenerate $4p\pi$ orbitals give rise to the $A^2\Pi$ state, while the $4p\sigma$ orbital results in the $B^2\Sigma^+$ excited state of the CaF molecule. Orbital mixing calculations performed for CaF by Rice *et al.* showed that the X state has ~80% $4s\sigma$ character and ~20%

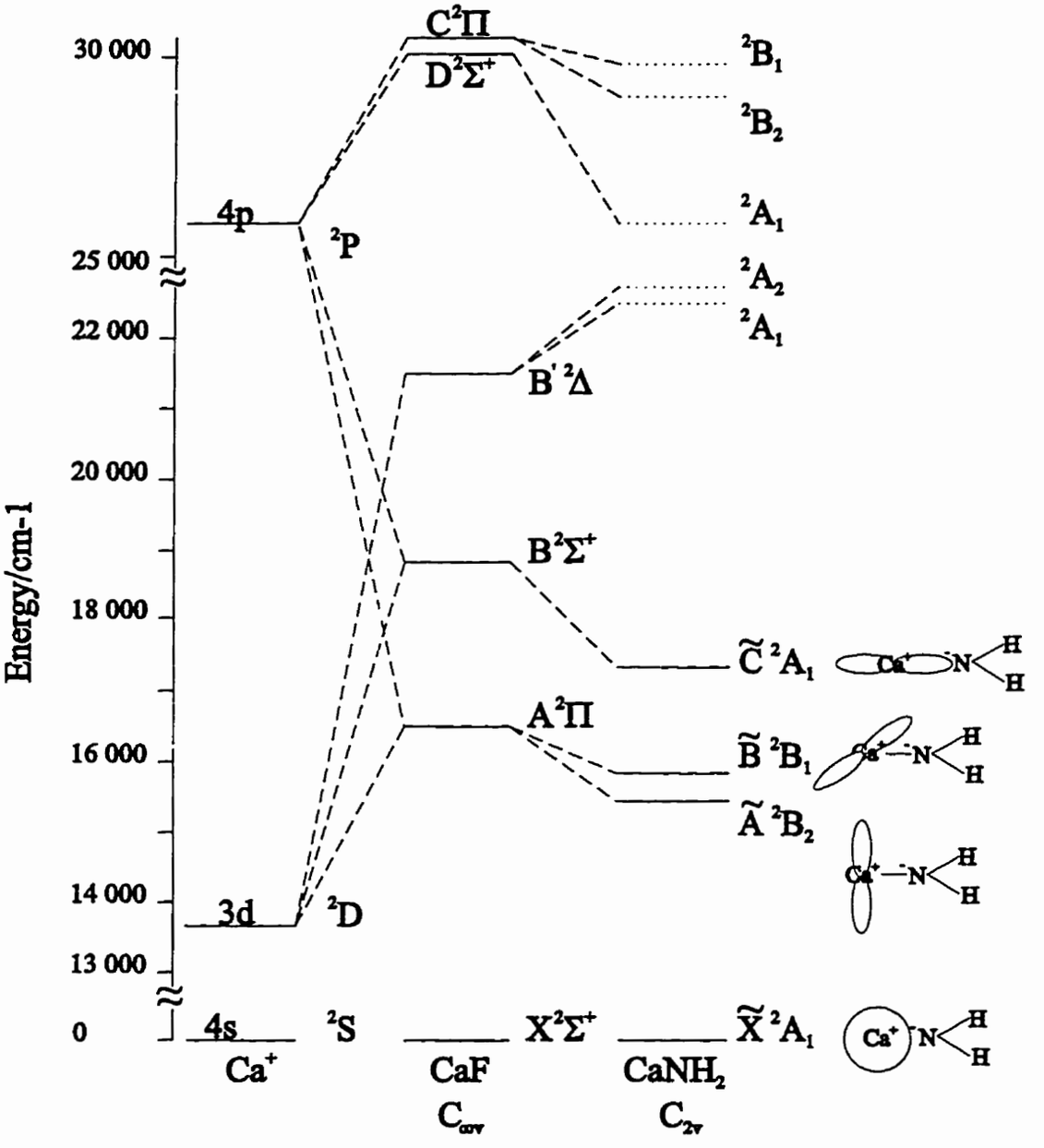

Figure 1.1: The correlation of atomic Ca^+ orbitals with the electronic states of CaF and $CaNH_2$. The solid lines represent known energy levels and the dashed lines are predicted [79] but not experimentally observed. The $^-NH_2$ group lies in the plane of the paper.

$4p\sigma$, while the $A^2\Pi$ state was a 70:30 mixture of $4p\pi$ and $3d\pi$ and the B $^2\Sigma^+$ state is approximately a 50:50 mixture of $4p\sigma$ and $3d\sigma$.

Further extension of the ligand field model is made by substituting the fluoride ligand with various polyatomic ligands such as OH^- [82], CCH^-, SH^-, NH_2^- or $C_5H_5^-$. This replacement lowers the symmetry of the molecule from $C_{\infty v}$ to C_{2v} for the NH_2^- ligand. In the $CaNH_2$ molecule, the $A^2\Pi$ state of CaF is further split into an in–plane ($\tilde{A}\ ^2B_2$ state) and an out–of–plane ($\tilde{B}\ ^2B_1$) state (fig. 1.1). The energy ordering of these two states can be deduced using a simple argument. There is a lone pair of electrons in a nitrogen $2p_x$ orbital perpendicular to the plane of the NH_2^- ligand. When the lone electron "belonging" to Ca^+ occupies the $4p\pi_x$ ($\tilde{B}\ ^2B_1$) orbital which is also perpendicular to the molecular plane, there will be greater electron–electron repulsion than if the lone electron occupied the $4p\pi_y$ orbital ($\tilde{A}\ ^2B_2$) that is parallel to the plane of the molecule (see fig. 1.2). Thus the $^2B_2$ state lies lower in energy than the $^2B_1$ state; this has been confirmed by *ab initio* electron propagator calculations by Ortiz [79].

Törring *et al.* [83] proposed another model to describe the electronic structure of the alkaline earth monohalides. Their ionic model allows for a displacement of the unpaired valence electron in order to take into account the polarization of this electron away from the ligand. The paper by Mestdagh *et al.* [82] states that the Törring *et al.* model is more flexible than the model of Rice *et al.* when dealing with polyatomic ligands such as OH^-. They extended the Törring *et al.* model to calculate dipole moments, bond dissociation energies and the location of excited electronic states for CaOH, SrOH and BaOH [82]. Their calculations of dipole

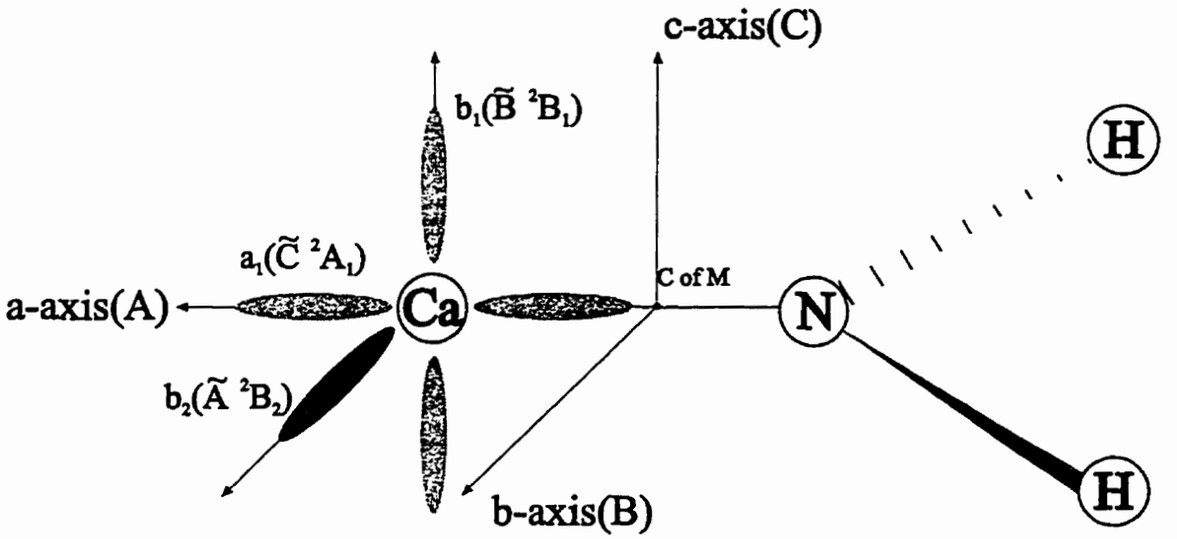

Figure 1.2: The direction of the principal axes and the atomic orbitals of Ca^+, which correlate to the electronic states of $CaNH_2$. This diagram should be compared with the correlation diagram of Fig. 1.1.

moments are in very good agreement with the ground state experimental dipole moments (for CaOH and SrOH [84]) which were not available to them at the time of publication. A natural extension of that work would be to carry out similar calculations for nonlinear ligands such as NH_2^-.

1.4 Chemistry Of Alkaline Earth Reactions

The chemistry and photochemistry of alkaline earth reactions were recently reviewed by Bernath [80]. The main aspects of the reaction mechanisms will be summarized here. Unlike the reactions of alkaline earth atoms in aqueous solutions, which can be vigorous and liberate substantial amounts of heat, the corresponding gas phase reactions are highly endothermic. The elementary reaction,

$$Ca(g) + H_2O(g) \longrightarrow CaOH(g) + H\ (g) \tag{1.1}$$

is endothermic by 27 kcal/mol, yet the CaOH molecule is generated in a Broida oven. The thermal energy available from vaporization is certainly not enough to overcome this reaction barrier. In fact, chemiluminescence from the excited electronic states of CaOH is observed, suggesting that CaOH is formed in its excited electronic states. It is also found that increasing the pressure inside the oven from 1 torr to about 10 torr increases the intensity of chemiluminescent emission. This suggests a mechanism that involves a third (inert) body in the rate controlling step.

There have been two possible mechanisms proposed [51]:

$$\begin{aligned} Ca + H_2O &\xrightarrow{Ar} HCaOH \\ HCaOH + Ca &\longrightarrow CaH + CaOH \\ CaH + H_2O &\longrightarrow CaOH + H_2 \\ \hline Ca + H_2O &\longrightarrow CaOH + \tfrac{1}{2}H_2 \end{aligned}$$

or the mechanism :

$$\begin{aligned} Ca + H_2O &\xrightarrow{Ar} HCaOH \\ HCaOH + H_2O &\longrightarrow Ca(OH)_2 + H_2 \\ Ca(OH)_2 + Ca &\longrightarrow 2CaOH \\ \hline Ca + H_2O &\longrightarrow CaOH + \tfrac{1}{2}H_2 \end{aligned}$$

It is still not clear which mechanism is appropriate and under what conditions. Reactions of Ca and Sr with the monocarboxylates [54] do form CaH or SrH which are observed in the spectrum, but reactions with alcohols [51] do not. Both mechanisms have the insertion of Ca in the OH bond of H_2O as the rate controlling step but the HCaOH molecule cannot be detected by conventional spectroscopic methods. It can be presumed that nonlinear derivatives such as $CaNH_2$ or CaCp involve insertion of Ca into the N–H or C–H bond but dynamical studies of these reactions have not been carried out. The dynamics of a few reactions of H_2O and ROH with alkaline earths have been studied and they show that the reactivity is strongly dependent on the electronic state of the alkaline earth atom [85–87] and

also on the size of the reacting species [88–90] . For example, ground state Ba atoms react with H_2O to give predominantly BaO product while ^1D Ba atoms favor the BaOH product, even though BaO is favored on energetic grounds [91]. There is a great need for experimental work on the kinetics and dynamics of the reactions before a good understanding of the reaction mechanisms can be achieved.

Table 1.1: Survey of the laboratory spectroscopic studies for the alkaline earth–containing polyatomic molecules up to June 1997.

Molecule	Method	Band System	Reference
CaOH and CaOD	A	$\tilde{X}$ state	[26,92]
	B,C	$\tilde{A}$–$\tilde{X}$	[14,15,84,93]
	B	$\tilde{C}$–$\tilde{X}$	[24,25]
	B (OODR)[1],D	high-lying states, $\tilde{D},\tilde{E},\tilde{F},\tilde{G}$	[27,28]
SrOH and SrOD	A	$\tilde{X}$ state	[94]
	B	$\tilde{A}$–$\tilde{X}$	[17]
	B,C	$\tilde{B}$–$\tilde{X}$	[18,95]
		$\tilde{C}$–$\tilde{X}$	
BaOH	B	$\tilde{A}$–$\tilde{X}$	[96]
MgOH and MgOD	A	$\tilde{X}$ state	[97]
CaNC	A	$\tilde{X}$ state	[98,99]
	B,C	$\tilde{A}$–$\tilde{X}$	[60,100]
SrNC	A	$\tilde{X}$ state	[98]
^{24}MgNC	A	$\tilde{X}$ state	[42,101]
^{25,26}MgNC	A	$\tilde{X}$ state	[102]
MgCN	A	$\tilde{X}$ state	[44,103]
CaCCH	A	$\tilde{X}$ state	[104]
	B,C	$\tilde{A}$–$\tilde{X}$	[19–22,105]
SrCCH	A	$\tilde{X}$ state	[106]
MgCCH	A	$\tilde{X}$ state	[107]
	C	$\tilde{A}$–$\tilde{X}$	[108]
SrNNN and CaNNN	B,C	$\tilde{A}$–$\tilde{X}$ and $\tilde{B}$–$\tilde{X}$	[57]
SrNCO	B	$\tilde{A}$–$\tilde{X}$	[58,109]
CaSH	A	$\tilde{X}$ state	[110]
	B	$\tilde{A}$–$\tilde{X}$	[59,111]
	C	$\tilde{B}$–$\tilde{X}$	[112]
SrSH			
$CaNH_2$	B,C	$\tilde{A}$–$\tilde{X}$	[49,55,105,113]
	B,C	$\tilde{B}$–$\tilde{X}$	[114,115]
	B,C	$\tilde{C}$–$\tilde{X}$	[116,117]
$SrNH_2$	B	$\tilde{A}$–$\tilde{X}$ and $\tilde{B}$–$\tilde{X}$	[118]
$CaCH_3$	B	$\tilde{A}$–$\tilde{X}$	[53,61,119]
$SrCH_3$	A	$\tilde{X}$ state	[120]
$MgCH_3$	A	$\tilde{X}$ state	[121]
	C	$\tilde{A}$–$\tilde{X}$	[122]
$CaBH_4$ and $SrBH_4$	B	$\tilde{A}$–$\tilde{X}$,$\tilde{B}$–$\tilde{X}$	[63]
$CaOCH_3$	B	$\tilde{A}$–$\tilde{X}$	[123]
CaC_5H_5	B,C	$\tilde{A}$–$\tilde{X}$	[52,65,67]
SrC_5H_5			
MgC_5H_5, $MgC_5H_4CH_3$, and MgC_4H_4N	C	$\tilde{A}$–$\tilde{X}$	[68]
CaC_4H_4N and SrC_4H_4N			[56]

A–Milimeter or microwave spectroscopy.
B– Laser–induced fluorescence (LIF) in a Broida oven.
C– LIF in a molecular beam.
D– REMPI in a molecular beam.
1–Optical–optical double resonance.

Chapter 2

Experimental Considerations

The alkaline earth molecules, particularly MOH were first identified and studied by emission in flames [32, 124]. As a source, flames are ideal for the production of alkaline earth hydroxides, but they suffer from extreme temperatures (~2000–3000K) and high pressures (~1 atm) which make high resolution spectroscopic studies rather difficult. The important advance that led to the study of not only the hydroxide molecules but also the amide species was made by Harris and co-workers [14,16,49,116]. They used a Broida oven, which is a suitable apparatus for vaporizing metals with low boiling points. Although high temperature versions of the Broida oven are possible, it is typically used for metals which can be vaporized at temperatures less than 1200°C. The Broida oven is therefore, a useful source to make alkaline earth containing diatomic and small linear polyatomic molecules for high resolution studies. In comparison to flames, the Broida oven is a relatively cool (400-500 K), low pressure (<10 torr) source of free radicals. Species can be produced by a suitable reaction of the metal atom with an oxidant molecule. This

reaction can produce fairly high concentrations of radicals ($\sim 10^{13}$ molecules/cm^3) which makes it possible to study them via chemiluminescent emission or by laser-induced fluorescence (LIF) techniques.

Spectral congestion and line broadening mechanisms play an important role in limiting the amount of information that can be derived from a spectrum of nonlinear polyatomic species synthesized in a Broida oven. This occurs because the metal atoms have to be thermally vaporized. For example, in order to obtain a 1 mtorr vapor pressure of calcium metal, the oven must be heated to 1000°C [125] before sufficient Ca atoms are present to yield the molecule of interest. Although the vaporized metal atoms are entrained in a flow of a room temperature inert bath gas (2–10 torr of Ar or He), the translational and internal temperature of the molecule can be quite high (400-500 K). Since large molecules have small rotational constants (< 0.1 cm^{-1}), a very large number of rotational quantum states can be populated at room temperature. This results in an enormous number of individual rotational lines present in a spectrum, leading to congestion. Another source of complexity arises from excited vibrational states. The vibrational degrees of freedom increase with the number of atoms in a molecule and this leads to the population of low frequency vibrational modes. Finally, spectral congestion can arise from Doppler and pressure broadening of rotational lines and collision–induced redistribution of excited state populations to produce non–resonant transitions. All of these mechanisms readily occur in the multiple collision environment of a Broida oven chamber. The combination of these factors cause the rotational structure to be washed out into broad features which give little information about molecular structure. The

complexity of the spectra can be avoided if the molecules were produced in an "ultracold", collision-free environment. The key requirements are that the product molecules remain in the gas phase with a density high enough to allow detection. The technique of supersonic molecular beam spectroscopy is the method of choice to meet these requirements.

2.1 Supersonic Free Jet Expansions

The typical way to cool a gas phase sample would be to use a cryogenic refrigerant such as liquid N_2 or He. As the gas of interest cools, it will most likely condense so this method is perhaps only useful for the study of molecules in the condensed phase. The ability to study isolated gas phase molecules, free of solvent or matrix effects, requires a free jet expansion. In the free jet, molecular rotations and vibrations are cooled to temperatures far below the freezing point with only a negligible amount of condensation. This takes place because the typical number of binary collisions a molecule experiences during the expansion is approximately 10^2 to 10^3 [126], most of which occur in the early stages of the expansion. Condensation is a n-body process ($n \geq 3$) and will therefore be an extremely slow process during the course of an expansion [127, 128].

A free jet is formed when gas molecules in a reservoir, kept at a high (> 1 atm) or ambient pressure, are allowed to expand through a small orifice into a region of low pressure. The gas flow is adiabatic and isentropic in the absence of viscous effects, heat transfer or shock waves caused by the background gas. The initially random thermal motion in the reservoir is converted to a directed forward motion

dependent on the pressure gradient between the reservoir and the expansion region. Since the gas will expand radially from the nozzle, the molecular density decreases as $1/x^2$ as the molecules move downstream from the source. The mean free path of a gaseous molecule in the expansion will eventually become >100 times the size of a typical molecule, so that collisions will be infrequent events when the molecules have traveled a short distance past the expansion nozzle.

The small number of collisions at relatively early stages of the expansion does not allow significant condensation, but rotational, vibrational, and translational cooling will readily take place. Translational cooling in a jet expansion does not result in a reduction in the average velocity of a gas, but corresponds to a narrowing of the velocity distribution. In fact the most probable velocity of a gas undergoing free jet expansion, termed the terminal velocity, is slightly higher than the r.m.s. speed of the same gas behind the nozzle before expansion (e.g. $v_{\text{r.m.s.}} = 1.37 \times 10^3$ m/s, $v_{\text{Terminal}} = 1.77 \times 10^3$ m/s for He at 300 K). The width of the velocity distribution is an important quantity because this gives a direct measure of the local translational temperature.

The molecules behind the nozzle move at many different velocities and in random directions. Since there is no preferred direction of motion the most probable velocity is zero for a static gas. The distribution of velocities is centered around this most probable velocity. The local temperature of the gas is reduced when most of the molecules move at velocities similar to the most probable velocity. Molecules with low energies have velocities close to zero, while at higher energies, molecules have higher velocities. Thus, as the temperature increases, the velocity distribution

becomes wider. In an expansion, the most probable velocity is non-zero, but most molecules move at velocities very close to the most probable velocity. At an early stage of an expansion, the pressure is relatively high. The molecules collide with each other allowing equilibration of the velocity components (transverse and longitudinal) along with the other degrees of freedom of the molecule. The temperature of the gas is lowered as additional molecules travel at approximately the same velocity as the most probable velocity. Since the gas molecules in the expansion travel in a uniform direction, the energy of collisions between molecules will eventually become relatively small even though their flow velocity can be large.

It has been shown that the translational temperature of an adiabatic isentropic expansion is given by [126, 127] :

$$\frac{T}{T_o} = W^{-1} \quad \text{where} \quad W = 1 + \frac{1}{2}(\gamma - 1)\mathrm{M}^2. \tag{2.1}$$

Here, $\gamma = \mathrm{C_p}/\mathrm{C_v} = 5/3$ for a monatomic gas, M is the Mach number, which is the ratio of the flow velocity divided by the local speed of sound. The other thermodynamic properties that can be calculated for an expansion are :

$$\frac{p}{p_o} = W^{-\gamma/(\gamma-1)} \quad \frac{\rho}{\rho_o} = W^{-1/(\gamma-1)}, \tag{2.2}$$

where, p is the pressure after expansion, p_o is the static pressure behind the nozzle, and ρ_o and ρ are the densities of the gas before and after expansion, respectively.

Free jet expansions are frequently characterized in terms of their Mach number. An expansion is referred to as supersonic not because of a high flow velocity but

because the local speed of sound has been reduced. This is because the local speed of sound is proportional to the square root of the translational temperature and is given by [126,127] :

$$v_s = \sqrt{\frac{\gamma RT}{m}}, \tag{2.3}$$

where R is the gas constant (8.314 J/K mol), T is the temperature in Kelvin and m is the molecular mass in kg/mol. The flow velocity remains essentially constant during an expansion, while the translational temperature dramatically decreases because the velocity distribution is narrowed. The flow quickly becomes supersonic (M>1). It should be noted that M reaches a finite terminal value because the ultimate flow velocity is limited by the initial kinetic energy of the gas prior to expansion :

$$v_T = \sqrt{\frac{C_p T_o}{m}} \qquad \text{and} \qquad M_T = 133(p_o D)^{\gamma/(\gamma-1)}. \tag{2.4}$$

Again, p_o(atm) and T_o(K) are the initial pressure and temperature of the gas before expansion and D is the nozzle diameter (cm), v_T and M_T are the terminal velocity and terminal Mach number. Thus, real expansions never reach the theoretical limit of infinitely narrow flow velocity distribution and zero translational temperature. Typical expansions of monatomic gases can reach very low translational temperatures. Calculations for a hypothetical expansion of He are shown in Table 2.1. The translational temperature and density decreases fairly rapidly for the first 5 nozzle diameters where the majority of collisions occur. In this distance, the mean velocity rises to within 98% of the terminal velocity. There is rough confirmation of these calculations in the published literature [129] and also in the work reported here, since the rotational temperatures approach within an order of magnitude for

Table 2.1: Thermodynamic properties of a free jet expansion measured in units of (x/D), the nozzle diameter. The various quantities were calculated for He gas assumed to have an initial temperature of 300 K and pressure of 10 atm, D for the calculations was 1 mm. The mean free path was calculated assuming a collisional cross-section of 50 Å^2. The last line in the table corresponds to the terminal Mach number from equation (2.4).

Distance (x/D)	Mach #	Velocity (m/s)	T (K)	Pressure (torr)	Density (molecules/cm^{-3})	mean free path (mm)
1	3.3	1551.4	66.04	172.81	2.78×10^{19}	5.09×10^{-5}
5	9.5	1728.5	9.59	1.39	1.54×10^{18}	9.20×10^{-4}
10	15.1	1745.4	3.88	0.14	3.96×10^{17}	3.57×10^{-3}
20	24.0	1752.3	1.55	1.46×10^{-2}	1.00×10^{17}	1.41×10^{-2}
30	31.5	1754.2	0.91	3.81×10^{-3}	4.46×10^{16}	3.17×10^{-2}
40	38.1	1755.0	0.62	1.46×10^{-3}	2.51×10^{16}	5.63×10^{-2}
50	44.3	1755.4	0.46	6.96×10^{-4}	1.61×10^{16}	8.78×10^{-2}
100	70.2	1756.3	0.18	6.92×10^{-5}	4.03×10^{15}	3.51×10^{-1}
150	92.0	1756.5	0.11	1.79×10^{-5}	1.79×10^{15}	7.89×10^{-1}
200	111.5	1756.6	0.07	6.87×10^{-6}	1.01×10^{15}	1.40
250	129.4	1756.7	0.05	3.27×10^{-6}	6.45×10^{14}	2.19
260.6	133.0	1756.7	0.05	2.85×10^{-6}	5.94×10^{14}	2.38

the calculated translational temperature of Table 2.1 at 150 nozzle diameters.

It can be seen that the internal degrees of freedom of the molecule should readily approach these characteristic low translational temperatures, especially for seeded expansions of a molecular species in He (or other inert gases). This is because a seeded expansion typically has low concentrations of a molecular species, so that most of the collisions a molecule experiences will be with the carrier gas. The rotational and vibrational cooling will take place primarily in the early portion of the expansion where most of the intermolecular collisions take place. This cooling is determined by the kinetics and not by the thermodynamics of the expansion. The internal energy of the molecule will quickly redistribute within the first few nozzle

diameters from the source. After an initial relaxation, the molecule will "freeze" into a non-equilibrium distribution. This is because the gas density decreases very rapidly away from the nozzle and collisions become infrequent. The rotational temperature will approach the translation temperature because only a moderate number of collisions (10–100) are required to cool rotational motion [126]. This is largely a function of the magnitude of the rotational constant (B) of a molecule. Molecules with small rotational constants require fewer collisions to cool their populations making this a very fast process in an expansion. Vibrational temperatures, on the other hand, will be significantly higher because vibrational spacings are $\sim$1000 times larger than rotational spacings which makes vibrational cooling a slower process then rotational cooling. Therefore, rotational temperatures of the order of 0.5 K can easily be achieved [130] but vibrational temperatures can typically range from 10–200 K depending on the vibrational frequencies. Condensation is the slowest process of all because, unlike rotational and vibrational cooling which only require energy exchanges between two bodies, condensation requires a minimum of two bodies to stick together. A third body is then required to remove the excess energy released in the formation of this bond. With the rapidly decreasing molecular density in an expansion, a third body colliding during the time of a two–body collision is highly unlikely. The molecules are therefore cooled far below their freezing point without condensation and, in effect, the molecules are supercooled.

The above discussion is appropriate for continuous beams but most researchers use pulsed molecular beam sources to reduce pumping requirements. Saengar and Fenn [131] used a simple model from gas dynamics and an idealized pulsed valve to

estimate the time required for a gas to reach steady–state flow of a molecular beam. They calculated minimum valve–open times for Ar, He and N_2 gases at pressures ranging from 200 to 2000 torr. It was found that valve–open times of the order of 1–5 μs were required for the gas flow to reach steady–state conditions. In the experiments reported here, the pulsed valve typically remains open for on the order of 100 μs.

2.2 Laser Vaporization and Radical Production

There have been several excellent reviews on the molecular beam spectroscopy of transient molecules in recent years [132–137]. The traditional method of studying metal–containing molecules in molecular beams was by using a high temperature oven to vaporize metals which were subsequently expanded with inert gases. This method was useful to study homogeneous metal clusters [138]. Techniques which generate more interesting metal–containing radicals relied on forming them prior to expansion in a molecular beam. These species proved difficult to synthesize because they are very reactive and short–lived and usually do not survive the high pressure (source) region of a molecular beam.

The use of a laser to vaporize metals was implemented shortly after the invention of the laser. The plasma emission of ablated metals was studied and researchers found sharp emissions lines in the UV and XUV which were attributable to highly excited and highly ionized atoms [139]. Lasers can have very short pulsewidths (few ns or less) that result in high power densities (10^8–10^9 W/cm^2). At these laser intensities, all metals, regardless of their physical properties can be vaporized.

A large portion of the laser radiation is absorbed by the metal so even refractory metals (Al, Pt [140], Ni [141], W, etc...) can be vaporized by this method [138]. A typical laser pulse will eject between 10^{13}–10^{17} atoms which are formed predominantly in their excited states. For metals such as Ca and Mg, approximately 10% of the atoms can be singly ionized [134] leading to chemical reactions producing novel ionic radicals containing metals [132].

An important development in the spectroscopic studies of free radicals was the discovery that chemical synthesis can be achieved with laser vaporized atoms. For example, Schaeffer *et al.* [142] showed that laser–vaporized carbon, expanded with H_2 gas, produced acetylene, while vaporized boron produced BCl_3 in a reaction with HCl. These molecules are not free radicals but the experiments showed that chemical reactions of laser–vaporized species was feasible. Further developments in this field included the study of heterogeneous metal clusters [138,143] and the study of organic free radicals through laser photolysis of an organic precursor [144]. The combination of these two methods opened a new area of study, the spectroscopy of organometallic free radicals [128]. This was an accidental discovery by the Smalley group, when the spectroscopy of small clusters of aluminum was being investigated. They were able to synthesize Al_x–acetone (x=1,2,...) and Al_x–acetyl complexes [143], where the acetone was present as a minor impurity in the helium seed gas. This was a breakthrough experiment because it combined the techniques of pulsed molecular beams, laser ablation of a metal, and detection via laser photoionization time–of–flight mass spectrometry (TOFMS). This work has now made the Smalley source ubiquitous in spectroscopic studies of metal–containing free radicals and

unstable molecules.

The spectroscopy of the alkaline–earth containing free radicals was first carried out by Whitham and co–workers [105,115]. In an interesting series of experiments, they studied reactions of laser vaporized calcium with H_2O, HCCH, CH_3CN and NH_3. They generated the CaOH, CaCCH, CaNC and $CaNH_2$ molecules using a Smalley source, with laser–induced fluorescence (LIF) detection. Partially resolved rotational spectra were recorded of the $\tilde{A}$–$\tilde{X}$ and $\tilde{B}$–$\tilde{X}$ transitions of these molecules. The spectra were only partially resolved because the pulsed dye laser had a line width of $\sim$0.15 cm^{-1} and the molecules were relatively hot because they were interrogated only 1 cm downstream from the nozzle. Simulations of the spectra were performed using previously published constants, and it was found the rotational temperature of CaOH was 100 K for an expansion in He and 15 K for an Ar expansion.

High resolution molecular beam studies were later completed by Steimle and co-workers [84] with a rotational temperature of $\leq$ 10 K. They combined a tunable single–mode cw laser (1 MHz linewidth) with a pulsed molecular beam. The signal–to–noise ratio in these experiments is lower than in the equivalent experiment using a pulsed laser because of the mismatch in the duty cycle of the pulsed source and the cw laser. Most of the photons of the cw laser are wasted since the interrogation time for molecular fluorescence is on the order of 20–40 μs. This method is perhaps the simplest way to carry out high resolution studies, and it has proven to be an effective method for recording the spectra of the electronic transitions of alkaline earth derivatives (see Table 1.1). Miller and co–workers have used another approach

by using a pulsed probe laser that has a near Fourier–transform limited line width (~200 MHz) obtained by pulse amplifying the light from a single–mode cw laser.

2.3 Experimental Setup

The experimental setup is a combination of a laser ablation source with a free jet supersonic molecular beam expansion. The apparatus consists of a dual compartment differentially pumped chamber. The source compartment is pumped by a 10" diffusion pump (250/2000 Edwards) while the detection compartment is pumped by a 4" (100/300 Edwards) diffusion pump. The experimental arrangement is shown in Fig. 2.1.

The supersonic molecular beam is produced with a commercial (General Valve) solenoid–type pulsed valve with a 1 mm nozzle diameter. Connected to the valve is a stainless steel holder which accepts a metal rod of up to 8 mm in diameter (Fig. 2.2). The metal rod is vaporized by the fundamental (1.064 μm) or the second harmonic (532 nm) of a pulsed (10 Hz) Nd:YAG laser. The rod is continuously rotated and vertically translated during the experiment allowing the laser to interrogate a fresh surface of the rod with each pulse. This is done to improve the shot–to–shot stability in the metal atom density by preventing the Nd:YAG laser from drilling a hole into the rod. The ablation laser is focused through a 1 mm hole of the stainless steel holder which is at the center of a 10×1 mm expansion channel. The channel is the region in which the vaporized metal atoms react with oxidant gas molecules. This gas is premixed on the high pressure side of the pulsed valve and typically consists of 5–10 % of the precursor in an inert gas (Ar or He). After the ensuing reaction

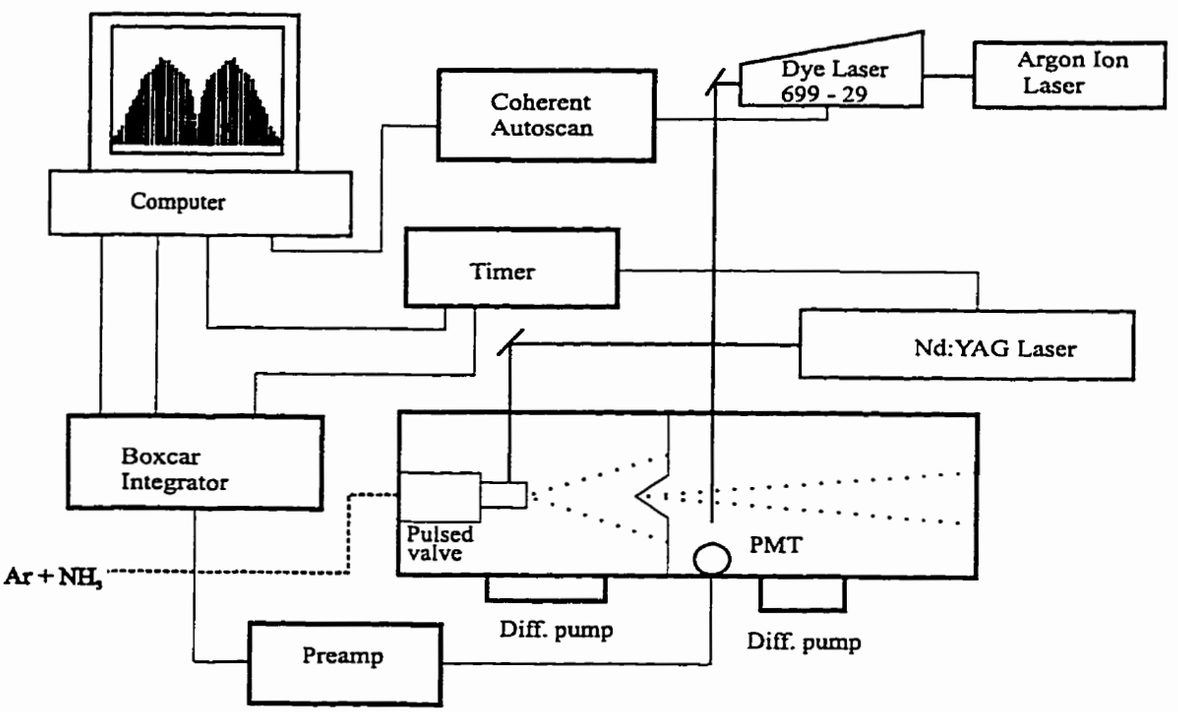

Figure 2.1: Block diagram of the experimental setup for the molecular beam apparatus.

occurs in the channel, the product molecules subsequently expand into the detection chamber. The molecular fluorescence signal is detected ~15 cm downstream from the point of ablation. This is achieved by crossing a probe laser perpendicular to the propagation of the molecular beam and monitoring the LIF. The LIF is collected in a mutually orthogonal axis to the laser and the molecular beam by a combination of two short focal length lenses separated by a 5 mm aperture. The aperture acts as a spatial filter which reduces Doppler broadening by imaging a small fraction of the molecular beam onto the cathode of a photomultiplier tube (PMT). Optical filtering is carried out using a narrow bandpass filter (±10 nm) to suppress noise caused by plasma emission and scattered laser light. The probe laser for these experiments is a cw argon ion (Coherent Innova 200) pumped ring dye laser (Coherent Autoscan 699-29). The laser is continuously tunable over the entire range of a dye (580–620 nm for R6G dye) with a 1 MHz linewidth in single–mode operation.

The timing of the experiment is hardware and software controlled by a 386 personal computer. A trigger pulse generated by an A/D interface card in the PC is sent to a home–built trigger control box. The control box sends a signal to a pulsed valve driver which in turn sends a high voltage to the pulsed valve. The high voltage pulse is generated 550 μs after the initial trigger pulse from the control box. The pulsed valve can remain open for a variable length of time (10–1000 μs) but for a typical experiment, the valve is open for ~100 μs. The Q–switch of a Nd:YAG (Continuum Surelite) is fired approximately 30 μs after the pulsed valve opens and generates a 10 ns pulse of laser light. The laser ablates the metal from the surface

of the rod forming a plasma which reacts with the gas pulse containing the oxidant molecules. The molecular beam, which now consists of a small concentration of radicals in an inert bath gas, expands through the channel into the detection region where it is intersected by the probe laser. A boxcar integrator is used to gate the fluorescent signal from the radicals as they pass through the detection volume of the probe laser. The time window to observe the LIF is 20–40 μs wide. The boxcar is gated to begin integration of the LIF signal approximately 200 μs after the ablation laser pulse in an expansion with Ar or 80 μs for a He expansion. The probe laser can either be scanned continuously or in step–scan mode. In both cases, data points are taken in 50 MHz frequency intervals (of the laser) at a sufficient rate to obtain 2–5 Nd:YAG laser shots per data point. Calibration of the probe laser is achieved by picking off a small fraction of the beam and simultaneously recording the LIF spectrum of I_2 [145, 146] in a static gas cell. The LIF spectrum from the molecular beam apparatus and I_2 is recorded digitally by the Coherent Autoscan software.

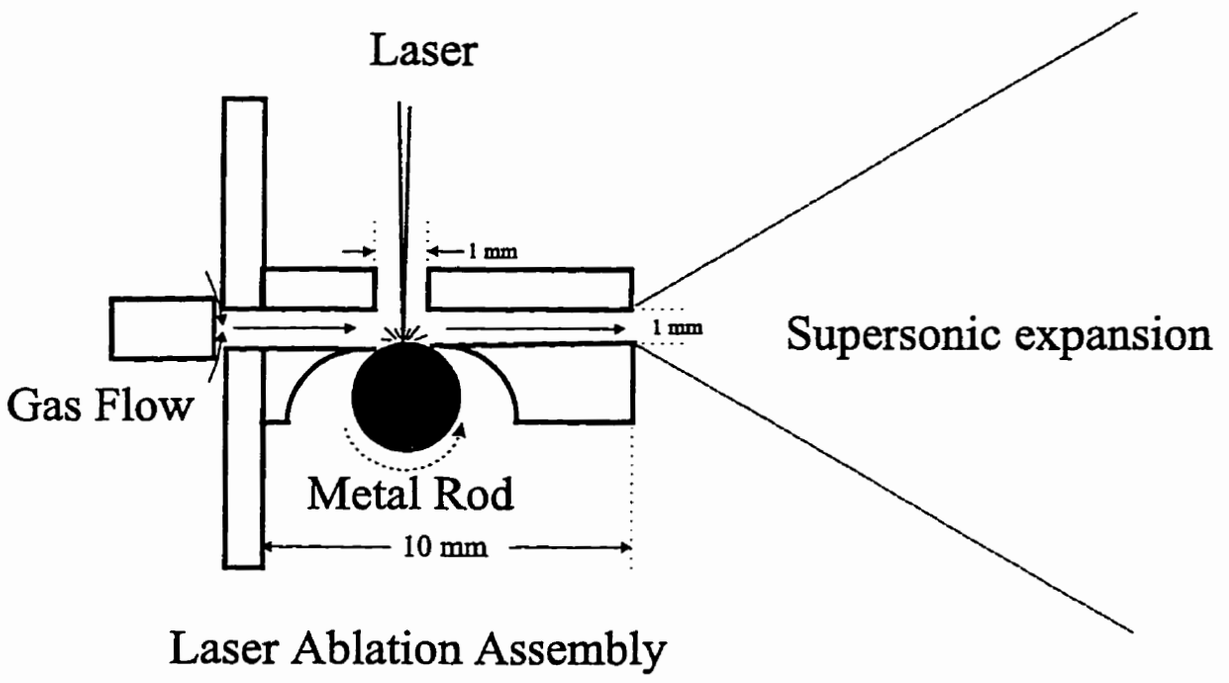

Figure 2.2: A schematic diagram of ablation assembly in the molecular beam spectrometer. Diagram is not to scale

Chapter 3

Molecular Hamiltonians

Molecular rotation is a very important aspect of high resolution spectroscopy. The coupling of this motion with that of the electrons, and with the vibrations of the nuclei gives rise to patterns (although very complex in some cases) in molecular spectra. The theoretical understanding of these interactions via quantum mechanics is necessary to interpret these signals from the microscopic world.

The different angular momenta in a molecule couple to give a resultant total angular momentum $\vec{\mathbf{J}}$. $\vec{\mathbf{J}}$ is the vector sum of the electron spin ($\vec{\mathbf{S}}$), electron orbital angular momentum ($\vec{\mathbf{L}}$) and molecular rotation angular momentum ($\vec{\mathbf{R}}$). For diatomic and linear polyatomic molecules, Hund described five limiting cases, denoted case (a) through to case (e) [147]. Hund's case (a) and case (b) are by far the most important and commonly observed cases in diatomic and linear polyatomic spectra. The difference between case (a) and case (b) is determined by the quantity $\mid \frac{A}{2BJ} \mid$, where A is the spin–orbit coupling constant and B is the rotational constant of the molecule and J is the rotational angular momentum quantum number. If

$| \frac{A}{2BJ} | \gg 1$ but less than the separation between electronic states then Hund's coupling case (a) results. In this scheme, the electronic motion ($\mathbf{L}$ and $\mathbf{S}$) is strongly coupled to the internuclear axis. The projection of the spin angular momentum (Σ) and orbital angular momentum (Λ) on to the molecular axis is well defined, even during molecular rotation. The sum of these two projections gives Ω, where $\Omega = \Lambda + \Sigma$. The nuclear rotational angular momentum ($\mathbf{R}$) couples with $\Omega\mathbf{r}$ to form the resultant total angular momentum $\mathbf{J}$, where $\mathbf{J} = \mathbf{R} + \Omega\mathbf{r}$, and $\mathbf{r}$ is a unit vector along the internuclear axis (Fig. 3.1). When the magnitude of $| \frac{A}{2BJ} |$ is small, the case (b) coupling case is appropriate. In this case, the electron spin ($\mathbf{S}$) is very weakly coupled to the internuclear axis. The orbital angular momentum $\mathbf{L}$ couples with nuclear rotation $\mathbf{R}$ to give, $\mathbf{N} = \mathbf{R} + \mathbf{L}$, which is the total angular momentum excluding electron spin. Then, $\mathbf{N}$ and $\mathbf{S}$ couple to give $\mathbf{J}$, the total angular momentum. This coupling case is illustrated in fig. 3.2. Notice that as a result of the J dependence in $| \frac{A}{2BJ} |$, it is possible to change from Hund's case (a) at low J to Hund's case (b) at high J. These limiting Hund's cases were first used to describe angular momentum coupling in diatomic and linear molecules, but in some cases, they are also applicable to nonlinear polyatomic molecules.

3.1 Symmetric Top Molecules

Molecular rotation of polyatomic molecules can be described in two different coordinate systems, the space–fixed coordinates X,Y,Z or the molecule–fixed coordinate system x,y,z (or a,b,c see below). These two coordinate systems have the same origin and are connected by a unitary transformation matrix whose elements are the

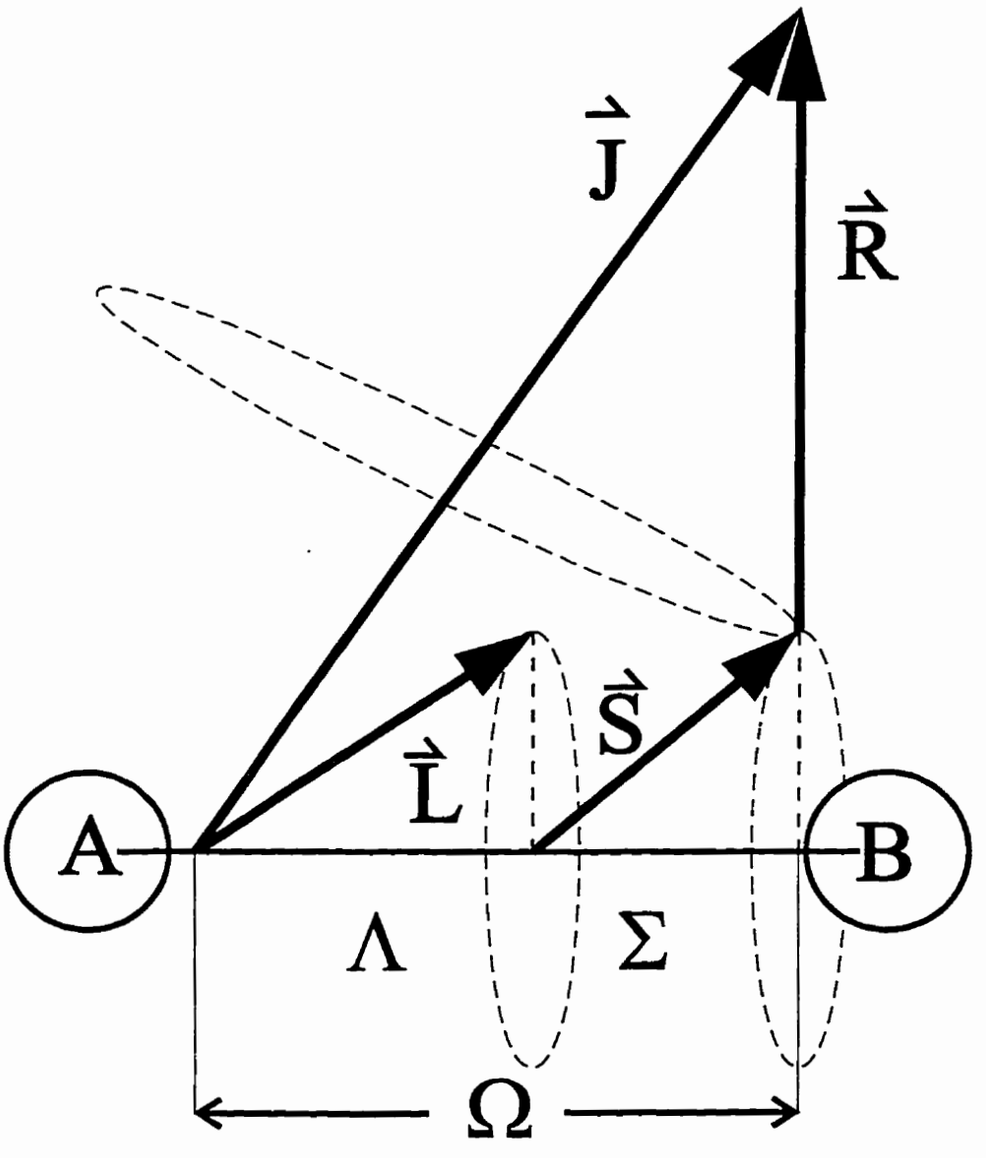

Figure 3.1: Hund's case (a) coupling.

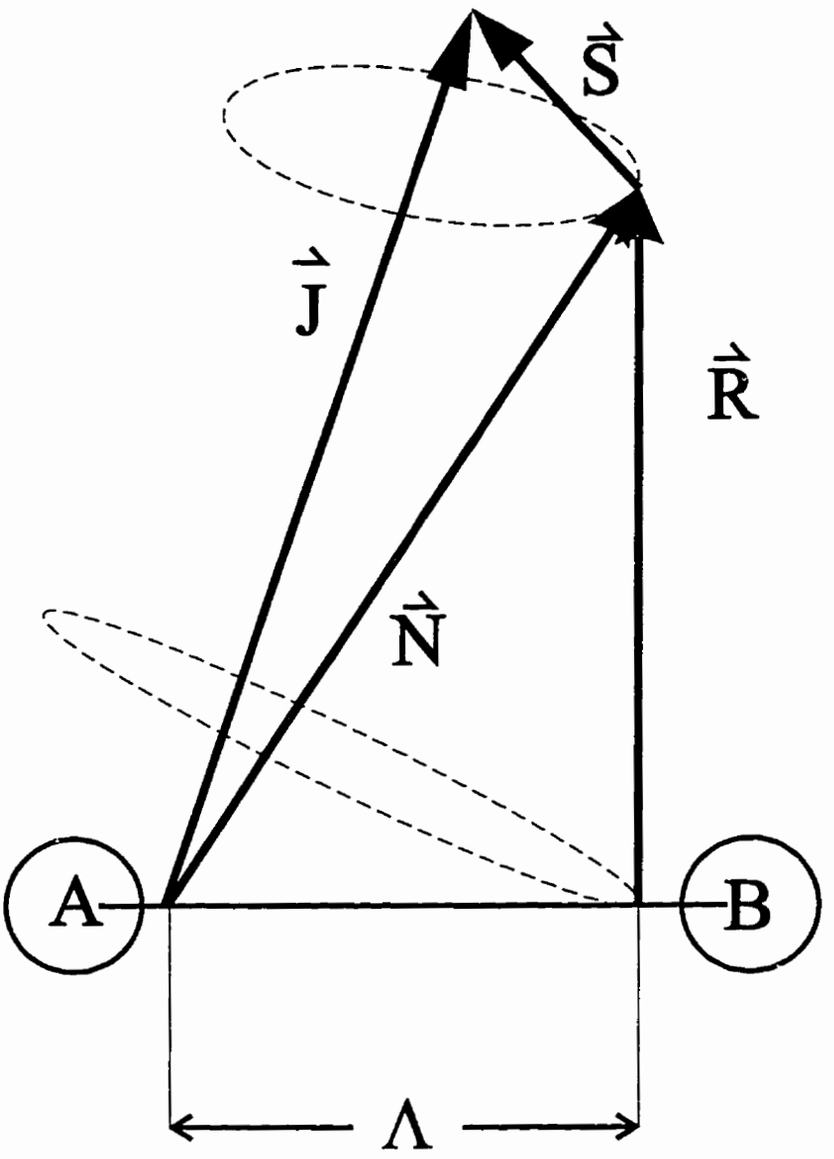

Figure 3.2: Hund's case (b) coupling.

direction cosines [1, 148] :

$$\begin{pmatrix} x \\ y \\ z \end{pmatrix} = \mathbf{S} \begin{pmatrix} X \\ Y \\ Z \end{pmatrix} = \begin{pmatrix} \phi_{xX} & \phi_{xY} & \phi_{xZ} \\ \phi_{yX} & \phi_{yY} & \phi_{yZ} \\ \phi_{zX} & \phi_{zY} & \phi_{zZ} \end{pmatrix} \begin{pmatrix} X \\ Y \\ Z \end{pmatrix} \tag{3.1}$$

where the elements of **S** are a 3×3 matrix of the direction cosines in vector algebra :

$$\mathbf{S} = \begin{pmatrix} \cos\theta\cos\phi\cos\chi & \cos\theta\sin\phi\cos\chi & -\sin\theta\cos\phi \\ -\sin\phi\sin\chi & +\cos\phi\sin\chi & \\ -\cos\theta\cos\phi\sin\chi & -\cos\theta\sin\phi\sin\chi & \sin\theta\sin\chi \\ -\sin\phi\cos\chi & +\cos\phi\cos\chi & \\ \sin\theta\cos\phi & \sin\theta\sin\phi & \cos\theta \end{pmatrix} \tag{3.2}$$

The θ, ϕ, and χ are the Euler angles which relate the space–fixed coordinates (X, Y, Z) to the molecular coordinate system $(x, y, z$, see Fig. 3.3). The angular momenta can be measured in the space–fixed frame or the molecular frame by the relations :

$$\hat{J}_x = \Phi_{xX}\hat{J}_X + \Phi_{xY}\hat{J}_Y + \Phi_{xZ}\hat{J}_Z \tag{3.3}$$

$$\hat{J}_y = \Phi_{yX}\hat{J}_X + \Phi_{yY}\hat{J}_Y + \Phi_{yZ}\hat{J}_Z \tag{3.4}$$

$$\hat{J}_z = \Phi_{zX}\hat{J}_X + \Phi_{zY}\hat{J}_Y + \Phi_{zZ}\hat{J}_Z \tag{3.5}$$

The total angular momenta $\hat{J}_i$ $(i = X, Y, Z)$ satisfy the usual commutatation

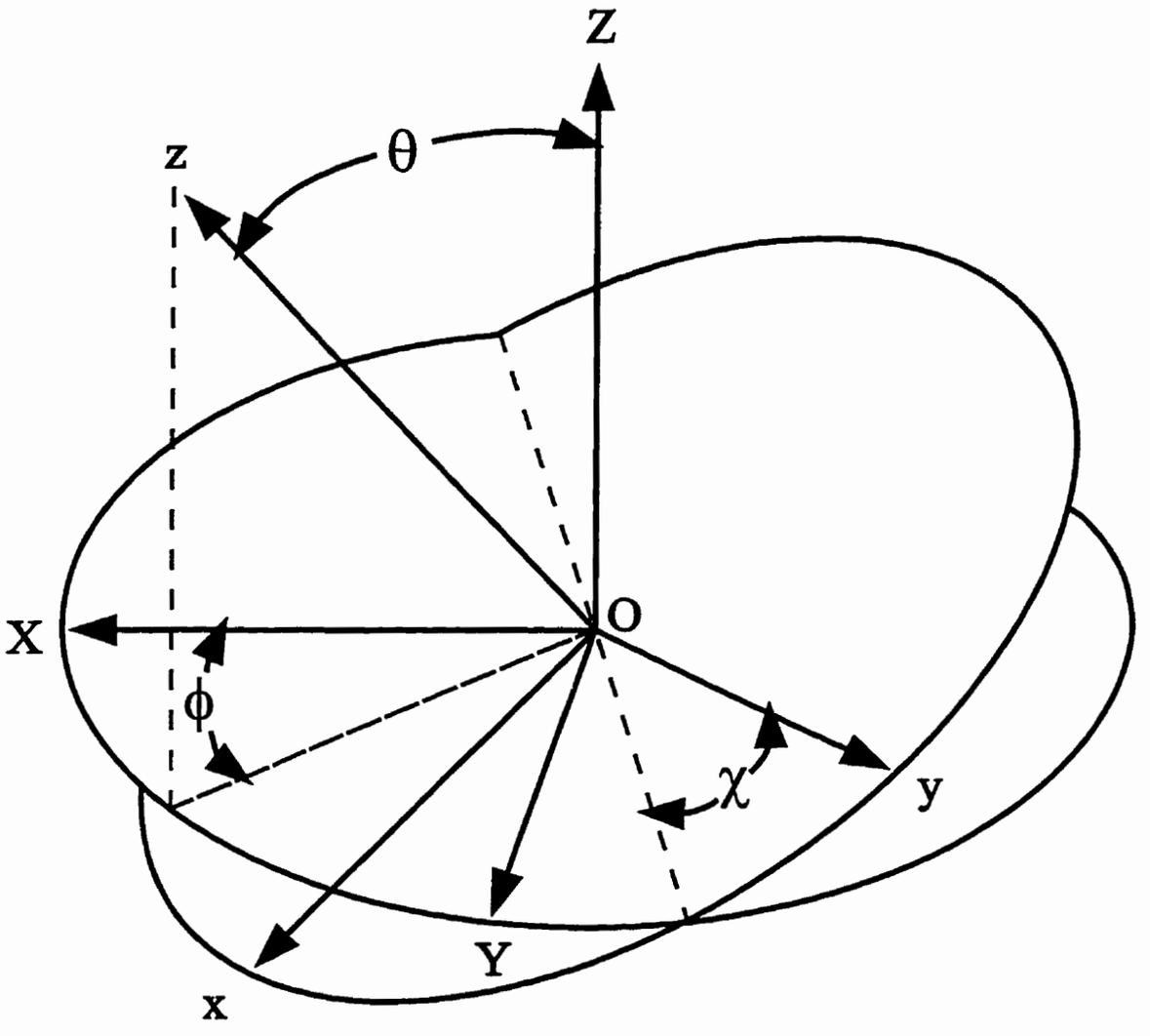

Figure 3.3: The Euler angles θ, ϕ and χ that relate the space–fixed coordinate system (X, Y, Z) to the molecular coordinate system (x, y, z).

relationships :

$$[\hat{J}_X, \hat{J}_Y] = i\hbar\hat{J}_Z, \tag{3.6}$$

and the square of the total angular momentum commutes with its components :

$$[J^2, \hat{J}_i] = 0. \tag{3.7}$$

The only unusual commutation relationships occur in the molecule fixed coordinate system :

$$[\hat{J}_x, \hat{J}_y] = -i\hbar\hat{J}_z, \tag{3.8}$$

$$[\hat{J}_y, \hat{J}_z] = -i\hbar\hat{J}_x, \tag{3.9}$$

$$[\hat{J}_z, \hat{J}_x] = -i\hbar\hat{J}_y. \tag{3.10}$$

These are called anomalous commutation relationships and they become important when defining the raising and lowering operators in the molecular frame. The space fixed raising and lowering operators, $\hat{J}_\pm$, give the usual result :

$$\hat{J}_\pm \mid J\,K\,M\rangle = \hbar[J(J+1) - M(M \pm 1)]^{\frac{1}{2}} \mid J\,K\;M \pm 1\rangle, \tag{3.11}$$

while the molecule fixed operators, $\hat{J}^\pm$, give an anomalous result :

$$\hat{J}^\pm \mid J\,K\,M\rangle = \hbar[J(J+1) - K(K \mp 1)]^{\frac{1}{2}} \mid J\,K \mp 1\;M\rangle. \tag{3.12}$$

The anomalous commutation relationships in the molecular frame mean that $\hat{J}^+(=$

$\hat{J}_x + i\hat{J}_y$) is a lowering operator and $\hat{J}^-$ is a raising operator.

Let us consider the rigid rotation of a symmetric top molecule. A symmetric top is defined as a molecule where two of the three principal moments of inertia are equal. It is usual to choose the z–axis as the symmetry axis. The classical energy expression for the rotational energy of a rigid body is given by :

$$\begin{aligned} \mathrm{E_R} &= \frac{1}{2}(I_x\omega_x^2 + I_y\omega_y^2 + I_z\omega_z^2) \\ &= \frac{1}{2}\Big(\frac{J_x^2}{I_x} + \frac{J_y^2}{I_y} + \frac{J_z^2}{I_z}\Big), \end{aligned} \tag{3.13}$$

where ω is the angular velocity and **J** is the angular momentum, with $\mathbf{J} = \mathrm{I}\omega$. From the classical expression we can write the quantum mechanical version of the rotational energy in the molecular frame :

$$\hat{\mathrm{H}}_\mathrm{R} = \frac{\hat{J}^2}{2I_B} + \Big(\frac{1}{2I_A} - \frac{1}{2I_B}\Big)\hat{J}_z^2. \tag{3.14}$$

The expression here is appropriate for a prolate symmetric top, where with $I_B = I_C$, $A = x$, $B = z$, $C = y$. For an oblate symmetric top ($I_A = I_B$), the I_A in eqn. (3.14) should be replace by I_C. The rotational constants are defined as :

$$A = \frac{\hbar^2}{2I_A} \qquad B = \frac{\hbar^2}{2I_B} \qquad C = \frac{\hbar^2}{2I_C} \tag{3.15}$$

with $A \geq B \geq C$, the equal sign is appropriate for symmetric tops and the greater than sign is for asymmetric tops. Clearly it can be seen that $\hat{J}^2$, $\hat{J}_z$, $\hat{J}_Z$ all commute

with $\hat{\mathrm{H}}_{\mathrm{R}}$; thus, we can obtain a common set of eigenfunctions $\mid JKM\rangle$ where :

$$\langle JKM \mid \hat{J}^2 \mid JKM\rangle = J(J+1)\hbar^2 \tag{3.16}$$

$$\langle JKM \mid \hat{J}_Z \mid JKM\rangle = M\hbar \tag{3.17}$$

$$\langle JKM \mid \hat{J}_z \mid JKM\rangle = K\hbar \tag{3.18}$$

The quantity $K\hbar$ is the projection of the total angular momentum J on the molecular z–axis. The expression for the energy obtained from the rigid rotor Hamiltonian H_{R} becomes;

$$\langle JKM \mid \hat{\mathrm{H}}_{\mathrm{R}} \mid J'K'M'\rangle = E_R \delta_{JJ'}\,\delta_{KK'}\,\delta_{MM'}$$

$$\text{where} \qquad E_R = BJ(J+1) + (A-B)K^2 \quad \text{(prolate top)}, \tag{3.19}$$

$$\text{or}$$

$$= BJ(J+1) + (C-B)K^2 \quad \text{(oblate top)}, \tag{3.20}$$

where A, B, C are defined in eqn. (3.15). The energy level expression for the matrix elements of $\hat{\mathrm{H}}_{\mathrm{R}}$ involve the square of the quantum number K (projection of J on the molecular z–axis) and does not include M (projection of J on the space fixed axis). There are $(2J+1)$ possible values of K for every J, but since a projection of a vector cannot be larger than the vector itself, $K \leq J$. A partial degeneracy of the $2J+1$ rotational states still remains, since states with $\pm K$, corresponding to clockwise or anticlockwise rotation about the molecular z–axis, have the same energy for a symmetric top molecule. For example, for a rotational state with $J=1$, there are a possible $2J+1=3$ levels, and in the prolate (oblate) symmetric

top limit, levels with $K = \pm 1$ are degenerate while $K = 0$ has a different energy. In an asymmetric top molecules, a three "K levels" are non–degenerate (Fig. 3.4). In an asymmetric top molecule K is no longer well–defined quantum number but remains a useful label.

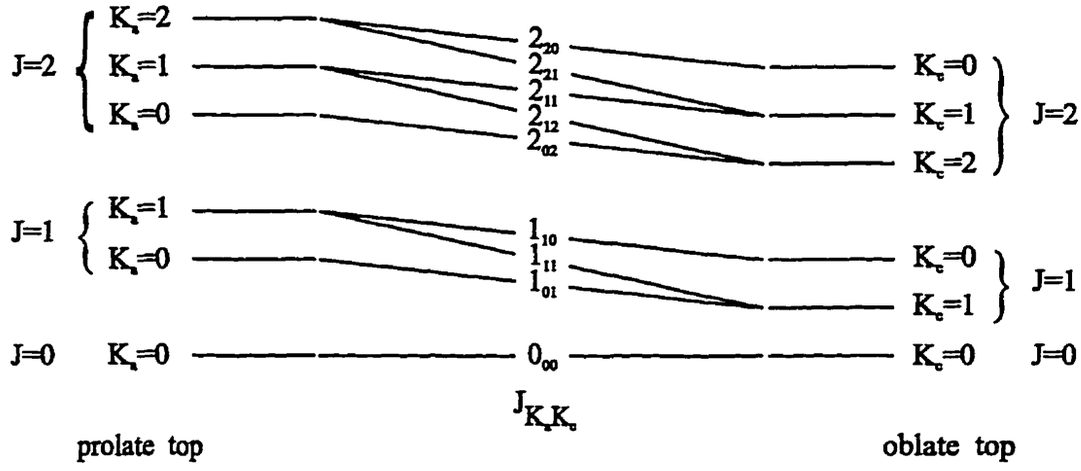

Figure 3.4: The correlation diagram of prolate and oblate symmetric top rotational levels. The center of the figure shows the labeling appropriate for asymmetric top levels.

3.2 Asymmetric Top Molecules

Asymmetric top molecules generally belong to Hund's case (b). This is because the orbital angular momentum in an asymmetric top is nearly quenched and is therefore not strongly coupled to the rotational axes of the molecule. Since asymmetric top molecules have three different moments of inertia, their energy levels are complicated functions of the three rotational constants. The effective Hamiltonian is

made up of the following terms :

$$\hat{H}_{eff} = \hat{H}_R + \hat{H}_{CD} + \hat{H}_{SR}. \tag{3.21}$$

$\hat{H}_R$ is the pure rotational Hamiltonian, $\hat{H}_{CD}$ is the centrifugal corrections to the rotational Hamiltonian and $\hat{H}_{SR}$ is the spin–rotational Hamiltonian.

The pure rotation Hamiltonian for an asymmetric rotor is :

$$\hat{H}_R = A\hat{J}_a^2 + B\hat{J}_b^2 + C\hat{J}_c^2, \tag{3.22}$$

where the molecule fixed coordinates are designated (a, b, c) rather than (x, y, z) by following the convention of the rotational constants, $A > B > C$. A simple analytical form for the eigenfunctions for $\hat{H}_R$ is not possible, but rearranging the eqn. (3.22) in terms of $\hat{J}^2$, can make the evaluation of matrix elements simpler. The Hamiltonian appropriate for a near prolate ($A \gg B \simeq C$) asymmetric top becomes:

$$\hat{H}_R = \frac{1}{2}(B+C)\hat{J}^2 + \left(A - \frac{1}{2}(B+C)\right)\hat{J}_a^2 + \frac{1}{2}(B-C)(\hat{J}_a^2 - \hat{J}_c^2). \tag{3.23}$$

The first two terms of eqn. (3.23) give diagonal matrix elements and the last term gives rise to matrix elements of the form $\Delta K = \pm 2$, see eqn. (3.27).

Centrifugal distortion corrections to the rotation energy of an asymmetric top have been derived in a classic paper by Watson [149]. In this procedure, the Hamiltonian is transformed into a form that removes redundant constants that cannot be experimentally determined. There are two convenient choices for the transformed effective Hamiltonian, [1] symmetric (S) reduction, and [2] asymmetric (A)

reduction. The basic difference between the S– and A–reduced Hamiltonians' is that matrix elements with $\Delta K = \pm 4$ are not present in the A–reduction [150]. They both, however, have matrix elements with $\Delta K = 0, \pm 2$. The more general S–reduced form is applicable to any molecule including asymmetric tops, regardless of the extent of asymmetry. Although the A–reduction diverges in the symmetric top limit, it is easier to use since the A–reduced Hamiltonian contains fewer off–diagonal matrix elements. The most general lowest order expression (quartic) for centrifugal distortion is :

$$\hat{\mathrm{H}}_{\mathrm{CD}} = \frac{1}{4} \sum_{\alpha} \sum_{\beta} \sum_{\gamma} \sum_{\delta} \tau_{\alpha\beta\gamma\delta} \hat{J}_{\alpha} \hat{J}_{\beta} \hat{J}_{\gamma} \hat{J}_{\delta}, \tag{3.24}$$

where the centrifugal distortion constants $\tau_{\alpha\beta\gamma\delta}$ are complicated functions of the force constants and the components of the moment of inertia tensor (see refs. [149, 151]). The α, β, γ, and δ are summation indices, which can have the labels a, b or c. It was shown by Watson that only 21 constants of the type $\tau_{\alpha\beta\gamma\delta}$ are independent, three of each of the types τ_{aaaa}, τ_{aabb}, $\tau_{\alpha\beta\alpha\beta}$, and six of the τ_{aaab} type. For molecules of orthorhombic symmetry (D_{2h}, D_2, C_{2v}, and C_{2h}), there are nonzero matrix elements for only the first three types. Secondly, a simplification can be made whereby terms of the type $\tau_{\alpha\beta\alpha\beta}$ can be absorbed into the τ_{aabb} terms using the commutation relations of eqns. (3.8)–(3.10). The centrifugal Hamiltonian, $\hat{\mathrm{H}}_{\mathrm{CD}}$, can be simplified to give :

$$\hat{\mathrm{H}}_{\mathrm{CD}} = \frac{1}{4} \sum_{\alpha} \sum_{\beta} \tau'_{aabb} \hat{J}_{\alpha}^2 \hat{J}_{\beta}^2, \tag{3.25}$$

where $\tau'_{\alpha\alpha\beta\beta} = \tau_{\alpha\alpha\beta\beta} + 2\tau_{\alpha\beta\alpha\beta} (\alpha \neq \beta)$ and $\tau'_{aaaa} = \tau_{aaaa}$. Eqn. (3.25) has 6 constants but Watson [149] showed that only five of the constants can be experimentally determined from the spectrum. Unitary transformations of eqn. (3.25) were made to remove the redundant constants to give either the S–reduction or the A–reduction. The Hamiltonian expression that is applicable for a near prolate symmetric top becomes :

$$\begin{aligned} \hat{H}_{CD} &= -\Delta_K \hat{J}_a^4 - \Delta_{JK} \hat{J}^2 (\hat{J}^2 - \hat{J}_a^2) - \Delta_J \hat{J}^4 - 2\delta_J \hat{J}^2 (\hat{J}_b^2 - \hat{J}_c^2) \\ &- 2\delta_K [\hat{J}_a^2 (\hat{J}_b^2 - \hat{J}_c^2) + (\hat{J}_b^2 - \hat{J}_c^2) \hat{J}_a^2] \end{aligned} \tag{3.26}$$

where the Δ's are centrifugal corrections due to rotation about the a–axis and the δ's are corrections for rotation about the b– and c–axes. Evaluating the matrix elements for $\hat{H}_R + \hat{H}_{CD}$ gives [151, 152] :

$$\begin{aligned} \langle JK \mid \hat{H}_R \mid JK \rangle &= AK^2 + \frac{1}{2}(B+C)[J(J+1) - K^2] \\ -\Delta_K K^4 &- \Delta_{JK} J(J+1) K^2 - \Delta_J J^2 (J+1)^2 \end{aligned} \tag{3.27}$$

$$\begin{aligned} \langle J\,K \mid \hat{H}_R + \hat{H}_{CD} \mid J\,K \pm 2 \rangle &= [\frac{1}{4}(B-C) - \delta_J J(J+1) - \frac{1}{2}\delta_K (K^2 + (K \pm 2)^2] \\ \times [J(J+1) &- (K \pm 1)]^{\frac{1}{2}} [J(J+1) - (K \pm 1)(K \pm 2)]^{\frac{1}{2}} \end{aligned} \tag{3.28}$$

The quantum numbers J and K are the total angular momentum excluding spin and its projection onto the a–axis, respectively.

3.3 Spin–Rotation Interactions

Nonlinear molecules in multiplet electronic states can have an interaction between the electron spin angular momentum and rotational angular momentum, called the spin–rotation interaction. The basic theory of these interactions was first considered by Van Vleck [153], where he derived an effective Hamiltonian that considered mixing of electronic states caused by a spin–orbit coupling and Coriolis terms in the rotational Hamiltonian. There are two major contributions to these interactions, a direct magnetic coupling between the the electronic spin and molecular rotation, and a second order spin–orbit coupling between the electron spin and the unquenched angular momentum of the unpaired electrons [154]. It has been shown (Curl [155], Dixon [156]) that the major contribution to the spin–rotation constants is through the second–order spin–orbit interaction. This can be derived if we recast the rotational Hamiltonian of an asymmetric top in terms of $\hat{\mathrm{R}}$, the rotational angular momentum, where $\hat{\mathrm{R}} = \hat{\mathrm{N}} - \hat{\mathrm{L}}$, $\hat{\mathrm{N}}$ is the total angular momentum exclusive of spin, and $\hat{\mathrm{L}}$ is the orbital angular momentum. With the inclusion of spin–orbit coupling the rotation of a rigid polyatomic molecule becomes :

$$\hat{\mathrm{H}} = A(\hat{\mathrm{N}}_a - \hat{\mathrm{L}}_a)^2 + B(\hat{\mathrm{N}}_b - \hat{\mathrm{L}}_b)^2 + C(\hat{\mathrm{N}}_c - \hat{\mathrm{L}}_c)^2 + \sum_j \hat{\eta}_{\mathrm{j}} \cdot \hat{\mathrm{s}}_{\mathrm{j}}. \tag{3.29}$$

The (a, b, c) are the principal axes in the molecular frame, $\hat{\eta}_{\mathrm{j}}$ is the spin orbit coupling operator for electron j, $\hat{s}_j$ is the electron spin operator and the sum j is over all electrons in the system. From eqn. (3.29) we can see that the purely rotational part of the Hamiltonian is :

$$\hat{\mathrm{H}}_{\mathrm{rot}} = A\hat{\mathrm{N}}_a^2 + B\hat{\mathrm{N}}_b^2 + C\hat{\mathrm{N}}_c^2, \tag{3.30}$$

and the perturbation to strict rigid rotation arises from the cross terms between between $\hat{\mathrm{H}}_1$ and $\hat{\mathrm{H}}_2$, where;

$$\hat{\mathrm{H}}_1 = -2A\hat{\mathrm{N}}_a\hat{\mathrm{L}}_a - 2B\hat{\mathrm{N}}_b\hat{\mathrm{L}}_b - 2C\hat{\mathrm{N}}_c\hat{\mathrm{L}}_c, \quad \hat{\mathrm{H}}_2 = \sum_j \hat{\eta}_j \cdot \hat{\mathbf{s}}_j. \tag{3.31}$$

This form of the Hamiltonian is very difficult to use, since it involves a sum of one–electron operators. In the Hund's case (b) basis, $\hat{s}_j$ does not commute with $\hat{\mathrm{N}}$ or $\hat{\mathrm{L}}$, and a common set of eigenfunctions can not be found. A common way to handle such problems is to use a Van Vleck transformation. It is basically a version of perturbation theory that allows one to obtain an approximate block diagonal effective Hamiltonian. When we perform a second–order treatment of this interaction, we get :

$$\Delta E = \sum_{n \neq n_0} \frac{2\langle n_0 \mid \hat{\mathrm{H}}_1 \mid n\rangle\langle n \mid \hat{\mathrm{H}}_1 \mid n_0\rangle}{E_{n_0} - E_n}, \tag{3.32}$$

where the sum n is over all electronic states in the molecule. The Van Vleck transformation also allows one to write an effective Hamiltonian for the spin–rotation interaction :

$$\hat{\mathrm{H}}_{\mathrm{SR}}^{(2)} = \frac{1}{2}\sum_{\alpha,\beta} \epsilon_{\alpha\beta}(\hat{\mathrm{N}}_\alpha\hat{\mathrm{S}}_\beta + \hat{\mathrm{S}}_\beta\hat{\mathrm{N}}_\alpha), \tag{3.33}$$

where the α and β are summations over the molecule fixed coordinates (a, b, c). It has been shown [155, 156] that the second order contributions (spin–orbit) to the

parameters $\epsilon_{\alpha\beta}$ were predominant over the first order (nuclear) contributions.

This effective Hamiltonian was used for asymmetric top molecules in doublet states but for some cases it was found inadequate to fit the energy levels [157]. Brown and Sears [152] used the approach of Watson to derive the centrifugal distortion corrections to the spin rotation constants. From Van Vleck theory the quartic spin–rotation Hamiltonian is written as :

$$\hat{H}_{SR}^{(4)} = \frac{1}{2}\sum_{\alpha\beta\gamma\delta}\eta_{\alpha\beta\gamma\delta}\Big(N_\alpha N_\beta N_\gamma S_\delta + S_\delta N_\gamma N_\beta N_\alpha\Big), \tag{3.34}$$

the $\eta_{\alpha\beta\gamma\delta}$ are the centrifugal distortion parameters of the spin-rotation interaction, analogous to $\tau_{\alpha\beta\gamma\delta}$ parameters of centrifugal distortion. Using the procedure of Watson, the A–reduced form of the Hamiltonian was derived by Brown and Sears, giving :

$$\begin{aligned}\hat{H}_{SR}^{(4)} &= \Delta_N^s N^2(N\cdot S) + \frac{1}{2}\Delta_{NK}^s(N^2N_zS_z + N_zS_zN^2) + \Delta_{KN}^s N_z^2(N\cdot S) + \Delta_K^s N_z^3 S_z \\ &+ \delta_N^s(N_+^2 + N_-^2)(N\cdot S) + \frac{1}{2}\delta_K^s\Big[(N_+^2 + N_-^2)N_zS_z + N_zS_z(N_+^2 + N_-^2)\Big] \end{aligned} \tag{3.35}$$

The matrix elements for the asymmetric reduction and its centrifugal distortion corrections for an asymmetric top molecule in a doublet electronic state are given in Table 3.1.

Table 3.1: Matrix elements of the spin–rotation interaction for a molecule in a doublet state in the A–reduction [151, 152].

$$\langle NKSJ \mid \hat{\mathrm{H}}_{\mathrm{SR}} \mid NKSJ\rangle = -[\Gamma(NSJ)/2N(N+1)]\{\epsilon_{aa}K^2 + (\epsilon_{bb}+\epsilon_{cc})$$
$$\times[N(N+1)-K^2]/2 + \Delta_K^S K^4 + (\Delta_{NK}^S + \delta_{KN}^S)K^2N(N+1) + \Delta_N^S N^2(N+1)^2\}$$

$$\langle NK\pm 1, SJ \mid \hat{\mathrm{H}}_{\mathrm{SR}} \mid NKSJ\rangle = -[\Gamma(NSJ)(2K\pm 1)/4N(N+1)]$$
$$\times[N(N+1)-K(K\pm 1)]^{\frac{1}{2}}(\epsilon_{ab}+\epsilon_{ba})/2$$

$$\langle NK\pm 2, SJ \mid \hat{\mathrm{H}}_{\mathrm{SR}} \mid NKSJ\rangle = -[\Gamma(NSJ)/4N(N+1)]\{[N(N+1)-K(K\pm 1)]$$
$$\times[N(N+1)-(K\pm 1)(K\pm 2)]^{\frac{1}{2}}(\epsilon_{bb}-\epsilon_{cc})/2 + 2\delta_N^S N(N+1) + \delta_K^S[K^2+(K\pm 2)]^2\}$$

$$\langle N-1, KSJ \mid \hat{\mathrm{H}}_{\mathrm{SR}} \mid NKSJ\rangle = -\phi(NSJ)(K/2N)(N^2-K^2)^{\frac{1}{2}}$$
$$\times\{(\epsilon_{aa}-(\epsilon_{ab}+\epsilon_{ba})/2) + \Delta_K^S K^2 + \Delta_{NK}^S N^2\}$$

$$\langle N-1, K\pm 1, SJ \mid \hat{\mathrm{H}}_{\mathrm{SR}} \mid NKSJ\rangle = -\phi(NSJ)[(N\pm 2K+1)/4N]$$
$$\times[(N\mp K)(N\mp K-1)]^{\frac{1}{2}}(\epsilon_{ab}+\epsilon_{ba})/2)$$

$$\langle N-1, K\pm 2, SJ \mid \hat{\mathrm{H}}_{\mathrm{SR}} \mid NKSJ\rangle = -[\phi(NSJ)/4N][((N\mp K)((N\mp K-1)((N\mp K-2)$$
$$\times(N\mp K+1)^{\frac{1}{2}}\{\pm((\epsilon_{bb}-\epsilon_{cc})/2) + \delta_K^S[K(N\pm K)+(K\pm 2)(N\pm K+2)]\}$$

$\Gamma(NSJ) = N(N+1)+S(S+1)-J(J+1)$ and $\phi(NSJ) = [(N-J+S))(N+J+S+1)(S+J-N+1)(N+J-S)/(2N+1)(2N-1)]^{\frac{1}{2}}$. $\phi(NSJ)$ is unity for a doublet state (S=$\frac{1}{2}$). $\Delta K = \pm 1$ matrix elements vanish for molecules with orthorhombic symmetry.

Chapter 4

The Spectroscopy of $CaNH_2$

The first spectroscopic investigation of $CaNH_2$ was completed by Wormsbecher *et al.* [49] using a Broida oven. They used a reaction of Ca vapor with hydrazine (N_2H_4) to generate $CaNH_2$. Hydrazine was admitted into the reaction zone of a Broida–oven through a leak valve, to give a total pressure of 1–3 torr inside the chamber. There was weak chemiluminescence attributed to the reaction product of Ca and hydrazine. The chemiluminescence was focused onto the slits of a 3/4 m monochromator and detected by a photomultiplier tube (PMT). Low resolution chemiluminescent spectra were recorded to locate the positions of the electronic transitions in the molecule. The motivation of the work was to determine if the MNH_2 spectra had any similarities to the spectra of the isoelectronic diatomic alkaline earth fluorides. This was a natural extension to nonlinear derivatives of alkaline earths since electronic and structural similarities had just recently (in 1983) been shown in the spectrum of CaOH [14] and SrOH [16]. The $CaNH_2$ spectra did show a strong resemblance to the spectra of the isoelectronic CaF molecule. The

first two transitions of $CaNH_2$ in the red were assigned as the $\tilde{A}\ ^2B_2$–$\tilde{X}\ ^2A_1$ and $\tilde{B}\ ^2B_1$–$\tilde{X}\ ^2A_1$ transitions, while the yellow emission was assigned as the $\tilde{C}\ ^2A_1$–$\tilde{X}\ ^2A_1$ transition of a planar molecule with C_{2v} symmetry. In a subsequent experiment, they attempted to record high resolution spectra of the $\tilde{C}$–$\tilde{X}$ transition [116]. It was estimated from the chemiluminescent spectra that the rotational and vibrational temperature of the $CaNH_2$ molecules was in the range of 500–700 K.

When high resolution laser experiments were carried out using a conventional technique, measuring the total laser excitation signal, rotational structure was not observed in the spectrum. They did, however, observe a weak fluorescence on a strong background signal. This indicated that the $\tilde{C}$–$\tilde{X}$ electronic transition was severely congested and conventional laser spectroscopic techniques would not provide rotationally–resolved spectra. To partially overcome of this problem, they used the technique of laser excitation with narrowband fluorescence detection [158, 159], a technique which can aid in the assignment of a complicated spectrum. In this method, a monochromator functions as a narrow bandpass filter to detect only part of the fluorescence spectrum of the molecule. Spectral complexity is greatly reduced in this way because the monochromator can filter out some or most of the non–resonant fluorescent signal, which is the most likely cause of the strong background. The spectrum is simplified because only those lines which fluoresce in the narrow spectral window monitored by the monochromator appear in the laser excitation scan. This technique cannot, however, remove Doppler broadening and is rather a tedious procedure for molecules with congested spectra. A partial analysis of the K_a=1 sub–band for the 0_0^0 transition of the $\tilde{C}\ ^2A_1$–$\tilde{X}\ ^2A_1$ system

was carried out [116]. High rotational temperatures precluded them from assigning any low J transitions or the K_a=0 sub-band. Our measurements on cold $CaNH_2$ molecules are not completely consistent with their reported line positions. This is in part due to their large spectral linewidths which were on the order of 0.05 cm^{-1}, and also because our data contains only low J rotational lines. In the jet-cooled spectra reported in this work, the typical linewidth obtained are on the order of 150-200 MHz ($\sim$0.007 cm^{-1}). Although it is possible that they recorded the K_a=1 sub-band, the uncertainty in their line positions ($\pm$ 0.02 cm^{-1}) was too large to aid in the assignment of the cold spectrum.

Whitham *et al.* [115] were the first to use a laser ablation/molecular beam spectrometer to produce $CaNH_2$. Again, these studies were limited in resolution (0.15 cm^{-1}), but this time by the probe laser. As a consequence, they were only able to perform a partial rotational analysis of the 0_0^0 bands of the $\tilde{A}\ ^2B_2$-$\tilde{X}\ ^2A_1$ and $\tilde{B}\ ^2B_1$-$\tilde{X}^2A_1$ systems. Simulated intensities of their rotational lines implied a rotational temperature of 180 K for a helium expansion.

Marr *et al.* [113] were the first to analyze the high resolution spectra of $CaNH_2$. They recorded the 0_0^0 band of the $\tilde{A}^2B_2$-$\tilde{X}^2A_1$ system, from which they derived the molecular constants for the ground and excited states. Using optical/Stark spectroscopy, they also measured dipole moments for the $\tilde{A}$ and $\tilde{X}$ states. The 0_0^0 band of the $\tilde{B}\ ^2B_1$-$\tilde{X}^2A_1$ system was analyzed by Zhao *et al.* [114], and we report here a high resolution analysis of the 0_0^0 band of the $\tilde{C}\ ^2A_1$-$\tilde{X}\ ^2A_1$ system. $CaNH_2$ is the first nonlinear alkaline earth derivative where all four of the ($\tilde{X}$,$\tilde{A}$,$\tilde{B}$,$\tilde{C}$) low-lying electronic states are characterized at high resolution, thus we shall discuss

the application of the simple "pure precession" model to polyatomic systems of low symmetry.

4.1 Observations

The approximate positions of the $\tilde{A}^2B_2$–$\tilde{X}^2A_1$, $\tilde{B}^2B_1$–$\tilde{X}^2A_1$ and $\tilde{C}^2A_1$–$\tilde{X}^2A_1$ band origins were known from the low resolution work of Bopegedera *et al.* [55], and the location of the C–X system was also known from the work of Wormsbecher *et al.* [116]. Preliminary experiments were performed using a Broida oven. These experiments showed that the spectrum of the $\tilde{C}$–$\tilde{X}$ system was extremely dense, with many K_a-rotational sub-bands and vibrational hot bands present (Fig. 4.1). The spectra recorded in this way were found to be extremely difficult to analyze, even when resolved fluorescence techniques were used, as shown in Fig 4.2.

A molecular beam experiment was carried out where the laser was scanned at high resolution in the region from 17365 cm^{-1} to 17395 cm^{-1}. Rotational structure of the spectrum was consistent with the parallel band structure of an a–type transition. The electronic transitions of asymmetric tops are classified as a–type, b–type or c–type, depending on the orientation of the transition dipole moment with respect to the principal axes. The $\tilde{C}^2A_1$—$\tilde{X}^2A_1$ transition is approximately described as the promotion of an electron from a predominantly $4s$ orbital to a $4p_z$ orbital on Ca. This will correspond to an oscillating dipole moment lying along the a–axis of the molecule, which for $CaNH_2$ is parallel to the Ca–N bond. Hence, this type of transition is also called a parallel transition (a–type). The $\tilde{A}$–$\tilde{X}$ and $\tilde{B}$–$\tilde{X}$ transitions are approximately the promotion of the $4s$ electron to $4p_x$ and

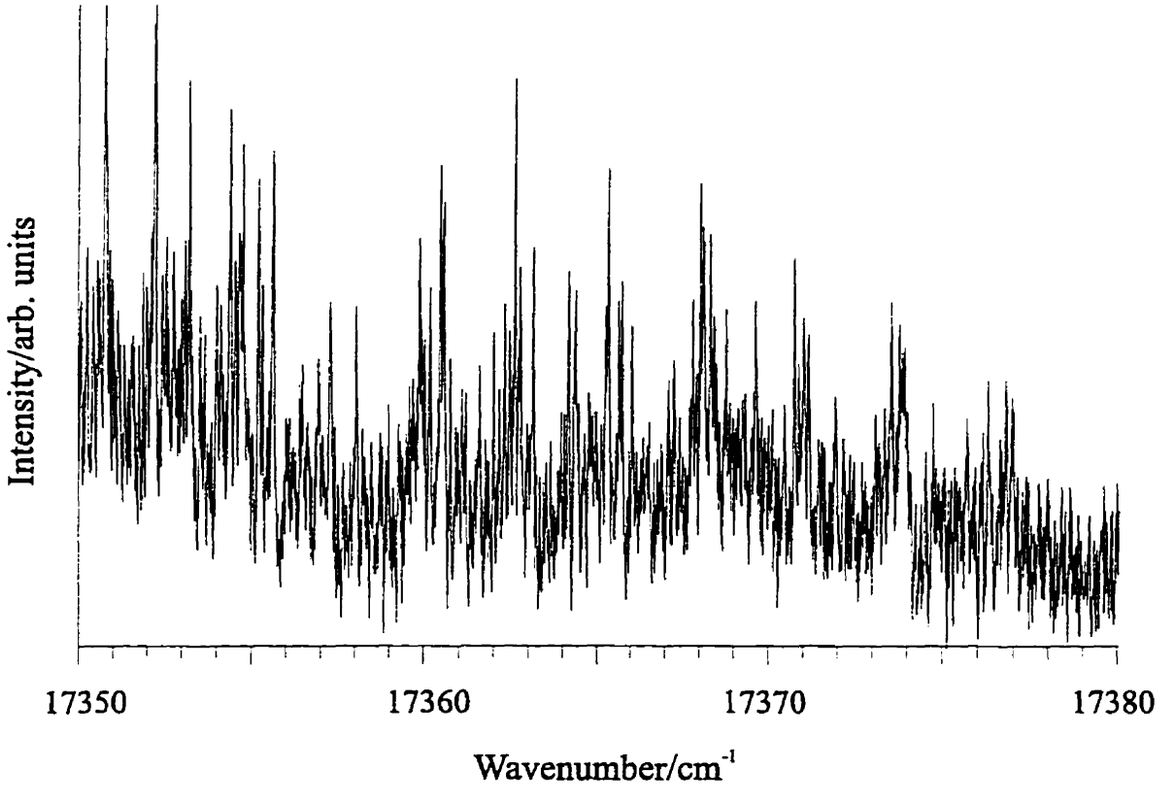

Figure 4.1: The overview spectrum of the $\tilde{C}\ ^2A_1$–$\tilde{X}\ ^2A_1$ transition of $CaNH_2$. This spectrum was recorded using a Broida oven and monitoring the total fluorescence of the $\tilde{B}^2B_1$–$\tilde{X}^2A_1$ system. Features such as band–heads or band–origins are not visible because of the background signal caused by non–resonant fluorescence and severe line congestion.

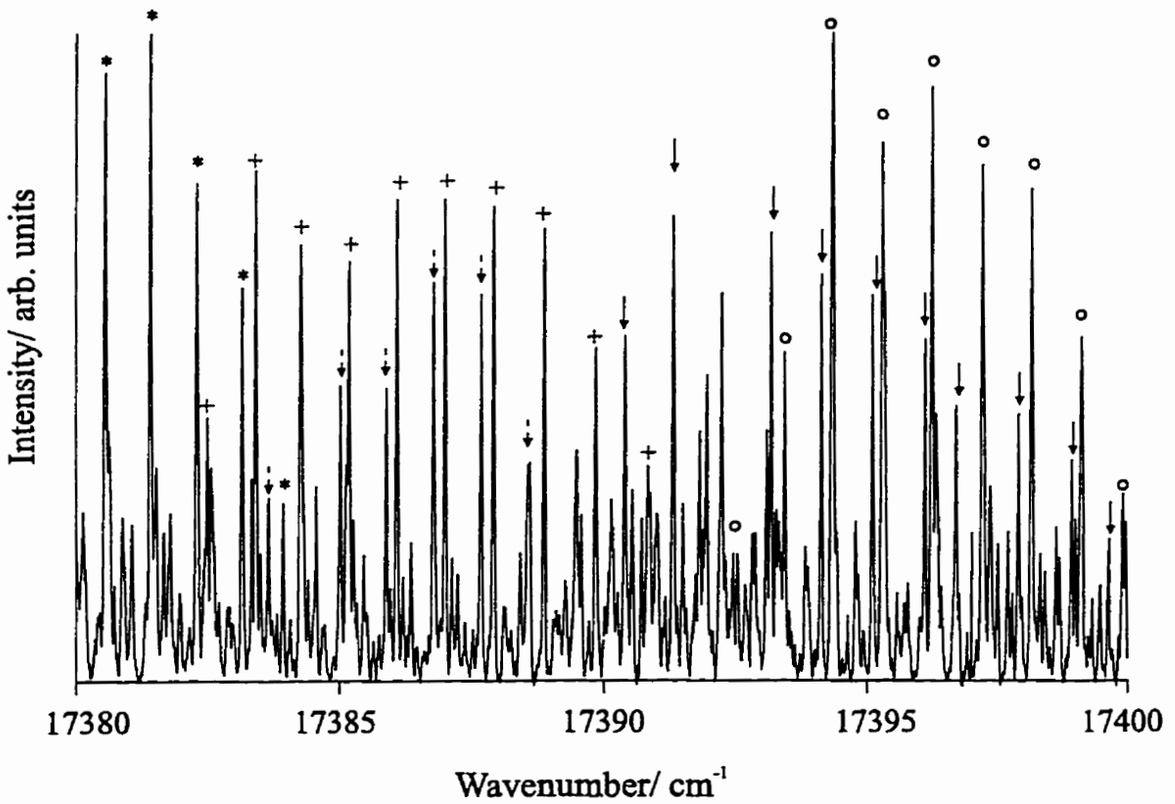

Figure 4.2: The resolved fluorescence spectrum of a portion of the R–branch of the $\tilde{C}\ ^2A_1$–$\tilde{X}\ ^2A_1$ transition of $CaNH_2$. This spectrum was also recorded with a Broida oven but only the resolved fluorescence was monitored. This was done by placing the monochromator in the P–branch region of $\tilde{C}\ ^2A_1$–$\tilde{X}\ ^2A_1$ transition. The symbols denote lines belonging to a particular R–branch series, but matching the corresponding P–branch lines was impossible due to spectral congestion.

$4p_y$ orbitals, both of which are perpendicular to the Ca–N bond. These are called perpendicular transitions.

The appearance in the spectra of parallel and perpendicular transitions are quite different. Since the oscillating dipole moment for an a–type transition is parallel to the a–axis, the projection of the total angular momentum (excluding spin), K_a, cannot change upon excitation. This leads to the selection rules $\Delta K_a = 0$ and $\Delta K_c = \pm 1$. Sub–bands within each electronic transition are denoted $K'_a \leftarrow K''_a$, so for a parallel transition 0–0, 1–1, 2–2 etc... sub–bands are allowed. This is analogous to diagonal vibronic transitions of diatomic molecules. Note that each sub-band originating from a different K''_a will have approximately the same origin. The rotational contour of this transition will appear simple, or in other words it will be a narrow transition. Perpendicular transitions (c–type) have the $\Delta K_a = \pm 1$, and $\Delta K_c = 0$ selection rules, giving 0–1, 1–0, 2–1, 1–2 etc... labelled sub–bands. Thus, sub–bands originating with different K''_a will have slightly different origins and the rotational contour will be open, i.e. it will appear relatively broad when compared to a parallel transition, see Fig 4.3.

The additional selection rules for a doublet a–type transition are, $\Delta J = \pm 1$, $F_1 \rightarrow F_1$, $F_2 \rightarrow F_2$ for a $K'_a = 0 \leftarrow K''_a = 0$ sub–band, and for a $K'_a = 1 \leftarrow K''_a = 1$ sub–band a Q–branch ($\Delta J = 0$) is also allowed. It is useful to introduce the label, γ, for the rotational energy levels (Jarman *et al.* [111]), where $\gamma = K_a + K_c - N$, so that γ can take on the values, 0 or 1. Therefore, we have $\gamma' = 0 \leftarrow \gamma'' = 0$ for a 0–0 sub–band and both $\gamma' = 0 \leftarrow \gamma'' = 0$ and $\gamma' = 1 \leftarrow \gamma'' = 1$ for a 1–1 sub–band.

The allowed transitions of the 0–0 sub–band are depicted in Fig. 4.4. Each

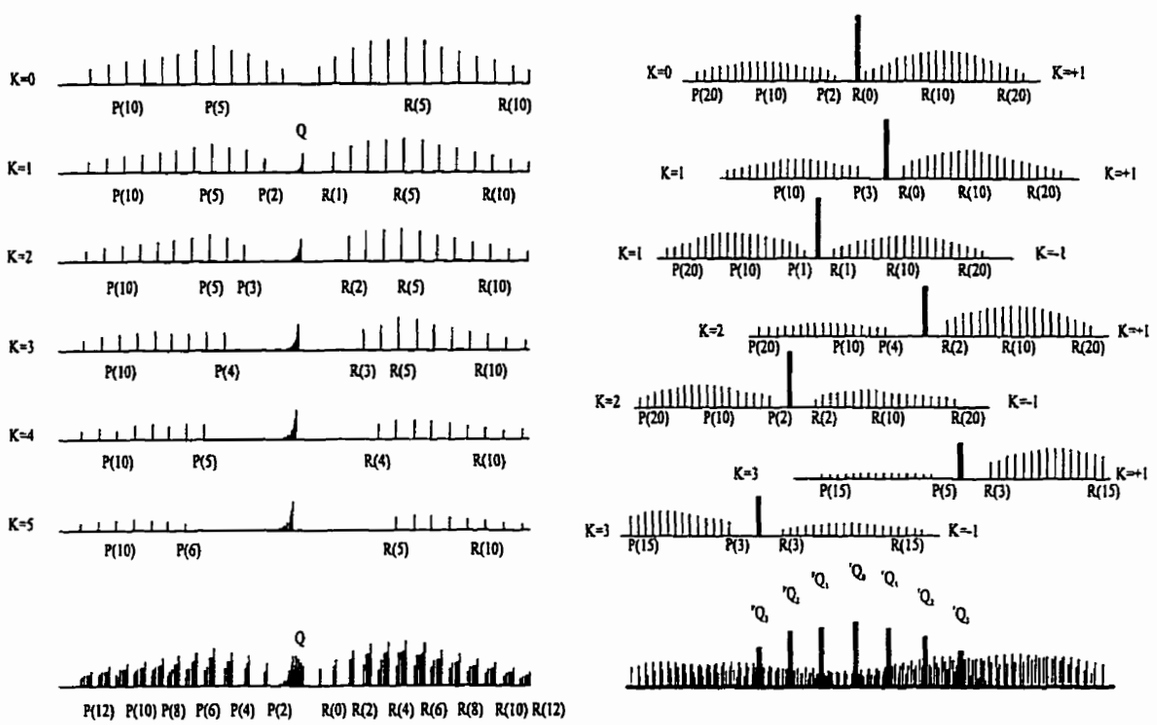

Figure 4.3: The comparison of the (a) parallel type and (b) perpendicular type transitions. The rotational contour of a parallel transition is much narrower than the contour of a perpendicular transition.

rotational level labelled $N_{Ka,Kc}$ is split into two fine structure levels by spin–rotation interactions. They are labelled F_1, for J=N+$\frac{1}{2}$, and F_2, for J=N-$\frac{1}{2}$. Only P and R branches are allowed for the 0–0 sub–band so the rotational spectrum is analogous to a $^2\Sigma^+$—$^2\Sigma^+$ transition of a diatomic molecule. Figure 4.5 shows the corresponding energy level diagram for a 1–1 sub–band. In this case each rotational level is split into four components, first by spin–rotation interactions (F_1 and F_2) and secondly by asymmetry doubling ($\gamma = 0$ or 1), as indicated by a superscript. The 1–1 sub–band resembles a Hund's case (b) $^2\Pi$—case (b)$^2\Pi$ transition of a diatomic molecule.

Figure 4.6 shows the overview of the $\tilde{C}$–$\tilde{X}$ band system recorded both in Ar and in He. The He spectrum has a slightly higher rotational temperature (T_{rot} = 13 K) than the Ar spectrum (T_{rot} = 6 K). Initially the Ar spectrum was used for data analysis, but the F_2 component of the 1–1 sub–band was absent. Subsequently the higher temperature He spectrum was used for the analysis. Rotational lines with J values as high as $19\frac{1}{2}$ were assigned for the 0–0 sub–band and J=$14\frac{1}{2}$ for the 1–1 sub–band. Some of the assigned transitions of the spectrum are shown in Fig. 4.7. All of the allowed branches (4 for 0–0, 12 for 1–1) were observed in the spectrum, however, it was found that the transitions involving the F_2 component of the 1–1 sub–band were very weak. The $\tilde{C}$–$\tilde{X}$ band system is an a–type transition with the $\Delta K_a = 0$ selection rule. The sub–bands of different K_a will have approximately the same origin, leading to a very congested spectrum. Fortunately, with the rotational cooling in a molecular beam, only two K_a'' values had significant population (K_a = 0,1). Because of nuclear spin statistics, the $K_a = 1$ rotational levels (ortho) cannot cool into the $K_a = 0$ (para) levels. Compare the cold spectrum of Fig. 4.6 to the

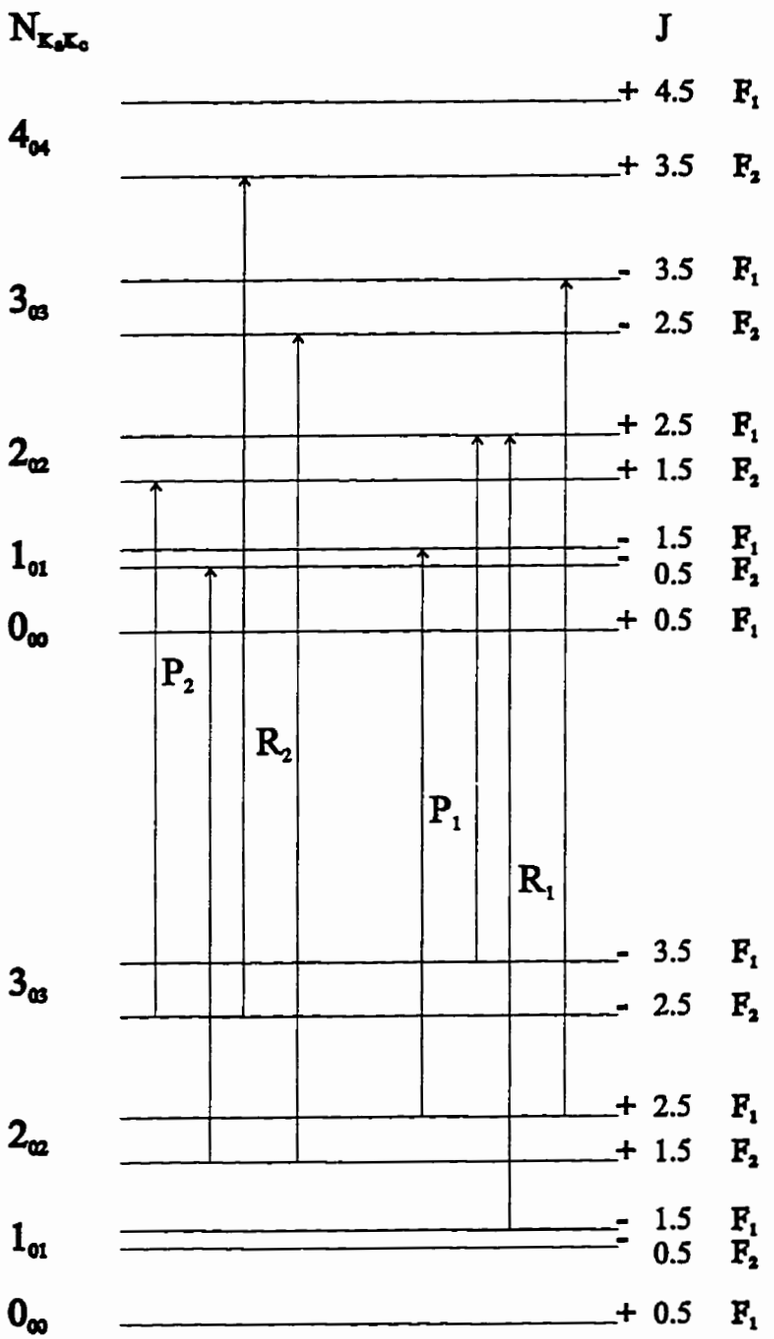

Figure 4.4: The energy level diagram associated with the $K_a'' = 0 \longleftarrow K_a' = 0$ sub–band of the $\tilde{C}\ ^2A_1$–$\tilde{X}\ ^2A_1$ transition of $CaNH_2$. The allowed transition are labelled by $\Delta J_{F_i''}$ $(i = 1, 2)$.

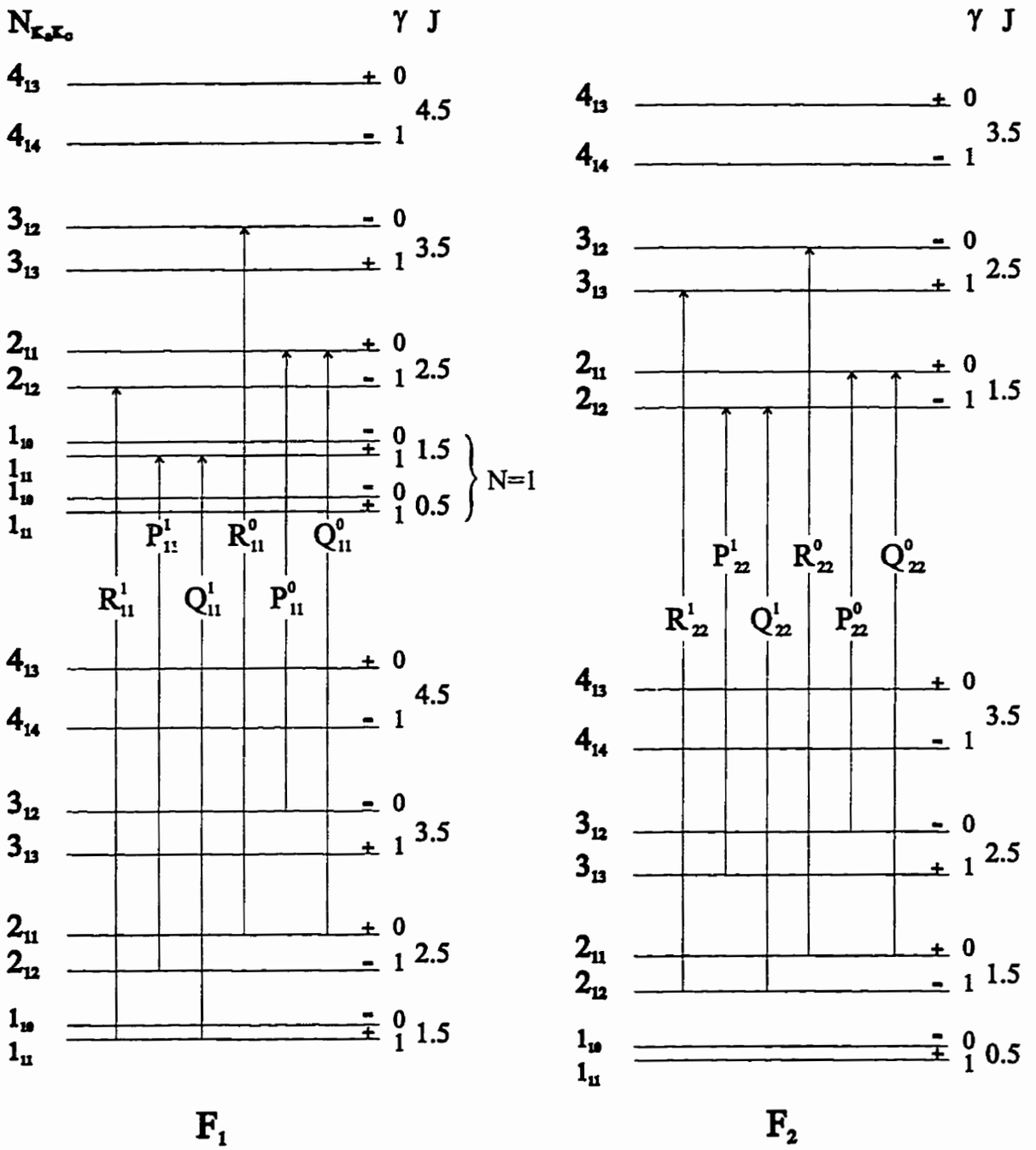

Figure 4.5: The allowed transition of the $K_a'' = 1 \longleftarrow K_a' = 1$ sub-band of the $\tilde{C}\ ^2A_1$–$\tilde{X}\ ^2A_1$ transition. Each transition is labelled by $\Delta J^{\tau}_{F_i'',F_i'}$ $(i = 1, 2)$, see text for details.

high temperature spectrum of Fig. 4.2.

4.2 Results

The analysis of the $\tilde{C}$–$\tilde{X}$ spectrum was partially aided by using a Loomis–Wood program to sort out the branches. Although this procedure [160] is useful in the analysis of congested spectra of $^1\Sigma$ diatomic molecules, more care must be taken with nonlinear molecules and non–$^1\Sigma$ diatomics. This is because the line spacing of connected P and R–branches can be quite different. For $CaNH_2$, a particular P or R branch can be found rather easily, but connecting the P and R branches was difficult (Fig. 4.2). With the help of the spectroscopic constants of Marr *et al.* [113], ground state combination differences were used to connect the branches. Once a single pair of branches of the $K'_a = 0 \leftarrow K''_a = 0$ sub-band was assigned and subsequently fitted with a nonlinear least squares program, the remaining branches were then assigned by prediction. The same procedure was used to assign the lines of the $K'_a = 1 \leftarrow K''_a = 1$ sub–band.

The data was fit using the effective rotational Hamiltonian (A–reduction) of Watson [150] and the spin–rotation Hamiltonian of Brown *et al.* [152]. The effective quadratic spin–rotation Hamiltonian is written as :

$$\hat{H}_{sr} = \frac{1}{2}\sum_{\alpha,\beta} \epsilon_{\alpha\beta}(\hat{N}_\alpha \hat{S}_\beta + \hat{S}_\beta \hat{N}_\alpha), \tag{4.1}$$

where α and β are the principal rotation axes, $\epsilon_{\alpha\beta}, \hat{S}_\beta$ and $\hat{N}_\alpha$ are defined in § 3.3.

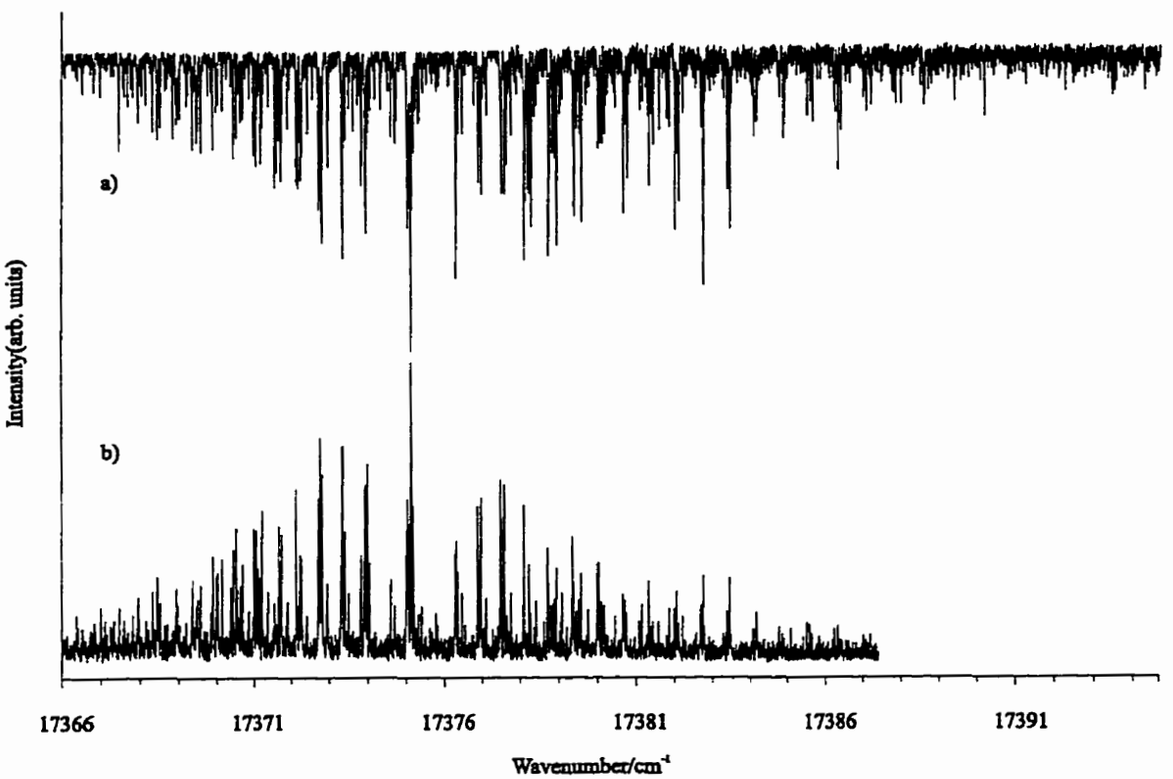

Figure 4.6: An overview of the high resolution spectrum of the 0_0^0 vibronic band of the $\tilde{C}\ ^2A_1$–$\tilde{X}\ ^2A_1$ transition (a) recorded in He and (b) in Ar.

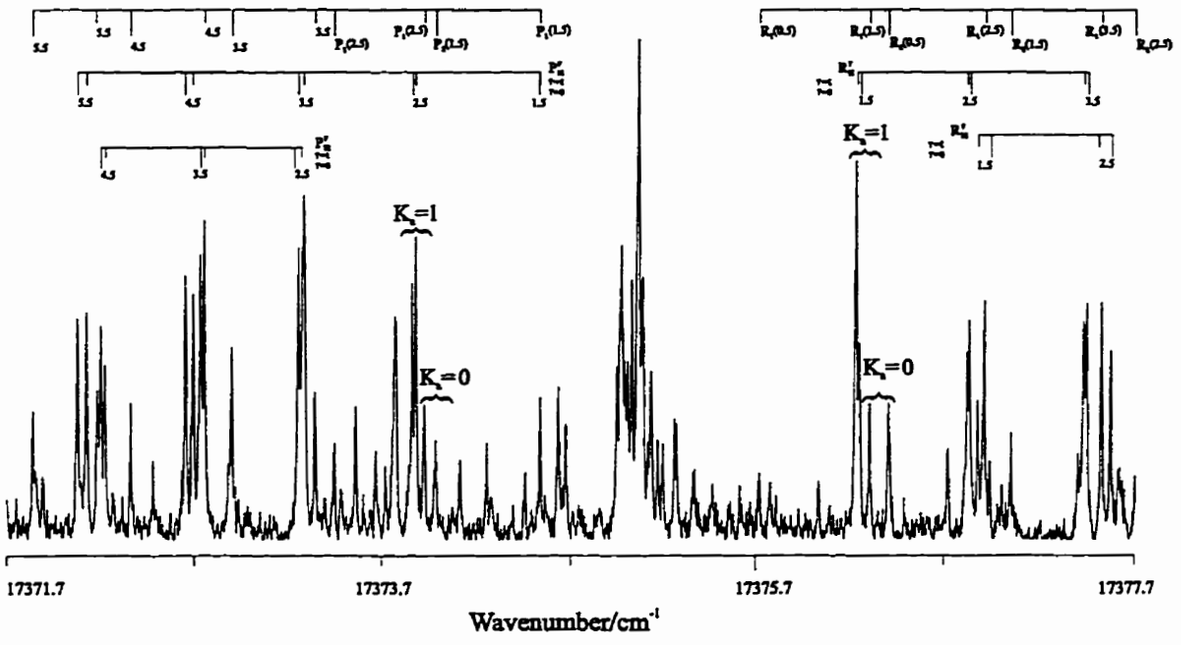

Figure 4.7: A portion of the high resolution spectrum of the 0_0^0 band of the $\tilde{C}\ ^2A_1$–$\tilde{X}\ ^2A_1$ transition of $CaNH_2$ near the origin. This spectrum was recorded with He carrier gas. Note the 3:1 intensity ratio of ortho ($K_a = 1$) and para ($K_a = 0$) levels and the small asymmetry splitting (γ) of the $K_a'' = 1 \longleftarrow K_a' = 1$ sub-band. The Q–branch transitions are not labelled for clarity.

A total of nine spin rotation constants are possible, but for a molecule with orthorhombic (C_{2v}) symmetry, only three, ϵ_{aa}, ϵ_{bb} and ϵ_{cc}, are nonzero. It will be shown (see §4.3) that the predominant contribution to these constants is from second–order spin–orbit interactions rather than true spin–rotation interactions. The matrix elements used in the nonlinear least squares program were taken from the literature (Watson [149], Hirota [151]). For the final fit the $\tilde{A}^2B_2$–$\tilde{X}^2A_1$ lines of Marr *et al.* [113], the $\tilde{B}^2B_1$– $\tilde{X}^2A_1$ lines of Zhao *et al.* [114] were added to this data set and a global fit of all the data was carried out. The rotational constants for the $\tilde{X}^2A_1$, $\tilde{A}^2B_2$, $\tilde{B}^2B_1$, $\tilde{C}^2A_1$ states are reported in Table 4.1 and the line positions of the $\tilde{C}^2C_1$– $\tilde{X}^2A_1$ system are listed in Appendix A.1.

4.3 Discussion: Pure Precession Model

The most interesting of the spectroscopic constants listed in Table 4.1 are the spin–rotation constants (ϵ_{aa}). This is because we can use the simple pure precession model to give a physical picture of the orbitals containing the unpaired electron. $CaNH_2$ is the first of the alkaline earth polyatomic molecules for which all of the low–lying electronic states are known, so a discussion of the pure precession model is warranted. In this model we will assume that only pure p–type orbitals give rise to the first three excited electronic states (Fig. 1.1) of $CaNH_2$, while the ground state has the unpaired electron in an s–type orbital.

It was shown by Dixon [156] that the second–order spin–orbit corrections to the

spin-rotation constants of a doublet state are :

$$\epsilon_{\alpha\alpha}^{(2)} = \sum_{n\neq 0}\sum_{j} \frac{4B_\alpha k_j \langle\psi_0|\,\hat{\mathrm{L}}_\alpha\,|\,\psi_n\rangle\langle\psi_n\,|\,\hat{\eta}_{\alpha,j}\,|\,\psi_0\rangle}{E_n^o - E_0^o}. \tag{4.2}$$

The sum j is over all electrons, k_j= +1 for promotion of an unpaired electron, k_j= -1 for promotion of an electron into a half–filled orbital or zero otherwise. The B_α's in eqn. (4.2) are the rotational constants in the principal axis system (e.g. $B_a = A$, $B_b = B$, $B_c = C$). The matrix element involving $\hat{\eta}_{\alpha,j}$ can be written in terms of the the one–electron orbital angular momentum operators, $\hat{\eta}_{\alpha,j} = \zeta_j\,\hat{\ell}_{\alpha,j}$, where ζ_j is the spin–orbit constant for the electron. In the pure precession limit, we can neglect all electrons except the unpaired valence electron on Ca^+. Thus, the sum over j can be replaced with a single term involving $\zeta_{3p}\hat{\ell}_\alpha$, leaving the second–order correction to the spin–rotation constants as :

$$\epsilon_{\alpha\alpha}^{(2)} = \sum_{n\neq 0} \frac{4B_\alpha \langle\psi_0\,|\,\hat{\ell}_\alpha\,|\,\psi_n\rangle\langle\psi_n\,|\,\zeta_{3p}\hat{\ell}_\alpha\,|\,\psi_0\rangle}{E_n^o - E_0^o}. \tag{4.3}$$

A similar analysis as above can be done for the second–order correction to the rotational constants (A, B, C). The result is :

$$B_\alpha^{(2)} = \sum_{n\neq 0} \frac{4B_\alpha^2 \langle\psi_0\,|\,\hat{\ell}_\alpha\,|\,\psi_n\rangle^2}{E_0^o - E_n^o}. \tag{4.4}$$

It will be shown below that the second–order correction to the A rotational constant is significant while the corrections to B and C are negligible.

A second simplification that can be made is the unique perturber approximation. Here, we assume that each electronic state interacts solely with a dominant

perturbing state [161]. Pairs of states interact if rotations of the molecule are taken into consideration. The faster the molecule rotates about a particular principal axis, the unpaired electron, localized in a particular p orbital mixes with the other p orbital that is perpendicular to the rotation axis. For example, rotation about the a–axis causes interactions between the $\tilde{B}^2B_1$ (p_x) and $\tilde{A}^2B_2$ (p_y) states, rotation about the c–axis causes interactions between the $\tilde{C}^2A_1$ (p_z), and the $\tilde{B}^2B_1$ (p_x) states and finally, rotation about the b–axis leads to interactions of the $\tilde{C}^2A_1$ (p_z) and $\tilde{A}^2B_2$ (p_x) states.

To determine the second–order correction to ϵ_{aa} in the $\tilde{A}^2B_2$ state, the wavefunctions for the two interacting states ($\tilde{B}^2B_1$, $\tilde{A}^2B_2$) and the integrals $\langle \tilde{B}\ ^2B_1 \mid \hat{\ell}_a \mid \tilde{A}\ ^2B_2\rangle$, $\langle \tilde{A}\ ^2B_2 \mid \zeta_{3p}\hat{\ell}_a \mid \tilde{B}\ ^2B_1\rangle$ must to be evaluated. However, in the pure precession limit we assume that each electronic state arises strictly from a pure p–type orbital. In Table 4.2 , the correlation of the electronic state with the principal axis system, and with the (x, y, z) coordinate system is shown. Table 4.3 shows the effect of the one-electron orbital angular momentum operators on the three p–orbitals. Using these results and eqn. (4.3) we can write the formula for the second order correction to ϵ_{aa} of the $\tilde{A}^2B_2$ state :

$$\begin{aligned} \epsilon_{aa}^{(2)} &= \frac{4A\langle p_y|\tilde{\ell}_z|p_x\rangle\langle p_x|\zeta_{3p}\tilde{\ell}_z|p_y\rangle}{E_{\tilde{B}}-E_{\tilde{A}}} \\ &= \frac{-4A\zeta_{3p}\ i^2}{E_{\tilde{B}}-E_{\tilde{A}}} \\ &= \frac{+4AA^{so}}{E_{\tilde{B}}-E_{\tilde{A}}}. \end{aligned} \tag{4.5}$$

In the last step we replace ζ_{3p} with A^{so}, which is the spin-orbit splitting in the hypothetical linear molecule. Clearly one can see that we get the negative of eqn. (4.5)

for ϵ_{aa} of the $\tilde{B}^2B_1$ state . Performing similar calculations we get $\epsilon_{bb}^{(2)} = 0$ for the $\tilde{A}^2B_2$ state, $\epsilon_{cc}^{(2)} = 0$ for the $\tilde{C}^2A_1$ state and :

$$\epsilon_{bb}^{(2)} = \pm\frac{4BA^{so}}{E_{\tilde{C}} - E_{\tilde{B}}}, \quad \epsilon_{cc}^{(2)} = \pm\frac{4CA^{so}}{E_{\tilde{C}} - E_{\tilde{A}}}. \tag{4.6}$$

In the above formulae the top sign corresponds to the lower energy electronic state of the interacting pair of states. The second order correction to the A rotational constant then becomes :

$$A^{(2)} = \pm\frac{4A^2}{E_{\tilde{B}} - E_{\tilde{A}}}. \tag{4.7}$$

One can see the close connection between the the above results and the perturbation treatment of Whitham and Jungen [115]. They considered the rotation about the a-axis as equivalent to an a-axis Coriolis interaction with an off-diagonal spin-orbit coupling. The Hamiltonian for this interaction is :

$$\hat{\mathrm{H}}_{\mathrm{int}} = A^{so}\hat{\mathrm{L}}_a\hat{\mathrm{S}}_a - 2A\hat{\mathrm{N}}_a\hat{\mathrm{L}}_a, \tag{4.8}$$

The a-axis of a (near) prolate symmetric top molecule plays the same role in quanitization as the internuclear axis of a diatomic molecule so they replaced the angular momentum operators $\hat{\mathrm{N}}_a$, $\hat{\mathrm{L}}_a$, $\hat{\mathrm{S}}_a$ by their corresponding quantum numbers K_a, Λ and Σ. The 2×2 energy matrix was then diagonalized for the interacting $\tilde{A}$ and $\tilde{B}$ states, and solved for the correction of their energies to second order. The relevant results from their analysis are :

$$A = A^{spec} \pm \frac{4\Lambda^2A^2}{E_{\tilde{B}} - E_{\tilde{A}}}, \quad \epsilon_{aa}^{(2)} = \pm\frac{4\Lambda^2AA^{so}}{E_{\tilde{B}} - E_{\tilde{A}}}. \tag{4.9}$$

The formula for $\epsilon_{aa}^{(2)}$ is equivalent to the formula derived from the pure precession limit, where we had already used the fact that $\Lambda = 1$ (Λ = the projection of the electronic orbital angular momentum on the top axis) for a p–orbital. A^{spec} is the rotational constant derived from fitting the line positions of the spectra, again the top sign of eqn. (4.9) refers to the lower electronic state. This result also shows that the observed value of the A^{spec} rotational constant contains a large second order contribution to the true A rotational constant.

On the basis of the molecular geometry, $\Delta A = A_{\tilde{B}}^{spec} - A_{\tilde{A}}^{spec}$ should be small. This is because the electron occupies either an in–plane or out–of–plane "non-bonding" p–orbital. However, the fitted rotational constants are significantly different ($A_{\tilde{A}}^{spec} = 11.449$ cm^{-1} vs. $A_{\tilde{B}}^{spec} = 14.366$ cm^{-1}), which would at first sight imply a large change in geometry between the $\tilde{A}$ and $\tilde{B}$ states. Applying the second order correction from eqn. (4.9), we find that the true rotational constant for the $\tilde{A}$ and $\tilde{B}$ states is 12.907 cm^{-1}, which is very similar to the A^{spec}=12.951 cm^{-1} for the $\tilde{C}$ state and to the A^{spec}=13.057 cm^{-1} of the ground state. The second–order corrections to the B (where $B^{(2)} = \pm\frac{4B^2}{E_{\tilde{C}}-E_{\tilde{B}}}$) and C rotational constants are small ($\sim 10^{-4}$ cm^{-1}) compared to experimental uncertainty of these constants.

The approach given by Whitham and Jungen is specific to the the $\tilde{A}$ and $\tilde{B}$ states and interactions about the a–axis. Our discussion here is more general, and for an electron that possesses a well defined orbital angular momentum we can write effective formulae for ϵ_{bb} and ϵ_{cc} :

$$\epsilon_{bb}^{(2)} = \pm\frac{2\ell(\ell+1)BA^{so}}{E_{\tilde{C}} - E_{\tilde{B}}}, \quad \epsilon_{cc}^{(2)} = \pm\frac{2\ell(\ell+1)CA^{so}}{E_{\tilde{C}} - E_{\tilde{A}}}, \tag{4.10}$$

where $\ell = 1$ for p orbitals.

The comparison of the observed spin–rotation constants to their corresponding pure precession values are shown in Table 4.4. All the values calculated from the pure precession formula are in reasonable agreement with the observed spin–rotation parameters in both magnitude and sign. The ϵ_{aa} parameter is extremely well predicted for the $\tilde{A}$, $\tilde{B}$ states, i.e. <10 % of the experimental value. Also, the spin–rotation parameters in the ground state are predicted to be zero by pure precession, since $\ell = 0$ for an s–orbital. Experimentally, we find an extremely small value for the constant $\frac{1}{2}(\epsilon_{bb} + \epsilon_{cc})$. The ground state of $CaNH_2$ correlates with a $^2\Sigma^+$ (Fig. 1.1) state in a linear molecule like CaOH. The ground state spin–rotation parameter, γ, for a diatomic (or linear) alkaline earth molecule is expected to be small. Since the constant, $\frac{1}{2}(\epsilon_{bb} + \epsilon_{cc})$, is equivalent to γ, the magnitude of $\frac{1}{2}(\epsilon_{bb} + \epsilon_{cc}) = 8.5 \times 10^{-4}$ cm^{-1} should be close to that of the isoelectronic CaOH molecule ($\gamma'' = 9.53 \times 10^{-4}$ cm^{-1}) or the diatomic CaF molecule ($\gamma'' = 1.3 \times 10^{-3}$cm^{-1}). The parameter ϵ_{aa} is equivalent to the spin–orbit (A^{SO}) constant of a diatomic (linear) molecule is zero for a $^2\Sigma^+$ state and this is what is observed for the ground state of $CaNH_2$.

The other spin–rotation parameters of Table 4.4 are in good qualitative agreement with experiment, except for ϵ_{aa} of the $\tilde{C}^2A_1$ state. This is most likely due to mixing of the pure p–orbitals (assumed in our pure precession model) with d–orbitals and vibronic interactions. The intermediate value of ϵ_{aa} for the $\tilde{C}^2A_1$ state corresponds to a Hund's case (b) coupling scheme while the significantly larger ϵ_{aa} of 8 cm^{-1} for the $\tilde{B}$ and $\tilde{A}$ states corresponds to Hund's case (a) coupling for

$K_a \neq 0$. Thus, the 1–0 sub-bands of the $\tilde{A}$–$\tilde{X}$ and $\tilde{B}$–$\tilde{X}$ would resemble a case (a) $^2\Pi$–$^2\Sigma^+$ transition of a diatomic molecule while a 2–1 transition resembles a case (a) $^2\Delta$– case (b)$^2\Pi$ ($\epsilon_{aa}(\tilde{X}^2A_1) = 0 \equiv A^{SO}$) of a diatomic molecule.

Finally, we have calculated values for the g–tensor from Curl's formula [162] :

$$g_{aa} = g_e - \frac{\epsilon_{aa}}{2B_a}, \tag{4.11}$$

where g_e is the electron g–factor. The predicted values are reported in Table 4.5.

4.3.1 Geometrical Parameters

The r_0 geometries have been calculated for all of the low–lying states of $CaNH_2$. Rotational constants are available for only one isotopomer ($^{40}Ca^{14}NH_2$), so that all three structural parameters r_{CaN}, r_{NH} and θ_{HNH} cannot be determined simultaneously for the planar $CaNH_2$ molecule. The inertial defects are 0.16, 0.13, 1.43 and 0.01 amu Å^2 for the $\tilde{X}$, $\tilde{A}$, $\tilde{B}$ and $\tilde{C}$ states, respectively. Thus, the r_{NH} bond distance was constrained to the value found in NH_2^- [163] $r_{NH} = 1.041$ Å or NH_2 [164] $r_{NH} = 1.023$ Å. For the $\tilde{A}$ and $\tilde{B}$ states we used the true value of the A rotational constant to calculate I_A. Fundamental constants and molecular masses were taken from ref. [165]. In each case we calculated the geometry with (I_A,I_B) or (I_A,I_C) pairs. Table 4.6 and 4.7 shows the results of the calculation, which are the average of the moment of inertia pairs, and these are compared with r_e *ab initio* calculations [166] performed for $CaNH_2$. The theoretical values are in reasonable agreement with experiment.

4.4 Summary

The high resolution spectrum of the $\tilde{C}\ ^2A_1$–$\tilde{X}\ ^2A_1$ transition $CaNH_2$ has been recorded in a laser ablation/molecular beam spectrometer. This molecule is the first alkaline–earth polyatomic molecule for which all of the low–lying electronic states have been analyzed at high resolution. We have derived some simple expressions for the spin–rotation parameters using a simple one–electron model. This so called pure precession model assumes that the first three electronic transitions of the molecule are purely metal-centered ($np \leftarrow ns$) in origin. This model does a good job in predicting the observed spin–rotation parameters of $CaNH_2$. It would be very interesting to see if the model works for similar molecules such as $SrNH_2$ and $BaNH_2$ and also with a molecule of lower symmetry such as CaSH.

Table 4.1: The spectroscopic constants for $CaNH_2$, all constants are in cm^{-1}.

	$\tilde{X}^2A_1$	$\tilde{A}^2B_2$	$\tilde{B}^2B_1$	$\tilde{C}^2A_1$
T_{0-0}	0	15464.367390(525)	15885.281096(869)	17375.166886(726)
A	13.057453(597)	11.448545(151)	14.36492(132)	12.951300(962)
$\frac{1}{2}(B+C)$	0.2966573(126)	0.3031126(161)	0.301799(194)	0.3015174(165)
$\frac{1}{4}(B-C)$	$1.89167(435)\times10^{-3}$	$1.9584(310)\times10^{-3}$	$3.6947(535)\times10^{-3}$	$1.7737(112)\times10^{-3}$
ϵ_{aa}	0	8.23690(128)	-7.54163(158)	0.99870(657)
$\frac{1}{2}(\epsilon_{bb}+\epsilon_{cc})$	$8.524(610)\times10^{-4}$	$3.0532(180)\times10^{-2}$	$2.05316(992)\times10^{-2}$	$-3.91334(106)\times10^{-2}$
$\frac{1}{4}(\epsilon_{bb}-\epsilon_{cc})$	0	$-1.2619(151)\times10^{-2}$	$8.321(132)\times10^{-3}$	$-3.29(189)\times10^{-4}$
Δ_K	–	–	$-4.0843(274)\times10^{-2}$	–
Δ_N	–	–	$-4.69(103)\times10^{-7}$	$1.0895(274)\times10^{-6}$
δ_K	–	–	$2.0053(462)\times10^{-3}$	–
Δ_K^S	–	$-6.0652(327)\times10^{-2}$	$-1.632(132)\times10^{-2}$	–
Δ_{KN}^S	–	–	$-6.629(121)\times10^{-2}$	$2.544(217)\times10^{-3}$
Δ_{NK}^S	–	–	$5.857(133)\times10^{-3}$	–

Table 4.2: Correlation between principal axis system and molecular coordinates. See fig. 1.2.

$\tilde{A}\ ^2B_2 = p_y$	$\hat{\ell}_a = \hat{\ell}_z$
$\tilde{B}\ ^2B_1 = p_x$	$\hat{\ell}_b = \hat{\ell}_y$
$\tilde{C}\ ^2A_1 = p_z$	$\hat{\ell}_c = \hat{\ell}_x$

Table 4.3: Effect of orbital angular momentum operators on the cartesian p–orbitals

$\hat{\ell}_x p_x = 0$	$\hat{\ell}_y p_x = -ip_z$	$\hat{\ell}_z p_x = ip_y$
$\hat{\ell}_x p_y = ip_z$	$\hat{\ell}_y p_y = 0$	$\hat{\ell}_z p_y = -ip_x$
$\hat{\ell}_x p_z = -ip_y$	$\hat{\ell}_y p_z = ip_x$	$\hat{\ell}_z p_z = 0$

Table 4.4: The spin rotation parameters for $CaNH_2$.

		$\tilde{X}^2A_1$	$\tilde{A}^2B_2$	$\tilde{B}^2B_1$	$\tilde{C}^2A_1$
	Observed	0	8.237	-7.542	0.999
ϵ_{aa}	Pure Precession	0	8.193	-8.193	0
	Formula [1]	–	$+\frac{4\Lambda^2 AA^{SO}}{\Delta E_{\tilde{B}-\tilde{A}}}$	$-\frac{4\Lambda^2 AA^{SO}}{\Delta E_{\tilde{B}-\tilde{A}}}$	–
	Observed	8.52×10^{-4}	0.00530	0.0372	-0.0398
ϵ_{bb}	Pure Precession	0	0	0.0554	-0.0534
	Formula	–	–	$+\frac{2\ell(\ell+1)BA^{SO}}{\Delta E_{\tilde{C}-\tilde{B}}}$	$-\frac{2\ell(\ell+1)BA^{SO}}{\Delta E_{\tilde{C}-\tilde{B}}}$
	Observed	8.52×10^{-4}	0.0558	0.00389	-0.0385
ϵ_{cc}	Pure Precession	0	0.0418	0	-0.0417
	Formula	–	$+\frac{2\ell(\ell+1)CA^{SO}}{\Delta E_{\tilde{C}-\tilde{A}}}$	–	$-\frac{2\ell(\ell+1)CA^{SO}}{\Delta E_{\tilde{C}-\tilde{A}}}$

[1]–$A^{SO} = 66.795$ cm^{-1} spin–orbit constant of CaOH.

Table 4.5: Estimated g–tensor from Curl's formula

	$\tilde{X}^2A_1$	$\tilde{A}^2B_2$	$\tilde{B}^2B_1$	$\tilde{C}^2A_1$
g_{aa}	2.0023	1.6426	2.2648	1.9638
g_{bb}	2.0009	1.9937	1.9421	2.0675
g_{cc}	2.0009	1.9091	1.9957	2.0669

Table 4.6: Geometrical Parameters

	$\tilde{X}^2A_1$	$\tilde{A}^2B_2$	$\tilde{B}^2B_1$	$\tilde{C}^2A_1$
θ_{HNH}	100.5°	101.3°	101.7°	101.1°
r_{NH} (Å)[1]		1.041		
r_{CaN} (Å)	2.118	2.098	2.090	2.102
θ_{HNH}	102.9°	103.8°	103.8°	103.5°
r_{NH} (Å)[2]		1.025		
r_{CaN} (Å)	2.140	2.120	2.125	2.125

[1]–Bond distance from NH_2^- ref. [163]
[2]–Bond distance from NH_2 ref. [164]

Table 4.7: Experimental and *ab initio* parameters for the $\tilde{X}^2A_1$ State.

		DFT [1]	Expt.	
θ_{HNH}		105.6°	100.5°	102.9°
r_{NH} (Å)		1.02	1.041[2]	1.025[2]
r_{CaN} (Å)		2.13	2.118	2.140
Vibration		DFT (cm^{-1})[1]	Expt. ($\pm$ 10 cm^{-1})[3]	
ν_6 anti–symm. NH bend	b_2	345	320	
ν_4 out–of–plane bend	b_1	455	347	
ν_3 Ca–N Stretch	a_1	544	520	
ν_2 symm. NH bend	a_1	1586	–	
ν_1 symm. NH stretch	a_1	3448	–	
ν_5 anti–symm. NH stretch	b_2	3535	–	

[1]–Ref. [166].
[2]–Fixed, see § 4.3.1.
[3]–From low resolution Broida oven experiment.

Chapter 5

Infrared Spectroscopy of Transient Molecules

The infrared region has traditionally been a difficult portion of the electromagnetic spectrum to work in, compared to the visible or microwave regions. An intrinsic limitation of vibration–rotation spectroscopy is the relatively weak transition dipole moments. They are of the order of 0.1 debye, which is small when compared to a typical electric dipole–allowed electronic transition. Since the relative intensity of a transition depends on the square of the transition dipole moment, methods to detect infrared signals from molecules therefore have to be very sensitive.

The most widely used instruments to date have been diode laser spectrometers and Fourier transform spectrometers. Diode lasers can have high power outputs (up to 50 mW) and narrow spectral linewidths (a few megahertz) which makes them suitable for high resolution and high sensitivity spectroscopic studies. The major drawback of diode lasers, however, is the sparse spectral coverage and the

tedious wavenumber calibration. Newer methods based on nonlinear optical techniques, such as difference mixing of two near IR (or visible) lasers [167, 168] and optical parametric oscillators are proving to be promising methods for infrared spectroscopy [169]. Fourier transform spectrometers are currently not as sensitive as laser–based techniques for recording the spectra of transient molecules. A Fourier transform spectrometer does, however, have inherent advantages over traditional dispersive or grating instruments. Fourier transform (FT) instruments have wide spectral coverage over a continuous wavenumber range (this is the so–called Connes advantage), and an internal wavenumber calibration.

The newer technique of infrared emission spectroscopy has made FT instruments a more sensitive tool for recording the spectra of transient molecules. It is widely known that techniques involving emission spectroscopy are superior in sensitivity when compared to absorption methods in the visible and UV regions. This is due to the possibility of performing essentially zero background measurements, while absorption spectroscopy requires monitoring the difference of a "weak" absorption in the presence of a bright and potentially noisy light source.

A major difficulty when recording the absorption spectra of transient molecules is the accumulation of sufficient gas phase concentration of the molecular species. For a low gas phase concentration, which is typical when recording spectra of transient species, it is rather difficult to observe an appreciable light absorption. An excellent example which shows the sensitivity of emission methods over absorption spectroscopy is the case of BaH [170]. In experiments performed under similar conditions, the infrared absorption signal of BaH was imperceptible over the noise,

while the emission spectrum could be recorded with a modestly high signal–to–noise ratio (~20:1). Performing a thermodynamic equilibrium calculation for the reaction, $Ba(\ell) + \frac{1}{2}H_2(g) \rightleftharpoons BaH(g)$, it was estimated estimated that the partial pressure of BaH was 35 mTorr inside a tube with a length of 80 cm. This work demonstrated that there was at least a factor of 20 greater sensitivity in the emission measurement, all conditions being equal. Alternatively, in accordance with Beer's law, the only way to obtain an appreciable absorption signal would be to increase the path length the radiation travels in order to achieve the equivalent signal from an absorption experiment. Typically, one uses multiple reflection techniques with a White–type cell [171,172] to obtain long path lengths. Thus, for free radical or transient species, which have relatively low gas phase concentrations, emission spectroscopy is perhaps the simplest method to record a molecular spectrum.

Some of the first observations of an infrared emission spectrum of a free radical recorded with an FT instrument were reported for PH [173], and later for FO [174]. It had been believed that infrared emission would only be observable if an energetic method to generate the molecules was employed. The PH molecules was made in a microwave discharge while FO was produced in an exothermic reaction of F radicals with ozone (O_3). Therefore, it was surprising when the first thermal infrared emission spectrum was reported by Uehara *et al.* [175]. In this work, GeS was heated to 900 K, where the vibration–rotation spectrum of the 1–0 to 3–2 bands of the $X^1\Sigma^+$ ground state was recorded. This technique was extended by Frum *et al.* [176] when they accidentally recorded emission spectra SiS at 800 cm^{-1} in an attempt to observe that species in absorption. Unlike PH produced

in a microwave discharge or FO produced from an exothermic reaction, the SiS and GeS spectra were simply a result of thermal emission. The universality of this technique was demonstrated when strong emission spectra were recorded for molecules such as AlH [177], InH [178], GaH [179] and HF [180, 181], all of which have vibrational frequencies $\geq$ 1500 cm^{-1}. Using relatively simple experimental conditions, coupling a high temperature furnace with an FT spectrometer, one can generate a wide variety of transient molecules that can be detected via emission spectroscopy [169, 182].

5.1 Introduction to Fourier Transform Spectroscopy

In 1891 Albert Michelson [183] reported a design for an interferometer which in most respects resembles the interferometer found in modern FT spectrometers. The so–called Michelson interferometer played a very important role in the history of physics of the late 19th century [184]. In the early 1880's, an earlier version of the modern interferometer was used to develop a state–of–the–art procedure to measure the unit of length. The standard meter prior to 1884 was defined as the distance between two scratches on a platinium–iridium bar kept at the Paris Academy of Sciences. Using a glow discharge of ^{86}Kr (λ = 6058 Å), a careful series of experiments was performed under controlled conditions by Michelson. He was able to precisely measure the number of fringes of the ^{86}Kr wavelength in the old standard meter. Based on these measurements the meter was redefined as 1 650 763.7 fringes of the ^{86}Kr wavelength. This new procedure was given wide approval when in 1903 the International Conference on Weights and Measures adopted the length of the

meter as 1 553 1963.5 wavelengths of the red radiation of cadmium. This definition was used until November 1983 when it was redefined in terms of a unit time (second). This new definition was based on the frequency of a hyperfine transition of the Cs atom. This definition fixed the value for the speed of light and from this the definition of a meter is obtained.

Another important application of the interferometer was the measurement of the motion of the earth with respect to the æther. Before the development of Einstein's theory of special relativity, physicists believed that electromagnetic radiation had to propagate through a mechanical medium, in much the same way sound propagates through air. Beginning in 1882, Michelson along with his colleague Morley, attempted to measure this motion. They surmised that if the instrument was moving with or against the æther, the path the light traveled through the interferometer would be slightly different and would therefore lead to a shift in the fringe pattern of the light. The experiment was designed so their entire instrument could be carefully rotated during an experiment to measure this shift. By 1887, their results showed no significant shift, so that despite orbital motion of the earth their appratus seemed at rest with respect to the æther. Physicists of the time were perplexed by these results and it would not be until 1905 when special relativity would shed *light* on the results of the Michelson–Morley experiment.

Michelson was aware of the possibility of using the interferometer to obtain spectra and manually calculated spectra of many interferograms. It was not until the 1960's, with the development of modern computers and a mathematical technique called the fast Fourier transform, that the FT spectrometer became a practical

instrument for spectroscopic measurements.

The essential elements of an interferometer are a beamsplitter (BS), a stationary mirror (M1) and a movable mirror (M2), as shown in Fig. 5.1. Electromagnetic radiation passes through an input aperture of the interferometer and is split into two orthogonal beams at the beamsplitter. One beam is reflected by the beamsplitter and goes to M1 and the other is transmitted to M2. Ideally, the two beams are of equal intensity and are reflected back to the beamsplitter by the two mirrors. If M1 and M2 are exactly the same optical distance from the beamsplitter (called zero path difference (ZPD)), then both light beams have traveled the same distance (2L). The beams recombine at the beamsplitter resulting in constructive interference giving the original beam that was incident on BS, neglecting any reflection or transmission losses. If M2 is displaced a distance x from BS with respect to M1, then an interference pattern will result when the two beams recombine at the BS. Depending on the position of the movable mirror, the beams will either interfere in a constructive or destructive manner, and a fringe pattern will emerge at the detector. This pattern will repeat itself at integral multiples of $\frac{\lambda}{2}$ of the M2 travel distance, where λ is the wavelength of the light. If the incident radiation is monochromatic with a frequency of $\nu = hc/\lambda$, the fringe pattern will appear as a sine wave. However, for polychromatic sources, which have many wavelengths of differing intensities, the pattern that emerges will be a complex sum of sine waves. The interference pattern recorded at the detector is now called an interferogram (Fig. 5.1). The interferogram is function of x, which is the displacement of M2 with respect to the distance from the stationary mirror to the beamsplitter. For

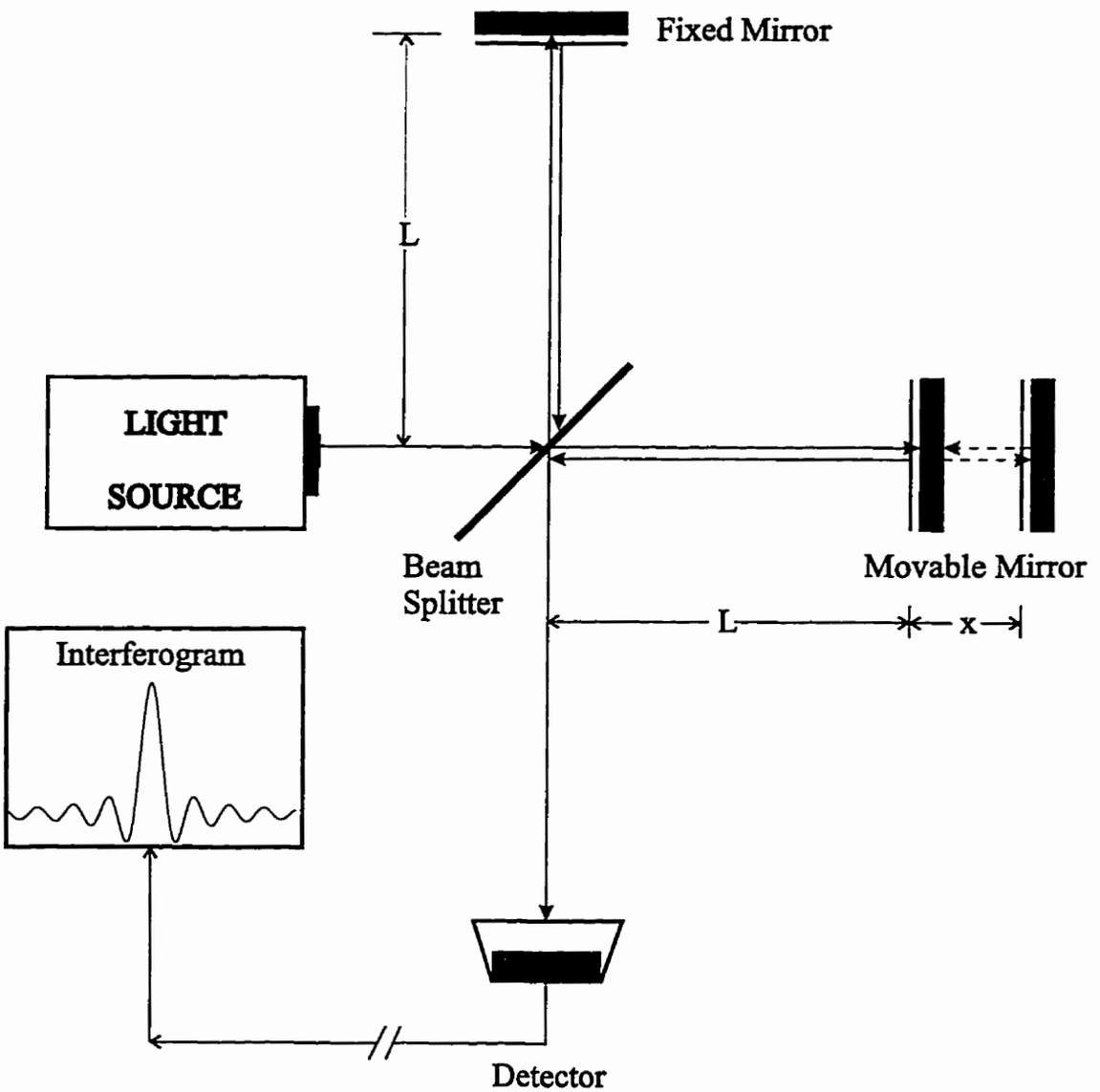

Figure 5.1: The schematic diagram of a Michelson interferometer

any optical path difference (OPD), the light intensity falling on the detector at frequency ν is given by [185] :

$$I'(x) = \frac{1}{2}I(\nu)[1 + \cos(2\pi\nu x)]. \tag{5.1}$$

$I'(x)$ is made up of a dc component $\frac{1}{2}I(\nu)$ which is the average intensity falling on the detector and an ac component :

$$I(x) = \frac{1}{2}I(\nu)\cos(2\pi\nu x). \tag{5.2}$$

For a source emitting a continuous spectrum, the complete interferogram is given by :

$$I(x) = \frac{1}{2}\int_{-\infty}^{+\infty} I(\nu)\cos(2\pi\nu x)\, d\nu, \tag{5.3}$$

This equation is valid for an ideal beamsplitter whose reflectivity and transmissivity are exactly 50%. In reality, this condition is rarely met and a beamsplitter efficiency term must be included in the equation :

$$I(x) = \int_{-\infty}^{+\infty} B(\nu)\cos(2\pi\nu x)\, d\nu, \tag{5.4}$$

where,

$$B(\nu) = \frac{1}{2}I(\nu)\eta(\nu). \tag{5.5}$$

Here, $\eta(\nu) = 4R(\nu)T(\nu)$ where $R(\nu)$ and $T(\nu)$ are the frequency dependent reflectance and transmittance of the beamsplitter, respectively. The interferogram

can be rewritten in its usual way :

$$I(x) = \int_{-\infty}^{+\infty} B(\nu) \exp(2\pi i \nu x)\, d\nu. \tag{5.6}$$

The spectrum $B(\nu)$ can be calculated by computing the complex Fourier transform of $I(x)$:

$$B(\nu) = \int_{-\infty}^{+\infty} I(x) \exp(-2\pi i \nu x)\, dx. \tag{5.7}$$

The integration limits of $B(\nu)$ are between $\pm\infty$, infinite mirror displacement, which for real FT spectrometers are impractical limits. The displacement (x) of the moving mirror is finite and this will limit the resolution ($\Delta\nu$) of a spectrum. The maximum spectral resolution that can be achieved for a Michelson interferometer with a finite OPD is :

$$\Delta\nu = \frac{0.6}{\text{OPD}}. \tag{5.8}$$

Thus, high resolution spectra (≤ 0.02 cm^{-1}) require an OPD greater than 30 cm. The quantity x in eqn. (5.7) is actually determined by the product of the velocity of the moving mirror and the time from ZPD. Thus, for a practical instrument, x must be precisely controlled. This is acheived by using a single mode laser (usually He–Ne) to accurately control the mirror motion. All commercial high resolution FT spectrometers use a single mode laser to track the displacement of the mirror and trigger data acquisition. This laser also provides a convenient internal wavenumber standard.

The sensitivity of an FTS is greater than that of a grating instrument because of two reasons. First, the use of circular aperatures allows maximum throughput

of light (Jacquinot's advantage), and secondly, light from the entire spectral region (of interest) falls on the detector (mutiplex advantage). The light at the detector is modulated by the moving mirror resulting in an interferrogram. The Fourier transform of the interferrogram gives the spectrum.

For an FTS, spectral information on the entire wavenumber interval is simultaneously acquired at the detector, rather than sequentially as with a grating instrument. If the dominant source of noise is the detector, then the time required to acquire a spectrum of equivalent signal–to–noise ratio (SNR) would be N times less with an FT instrument than with a grating instrument. Here, N is the number of resolution elements. For example, a spectrum measured between 400 to 1000 cm^{-1} at 1 cm^{-1} resolution would have 600 resolution elements (N). If a grating instrument could measure this spectrum in 10 minutes (600 s) with a certain SNR, the FT would require 1s to achieve the same performance. This can also be expressed in terms of sensitivity, which is proportional to $\sqrt{N}$; i.e. the FT has $\sqrt{600}$ ($\sqrt{N}$) or 24.5 times better SNR over a grating spectrometer with equal integration times.

The aperture size also dictates the resolution that can be acheived by an FTS. The light rays entering an FTS are generally not perfectly collimated, so some of the light rays travel a slightly displaced path from the central optical axis of the spectrometer, thereby degrading resolution. A small entrance aperture will reduce this problem, but at the same time this will reduce the light intensity falling onto the detector. There are two contradictory requirements at work here: a large aperture size will increase the sensitivity which is important when attempting to record weak signals, but this will degrade the spectral resolution necessary for high

resolution studies. This maximum possible angular divergence or maximum solid viewing angle (Ω) for a resolution $\Delta\nu$ is :

$$\Omega_{\max} = 2\pi\left(\frac{\Delta\nu}{\nu_{\max}}\right) \text{ steradians} \tag{5.9}$$

where $\nu_{\max}$ is the largest wavenumber in the spectral region of interest. Equivalently, for a light source of finite area the maximum achievable resolution is :

$$\Delta\nu = \frac{\nu_{\max} d^2}{8F^2}, \tag{5.10}$$

where d is the diameter of the input aperture and F is the focal length of the interferometer. Thus in many cases, the choice of increased sensitivity is made at the expense of spectral resolution. The circular aperture does, however, have a significant advantage over the slits found in grating instruments. The optical throughput, given by the product of the input beam area and subtended solid angle, is greater for an FTS than for a grating spectrometer at any given wavelength or resolution [186].

Chapter 6

Theory of Diatomic Spectroscopy

6.1 Born–Oppenheimer Approximation

The time independent Schrödinger equation gives the quantum mechanical description of electronic and nuclear interactions in a diatomic molecule,

$$\hat{\mathrm{H}}\Psi(\{\mathbf{r_i}\},\mathbf{R}) = E\Psi(\{\mathbf{r_i}\},\mathbf{R}) \tag{6.1}$$

where $\hat{\mathrm{H}}$ is the Hamiltonian of the system, $\Psi(\{\mathbf{r_i}\},\mathbf{R})$ is the wavefunction, $\mathbf{r_i}$ is the position vector of electron i, $\mathbf{R}$ is the position vectors of the nuclei, and E is the eigenvalue of the Hamiltonian. The solution of the Schrödinger equation is, in general, a very difficult problem and an analytical solution can never be found except for the simplest systems.

The mass of an electron is much smaller than the mass of the nuclei therefore the approximation that the motion of the electrons is independent of the motion

of nuclei is made as a first–order approximation. The electronic motion occurs on a much faster time scale than nuclear motion thus Born and Oppenheimer made the rather reasonable assumption that the electrons see an effective or average potential. The internuclear distance can be considered constant and the diatomic molecule will have a effective energy U for each $\mathbf{R}$. The separation of these motions simplifies the mathematical analysis of the problem, and the wavefunction in the Schrödinger equation becomes a product of electronic and nuclear terms, $\Psi(\{\mathbf{r}_i\},\mathbf{R}) = \psi_e(\{\mathbf{r}_i\};\mathbf{R})\psi_N(\mathbf{R})$. The total Hamiltonian for a diatomic molecule is :

$$\hat{\mathbf{H}} = \hat{T}_N + \hat{T}_e + \hat{V}_{NN} + \hat{V}_{ee} + \hat{V}_{Ne}, \tag{6.2}$$

where,

$$\hat{T}_N = -\frac{\hbar^2}{2}\left(\frac{1}{M_A}\nabla_A^2 + \frac{1}{M_B}\nabla_B^2\right) \qquad \hat{T}_e = -\frac{\hbar^2}{2m_e}\sum_i \nabla_i^2. \tag{6.3}$$

$$\hat{V}_{NN} = \frac{Z_A Z_B e^2}{R_{AB}} \qquad \hat{V}_{ee} = \sum_{i>j}\frac{e^2}{r_{ij}} \qquad \hat{V}_{Ne} = -\sum_{\gamma=A,B}\frac{Z_\gamma e^2}{R_{i\gamma}}. \tag{6.4}$$

The terms in eqn. (6.3) are the nuclear and electronic kinetic energy operators with M_γ being the mass of the nucleus A or B, and m_e is the electron mass. In eqn. (6.4), Z_γ is the nuclear charge and e is the elementary charge of the electron, $\hat{V}_{NN}$ represents the internuclear repulsion term, $\hat{V}_{ee}$ is the coulombic repulsion of electrons, and $\hat{V}_{Ne}$ is the nuclear–electron attraction term. If the nuclei are considered fixed in space, then $\hat{T}_N = 0$ and $\hat{V}_{NN}$ is constant for the nuclear configuration. We can write an electronic Hamiltonian $\hat{H}_e = \hat{T}_e + \hat{V}_{NN} + \hat{V}_{ee} + \hat{V}_{Ne}$ and the electronic part

of the wave equation becomes :

$$\hat{H}_{\rm e}\psi_{\rm e}(\{\mathbf{r_i}\},\mathbf{R}) = E_{el}(R)\psi_{\rm e}(\{\mathbf{r_i}\},\mathbf{R}) = U(R)\psi_{\rm e}(\{\mathbf{r_i}\},\mathbf{R}). \tag{6.5}$$

Again, $\psi_{\rm e}$ and E_{el} are the electronic wavefunction and energy of the molecule, the symbols $\{\mathbf{r_i}\}$, are the set of electronic coordinates and R is the nuclear separation. The $\mathbf{R}$ in eqn. (6.5) occurs as a parameter in ψ_e and E_{el}, thus the electronic energy and wavefunction depends on the internuclear separation. A change in the position of the nuclei will affect the electronic charge distribution which is described by the effective internuclear potential $U(R)$. The solution of the nuclear part of the Schrödinger equation requires knowledge of $U(R)$. The complete wave equation that includes nuclear motion of the molecule becomes :

$$\hat{\mathbf{H}}\Psi(\{\mathbf{r_i}\},R) = (\hat{H}_{\rm e} + \hat{T}_{\rm N})\Psi(\{\mathbf{r_i}\},R) = E_{\rm TOT}\psi_{\rm e}(\{\mathbf{r_i}\},R)\psi_{\rm N}(R) \tag{6.6}$$

If the nuclear–electronic coupling effects are small for a given electronic state of the molecule then we can neglect the cross terms in the rigorous expansion of $\hat{\mathbf{H}}\Psi$ in eqn. (6.6) i.e. $\hat{H}_{\rm e}\psi_{\rm N}(R) = 0$ and $\hat{T}_{\rm N}\psi_{\rm e}([\mathbf{r_i}],R) = 0$. Eqn. (6.6) can be rewritten as :

$$\psi_{\rm e}(\{\mathbf{r_i}\},R)\hat{T}_{\rm N}\psi_{\rm N}(R) = [E_{\rm TOT} - U(R)]\psi_{\rm N}(R)\psi_{\rm e}(\{\mathbf{r_i}\},R). \tag{6.7}$$

Now, by dividing both sides by $\psi_{\rm e}([\mathbf{r_i}],R)$ the wave equation becomes an effective equation for nuclear motion :

$$\hat{T}_{\rm N}\psi_{\rm N}(R) = [E_{\rm tot} - U(R)]\psi_{\rm N}(R). \tag{6.8}$$

For a diatomic molecule in a $^1\Sigma^+$ electronic state, $\psi_N(R)$ can be written in its customary way, $\psi_N(R) = R^{-1}\psi_{v,J}(R)Y_{lm}(R)$, where the Y_{lm}'s are the spherical harmonic functions and $\psi_{v,J}$ is the vibrational wavefunction. By removing the center of mass motion in the Schrödinger equation for vibration–rotation motion, the effective one–dimensional equation in the scalar parameter R for a diatomic molecule becomes :

$$-\frac{\hbar^2}{2\mu}\frac{d^2}{dR^2}\psi_{v,J}(R) + \left(U(R) + \frac{J(J+1)}{2\mu R^2}\right)\psi_{v,J}(R) = E(v,J)\psi_{v,J}(R). \qquad (6.9)$$

A general mathematical form of $U(R)$, applicable to all systems, is not necessarily required before solving eqn. (6.9). An empirical function for $U(R)$ is typically used and eqn. (6.9) can be solved by numerical or analytical methods. Analytical procedures are usually require further approximations (see §6.2). The choice of the potential model is very important for the fitting of high precision rovibrational spectral data. The asymptotic behavior of $U(R)$ should be physically meaningful to avoid problems such as unrealistic dissociation energies or irregular behavior at small internuclear distances, i.e. $U(R)$ should be a smooth monotonically increasing function for $R > R_e$ and for $R < R_e$, where R_e is the minimum of the potential.

6.2 Dunham Potential

Analytical expressions for the energy levels of a vibrating rotor were calculated by J.L. Dunham [187] in 1932. In his treatment, Dunham rewrote the Schrödinger equation of eqn. (6.9) in terms of ξ, where $\xi = (R - R_e)/R_e$. The analytical form

of the potential function was expanded as a power series in ξ in the region of the potential minimum :

$$U(\xi) = a_0\xi^2\Big(1 + \sum_{i\geq 1} a_i\xi^i\Big), \tag{6.10}$$

where $\{a_i\}$ are the potential parameters. An analytical expression for the eigenvalues of the Schrödinger equation cannot be derived using this form of the potential. Thus, Dunham used a semiclassical approach, the first-order Wentzel-Kramers-Brillouin (WKB) approximation, to obtain an approximate solution of the problem. The WKB quantization condition is given by [188] :

$$\Big(\frac{2\mu}{\hbar^2}\Big)\int_{R_-}^{R_+}\sqrt{E(v,J) - U(R)}\;dR = (v + \frac{1}{2})\pi. \tag{6.11}$$

$E(v,J)$ are the energy levels of the molecule, R_- and R_+ are the classical inner and outer turning points of the potential curve for each $E(v,J)$. The result of the formal inversion of the quantization condition using the power series potential of eqn. (6.10) is a simple and rather compact energy level formula :

$$E(v,J) = \sum_{i,j} Y_{i,j}(v + \tfrac{1}{2})^i[J(J+1)]^j, \tag{6.12}$$

where the Y_{ij} coefficients can be related back to the $\{a_i\}$ potential parameters. The beauty of the Dunham formula is the approximate relationship of the Dunham

coefficients to the normal band spectroscopic constants, such as :

$$\begin{array}{llll} Y_{10} \approx \omega_e & Y_{20} \approx -\omega_e x_e & Y_{30} \approx \omega_e y_e & Y_{40} \approx \omega_e z_e \\ Y_{01} \approx B_e & Y_{11} \approx -\alpha_e & Y_{21} \approx \gamma_e & \\ Y_{02} \approx -D_e & Y_{12} \approx -\beta_e & Y_{22} \approx -\delta_e & \\ Y_{03} \approx H_e & Y_{04} \approx L_e. & & \end{array} \tag{6.13}$$

The relationship between the Dunham coefficients for different isotopomers of a molecule is given by [189] :

$$Y_{ij}^{*} = Y_{ij}\left(\frac{\mu}{\mu^{*}}\right)^{[(i+2j)/2]} \tag{6.14}$$

where $\mu = (M_A M_B)/(M_a + M_b)$ is the reduced mass of the molecule and the asterisk denotes an isotopomer. In a conventional spectroscopic analysis of multiple isotopic species, each isotopomer is fit individually to eqn. (6.12). To compactly represent the data from many isotopomers, it is possible to factor out the isotopic dependence of Y_{ij} and write an isotopically independent form of the Dunham expression :

$$E(v, J) = \sum_{i,j} \mu^{-[(i+2j)/2]} U_{ij} (v + \tfrac{1}{2})^i [J(J+1)]^j, \tag{6.15}$$

and generate one set of mass-reduced constants (U_{ij}). The U_{ij}'s represent data from two or more isotopomers of a molecule.

This expression is only valid within the Born-Oppenheimer approximation and the first-order WKB approximation. For light molecules, breakdown of the Born-Oppenheimer and first-order WKB is very significant and eqn. (6.15) is not ade-

quate to the represent data. An expression designed to handle this problem was empirically applied by Ross *et al.* [190] and later, was theoretically derived by Watson [189]. The expression of eqn. (6.16) came from taking higher–order WKB terms into account as well as Born–Oppenheimer breakdown effects. The Dunham expression with Watson's correction for Born–Oppenheimer breakdown becomes :

$$E(v,J) = \sum_{i,j} \mu^{-[(i+2j)/2]} \quad U_{ij} \quad \left(1 + \left(\frac{m_e}{M_A}\right)\Delta_{ij}^{A} + \left(\frac{m_e}{M_B}\right)\Delta_{ij}^{B}\right) \times \quad (v+\tfrac{1}{2})^{i}[J(J+1)]^{j}, \tag{6.16}$$

where m_e is the electron mass, M_A, and M_B are the atomic masses of atom A and atom B, and the Δ_{ij}^{k}'s are the Born–Oppenheimer breakdown constants. The magnitude of the Δ_{ij}^{k}'s have no direct physical meaning because they collectively account for higher–order WKB terms and non–Born–Oppenheimer behavior.

The Δ_{ij}^{k}'s can be expressed in terms of a sum of adiabatic, non–adiabatic and Dunham (WKB breakdown) correction terms :

$$\Delta_{ij}^{k} = (\Delta_{ij}^{k})^{\text{adiabatic}} + (\Delta_{ij}^{k})^{\text{non-adiabatic}} + (\Delta_{ij}^{k})^{\text{Dunham}}. \tag{6.17}$$

Adiabatic in this context is defined as the corrections necessary to account for the neglect of the kinetic energy of the nuclei in each electronic state ($\hat{T}_{\text{N}}\psi_e \neq 0$) and non-adiabatic corrections are due to interactions with other electronic states. The Dunham correction term accounts for the failure of the first–ordersemiclassical WKB quantization condition to fully explain quantum mechanical effects [189,191].

The Δ_{01}^{k} parameter has been studied in detail by Tiemann *et al.* [192]. An

analytical expression has been derived for Δ_{01}^{k} for diatomic molecules :

$$(\Delta_{01}^{k})^{\text{Dunham}} = \frac{\mu \Delta Y_{01}^{(\text{D})}}{m_e B_e}, \tag{6.18}$$

where $\Delta Y_{01}^{(\text{D})}$[1] is the higer–order WKB correction to the rotational constant B_e. The expression orf the non–adiabatic correction is given by :

$$(\Delta_{01}^{k})^{\text{non-adiabatic}} = \frac{\mu g_j}{m_p}. \tag{6.19}$$

Here, g_J is the rotational g–factor and m_p is the mass of the proton. A method to calculate $(\Delta_{01}^{k})^{\text{adiabatic}}$ in a closed form expression has not been derived.

The Δ_{01}^{k} parameters are expected to be close to unity for a well–isolated electronic state. In the Tiemann *et al.* work, it was found that the $(\Delta_{01}^{k})^{\text{non-adiabatic}}$ contributes approximately 20–30% of the total Δ_{01}^{k} term. The $(\Delta_{01}^{k})^{\text{non-adiabatic}}$ value was predominantly characteristic of the atomic center and was independent of the nature of the bonding atom. The adiabatic correction was found, in general, to be much smaller the non—adiabatic corrections to Born–Oppenheimer breakdown. It should be noted that a large value for any Δ_{ij}^{k} could be the result of an accidentally small value of U_{ij}. Since these terms are fitted as a product $U_{ij} \cdot \Delta_{ij}^{k}$, there can be strong statistical correlations between these two terms. The meanings of the Δ_{ij}^{k} parameters are therefore not simple, and do not necessarily reflect the extent of Born–Oppenheimer breakdown.

The Dunham Y_{ij} or U_{ij} coefficients are not all independent parameters. The

[1] $\Delta Y_{01}^{(\text{D})} = (B_e^3/4\omega^2)(30 + 28a_1 + 21a_1^2 + 21a_1^3 - 18a_2 - 46a_1a_2 + 30a_3)$ [187].

potential constants (a_i's) have the unique property that the values of U_{i0}'s and U_{i1}'s can used to calculate all the higher–order coefficients of the potential. A few examples are as follows :

$$a_0 = -\frac{Y_{10}^2}{4Y_{01}} \tag{6.20}$$

$$a_1 = \frac{Y_{11}Y_{10}}{6Y_{01}^2} \tag{6.21}$$

$$a_2 = \frac{2Y_{20}}{3Y_{01}} + \frac{5a_1^2}{4} \tag{6.22}$$

Generally the higher–order potential constants are very complicated functions of the Dunham coefficients. By inverting the series in eqn. (6.10), the higher–order U_{ij}'s $j \geq 2$ can be algebraically expressed in terms of the lower order U_{ij}'s, $0 \leq j \leq 1$. These constraints are important because without them, the U_{ij} constants become arbitrary fitting parameters of a polynomial expansion which lacks physical meaning. Examples of a few relations are :

$$\begin{aligned} U_{02} &= -\frac{4U_{01}^3}{U_{10}^2}, \\ U_{12} &= \frac{-120U_{10}U_{11}U_{01}^2}{3U_{10}^4}, \\ U_{03} &= \frac{8U_{01}^3(U_{10}U_{11} + 12U_{01}^2)}{3U_{10}^4}. \end{aligned} \tag{6.23}$$

Ogilvie [193, 194] derived a complete set of U_{ij} relationships for $0 \leq i \leq 5$ and $2 \leq j \leq 12$. These results are used in the work reported here.

Another important use of a model is the prediction of unobserved transitions. The inclusion of high–order U_{0j} rotational terms are useful for predicting high–J

transitions and the constrained relationships allow for fewer independent parameters in a fit. However, the long–range behavior of the Dunham model is not adequate and the terms U_{i0} and U_{i1} cannot predict high v transitions beyond the range of the data.

6.3 Parameterized Potential Model

A new method to treat spectroscopic data has recently been developed because of the limitations of the Dunham model. Dunham's polynomial form of the potential has the unfortunate property that it diverges as R$\rightarrow \infty$, for any finite number of terms. The Dunham coefficients thus reproduce the input dataset, but extrapolate poorly. The approach described here is to directly fit the spectroscopic data to calculated eigenvalues of the radial Schrödinger equation. The choice of the potential model can be flexible, and is chosen for a specific molecular system. An early application of this method was applied to the energy levels of the $X^2\Sigma^+$ state of HgH by Kosman and Hinze [195], they called their procedure the inverse perturbation analysis (IPA). Further refinements of this technique were developed by Bunker and Moss [196] and more recently by Coxon [197–201], and Dulick, Bernath and co-workers [177–179, 202].

The parameterized potential model is different from the semiclassical Dunham model or the numerical RKR (Rydberg–Klein–Rees) model because adjustments are made to the potential function rather than to the analytical expression approximating the eigenvalues of the potential. This requires numerically solving the second order differential equation eqn. (6.9) to find the eigenvalues. The advantage

of this technique is that it utilizes all the data from a spectrum in contrast to the RKR method which uses this data indirectly (i.e. from G_v and B_v expansions). In addition, the parameterized potential model allows more flexibility since it can easily accommodate adiabatic and non–adiabatic (Born–Oppenheimer breakdown) corrections to the Schrödinger equation. It also avoids errors caused by the semiclassical approximation in the Dunham and RKR methods. Cumbersome higher–order corrections are not required when the Schrödinger equation is solved directly.

Direct numerical integration of the Schrödinger equation is a robust method if done correctly, so the calculation of molecular properties (extrapolation of unobserved energy levels) from the potential can give reliable results. The potentials derived in this manner are in excellent agreement with fully quantum mechanical *ab initio* potentials [177, 202]. The disadvantage of this technique, however, is that the fitting procedure is nonlinear and requires very good estimates of the first few potential parameters. Without these estimates, it is very difficult to achieve convergence in a fit.

The radial Schrödinger equation appropriate for a diatomic molecule in a $^1\Sigma^+$ electronic state is given by :

$$\left(\frac{\hbar^2}{2\mu}\frac{d^2}{dR^2} - U^{eff}(R) + E(v,J) - \frac{\hbar^2}{2\mu}[1+q(R)]\frac{(J(J+1)}{R^2}\right)\psi(R;v,J) = 0, \quad (6.24)$$

where the effective internuclear potential is a modification of that used by Coxon and Hajigeorgiou [197–199]. It is comprised of a Born–Oppenheimer component and adiabatic and non–adiabatic terms which take into account Born–Oppenheimer breakdown. Adiabatic corrections account the mass dependence introduced into the

potential by neglecting the kinetic energy of the nuclei in an electronic state. In vibration-rotation spectroscopy this means the nuclear and electronic motions of an isolated electronic state are coupled. The effective internuclear potential becomes a sum of Born–Oppenheimer and non–Born–Oppenheimer terms :

$$U^{eff}(R) = U^{BO}(R) + \frac{U_A(R)}{M_A} + \frac{U_B(R)}{M_B}. \tag{6.25}$$

The choice of the Born–Oppenheimer component, which describes pure vibrational motion of the nuclei, is a Morse–type potential :

$$U^{\mathrm{BO}}(R) = D_e \left(\frac{1 - \exp\left[-\beta(R)\right]}{1 - \exp\left[-\beta(\infty)\right]} \right)^2. \tag{6.26}$$

D_e is the dissociation energy of the molecule, which is a fixed constant in the fitting procedure. The $\beta(R)$ term is the anharmonic or curvature function of the potential, which is given by a polynomial expansion :

$$\beta(R) = z \sum_{i=0} \beta_i z^i, \tag{6.27}$$

$$\beta(\infty) = \sum_{i=0} \beta_i, \tag{6.28}$$

where z which is one–half the Ogilvie–Tipping parameter [203].

$$z = \frac{R - R_e}{R + R_e}. \tag{6.29}$$

The parameter z is used rather than $\Delta R = R - R_e$ of Coxon *et al.* because the long–range behavior of z is physically reasonable. As $R \to 0$, $\Delta R \to \infty$, while

$z \rightarrow 1$, so that the potential will smoothly converge to the dissociation limit (D_e) of the molecule. This form also ensures that $\beta(R)$ remains finite as $R \rightarrow 0$ and prevents numerical "blowup" of U^{BO} if $\beta(R)$ becomes negative at large R. The denominator of U^{BO}, $(1 - \exp[-\beta(\infty)])^2$ ensures that U^{BO} approaches D_e, i.e. the physically meaningful asymptotic behavior is maintained as $z \rightarrow 1$.

The remaining two terms in eqn. (6.25) are Born–Oppenheimer breakdown terms for the atomic centers A and B, accounting for adiabatic nuclear–electronic coupling effects and homogeneous (J–independent) non–adiabatic mixing with distant $^1\Sigma$ states. These are given by series expansions :

$$U_A(R) = \sum_{i=1} u_i^A (R - R_e)^i, \tag{6.30}$$

$$U_B(R) = \sum_{i=1} u_i^B (R - R_e)^i. \tag{6.31}$$

Finally, the J–dependent or heterogeneous non-adiabatic interactions with distant Π states are taken into account by the $q(R)$ term in the radial Schrödinger equation :

$$q(R) = M_A^{-1} \sum_{i=0} q_i^A (R - R_e)^i + M_B^{-1} \sum_{i=0} q_i^B (R - R_e)^i \tag{6.32}$$

This term is important for high J transitions because as the rotational motion increases the angular momentum of the nuclei couples more strongly with the electrons, resulting in a non-zero electronic angular momentum, thereby mixing the ground ($^1\Sigma^+$) state with excited $^1\Pi$ states.

6.4 Numerical Analysis

The spectra are assigned by various methods (combination differences, Loomis–Wood diagrams) and the assignments are verified by fitting the data to an appropriate model for the system. Typically, the Dunham model is used in the first stage of the data analysis. Each isotopomer is fit individually to the conventional expression, eqn. (6.15), to yield the Dunham coefficients. When this procedure is completed for each isotopomer, the data are combined and fit to the mass–reduced Dunham expression. Since we are dealing with light molecules, Born–Oppenheimer breakdown effects are significant and the data must be fit to Watson's corrected formula of eqn. (6.16). In the initial fits, all Y_{ij} or U_{ij} are treated as independent parameters, and these are called "unconstrained" fits. Another set of fits are carried out using the relationships between the lower order U_{ij}'s and the higher order U_{ij}'s, as in eqn. (6.23). These are called "constrained" fits where a minimum number of parameters are adjusted since the higher order U_{ij}'s are calculated analytically from the lower order U_{ij}'s. In many cases, these fits give the same standard deviation with fewer adjustable parameters. The data reduction for these fits were carried out using a weighted nonlinear least squares fitting program.

The fitting of the parameterized potential model is also done with a weighted nonlinear least squares fitting program, written by M. Dulick. The Hamiltonian parameters are fit directly to the spectroscopic line positions with a program that uses the Cooley–Numerov [204,205] method to numerically integrate the second order differential equation. A practical procedure outlining this methodology is given in a paper by Blatt [206]. In brief, the method is as follows; the one-dimensional

Schrödinger equation is written in the following manner :

$$\frac{d^2\psi_{vJ}}{dR^2} = f(R)\psi_{vJ}(R), \tag{6.33}$$

where,

$$f(R) = \left(\frac{2\mu}{\hbar^2}\right)[U(R) - E_{vJ}], \tag{6.34}$$

and μ , $U(R)$, E_{vJ} and $\hbar$ have their usual meanings. The wave function $\psi_{vJ}(R)$ also must have its usual properties, i.e. bounded, square–integrable for $R \geq 0$, and $\psi_{vJ}(0) = 0$. The properties of an eigenvalue equation can be used to help simplify the problem. For example, $\psi_{vJ}(R)$ must have v nodes for the eigenvalue E_{vJ} and the energy E_{vJ} must be negative. Also, values of ψ for $R \sim 0$ or $R \geq 5R_e$ need not be considered since the wavefunction is exponentially small in these regions. The solution makes use of the classical turning point of the potential ($U(R) = E_{vJ}$) such that $\psi_{vJ}(R)$ is exponentially decreasing between between $0 < R < R_{\text{in}}$ (inner turning point) and $R > R_{\text{out}}$ (outer turning point) and can be oscillatory in the region between $R_{\text{in}} < R < R_{\text{out}}$.

The Numerov method requires writing a Taylor series expansion of $\psi_{vJ}(R + h)$ around a point r :

$$\psi_{vJ}(r + h) = \sum_{h=0}^{\infty} \frac{h^{(n)}}{n!}\psi_{vJ}^{(n)}, \tag{6.35}$$

where $\psi_{vJ}^{(n)}$ is the n^{th} derivative of ψ_{vJ} evaluated at r. Expanding the series, we

obtain :

$$\frac{1}{2}\Big[\psi_{vJ}(r+h)-\psi_{vJ}(r-h)\Big] = \psi_{vJ}(r)+\frac{1}{2!}h^2\psi_{vJ}^{(2)}(r)+\frac{1}{4!}h^4\psi_{vJ}^{(4)}(r)+\frac{1}{6!}h^6\psi_{vJ}^{(6)}(r)+\cdots. \tag{6.36}$$

Taking the second derivative of eqn. (6.36) and making the appropriate substitution ($\psi^{(2)} = f(R)\psi(R)$) one arrives at the basic formula of the Numerov method,

$$\Big[1-T(r+h)\Big]\psi(r+h)+\Big[1-T(r-h)\Big]\psi(r-h) = \Big[2+10T(r)\Big]\psi(r)-\frac{h^{(6)}}{240}\psi^{(6)}+\cdots, \tag{6.37}$$

where,

$$T(r) = \frac{h^2}{12}f(r) = \frac{h^2}{12}\frac{2\mu}{\hbar^2}[U(r)-E_{vJ}]. \tag{6.38}$$

The integration is initiated with a trial energy and an arbitrary wavefunction, and performing the integration where the wavefunction is known to be exponentially small, i.e. in the classically forbidden region of the wavefunction. If $\psi(r-h)$ and $\psi(r)$ are known, then, $\psi(r+h)$ can be found directly from eqn. (6.37), if the sixth derivative ($\psi^{(6)}$) is ignored.

The procedure begins with an outward integration from "small" $R = R_{\text{min}}$ to a central point $R = R_0$ and an inward integration from large R ($R = R_{\text{max}}$) to the same point. In practice R_0 can be anywhere inside the classically allowed region of the potential so a convenient choice for R_0 is the minimum of the potential (R_e). The wavefunction at R_{min} (or R_{max}) is set to the value $\psi_{vJ}(R_{\text{min}}) = 0$ and has a non-zero value $\psi_{vJ}(R_{\text{min}}+h)$. The necessary condition for the two integrations is that the values of the wavefunction from the inward and outward integrations must be

equal at the matching point, i.e. the wavefunction must be smooth and continuous. If there is a discontinuity, then the slopes at R_0 are used to make corrections to the trial wavefunctions by adjusting the energy E_{vJ}. Iterative corrections are made to the energy and wavefunction until a convergence criteria is met at the matching point of the inward and outward integrations.

Once an optimized wavefunction and energy is achieved for a set of initial potential parameters, optimization of the potential is begun. This calculation is started with a trial set of parameters in the Hamiltonian :

$$\{p_k\} = \Big[R_e\,, \{\beta_i\}\,, \{u_i^A\}\,, \{u_i^B\}\,, \{q_i^A\}\,, \{q_i^B\}\Big], \tag{6.39}$$

and nonlinear optimization of the model is carried out by minimizing the χ^2 merit function :

$$\chi^2(\{p_k\}) = \sum_{i=1}^{N} w_i \Big[\nu_{\rm obs}(i) - \nu_{\rm calc}(\{p_k\}, i)\Big]^2, \tag{6.40}$$

where $w_i = \sigma_i^{-2}$, is the weight of the observation (line position) with σ_i being the experimental uncertainty of the observation, and $\nu_{\rm obs}$, $\nu_{\rm calc}$ are the observed and calculated line positions. Minimization of the χ^2 function is carried out by calculating the partial derivatives with respect to each parameter :

$$\frac{\partial \chi^2}{\partial p_k} = -2 \sum_{i=1}^{N} w_i \Big[\nu_{\rm obs}(i) - \nu_{\rm calc}(\{p_k\}, i)\Big] \frac{\partial \nu_{\rm calc}(\{p_k\}, i)}{\partial p_k}. \tag{6.41}$$

To minimize χ^2, the partial derivative of the calculated line position with respect

to a parameter in the Hamiltonian must be evaluated :

$$\frac{\partial \nu_{\rm calc}(\{p_k\},i)}{\partial p_k} = \frac{\partial E_u(i)}{\partial p_k} - \frac{\partial E_l(i)}{\partial p_k}, \tag{6.42}$$

where, $E_u(i)$, $E_l(i)$ are the upper and lower energy states for the transition $\nu(i) = E_u(i) - E_l(i)$, and u and l are the appropriate quantum numbers for the energy levels. It is very difficult to obtain these partial derivatives analytically, and it is expensive to obtain them numerically, so the generalized Hellman–Feynman [207] theorem is utilized :

$$\frac{\partial E_{vJ}}{\partial p_k} = \langle \psi_{vJ} \mid \partial H(R)/\partial p_k \mid \psi_{vJ} \rangle = \langle \psi_{vJ} \mid \partial U(R)/\partial p_k \mid \psi_{vJ} \rangle. \tag{6.43}$$

Since the Hamiltonian and the potential are modelled analytically, these partial derivatives can be computed exactly. Now the procedure is repeated to optimize for a new wavefunction and then a better set of potential parameters. Iterations are continued until the potential parameters reproduce the dataset within the experimental uncertainty. Thus with a good choice of initial potential parameters, convergence can be achieved within a few iterations.

As mentioned earlier, a good estimate of the first few (R_e, β_0, β_1) potential parameters are required because of the nonlinearity of the fit. One can calculate initial estimates of β_i's using the relationship between the Dunham a_i's to the β_i's of the modified Morse potential. This is carried out by taking the Born–Oppenheimer potential $(U^{BO}(R))$ and converting it to the Dunham form by a series expansion of the $U^{BO}(R)$ about $R = R_e$. Equating terms of the same power in $(R - R_e)^i$, for

the Dunham and U^{BO} expansions one obtains [202] :

$$a_0 = \frac{R_e^2}{2}\left[\frac{d^2U^{BO}(R)}{dR^2}\right]_{R=R_e}, \tag{6.44}$$

for $i = 0$, and for $i > 0$ the expansion gives,

$$a_i = [a_0(i+2)!]^{-1} R_e^{i+2}\left[\frac{d^{i+2}U^{BO}(R)}{dR^{i+2}}\right]_{R=R_e}. \tag{6.45}$$

The first few relations between the a_i's and the β_i's are :

$$a_0 = \frac{D_e\beta_0^2}{2[1-\exp(-\beta(\infty))]^2} \tag{6.46}$$

$$a_1 = \frac{\beta_0^2 + 2\beta_0 - 2\beta_1}{2\beta_0} \tag{6.47}$$

$$a_2 = \frac{7\beta_0^4 + 36\beta_0^3 + 36(1-\beta_1\beta_0^2 + 24(\beta_2 - 3\beta_1)\beta_0 + 12\beta_1^2}{48\beta_0^2}. \tag{6.48}$$

The values for the a_i's are determined from fits to the Dunham expansion and using the relations in eqns. (6.20)–(6.22), then the β_i's are calculated from eqns. (6.46)–(6.48).

When performing a potential fit, the parameters D_e, R_e and at least one β parameter is required (β_0). The dissociation energy (D_e) is usually fixed to the thermochemical or spectroscopic value found in Huber and Herzberg [208], while R_e is calculated from the rotational constant, B_e (Y_{01}), or set to the *ab initio* value, if available. It has been found that the estimates provided from eqns. (6.46)–(6.48) are not good enough to perform a nonlinear fit, i.e. the trial values calculated for β_0 and β_1 are too far away from the true values to achieve convergence for a fit.

The nonlinear least squares procedure is extremely sensitive to the value of β_0, since this term occurs in the exponential in U^{BO}. Empirically, it was found that multiplying the calculated value of β_0 by the factor 1.413 allowed the nonlinear least squares program to proceed with a fit. It is best to perform the initial fit with the scaled β_0 parameter and with the rest of the β_i's set to zero. Once completed, β_0 should be readjusted to the newly determined value and β_1 can be set the the value calculated from eqns. (6.20)–(6.22); scaling of β_1 is not required at this point. Then, one can proceed with subsequent fits by adding enough parameters to properly fit the data to the experimental uncertainty. One usually begins by fitting each isotope individually. Once this is complete, data from all isotopomers can be combined together and a global fit is carried out to determine the Born–Oppenheimer breakdown terms of eqns. (6.30)–(6.32).

Chapter 7

Results and Discussion

There is considerable interest in the infrared spectra of light metal–containing diatomic molecules, both experimentally and theoretically. They can be found in astrophysical sources and they are ideal to study the breakdown of the Born–Oppenheimer approximation. The simple–mass scaling of Dunham or diatomic band spectroscopic constants fails to accurately predict the energy levels of isotopic species. This is especially true for hydride molecules [197–199] where Born–Oppenheimer breakdown becomes more noticeable with high precision data (such as that obtained with a FT spectrometer) and also with higher energy levels obtained from high temperature studies.

7.1 InF

The first spectroscopic analysis of InF was carried out in the 1950's in the research group of Barrow at Oxford University. They were looking at low resolution

absorption and emission spectra of indium and gallium monofluorides in the UV, where they identified the $A^3\Pi_0$–$X^1\Sigma^+$, the $B^3\Pi_1$–$X^1\Sigma^+$ and the $C^1\Pi$–$X^1\Sigma^+$ systems [209, 210]. These assignments were confirmed by rotational analysis of the A–X and B–X systems by Barrow and co–workers [211] and for the C–X system by Nampoori *et al.* [212].

Recently, the majority of investigations have been in the microwave and infrared regions of the spectrum. Lovas and Törring [213] analyzed the hyperfine structure (hfs) of the $v = 0$ and 1 vibrational levels of ^{115}InF for the $J = 2 \leftarrow 1$ and $J = 3 \leftarrow 2$ pure rotational transitions. The subsequent studies by Hoeft *et al.* [214] extended the hfs analysis by recording $J = 1 \leftarrow 0$, $J = 17 \leftarrow 16$, $J = 18 \leftarrow 17$, and $J = 19 \leftarrow 18$ transitions for v=0–3 levels of ^{115}InF, and $J = 1 \leftarrow 1$, $J = 17 \leftarrow 16$, and $J = 18 \leftarrow 17$ for $v = 0$ of ^{113}InF. Radiofrequency molecular beam resonance experiments by Hammerle *et al.* [215] lead to a further refinement of the quadrupole hfs constants for the lower v, J levels as well as establishing an upper limit for the hexadecapole hfs constant.

Hensel and Gerry [216] have recently remeasured the rotational, spin–rotational and nuclear quadrupole coupling constants for ^{115}InF, along with ^{115}InBr and ^{115}InCl, using a laser–ablation FT microwave (FTMW) spectrometer. The only measurable transition in the frequency range of their FTMW spectrometer was the $J = 1 \leftarrow 0$ transition of $v = 0$ and $v = 1$ of ^{115}InF. For this reason, they were unable to determine the B_0 rotational constant without fixing D_0 to the value reported in our work. Their rotational constants for InF are not as accurate as those reported in the literature [213, 214, 217]. The hyperfine coupling constants measured

for the indium halides were used to discuss the electronic stucture in this series of molecules. The bonding in these moleclues could be entirely described in terms of $5s$ and $5p$ orbitals on In, and ns, np (n=3,4,5) on the halogens.

In the infrared region, Uehara *et al.* [218] were the first to record a low resolution (0.1 cm^{-1}) FT emission spectrum of ^{115}InF. Band heads up to $v = 6$ were observed but rotational structure was only well-resolved for P-branch transitions. This work was then superseded by high resolution diode laser measurements of Ozaki *et al.* [219] that sparsely covered rotational transitions from v = 0–9 for ^{115}InF and v = 0–4 for ^{113}InF. Because of the lack of tunability of diode lasers, they obtained only sparse coverage of rotational lines. In this work we report a high resolution analysis of the infrared emission spectrum of ^{115}InF and ^{113}InF. The continuous wavenumber coverage of the FT spectrum has enabled us to fill in many of the gaps in the tables of the measured line positions given in ref. [219]. In addition, we also report revised values of Dunham Y_{ij}'s and isotopically invariant Dunham U_{ij}'s. Fits to the parameterized potential model were also carried out. The lines measured from in this work was combined with the previously measured microwave rotational lines [213] in all the fits.

7.1.1 InF Experiment

The gas-phase spectrum of InF was accidently recorded in an experiment designed to generate BaS. In this experiment, approximately 10 g of Ba metal was placed in a 1.2 meter mullite ($3Al_2O_3 \cdot 2SiO_2$) tube. The metal was gradually heated to a temperature of 1200 °C using a commercial CM Rapid Temp furnace controlled

by a Honeywell universal temperature controller (Fig. 7.1). At a temperature of

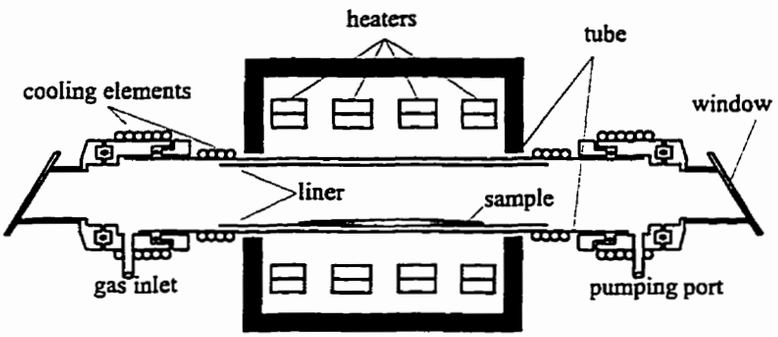

Figure 7.1: A schematic of the furnace used in the InF experiment.

~400 °C, approximately 10 torr of Ar gas was introduced into the mullite tube to prevent deposition of any solid material onto the windows (KRS-5) of the tube. At ~1200 °C, a slow continuous flow of SF_6 gas was introduced through a needle valve into the tube. The pumping speed was adjusted in such a way as to keep the total pressure inside the tube below 10 torr. The rovibrational emission spectrum of BaS was expected to be observed at a frequency of 380 cm^{-1} [220]. Although the emission spectrum of BaS was not present, a feature centered at 535 cm^{-1} was observed. Indium metal was present as an impurity in the mullite tube from a previous experiment [178]. The small amount of In impurity had reacted with SF_6 to produce gas-phase InF. Thus, the high resolution emission spectrum was recorded in the 360-760 cm^{-1} wavenumber range with the Bruker IFS 120 HR spectrometer over a temperature range of 1200-1500 °C (Fig. 7.2). The spectra

were recorded by coadding 20 individual scans at a resolution of 0.006 cm^{-1} with a liquid helium cooled Si:B detector and a 3.5 μm mylar beamsplitter. A portion of the spectrum in the vicinity of the 1–0 R branch band–head is displayed in Fig. 7.3.

The measured InF rotational lines were calibrated with respect to HF emission lines which are also present in the spectrum [180, 181]. Intense and unblended InF lines with a signal-to-noise ratio of ~25 were measured to a precision of ±0.0001 cm^{-1}. Typically, however, weak and blended lines which constituted the vast majority of lines in the data set were measured with a maximum precision of ±0.0008 cm^{-1}.

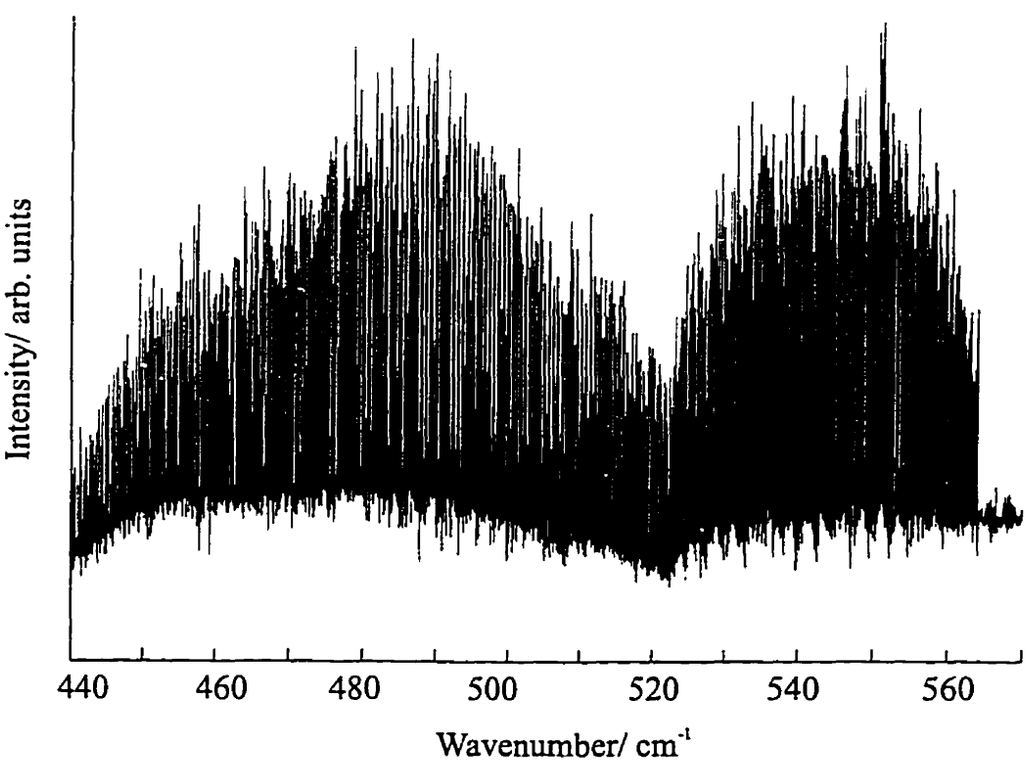

Figure 7.2: The overview of the infrared thermal emission spectrum of InF.

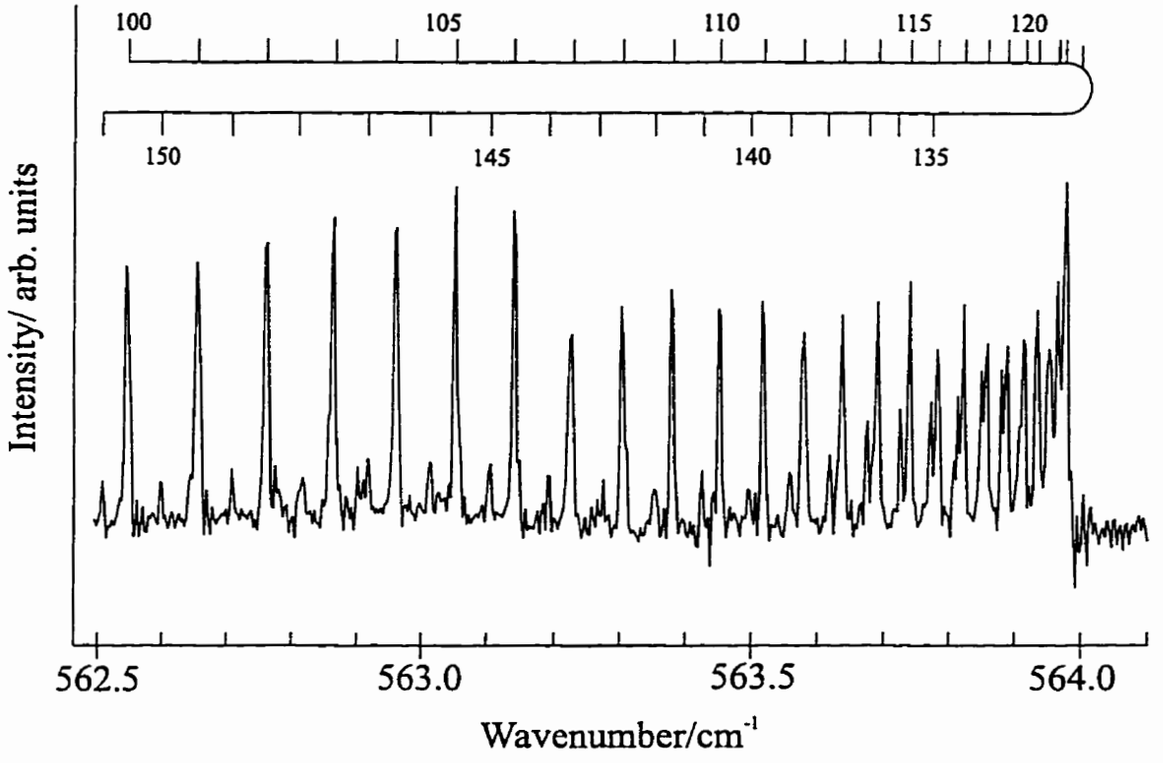

Figure 7.3: A portion of InF emission spectrum, the lines of the R-branch band head in the 1–0 band of ^{115}InF are labelled.

7.2 CuH and CuD

Interest in the transition metal hydrides arises partly because of their importance in heterogeneous catalysis [221] and their presence in interstellar enviroments. The $A^1\Sigma^+$–$X^1\Sigma^+$ transition of CuH has been observed in sunspot spectra [222] and tentatively identified in the spectrum of the star 19 Piscium [223]. The first laboratory study of CuH was carried out in 1923 [224]. The visible and vacuum UV spectra of

CuH and CuD have been studied by extensively by many investigators. The most comprehensive work has been carried out by Ringström, who observed five excited electronic states $A^1\Sigma^+$, $b\Delta_2$, $B^3\Pi_{0^+}$, $C1$, $c1$ in the 3440–3780 Å [225] region and the $E^1\Sigma^+$–$X^1\Sigma^+$ transition in the 2744–2270 Å region [226]. Grundström [227] analyzed the $D^1\Sigma^+$–$X^1\Sigma^+$ transition in the 2260–2228 Å region and more recently Brown and Ginter recorded absorption spectra from 2350–2890 Å. Along with the reanalysis of the E–X and D–X systems, they found four new transitions $F1^{\pm}$–$X^1\Sigma^+$, $G0^+$–$X^1\Sigma^+$, $H1^{\pm}$–$X^1\Sigma^+$ and $I1^{\pm}$–$X^1\Sigma^+$. These states are labelled using Hund's case (c) notation. All of the excited states exhibited perturbations and the H and I states also showed signs of predissociation. Recently, molecular emission of the $A^1\Sigma^+$–$X^1\Sigma^+$ band system of CuH has been observed in the laser evaporation of copper to form aerosols in a static gas cell [228]. The visible spectra of CuD have not been as extensively studied as CuH, however, the $A^1\Sigma^+$–$X^1\Sigma^+$ system was recorded by Heimer [229] , Jeppesen [230], Ringström [225] and most recently by FT emission spectroscopy in a hollow cathode discharge by Fernando *et al.* [231].

In the infrared, the vibration–rotation spectrum of the ground state of CuH was accidentally observed. A copper hollow cathode lamp was used in an experiment with a continuous flow of Ne and H_2 gases to record the spectrum of NeH^+ [232]. Copper atoms were sputtered off the cathode material and in the presence of H_2, the CuH molecule was formed [233]. The 1-0, 2-1 and the 2-0 overtone band of both isotopes (^{63}CuH,^{65}CuH) were recorded with a FT spectrometer at 0.05 cm^{-1} resolution in the 1800–5000 cm^{-1} region. Ram *et al.* [233] attempted to record CuD under the same conditions but were unsuccessful. The pure rotational

spectra of ^{63,65}CuH [234, 235] and ^{63,65}CuD [235] have been measured by tunable far–infrared spectroscopy (TuFIR). For these measurements, the Evenson group at NIST, Boulder, were able to generate both CuH/D molecules in a hollow cathode discharge. The pure rotational transitions were probed by mixing mid–infrared radiation from two CO_2 lasers (ν_1 and ν_2) and a microwave source (ν_μ). The FIR radiation ($\nu_{\rm FIR} = \mid \nu_1 - \nu_2 \mid \pm \nu_\mu$) was passed through the cell and rotational transitions of $X^1\Sigma^+$ ($v = 0$) were recorded from of $J = 1 \leftarrow 0$ to $J = 10 \leftarrow 9$ for ^{63,65}CuH and $J = 2 \leftarrow 1$ to $J = 19 \leftarrow 18$ for ^{63,65}CuD. These lines were included in the fits of the infrared measurements reported here.

7.3 AgH and AgD

There has been relatively little spectroscopic work done on the four isotopic forms of silver hydride. Apart from classical UV work on AgH in 1931 [236], there have been two infrared diode laser experiments. The Jones group measured 21 rovibrational transitions of the 1–0, 2–1, 3–2 bands [237] for ^{107,109}AgH and 33 transitions for the same bands in ^{107,109}AgD [238].

Theoretical studies, however, have been numerous. In heavy molecules relativistic effects are important for a quantitative calculation of molecular properties. For example, relativistic and non-relativistic calculations of the vibrational frequency differ by over 100 cm^{-1}. The best relativistic calculation to date has been done by Ziegler *et al.* [239], where they calculated a vibrational frequency of $\omega_e = 1709$ cm^{-1} and an equilibrium bond length of $R_e = 1.61$ Å. In contrast, their nonrelativistic calculation gave $\omega_e = 1605$ cm^{-1} and $R_e = 1.71$ Å. These values should be

compared to the experimental values of Tables (7.9) and (7.11).

7.4 AuH and AuD

The most comprehensive study on AuH/D is the absorption spectra recorded by Ringström [240, 241] in the 2200-3000 Å region. There were five excited electronic states identified in this work, four of which display Hund's case (c) coupling. These states were found to have large equilibrium internuclear distances and small dissociation energies along with many perturbations. The only high resolution infrared spectroscopic study on AuH and AuD was performed by Lee *et al.* using a Fourier transform spectrometer [242]. The measured lines of Lee *et al.* are used in the parameterized potential fits for comparison with the other coinage metal hydrides.

Although rarely studied experimentally, there have been numerous theoretical studies of AuH and AuD. This is because the gold atom, a heavy atom like silver, provides a good example to illustrate the influence of relativistic effects on atomic and molecular properties [243, 244]. Nonrelativistic calculations usually give incorrect results, for example, on the location of the first two excited states, ^2P and ^2D, of Au. Nonrelativistic calculations [245] predict that these states have the wrong energy order while relativistic calculations agree well with the experimental results [246]. Calculations have been carried out on the $X^1\Sigma^+$ ground state of AuH in order to study the effect of relativity on the bond length [247], the energy order of low-lying electronic states [248], the ionization energy [249] and the dipole [250] and quadrupole moments [251].

7.5 Spectroscopy of the Coinage Metal Hydrides

The infrared emission spectra of the coinage metal hydrides was recorded with the Bruker IFS 120 HR Fourier transform spectrometer. In these experiments a very high temperature (VHT) carbon–tube furnace was employed to melt the coinage metals. The commercial furnace used in the InF experiment has a maximum temperature of 1600°C and could not therefore be used to vaporize the coinage metals. Also, the tube materials, mullite or alumina (Al_2O_3), soften and can be very reactive above 1600°C. The VHT furnace, sometimes called a King funace, is 0.5 m in length and the central section of the tube has a 40 mm inner diameter. The tube windows are 1″ (25.4 mm) in diameter with a tube bore on the outer section of 15 mm. The furnace is heated by an analog (Astra Industries) SCR power supply, and temperature control of the furnace is maintained by manually adjusting the current fed to the heating elements. The temperature inside the furnace is measured with an optical pyrometer by sighting on the thermal emission down the center of the tube. This method is imprecise at these temperatures. An accurate temperature measurement would require a clear view of the furnace wall and this is not possible with the present experimental arrangement. The windows and the outer jacket of the furnace are cooled by a flow of cooling water from a liquid/liquid heat exchanger and recirculator.

In the Cu experiments, a small piece of Cu rod ($\sim$ 5 g) was placed in a carbon boat inside the VHT furnace. The furnace was rapidly heated to $\sim$1500 °C and a flow H_2 or D_2 gas was continously maintained through the tube. For the CuH experiment, the total pressure inside the tube was approximately 120 torr and the

spectrum was recorded by coadding 10 scans at 0.02 cm^{-1} resolution. The instrumental parameters for the spectrometer were: a CaF_2 beamsplitter (BS), liquid N_2 cooled HgCdTe (MCT) detector and, KRS–5 (Tl_2BrI) windows on the external emission port of the spectrometer. The spectrum was recorded at a temperature exceeding 1700 °C in the 1300–2100 cm^{-1} wavenumber range. The conditions for all of the experiments are summarized in Table 7.1.

The silver experiments were carried out by placing a few grams of Ag ingot in a carbon boat inside the furnace. For the experiments with gold, a single troy ounce of 99.9% purity gold was purchased locally from the Canadian Imperial Bank of Commerce (Johnson&Matthey). The CuH and CuD experiments were performed on different days (as were the AgH and AgD measurements) while the AuH and AuD experiments were performed on the same day. In this experiment 0.5 troy ounce of Au was placed inside the VHT furnace and melted, first under an atmosphere of D_2 gas to record the AuD spectrum, and subsequently with H_2 gas to record the spectrum of AuH. Sample spectra of all these species are shown in figs. 7.4–7.8. The rotational constants for the coinage metal hydrides ($\geq$ 3.2 cm^{-1}) are fairly large so that each rotational line is well isolated (line spacing $\sim 2B$ near the origin). The signal–to–noise ratio for the CuH and CuD was approximately 40:1 for the best lines giving a measurement precision of $\pm$0.0002 cm^{-1} for most lines. The signal–to–noise ratio for AgH and AgD is much poorer, approximately 10:1 giving a measurement precision of $\pm$0.0005 cm^{-1} for the best lines and $\pm$0.001 cm^{-1} for the weaker lines. Both the AuD and AgH emission spectra are overlaped with strong absorption lines of H_2O, leading to blending of some rotational lines but the H_2O

Table 7.1: The instrumental and experimental conditions for the coinage metal hydrides.

	^{63,65}CuH	^{63,65}CuD	^{107,109}AgH	^{107,109}AgD	^{197}AuH	^{197}AuD
Reactants	Cu + H_2	Cu + D_2	Ag + H_2	Ag + D_2	Au + H_2	Au + D_2
Region (cm^{-1})	1300–2100	1000–1500	1200–1900	1000–1400	1600-2500	1100–1700
Beamsplitter	CaF_2	KBr	KBr	KBr	CaF_2	KBr
Detector	MCT	MCT	MCT	MCT	InSb	MCT
Temp (°C)	>1700	>1700	>1600	>1600	>1700	>1700
Pressure (torr)	~120	~200	~150	~250	~170	~200
Resolution (cm^{-1})	0.02	0.02	0.02	0.02	0.02	0.02
# of scans	10	50	50	50	40	40

absorption gives an absolute calibration of the spectrum. The AgD spectrum did not overlap with any other spectral feature while AuH was overlapped with strong CO_2 emission lines.

7.6 InF Results

The two types of Dunham fits were carried out for InF in the initial analysis. The results are shown in tables 7.3 and 7.6. The rotational line positions were measured using a computer program [1] which fits the recorded line to a Voigt lineshape function. A total of 2840 lines were measured with 2664 lines from the major isotopomer ^{115}InF (95 %) and 179 from the minor isotopomer ^{113}InF (5 %). The lines of ^{115}InF were observed in both the P and R–branches of the 1–0 through 12–11 bands while spectral congestion limited the observation of ^{113}InF lines to only the R–branches of the 1–0 and 2–1 bands. For this reason P–branch lines from the diode laser

[1] PC-DECOMP–developed by Jim Brault of Kitt Peak Observatory, Arizona.

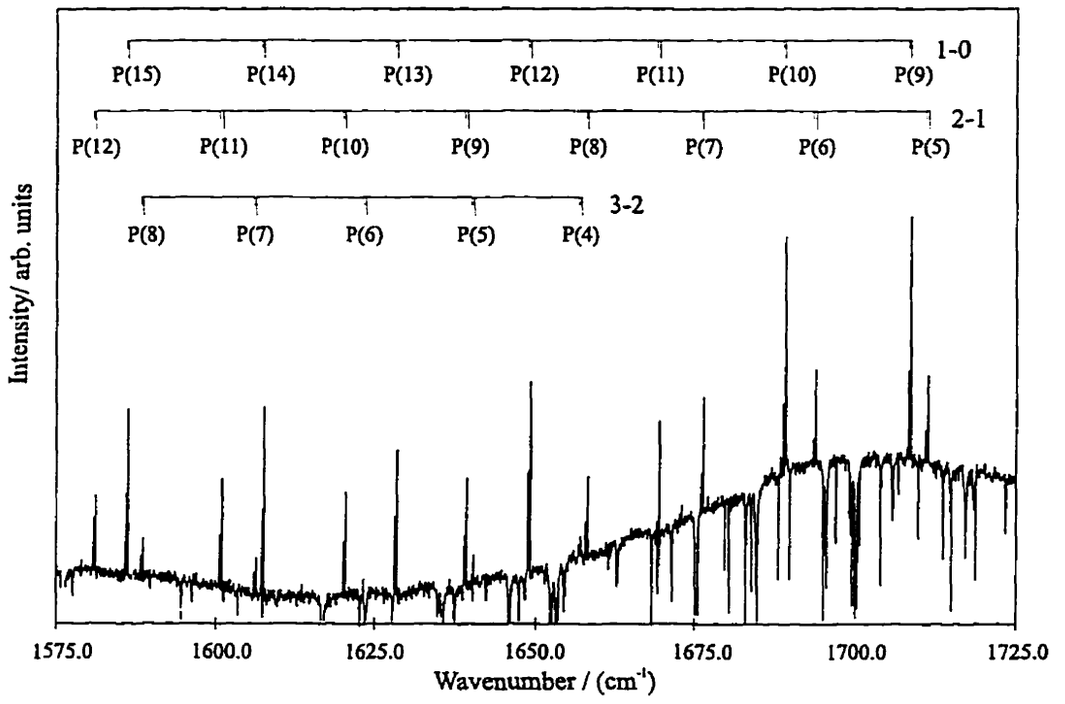

Figure 7.4: The spectrum of CuH in the P-branch region. The absorption lines are due to H_2O present as an impurity the furnace.

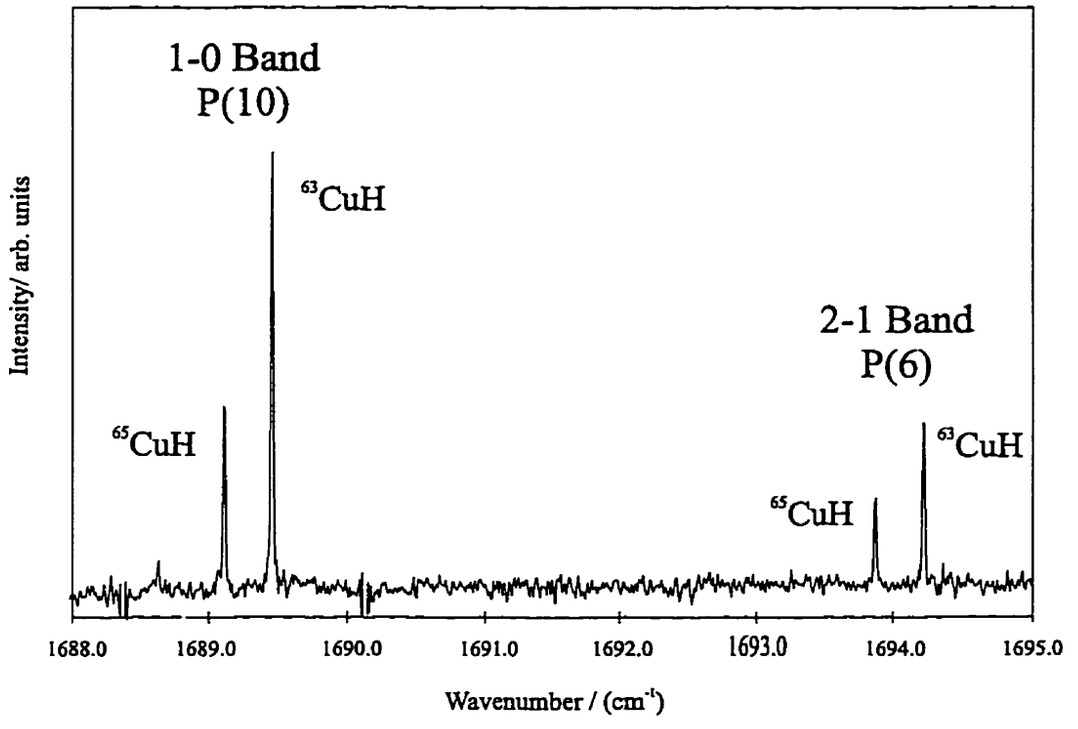

Figure 7.5: The spectrum of CuH showing the isotopic shift between ^{63}CuH and ^{65}CuH.

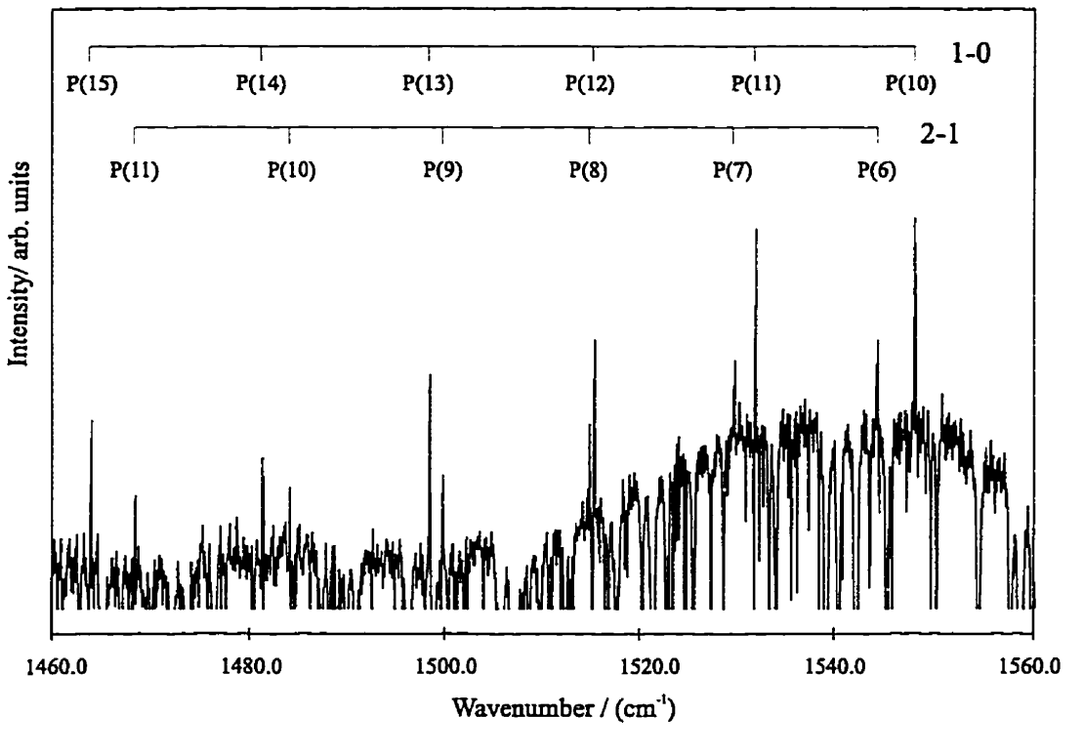

Figure 7.6: A portion of the P-branch spectrum of AgH. Strong absorption lines are due to H_2O.

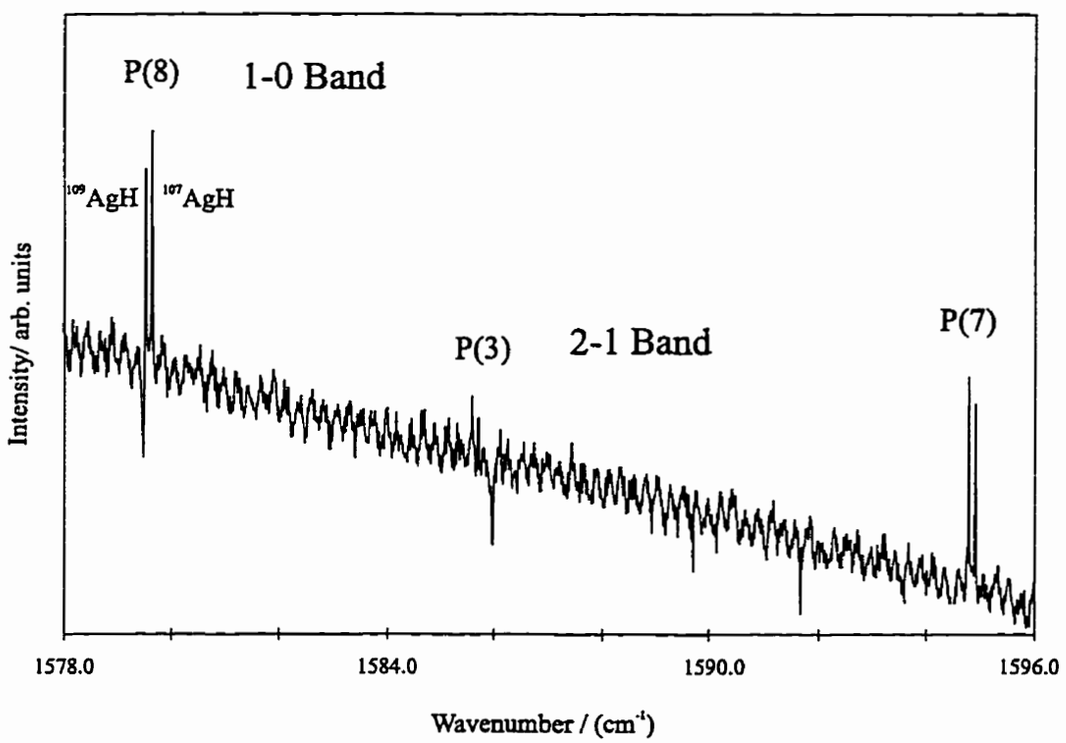

Figure 7.7: The spectrum of AgH showing the small isotopic shift between ^{107}AgH and ^{109}AgH.

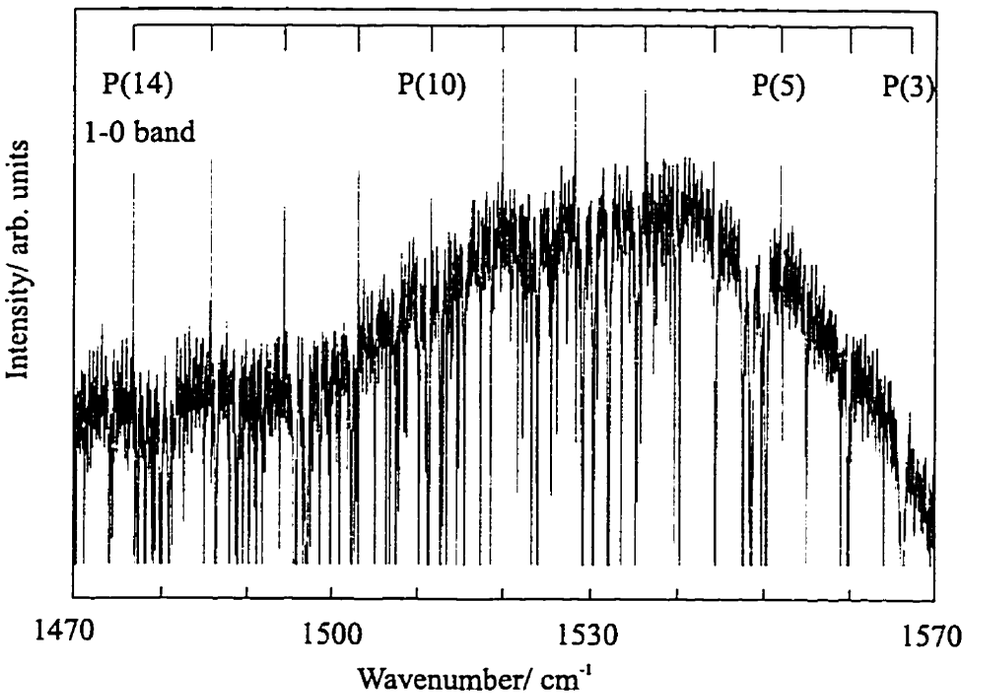

Figure 7.8: A portion of the AuD spectrum. The SNR is very low (5:1 for the best lines) in this spectrum compared to the H_2O absorption lines.

measurements of Ozaki *et al.* [219] were included in the fits to prevent distortions to the ^{113}InF constants by exclusively fitting R–branch transitions. A total of 52 P–branch and 34 R–branch lines were included from ref. [219]. It was found that there was no systematic shifts between lines common to our data set and that of Ozaki *et al.*. A total of 2937 transition were used in the fits, the complete list of these line positions is given in Appendix B.

Since there is only one isotope of F (^{19}F), any measured Born–Oppenheimer breakdown come from the In center. The mass reduced Dunham fits on InF showed that there were no determinable Born–Oppenheimer breakdown terms. However, in the mass–reduced fits for the InH and InD [178] isotopomers, the $\Delta_{10}^{\rm In} = -1.520(647)$ and $\Delta_{01}^{\rm In} = 38.08(625)$ parameters were determined. These terms are not well determined, as would be expected for a heavy center. The magnitude of $\Delta_{10}^{\rm In}$ and $\Delta_{01}^{\rm In}$ are actually quite large, which could result from significant statistical correlation between the $\Delta_{ij}^{\rm In}$'s and the U_{ij}'s parameters. This is further confirmed by the fact that the parameterized potential fits of InH/D showed no Born–Oppenheimer breakdown for the In center. That is, all breakdown effects for the InH/D isotopomers were caused by the H center.

The results of the parameterized potential fits are shown in Table 7.4. In this fit the value of D_e was take from Huber and Herzberg [208] and the atomic masses were obtained from ref. [165]. Numerical integration of the Schrödinger equation was performed over the range, 1.0 Å$\leq$ R $\leq$ 3.5 Å, with a grid spacing of 0.0025 Å. These fits also show no Born–Oppenheimer breakdown effects consistent with the mass–reduced fits. The superiority of parameterized potential model compared

Table 7.2: Isotopically dependent Dunham constants for InF (cm^{-1}).

Constant		^{115}InF	^{113}InF
	Y_{10}	535.36334(12)	536.03489(56)
	Y_{20}	−2.672556(37)	−2.67874(24)
10^3	Y_{30}	8.4726(41)	8.324(32)
10^5	Y_{40}	−1.741(15)	
	Y_{01}	0.262323787(32)	0.26298299(12)
10^3	Y_{11}	−1.879650(18)	−1.88693(16)
10^6	Y_{21}	4.9364(37)	5.044(18)
10^9	Y_{31}	1.67(16)	
10^7	Y_{02}	−2.51851(19)	−2.5291(22)
10^{11}	Y_{12}	6.01(20)	7.8(21)
10^{12}	Y_{22}	8.53(14)	
10^{13}	Y_{03}	−1.1152(78)	−1.19(28)
10^{16}	Y_{13}	9.60(71)	
χ^2 :		0.8663	0.6532
Transitions :		2680	257
Adjustable Parameters :		13	9

Table 7.3: Isotopically invariant Dunham constants for InF (cm^{-1}).

Constant	unconstrained	constrained
U_{10}	2161.62571(46)	2161.62542(44)
U_{20}	-43.57016(58)	-43.56999(56)
U_{30}	0.55766(26)	0.55769(26)
$10^3\ U_{40}$	-4.621(40)	-4.641(40)
U_{01}	4.27662818(32)	4.27662969(18)
U_{11}	-0.12372949(84)	-0.12373059(57)
$10^3\ U_{21}$	1.31209(90)	1.31054(60)
$10^6\ U_{31}$	1.78(16)	2.39(16)
$10^5\ U_{02}$	-6.69386(48)	-6.69582
$10^8\ U_{12}$	6.46(17)	6.95459
$10^8\ U_{22}$	3.689(53)	3.80105
$10^{10}\ U_{32}$		-6.96141
$10^{10}\ U_{03}$	-4.828(33)	-4.58408
$10^{11}\ U_{13}$	1.68(11)	1.37535
$10^{14}\ U_{23}$		1.48589
$10^{14}\ U_{04}$		-1.10195
$10^{16}\ U_{14}$		6.33334
$10^{17}\ U_{24}$		2.32341
$10^{19}\ U_{05}$		-2.28845
$10^{21}\ U_{15}$		6.99242
$10^{24}\ U_{06}$		-4.76553
$10^{25}\ U_{16}$		8.00680
$10^{28}\ U_{07}$		-1.23521
$10^{33}\ U_{08}$		-2.05250
χ^2 :	0.8514	0.8587
Transitions :	2937	
Adjustable Parameters :	13	8

Table 7.4: Born-Oppenheimer potential parameters for InF.

D_e (cm^{-1})	42300.0
R_e (Å)	1.9853973006(214)
β_0	5.082289283(117)
β_1	0.52803082(235)
β_2	2.0135599(691)
β_3	10.99445(153)
M_A (^{115}In)	114.903882
M_A (^{113}In)	112.904061
M_B (^{19}F)	18.99840322
χ^2 :	0.8849
Transitions :	2937
Adjustable Parameters :	5

to the Dunham potential form for the long range behaviour is shown in Fig. 7.9. The Dunham potential parameters, given in Table 7.5 and are calculated using eqns. (6.46)–(6.48). Good agreement between the two potential forms (i.e $\mid U^{BO} - U^{Dun} \mid \leq 0.006$ cm^{-1}) occurs in the region of 1.87 Å $\leq R \leq$ 2.12 Å. The range of the data set for the major isotopomer ($v = 12$) corresponds to 1.75 Å $\leq R \leq$ 2.38 Å. Significant divergence ($\mid U^{BO} - U^{Dun} \mid \geq 1$ cm^{-1}) begins at $R = 2.24$ Å, and beyond this point the Dunham form diverges completely away from the dissociation limit of the molecule.

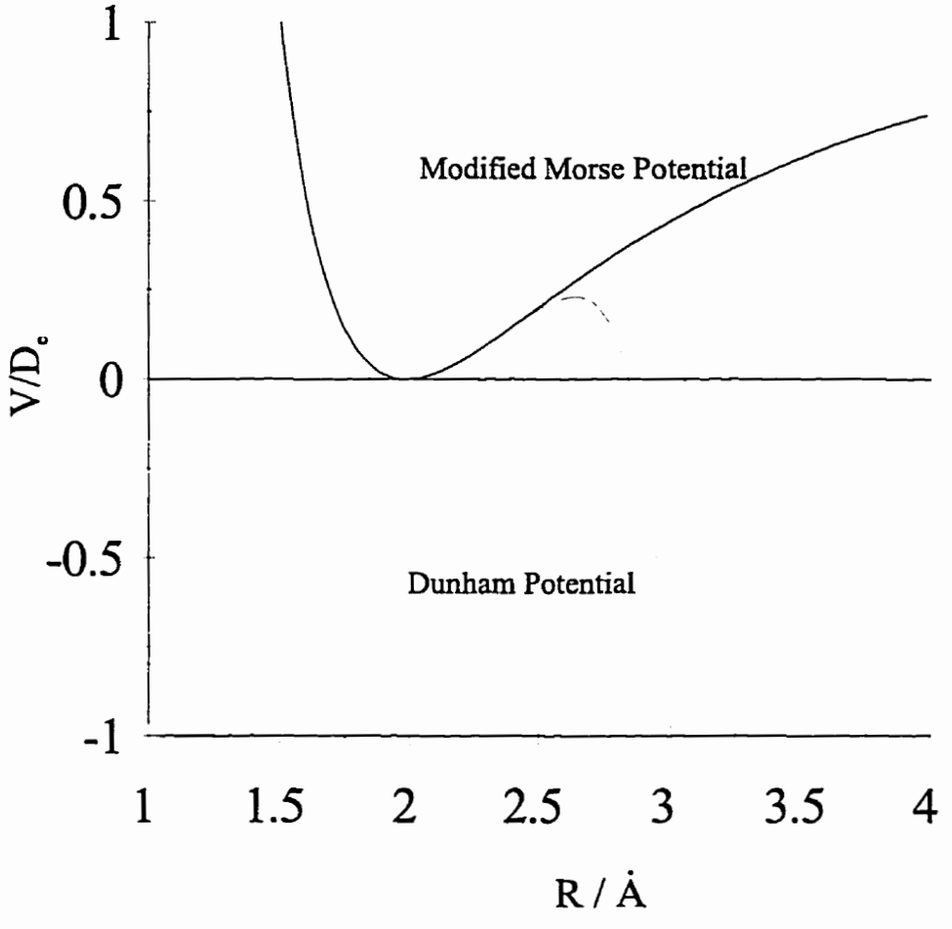

Figure 7.9: The comparison of Dunham and Born–Oppenheimer potential of InF.

Table 7.5: Calculated Dunham potential constants derived from the β parameters listed in Table 7.4.

a_0	273148.7050(126)
a_1	-3.437248389(414)
a_2	7.97746988(498)
a_3	-14.843201(106)
a_4	23.124547(579)
a_5	-30.22096(195)
a_6	31.56595(502)
a_7	-20.9249(107)
a_8	-8.4051(197)
a_9	61.3678(317)
a_{10}	-138.1082(448)

7.7 Coinage Metals Results

The Born–Oppenheimer separation of nuclear and electronic motion is based on the large ratio nuclear to electron mass. Since hydrogen and deuterium have the lightest nuclei, molecules containing these atoms will show the largest deviations from Born–Oppenheimer behavior. Thus, the presense of nearby electronic states and the coupling of nuclear and electronic motion have important contributions in the simultaneous analysis of many isotopomers. Copper has two naturally occurring isotopes, ^{63}Cu (69.17%), ^{65}Cu (30.83%) as does silver, ^{107}Ag (51.839%), ^{109}Ag (48.161%), while gold has one major isotope, ^{197}Au. The fits to the mass-reduced Dunham and parameterized potential both show that Born–Oppenheimer breakdown is much more prevalent on the hydrogen center than on the heavy metal center. The Dunham fits for each isotopomer of CuH are shown in Table 7.6. Each

one of these fits reproduced the data to better then the experimental uncertainty (0.0005 cm^{-1}), but a large number of parameters were required. We can calculate the simple Born-Oppenheimer relationship between the rotational constants of two isotopes :

$$\frac{Y_{01}^{i}}{Y_{01}^{k}} = \frac{\mu^{k}}{\mu^{i}}, \tag{7.1}$$

where the i and k labels denote two different isotopes. Using the constants from Table 7.6, the calculated value for $Y_{01}(^{65}CuH)$, using the experimentally derived value of $Y_{01}(^{63}CuH)$, is 7.940964 cm^{-1}, while the observed value for $Y_{01}(^{65}CuH)$ = 7.941007 cm^{-1}. The difference between the observed–calculated value is 4.4×10^{-5} cm^{-1}, which is approximately a factor of 10 greater then the uncertainty in the $Y_{01}(^{65}CuH)$ constant. Thus, Born–Oppenheimer breakdown is significant in the CuH molecule where a similar calculation for Y_{01} of ^{115}InF and ^{113}InF gives a difference of 7.2×10^{-8} cm^{-1}, which is well within the uncertainty of $Y_{01}(^{113}InF)$ ($1\sigma = 1.2 \times 10^{-7}$). The unconstrained and constrained mass–reduced Dunham fits required only 26 and 18 adjustable parameters, respectively, for the 451 transitions, while the individual fits required a total of 58 parameters. Since each isotopomer is fit independently, no conclusions about the extent of Born–Oppenheimer breakdown can be made from these fits.

The data can also be represented compactly with the parameterized potential model. In this case 18 parameters were varied (compared with 58), with a slightly better standard deviation for the parameterized potential fit (χ^2_{pot}=1.041) compared to the constrained mass–independent Dunham fit (χ^2_{Dun}=1.294). In these fits, the extent of Born–Oppenheimer breakdown is greater on the hydride atomic center

than on the copper center. The two parameters Δ_{01} and Δ_{10} were not as well determined for the Cu center as they were for the H center in the Dunham U fits due in part to the large mass difference between the Cu and H atoms. The potential fits also show the same phenomenon, only 4 Born–Oppenheimer breakdown ($2u_i$'s, $2q_i$'s) parameters are determined for the Cu center while 9 are required for the H center ($5u_i$'s, $4q_i$'s). The lighter mass of the H atom results in a larger kinetic energy of vibration thus, adiabatic coupling between nuclear and electronic motion is stronger at the H center. Also, heterogeneous non–adiabatic mixing of $^1\Pi$ states is evident from the number of q_i's required in the fit.

The constrained Dunham fits do not represent the data as well as the parameterized model fits. For example, compare the χ^2 values (see Table 7.15) of the constrained and potential fits. This is different than in the cases of InH/D [178], AlH/D [177] and GaH/D [179] where the constrained fits worked slightly better than the potential fits. This problem arises because the constraining relationships are only valid for isolated electronic states. In Table 7.15 it can be seen that there are low–lying electronic states of the proper symmetry that can interact with the ground state. The parameterized potential model accounts for such interactions through the u_i ($^1\Sigma$) and q_i ($^1\Sigma$,$^1\Pi$) parameters. Thus for equal number of adjustable parameters, the parameterized potential model works much better than the "constrained" Dunham fits in the coinage metal hydrides. If more Δ_{ij}'s are added, this would allow the U_{ij}'s to be different from the constrained values for each isotope, which would reduce the χ^2 of the fit. This will basically undo the constrained relationships but will increase the number adjustable parameters in the

fit. Adding one more Δ_{ij} for the metal center in the AgH/D fits reduced the χ^2 of the fit by ~10%. A systematic set of fits to explore this phenomena was not carried out.

The parameters of the potential function can be used to calculate the approximate values of the Δ_{01} parameter of the Dunham model. This was first described in the work of Coxon *et al.* [197,201],

$$\Delta_{01}^{i} \simeq 2[m_e k^{BO} R_e^{BO}]^{-1} \left(\frac{\partial U_i(R)}{\partial R}\right)_{R=R_e}, \tag{7.2}$$

where U_i is given by eqn. (6.30) and k^{BO} is the harmonic force constant, which can be calculated from the second derivative of the Born–Oppenheimer potential,

$$k^{BO} = \left(\frac{\partial^2 U^{BO}(R)}{\partial R^2}\right)_{R=R_e}. \tag{7.3}$$

Substituting eqn. (6.30) into eqn. (7.2) and eqn. (6.26) into eqn. (7.3) we get the following result,

$$\Delta_{01}^{i} \simeq \frac{4R_e^{BO}\left(1 - e^{-\beta(\infty)}\right)^2}{D_e \beta_0^2 m_e} u_1^i. \tag{7.4}$$

These Δ_{01}^{i} values were calculated for the coinage metals (Table 7.16) and compared with the experimental values. Using the parameter values from Table 7.8 gives Δ_{01}^{Cu} = -1.926 and Δ_{01}^{H} = -0.6355. These values are in fairly good agreement with the Δ_{01} parameters listed in Table 7.7. This is because eqn. (7.4) was used at a point where non–adiabatic corrections to the potential are small, i.e. near the potential minimum. This point was shown by Coxon *et al.* [197] where they proved that the

non–adiabatic corrections to the potential at the minimum are exactly zero (i.e. $q(R_e^{BO}) = 0$). The values calculated for the rest of coinage metal hydrides are in fairly good agreement with the experimental values. The calculated Δ_{01}^{Cu} value is in much better agreement than with the case for GaH. The $\Delta_{01}^{Ga}(calc)$ value was found to be a factor of 6 larger then the observed value of Δ_{01}^{Ga} [179]. The large discrepancy for GaH was due largely to statistical correlations of U_{ij}'s to R_e.

Finally the Born-Oppenhiemer potentials of the coinage metals are shown in Fig. 7.10. The shapes of the potentials are similar in appearance because the potential energy curves were scaled by the dissociation energy of the molecule. The minima of the potentials (R_e) show an interesting trend. It increases from CuH to AgH, as would be expected when going down a group in the periodic table, but the R_e for AuH is smaller than AgH and approaches the R_e of CuH. The reason for this is that the 6^{th} period transition elements follow the lanthanide series, and have filled the *4f* orbitals. The filling of *4f* orbitals causes a decrease in atomic radius which is called the lanthanide contraction. The *f* orbitals have low probabilities near the nucleus and therefore do not shield the nucleus as well as *s* or *p* orbitals. The valence electron "sees" a larger effective nuclear charge thereby reducing the atomic radius and the internuclear distance of the diatomic molecule.

7.8 Summary

The Fourier transform emission technique has been used to record the spectra of high temperature molecules. It has proven to be an effective technique for the measurements of the infrared vibration–rotation spectra of the coinage metal hydrides.

The analysis of high quality data from multiple isotopomers was carried out using conventional models which are compared to the newer method of directly solving the one–dimensional Schrödinger equation. The presence of low–lying electronic states in the coinage metal hydrides causes non–adiabatic coupling of the ground state with the first excited states. The potential model has been shown to be superior in representing the dataset due to its ability to handle these Born–Oppenheimer breakdown effects. The Dunham "constrained" model with the inclusion of the Δ_{ij} parameters, derived for isolated electronic states, cannot adequately describe the Born–Oppenheimer breakdown in these coinage metal hydrides.

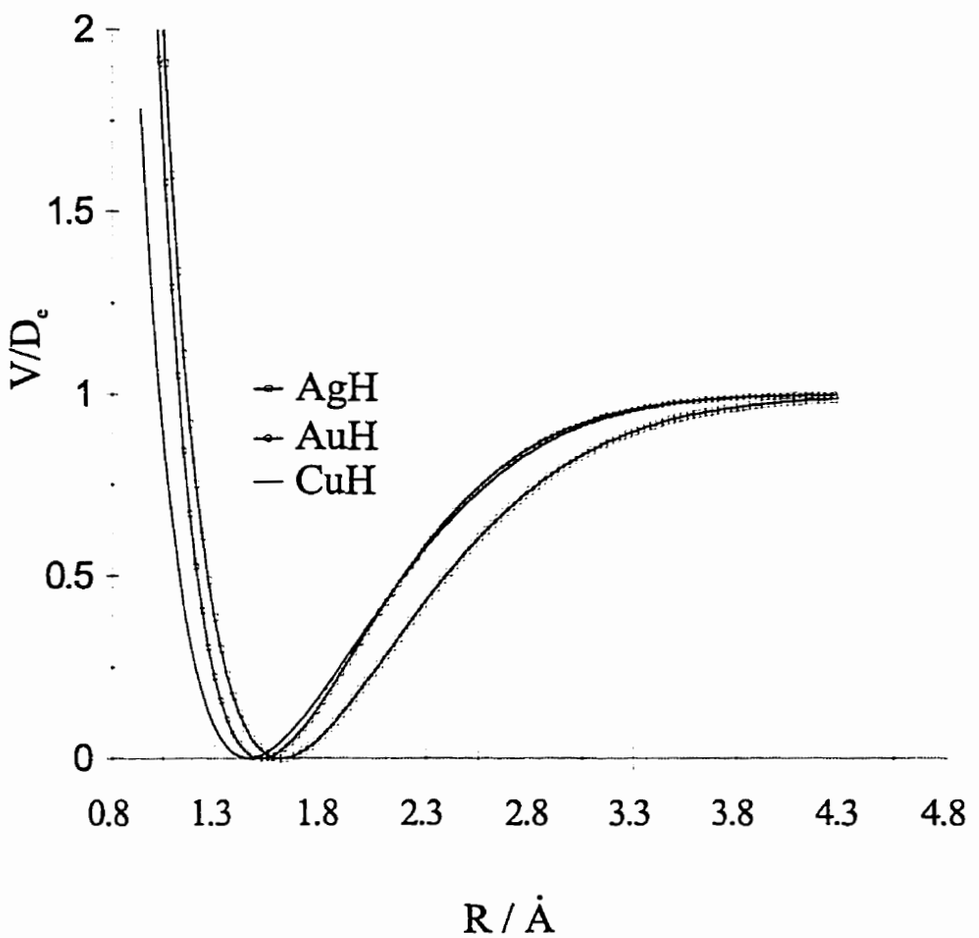

Figure 7.10: The comparison of Born–Oppenheimer potentials of the coniage metal hydrides (CuH, AgH, AuD).

Table 7.6: Isotopically dependent Dunham constants for CuH and CuD (cm^{-1}).

Constant	^{63}CuH	^{65}CuH
Y_{10}	1941.6099(133)	1940.91309(101)
Y_{20}	-37.88711(108)	-37.645582(633)
Y_{30}	0.192391(334)	0.108950(112)
10^2Y_{40}	-1.04230(346)	–
Y_{01}	7.94481811(446)	7.94100763(432)
Y_{11}	-0.2557092(125)	-0.2556509(114)
10^3Y_{21}	1.51073(850)	1.62248(649)
10^5Y_{31}	-6.320(219)	-1.0290(123)
10^6Y_{41}	-5.436(201)	–
10^4Y_{02}	-5.317385(122)	-5.3124389(149)
10^6Y_{12}	8.2030((289)	8.2507(304)
10^7Y_{22}	-2.251(131)	-2.295(141)
10^8Y_{32}	-2.465(151)	-4.043(264)
10^8Y_{03}	2.45020(173)	2.44741(305)
$10^{10}Y_{13}$	-7.755(162)	-8.393(261)
$10^{11}Y_{33}$	-2.497(260)	–
$10^{12}Y_{04}$	-1.6598(182)	-1.6734(422)
	^{63}CuD	^{65}CuD
Y_{10}	1384.46077(110)	1383.79995(194)
Y_{20}	-19.199373(674)	-19.17964(100)
10^2Y_{30}	4.6941(118)	4.6461(160)
Y_{01}	4.03877847(289)	4.03492251(530)
10^2Y_{11}	-9.271551(760)	-9.25700(124)
10^4Y_{21}	4.0562(440)	3.9123(460)
10^5Y_{31}	-1.6903(782)	-1.4390(620)
10^4Y_{02}	-1.3744124(504)	-1.371990(120)
10^6Y_{12}	1.5567(113)	1.588(221)
10^8Y_{22}	-3.721(544)	-4.252(279)
10^9Y_{32}	2.51(100)	–
10^9Y_{03}	3.22943(539)	3.2563(174)
$10^{11}Y_{13}$	-9.492(470)	-1.371(189)
$10^{11}Y_{04}$	-1.0855(483)	-1.301(199)

Table 7.7: Isotopically invariant Dunham constants for CuH and CuD (cm^{-1}).

Constant	Unconstrained	Constrained
U_{10}	1934.65023(392)	1934.69815(263)
U_{20}	-37.58787(146)	-37.61031(132)
10^2U_{30}	1.84153(384)	1.89751(362)
10^2U_{40}	-1.025626(359)	-1.04902(486)
U_{01}	7.88376993(271)	7.88378257(272)
U_{11}	-0.2527918(106)	-0.25287765(670)
10^3U_{21}	1.47856(753)	1.56095(566)
10^5U_{31}	-5.782(199)	-8.322(185)
10^6U_{41}	-5.666(189)	-2.771(173)
10^4U_{02}	-5.2365678(653)	-5.23645619
10^6U_{12}	8.0927(248)	8.05333088
10^7U_{22}	-2.286(116)	-2.08747757
10^8U_{32}	-2.849(167)	-3.76314517
10^8U_{03}	2.39921(139)	2.39324572
$10^{10}U_{13}$	-8.021(156)	-5.95969283
$10^{11}U_{23}$	–	-8.31664255
$10^{11}U_{33}$	-1.516(244)	59.2400591
$10^{12}U_{04}$	-1.6130(210)	-1.65903377
$10^{14}U_{14}$	–	-2.23754354
$10^{14}U_{24}$	–	-1.03840761
$10^{16}U_{05}$	–	1.03194936
$10^{17}U_{15}$	–	-1.44895707
$10^{18}U_{25}$	–	3.99213835
$10^{20}U_{06}$	–	-1.01801779
$10^{22}U_{16}$	–	-1.73738083
$10^{25}U_{07}$	–	3.87728302
$10^{25}U_{17}$	–	3.09714045
$10^{29}U_{08}$	–	-6.01969965
$10^{33}U_{09}$	–	6.93222867
Δ_{10}^{Cu}	-2.312(206)	-3.611(147)
Δ_{01}^{Cu}	-1.6801(224)	-1.6471(330)
Δ_{10}^{H}	-0.79924(195)	-0.81756(258)
Δ_{20}^{H}	-0.2859(758)	-0.1094670(975)
Δ_{30}^{H}	59.03(354)	22.26(434)
Δ_{01}^{H}	-0.670392(446)	-0.665921(319)
Δ_{11}^{H}	-1.2054(159)	-1.0845(203)
Δ_{02}^{H}	-1.5258(233)	-1.51606(754)
Δ_{03}^{H}	-5.25(141)	-3.946(546)

Table 7.8: Born-Oppenheimer potential parameters for CuH and CuD.

D_e (cm^{-1})	23000.0
R_e (Å)	1.462282508(148)
β_0	4.54334158(236)
β_1	4.362224(106)
β_2	7.392779(568)
β_3	13.13481(808)
β_4	22.5640(397)
β_5	22.913(448)
u_1^{Cu}	-69.09(102)
u_2^{Cu}	24.98(174)
u_1^H	-28.8055(113)
u_2^H	19.9697(623)
u_3^H	14.253(531)
u_4^H	-20.20(100)
u_5^H	3.67(133)
q_1^{Cu}	$1.442(130)\times10^{-3}$
q_2^{Cu}	$-1.129(172)\times10^{-2}$
q_1^H	$4.6933(242)\times10^{-4}$
q_2^H	$-2.295(174)\times10^{-4}$
M_A (^{65}Cu)	64.9277929
M_A (^{63}Cu)	62.9295989
M_B (^1H)	1.007825035
M_B (^2H)	2.014101779
χ^2 :	1.041
Transitions :	451
Adjustable Parameters :	18

Table 7.9: Isotopically dependent Dunham constants for AgH and AgD (cm^{-1}).

Constant	^{107}AgH	^{109}AgH
Y_{10}	1759.74718(137)	1759.59636(165)
Y_{20}	-33.978980(890)	-33.97316(109)
10^3Y_{30}	-5.483(168)	-5.209(205)
Y_{01}	6.4500078(201)	6.4489143(229)
Y_{11}	-0.202115(167)	-0.201990(241)
10^4Y_{21}	6.885(108)	6.35(152)
10^4Y_{31}	-1.0504(206)	-1.0072(267)
10^4Y_{02}	-3.46206(106)	-3.46421(123)
10^6Y_{12}	4.2406(418)	3.9176(744)
10^7Y_{22}	-2.493(250)	-70.6(433)
10^8Y_{32}	-3.249(493)	-4.002(661)
10^8Y_{03}	1.0038(171)	1.0753(194)
$10^{10}Y_{13}$	-5.521(345)	-1.250(557)
$10^{10}Y_{23}$	–	-1.374(193)
χ^2 :	0.7488	0.7510
Transitions :	112	99
Adjustable Parameters :	13	12

	^{107}AgD	^{109}AgD
Y_{10}	1250.89686(159)	1250.68475(129)
Y_{20}	-17.220706(929)	-17.214784(797)
10^3Y_{30}	6.489(162)	6.510(137)
Y_{01}	3.2578956(158)	3.2568421(136)
10^2Y_{11}	-7.26204(143)	7.254924(837)
10^4Y_{21}	2.0291(835)	1.7659(409)
10^5Y_{31}	-2.375(148)	-1.9313(625)
10^5Y_{02}	-8.83449(481)	-8.84845(363)
10^7Y_{12}	9.439(284)	8.514(157)
10^7Y_{22}	-1.12(143)	-5.227(239)
10^8Y_{32}	1.068(258)	–
10^9Y_{03}	1.2294(453)	1.4194(282)
$10^{10}Y_{13}$	-1.090(141)	-91.1(115
χ^2 :	0.6470	0.6927
Transitions :	79	79
Adjustable Parameters :	13	14

Table 7.10: Isotopically invariant Dunham constants for AgH and AgD (cm^{-1}).

Constant	Unconstrained	Constrained
U_{10}	1759.17978(84)	1759.26565(334)
U_{20}	-34.16256(172)	-34.19077(591)
10^2U_{30}	4.2062(404)	4.860(145)
U_{01}	6.4410323(324)	6.4407974(559)
U_{11}	-0.2017435(164)	-0.2017269(201)
10^4U_{21}	6.644(110)	6.512(124)
10^4U_{31}	-1.0241(205)	-92.00(210)
10^4U_{02}	-3.45574(108)	-3.45315498
10^6U_{12}	4.1689(536)	4.24311981
10^7U_{22}	-2.187(332)	-3.41462867
10^8U_{32}	-3.059(533)	-3.05931359
10^8U_{03}	1.0021(149)	1.06301760
$10^{10}U_{13}$	-4.826(444)	-5.09393126
$10^{11}U_{23}$	-3.27(176)	-3.45276905
$10^{13}U_{04}$	–	-5.86818904
$10^{14}U_{14}$	–	-4.22570034
$10^{17}U_{05}$	–	1.31719830
$10^{18}U_{15}$	–	-2.80552833
$10^{21}U_{06}$	–	-2.53260626
Δ_{10}^{Ag}	1.474(912)	-4.36(364)
Δ_{10}^{H}	-0.88225(244)	-0.93442(869)
Δ_{20}^{H}	-12.8347(954)	-14.911(332)
Δ_{30}^{H}	-2080.73(797)	-2138.80(197)
Δ_{01}^{H}	-0.3635(103)	-0.1876(215)
Δ_{11}^{H}	-1.2953(400)	-1.548(124)
Δ_{02}^{H}	-2.388(434)	5.267(380)
χ^2 :	1.051	4.2454
Transitions :	369	
Adjustable Parameters :	21	14

Table 7.11: Born-Oppenheimer potential parameters for AgH and AgD.

D_e (cm^{-1})	19278.0
R_e (Å)	1.61780074(170)
β_0	4.99216653(629)
β_1	5.345143(164)
β_2	10.17092(128)
β_3	17.6335(143)
β_4	35.292(114)
β_5	34.834(781)
u_1^H	-10.107(191)
u_2^H	-2.451(423)
u_3^H	13.729(372)
q_1^H	0
q_2^H	$1.3669(421)\times10^{-3}$
q_3^H	$-1.8618(902)\times10^{-3}$
M_A (^{107}Ag)	106.905092
M_A (^{109}Ag)	108.904756
M_B (^{1}H)	1.007825035
M_B (^{2}H)	2.014101779
χ^2 :	1.030
Transitions :	369
Adjustable Parameters :	12

Table 7.12: Isotopically dependent Dunham constants for AuH and AuD (cm^{-1}).

Constant	^{197}AuH	^{197}AuD
Y_{10}	2305.53156(404)	1635.25297(57)
Y_{20}	-43.389894(148)	-21.820758(331)
Y_{01}	7.24137326(998)	3.64224729(636)
10^3Y_{30}	–	-1.4677(542)
10^2Y_{11}	-21.321141(739)	-7.62695(279)
10^4Y_{21}	30.33(257)	1.2556(116)
10^5Y_{31}	–	-1.9573(161)
10^5Y_{02}	-28.57212(412)	-7.23927(165)
10^7Y_{12}	25.334(289)	4.3383(471)
10^8Y_{22}	-34.617(861)	-3.7251(649)
$10^{10}Y_{03}$	4.7718(486)	7.360(134)
$10^{11}Y_{13}$	-42.22(227)	-1.882(324)
χ^2 :	0.7806	1.030
Transitions :	69	142
Adjustable Parameters : 10		12

Table 7.13: Isotopically invariant Dunham constants for AuH and AuD (cm^{-1}).

Constant	Unconstrained	Constrained
U_{10}	2309.31423(105)	2309.31476(206
U_{20}	-43.521977(811)	-43.52497(167)
10^3U_{30}	-4.367(188)	-3.973(393)
U_{01}	7.2619588(213)	7.2619861(193)
U_{11}	-0.21479366(996)	-0.2147786(106)
10^4U_{21}	4.9963(555)	5.4533(973)
10^4U_{31}	-1.0766(107)	-1.1197(214)
10^4U_{02}	-2.871647(533)	-2.87249955
10^6U_{12}	2.6557(269)	2.49570379
10^7U_{22}	-3.2011(530)	-4.00588160
10^9U_{03}	5.0572(519)	4.91398996
$10^{10}U_{13}$	-4.500(218)	-3.04865128
$10^{11}U_{23}$	–	-1.64427910
$10^{13}U_{04}$	–	-2.15812167
$10^{14}U_{14}$	–	-4.98835897
$10^{18}U_{05}$	–	-1.23825084
$10^{19}U_{15}$	–	5.61009582
$10^{21}U_{06}$	–	-1.09609301
$10^{27}U_{07}$	–	-2.62058672
Δ^H_{10}	-0.562082(717)	-0.55820(146)
Δ^H_{20}	-1.5181(115)	-1.5140(240)
Δ^H_{01}	-0.21417(679)	-0.21928(728)
Δ^H_{11}	-1.1715(566)	-0.3378(553)
Δ^H_{02}	1.705(356)	0.589(173)
Δ^H_{12}	-112.1(124)	97.71(683)
χ^2 :	1.3112	2.778
Transitions :		211
Adjustable Parameters : 18		13

Table 7.14: Born-Oppenheimer potential parameters for AuH and AuD.

D_e (cm^{-1})	27135.0
R_e (Å)	1.523596412(979)
β_0	5.20234379(351)
β_1	5.382001(160)
β_2	9.916858(478)
β_3	16.1247(225)
β_4	19.3037(985)
u_1^H	-13.160(208)
u_2^H	-5.643(517)
u_3^H	27.216(482)
q_1^H	$4.361(287)\times10^{-4}$
q_2^H	0
q_3^H	$1.437(454)\times10^{-3}$
q_4^H	$-3.079(988)\times10^{-3}$
M_A (^{197}Ag)	196.966540
M_B (^{1}H)	1.007825035
M_B (^{2}H)	2.014101779
χ^2 :	1.144
Transitions :	211
Adjustable Parameters :	12

Table 7.15: Comparison of "constrained" Dunham fits and parameterized potential fits. Positions of the lowest lying electronic states are taken from [208].

M	State	MH (cm^{-1})	MD (cm^{-1})	D_e (cm^{-1})	χ^2_{dun}	χ^2_{pot}
Cu	$T_e(^1\Sigma^+)$	23434	23412	22019	1.294	1.041
Ag	$T_e(^1\Sigma^+)$	29959	29960	20083	4.245	1.030
Au	$T_e(^1\Pi)$	27665	27664	26294	2.788	1.144

Table 7.16: Comparison of Δ^A_{01}.

Molecule	Δ^A_{01}(calc)	Δ^A_{01}(obs)
CuH (A=Cu)	-1.552	-1.6471(330)
CuH (A=H)	-0.630	-0.81756(258)
AgH (A=H)	-0.248	-0.1876(215)
AuH (A=H)	-0.199	-0.21928(728)

References

1. P.F. Bernath, *Spectra of Atoms and Molecules* (Oxford University Press, Oxford, 1995).

2. N.G. Norrish and G. Porter, Nature **164**, 658 (1949).

3. G. Herzberg, Ann. Rev. Phys. Chem. **36**, 1 (1985).

4. S. Green, Ann. Rev. Phys. Chem. **32**, 103 (1981).

5. G. Herzberg, *The Spectroscopy of Diatomic Free Radicals* (Cornell University Press, Ithaca, NY, 1975).

6. R.P. Wayne, *Chemistry of Atmospheres*, 2nd ed. (Clarendon Press, Oxford, 1991).

7. E. Hirota, J. Phys. Chem **87**, 3375 (1983).

8. J.G. Anderson, Ann. Rev. Phys. Chem. **38**, 489 (1987).

9. G.C. Dousmanis, T.M Sanders, Jr and C.H. Townes, Phys. Rev. **100**, 1795 (1955).

10. G. Ehrenstein, C.H. Townes and M.J. Stevenson, Phys. Rev. Lett. **3**, 40 (1959).

11. S. Weinreb, A.H. Barret, M.L. Meeks and J.C. Henry, Nature **200**, 829 (1963).

12. A.C. Cheung, D.M. Rank, C.H. Townes and W.J. Welch, Nature **221**, 917 (1969).

13. E. Hirota, Chem. Rev. **92**, 141 (1992).

14. R.C. Hilborn, Q. Zhu and D.O. Harris, J. Mol. Spec. **97**, 73 (1983).

15. P.F. Bernath and C.R. Brazier, Astrophys. J. **288**, 373 (1985).

16. J. Nakagawa, R.F. Wormsbecher and D.O. Harris, J. Mol. Spec. **97**, 37 (1983).

17. P.I. Presunka and J.A. Coxon, J. Chem. Phys. **101**, 201 (1994).

18. P.I. Presunka and J.A. Coxon, Can. J. Chem. **71**, 1689 (1993).

19. A.M.R.P. Bopegedera, C.R. Brazier and P.F. Bernath, Chem. Phys. Lett. **136**, 97 (1987).

20. A.M.R.P. Bopegedera, C.R. Brazier and P.F. Bernath, J. Mol. Spec. **129**, 268 (1988).

21. M. Li and J.A. Coxon, J. Mol. Spec. **176**, 206 (1996).

22. M. Li and J.A. Coxon, J. Mol. Spec. **180**, 287 (1996).

23. J.B. West, R.S. Bradford, J.D. Eversole and C.R. Jones, Rev. Sci. Instrum. **46**, 164 (1975).

24. C.N. Jarman and P.F. Bernath, J. Chem. Phys. **97**, 1711 (1992).

25. Z.J. Jakubek and R.W. Field, J. Chem. Phys. **98**, 6574 (1993).

26. C.T. Scurlock, D.A. Fletcher and T.C. Steimle, J. Mol. Spec. **159**, 350 (1993).

27. R. Pereira and D. H. Levy, J. Chem. Phys. **105**, 9733 (1996).

28. R.A. Hailey, C.N. Jarman and P.F. Bernath, J. Chem. Phys. **107**, 669 (1997).

29. J.F.W Herschel, Trans. Roy. Soc. Edinburgh **9**, 445 (1823).

30. A.S. King, Astrophys. J. **27**, 353 (1908).

31. P.C. Mahanti, Phys. Rev. **42**, 609 (1932).

32. C.G. James and T.M. Sugden, Nature **175**, 333 (1955).

33. A.G. Gaydon, Proc. Roy. Soc. London **231**, 437 (1955).

34. M. Charton and A.G. Gaydon, Proc. Phys. Soc. A. **69**, 520 (1956).

35. A. Vallance Jones, Ann. Geophys. **14**, 179 (1958).

36. E. Murad, J. Geophys. Res. **22**, 599 (1969).

37. E. Murad, W. Swider and S.W. Benson, Nature **289**, 273 (1981).

38. R. Ganapathy and D.E. Brownlee, Science **206**, 1075 (1979).

39. T. Tsuji, Astron. Astrophys. **23**, 411 (1973).

40. P. Pesch, Astrophys. J. **174**, L155 (1972).

41. B.R. Pettersen and S.L. Hawley, Astron. Astrophys. **217**, 187 (1989).

42. K. Kawaguchi, E. Kagi, T. Hirano, S. Takano and S.Saito, Astrophys. J. **406**, L39 (1993).

43. K. Ishii, T. Hirano, U. Nagashima, B. Weis and K. Yamashita, Astrophys. J. **410**, L43 (1993).

44. L.M. Ziurys, A.J. Apponi, M. Guelin and J. Cernicharo, Astrophys. J. **439**, L47 (1995).

45. J.B. Howard and W.J. Kausch, Jr., Prog. Energy Combust. Sci. **6**, 263 (1980).

46. P.A. Bonczyk, Combust. Sci. and Tech. **59**, 143 (1988).

47. S.J. Harris and A.M. Weiner, Ann. Rev. Phys. Chem. **36**, 31 (1985).

48. P.A. Bonczyk, Combust. Flame **67**, 179 (1987).

49. R.F Wormsbecher, M. Trkula and C. Martner and R.E. Penn and D.O. Harris, J. Mol. Spec. **97**, 29 (1983).

50. P.F. Bernath, Science **254**, 665 (1991).

51. C.R. Brazier, L.C. Ellingboe, S. Kinsey-Neilson and P.F. Bernath, J. Am. Chem. Soc. **108**, 2126 (1986).

52. L.C. O'Brien and P.F. Bernath, J. Am. Chem. Soc. **108**, 5017 (1986).

53. C.R. Brazier and P.F. Bernath, J. Phys. Chem. **86**, 5918 (1987).

54. L.C. O'Brien, C.R. Brazier, S. Kinsey-Neilson and P.F. Bernath, J. Phys. Chem. **94**, 3543 (1990).

55. A.M.R.P Bopegedera, C.R. Brazier and P.F. Bernath, J. Phys. Chem. **91**, 2779 (1987).

56. A.M.R.P. Bopegedera, W.T.M.L. Fernando and P.F. Bernath, J. Phys. Chem. **94**, 4476 (1990).

57. C.R. Brazier and P.F. Bernath, J. Chem. Phys. **88**, 2112 (1988).

58. L.C. O'Brien, A.M.R.P. Bopegedera and P.F. Bernath, Chem. Phys. Lett. **126**, 285 (1986).

59. W.T.M.L. Fernando, R.S. Ram. L.C. O'Brien and P.F. Bernath, J. Phys. Chem. **95**, 2665 (1991).

60. M. Douay and P.F. Bernath, Chem. Phys. Lett. **174**, 230 (1990).

61. C.R. Brazier and P.F. Bernath, J. Phys. Chem. **91**, 4548 (1989).

62. L.C. O'Brien, C.R. Brazier and P.F. Bernath, J. Mol. Spec **130**, 33 (1988).

63. F.S. Pianalto, A.M.R.P. Bopegedera, W.T.M.L. Fernando, R. Hailey, L.C. O'Brien, C.R. Brazier, P.C. Keller and P.F. Bernath, J. Am. Chem. Soc. **112**, 7900 (1990).

64. A.M.R.P. Bopegedera, W.T.M.L. Fernando and P.F. Bernath, J. Phys. Chem. **94**, 3547 (1990).

65. A.M. Ellis, E.S.J. Robles and T.A. Miller, J. Chem. Phys. **94**, 1752 (1991).

66. E.S.J. Robles, A.M. Ellis and T.A. Miller, J. Am. Chem. Soc. **114**, 7171 (1992).

67. T.M. Cerny, J.M. Williamson and T.A. Miller, J. Chem. Phys. **102**, 2372 (1995).

68. E.S.J. Robles, A.M. Ellis and T.A. Miller, J. Phys. Chem. **96**, 8791 (1992).

69. E.S.J. Robles, A.M. Ellis and T.A. Miller, J. Phys. Chem. **96**, 3247 (1992).

70. E.S.J. Robles, A.M. Ellis and T.A. Miller, J. Phys. Chem. **96**, 3258 (1992).

71. C.T. Scurlock, S.H. Pullins, J.E. Reddic and M.A. Duncan, J. Chem. Phys. **104**, 4591 (1996).

72. K.F. Willey, C.S. Yeh, D.L. Robbins, J.S. Pilgrim and M.A. Duncan, J. Chem. Phys. **97**, 8886 (1992).

73. M.H. Shen and J.M. Farrar, J. Chem. Phys. **94**, 624 (1991).

74. M.H. Shen and J.M. Farrar, J. Phys. Chem. **93**, 4386 (1989).

75. E. Kochanski and E. Constantin, J. Chem. Phys. **87**, 1661 (1987).

76. C.W. Bauschlicher, S.R. Langoff and H. Partridge, J. Chem. Phys. **94**, 901 (1986).

77. A.J. Merer, Ann. Rev. Phys. Chem. **40**, 407 (1989).

78. M.D. Morse, Chem. Rev. **86**, 1049 (1986).

79. J.V. Ortiz, J. Chem. Phys. **92**, 6728 (1990).

80. P. F. Bernath, in *Spectrosopy and Photochemistry of Polyatomic Alkaline Earth-Containing Molecules*, Vol. 23 of *Advances in Photochemistry*, edited by D.H. Volman and D.C Neckers (Wiley, New York, 1997).

81. S.F. Rice, H. Martin and R.W. Field, J. Chem. Phys. **82**, 5023 (1985).

82. J. M. Mestdagh and J. Visticot, Chem. Phys. **155**, 79 (1991).

83. T. Törring, W.E. Ernst and S. Kindt, J. Chem. Phys. **81**, 4614 (1984).

84. T.C. Steimle, D.A. Fletcher, K.Y. Jung and C.T. Scurlock, J. Chem. Phys. **96**, 2556 (1992).

85. M.D. Oberlander and J.M. Parson, J. Chem. Phys. **105**, 5806 (1996).

86. H.F. Davis, A.G. Suits, H. Hongtao, Y.T. Lee, Ber. Bunsenges Phys. Chem. **94**, 1193 (1990).

87. J.P. Visticot C. Alcaraz, J. Berlande, J. Cuvellier, T. Gustavsson, J.M. Mestdagh, P. Meynadier, P. de Pujo, O. Sublemontier, J. Chem. Phys. **94**, 4913 (1991).

88. M. Esteban, M. Garay, J.M. Garcia-Tijero, E. Verdasco and A. Gonzalez Urena, Chem. Phys. Lett. **230**, 525 (1994).

89. J.M. Mestdagh, J.P. Visticot and P.F. Bernath, Chem. Phys. Lett. **237**, 568 (1995).

90. A. Gonzalez Urena and M. Garay, Chem. Phys. Lett. **237**, 570 (1995).

91. H.F. Davis, A.G. Suits, Y.T. Lee, C. Alcaraz and J.M. Mestadagh, J. Chem. Phys. **98**, 9595 (1993).

92. C.T Scurlock, D.A. Fletcher and T.C. Steimle, J. Chem. Phys. **159**, 350 (1993).

93. M. Li and J.A. Coxon, J. Chem. Phys. **102**, 2663 (1995).

94. M.A. Anderson, W.L. Barclay and L.M. Ziurys, Chem. Phys. Lett. **196**, 166 (1992).

95. C. Zhao, P.G. Hajigeorgiou, P.F. Bernath and J.W. Hepburn, J. Mol. Spec. **176**, 268 (1996).

96. W.T.M.L. Fernando, M. Douay and P.F. Bernath, J. Mol. Spec **144**, 344 (1990).

97. P.R. Bunker, M. Kolbuszewski, P. Jensen, M. Brumm, M.A. Anderson, W.L. Barclay, L.M. Ziurys, Y. Ni and D.O. Harris, Chem. Phys. Lett. **239**, 217 (1995).

98. T.C. Steimle, S. Saito and S. Takano, Astrophys. J. **410**, L49 (1993).

99. C.T. Scurlock, T.C. Steimle, R.D. Suenram and F.J. Lovas, J. Chem. Phys. **100**, 3497 (1994).

100. T.C. Steimle, D.A. Fletcher, K.Y Jung and C.T. Scurlock, J. Phys. Chem. **97**, 2909 (1992).

101. E. Kagi, K. Kawaguchi, S. Takano and T. Hirano, J. Chem. Phys. **104**, 1263 (1996).

102. M.A. Anderson and L.M. Ziurys, Chem. Phys. Lett. **231**, 164 (1994).

103. M.A. Anderson, T.C. Steimle and L.M. Ziurys, Astrophys. J. **429**, L41 (1994).

104. M.A. Anderson and L.M. Ziurys, Astrophys. J. **444**, L57 (1995).

105. C.J. Whitam, B. Soep, J-P. Visticot and A. Keller, J. Chem. Phys. **93**, 991 (1990).

106. B.P. Nuccio, A.J. Apponi and L.M. Ziurys, Chem. Phys. Lett. **247**, 283 (1995).

107. M.A. Anderson and L.M. Ziurys, Astrophys. J. Lett. **439**, L25 (1995).

108. G.K. Corlett, A.L. Little and A.M. Ellis, Chem. Phys. Lett. **249**, 53 (1996).

109. L.C. O'Brien and P.F. Bernath, J. Chem. Phys. **88**, 2117 (1988).

110. A. Taleb-Bendiab, F. Scappini, T. Amano and J.K.G. Watson, J. Chem. Phys. **104**, 7431 (1996).

111. C.N. Jarman and P.F. Bernath, J. Chem. Phys. **98**, 6697 (1993).

112. C.T. Scurlock, T. Henderson, S. Bosely, K.Y. Jung and T.C. Steimle, J. Chem. Phys. **100**, 5481 (1994).

113. A.J. Marr, M. Tanimoto, D. Goodridge and T.C. Steimle, J. Chem. Phys. **103**, 4466 (1995).

114. C. Zhao, Ph.D. thesis, University of Waterloo, 1997.

115. C.J. Whitham and Ch. Jungen, J. Chem. Phys. **93**, 1001 (1990).

116. R.F. Wormsbecher, R.E. Penn and D.O. Harris, J. Mol. Spec. **97**, 65 (1983).

117. Z. Morbi, C. Zhao and P.F. Bernath, J. Chem. Phys. **106**, 4860 (1997).

118. C.R. Brazier and P.F. Bernath (unpublished).

119. A.J. Marr, F. Grieman and T.C. Steimle, J. Chem. Phys. **105**, 3930 (1996).

120. M.A. Anderson, J.S Robinson and L.M. Ziurys, Chem. Phys. Lett. **257**, 471 (1996).

121. M.A. Anderson and L.M. Ziurys, Astrophys. J. **452**, L157 (1995).

122. R. Rubino, J.M Williamson and T.A Miller, J. Chem. Phys. **103**, 5964 (1995).

123. R.F. Wormsbecher and R.D. Suenram, J. Mol. Spec. **95**, 391 (1982).

124. D.E. Jensen and G.A. Jones, Proc. Roy. Soc. Lond. A. **364**, 509 (1978).

125. *Thermochemical Properties of Inorganic Substances*, 2nd ed., edited by O. Knacke, O. Kubascheski, K. Hesselmann (Springer–Verlag, Berlin, 1991).

126. D.R. Miller, in *Atomic and Molecular Methods*, edited by G. Scoles (Oxford University Press, New York, 1988), Vol. 1, Chap. 2, p. 14.

127. M.D. Morse, *Experimental Methods in Physical Sciences* (Academic Press Inc., New York, 1996), Vol. 29B.

128. T. A. Miller, Science **223**, 545 (1984).

129. K. Lui, G. Hall, M.J. McAuliffe, C.F. Guise and W.R Gentry, J. Chem. Phys **80**, 3494 (1984).

130. D.H. Levy, Science **214**, 263 (1981).

131. K.L. Saenger and J.B. Fenn, J. Chem. Phys. **79**, 6043 (1983).

132. P.C. Engelking, Chem. Rev. **91**, 399 (1991).

133. D.H. Levy, Ann. Rev. Phys. Chem. **31**, 197 (1980).

134. V.E Bondybey, A.M. Smith and J. Agreiter, Chem. Rev. **96**, 2113 (1996).

135. S.C. Foster and T.A. Miller, J. Phys. Chem. **93**, 5986 (1989).

136. M. Ito, T. Ebata and N. Mikami, Ann. Rev. Phys. Chem. **39**, 123 (1988).

137. X.Q. Tan, T.G. Wright and T.A. Miller, in *Jet Spectroscopy and Molecular Dynamics*, edited by J. Hollas and D. Phillips (Blackie Academic & Professional, London, 1995), Chap. 3, pp. 74–113.

138. V.E. Bondybey, Science **227**, 125 (1985).

139. P. Dehz, P. Jeagle, S. Leach and M. Velghe, J. Appl. Phys. **40**, 2545 (1969).

140. S. Taylor, G.W. Lemire, Y.M. Hamrick, Z. Fu and M.D. Morse, J. Chem. Phys. **89**, 5517 (1988).

141. M.D. Morse, G.P. Hansen, P.R.R Langridge–Smith, L.S. Zeng, M.E. Geusic, D.L. Michalopoulo and R.E. Smalley, J. Chem. Phys. **80**, 5400 (1984).

142. R. Schaeffer and R.K. Pearson, J. Am. Chem. Soc. **91**, 2153 (1969).

143. T. Dietz, M.A. Duncan, D.E. Powers and R.E. Smalley, J. Chem. Phys. **74**, 6511 (1981).

144. D.L. Monts, T.G. Deitz, M.A. Duncan and R.E. Smalley, Chem. Phys. **45**, 133 (1980).

145. S. Gerstenkorn and P. Luc, *Atlas du Spectre d'Asorption de la Molécule d'Iode* (CNRS II, 91405 Orsay, France, 1978).

146. S. Gerstenkorn and P. Luc, Rev. Phys. Appl. **14**, 791 (1978).

147. G. Herzberg, *Spectra of Diatomic Molecules* (Van Nostrand Reinhold, New York, 1950).

148. R.N. Zare, *Angular Momentum* (Wiley, New York, 1988).

149. J.K.G. Watson, in *Aspects of Quartic and Sextic Centrifugal Effects on Rotational Energy Levels*, Vol. 6 of *Vibrational Spectra and Structure*, edited by J.R. Durig (Elseiver Scientific, Amsterdam, 1977), .

150. J.K.G. Watson, J. Chem. Phys. **46**, 1935 (1967).

151. E. Hirota, *High-Resolution Spectroscopy of Transient Molecules*, Vol. 40 of *Springer Series in Chemical Physics* (Springer–Verlag, Berlin, 1985), .

152. J.M. Brown and T.J. Sears, J. Mol. Spec. **75**, 111 (1979).

153. J.H. Van Vleck, Rev. Mod. Phys. **23**, 213 (1965).

154. G. Duxbury, *The Electronic Spectra of Triatomic Molecules and the Renner-Teller Effect*, Vol. 3 of *Molecular Spectroscopy: A Specialist Periodical Reports* (The Chemical Society, Burlington House, London, 1975).

155. R.F. Curl, Mol. Phys. **9**, 585 (1965).

156. R.N. Dixon, Mol. Phys. **10**, 1 (1965).

157. R.N. Dixon, G. Duxbury and D.A. Ramsay, Proc. Roy. Soc. A **296**, 137 (1966).

158. C. Linton, J. Mol. Spec. **69**, 251 (1978).

159. M. Dulick, P.F. Bernath and R.W. Field, Can. J. Phys. **58**, 703 (1980).

160. F.W. Loomis and R.W. Wood, Phys. Rev. **32**, 223 (1928).

161. R.N. Dixon, Mol. Phys. **13**, 77 (1967).

162. R.F. Curl, J. Chem. Phys. **37**, 779 (1962).

163. L.M Tack, N.H. Rosenbaum, J.C. Owrutsky and R.J. Saykally, J. Chem. Phys. **84**, 7056 (1986).

164. K. Su, X. Hu X. Li, Y. Wang and Z. Wen, Chem. Phys. Lett. **258**, 431 (1996).

165. I. Mills *et al.*, *Quantities, Units and Symbols in Physical Chemistry* (Blackwell Scientific Publishing, Alden Press, Oxford, 1988).

166. W. Chan and I. Hamilton (unpublished).

167. A.H. Heilscher, C.E. Miller, D.C. Bayard, U. Simon, K.P. Smolka, R.F. Curl and F.K. Tittel, J. Opt. Soc. B. **9**, 1962 (1992).

168. C.E. Miller, W.C. Eckhoff and R.F. Curl, J. Mol. Stuct. **352/353**, 435 (1995).

169. P. F. Bernath, Ann. Rev. Phys. Chem. **41**, 91 (1990).

170. K.A. Walker, H.G. Hedderich, and P.F. Bernath, Mol. Phys. **78**, 577 (1993).

171. J.U. White, J. Opt. Soc. Am. **32**, 285 (1942).

172. H.J. Bernstein and G. Herzberg, J. Chem. Phys. **16**, 30 (1948).

173. R.S. Ram and P.F. Bernath, J. Mol. Spec. **122**, 275 (1987).

174. P.D. Hammer, A. Sinha, J.B. Burkholder and C.J. Howard, J. Mol. Spec. **129**, 99 (1988).

175. H. Uehara, K. Horiai, K. Sueoka and K. Nakagawa, Chem. Phys. Lett. **160**, 149 (1989).

176. C.I. Frum, R. Engleman and P.F. Bernath, J. Chem. Phys. **93**, 5457 (1990).

177. J.B White, M. Dulick, and P.F. Bernath, J. Chem. Phys. **99**, 8371 (1993).

178. J.B. White, M. Dulick and P.F. Bernath, J. Mol. Spec. **169**, 410 (1995).

179. J.M. Campbell, M. Dulick, D. Klapstein, and P.F. Bernath, J. Chem. Phys. **99**, 8379 (1993).

180. R. Le Blanc, J.B. White and P.F. Bernath, J. Mol. Spec. **164**, 574 (1994).

181. H. G. Hedderich, C. I. Frum, R. Engleman and P. F. Bernath, Can. J. Chem. **69**, 1659 (1991).

182. P.F. Bernath, Chem. Soc. Rev. **25**, 111 (1996).

183. A. Michelson, Phil. Mag. **31**, 256 (1891).

184. A. A. Michelson, *Studies in Optics, Phoenix Science Series* (The University of Chicago Press, Chicago, 1962).

185. P.R. Griffiths, in *Laboratory Methods in Vibrational Spectroscopy*, edited by H.A. Willis, J.H. van der Maas and R.G.J. Miller (John Wiley & Sons, New York, 1987), Chap. 6.

186. P.R. Griffiths, *Fourier Transform Infrared Spectrometry*, Vol. 83 of *Chemical Analysis* (John Wiley & Sons, New York, 1986).

187. J.L. Dunham, Phys. Rev. **41**, 721 (1932).

188. J.L. Dunham, Phys. Rev. **41**, 712 (1932).

189. J.K.G. Watson, J. Mol. Spec. **80**, 411 (1980).

190. A.H.M. Ross, R.S. Eng and H. Kildal, Opt. Comm. **12**, 433 (1974).

191. J.K.G. Watson, J. Mol. Spec. **45**, 99 (1973).

192. E. Tiemann, H. Arnst, W.U. Stieda, T. Törring and J. Hoeft, Chem. Phys. **67**, 133 (1982).

193. J. Ogilvie, Comput. Phys. Comm. **30**, 101 (1983).

194. J. Ogilvie (unpublished).

195. W. Kosman and J. Hinze, J. Mol. Spec. **56**, 93 (1975).

196. P.R. Bunker and R.E. Moss, Mol. Phys. **33**, 417 (1977).

197. J.A. Coxon and P.G. Hajigeorgiou, J. Mol. Spec. **150**, 1 (1991).

198. J.A. Coxon and P.G. Hajigeorgiou, J. Mol. Spec. **142**, 254 (1990).

199. J.A. Coxon and P.G. Hajigeorgiou, J. Mol. Spec. **139**, 84 (1990).

200. J.A. Coxon and P.G. Hajigeorgiou, Can. J. Phys. **70**, 40 (1992).

201. J.A. Coxon and P.G. Hajigeorgiou, Chem. Phys. **167**, 327 (1992).

202. H.G. Hedderich, M. Dulick and P.F. Bernath, J. Chem. Phys. **99**, 8363 (1993).

203. J.F. Ogilvie, Proc. Royal. Soc. A **378**, 287 (1981).

204. J.W. Cooley, Math Computation. **15**, 363 (1961).

205. J.K. Cashion, J. Chem. Phys. **39**, 1872 (1963).

206. J.M. Blatt, J. Comp. Phys. **1**, 382 (1967).

207. J.I. Musher, Am. J. Phys. **34**, 267 (1966).

208. K. Huber and G. Herzberg, *Constants of Diatomic Molecules* (Van Nostrand Reinhold, New York, 1979).

209. D. Welti and R.F. Barrow, Nature **168**, 161 (1951).

210. R.F. Barrow, J.A.T. Jacquest and E.W. Thompson, Proc. Phys. Soc. A **67**, 528 (1954).

211. R.F. Barrow, D.V. Glaser and P.B. Zeeman, Proc. Phys. Soc. A. **68**, 962 (1955).

212. V.P.N. Nampoori, M.N. Kamalasanan and M.M. Patel, J. Phys. B: Atom. Molec. Phys. **8**, 2841 (1975).

213. F.J. Lovas and T. Törring, Z. Naturforsch **24A**, 634 (1969).

214. J. Hoeft, F.J. Lovas, E. Tiemann and T. Törring, Z. Naturforsch **25A**, 1029 (1970).

215. R.H. Hammerle, R. Van Ausdal and J.C. Zorn, J. Chem. Phys. **57**, 4068 (1972).

216. K.D. Hensel and M.C.L. Gerry, J. Chem. Soc., Faraday Trans. **93**, 1053 (1997).

217. T. Karkanis, M. Dulick, Z. Morbi, J.B. White, and P.F. Bernath, Can. J. Phys. **72**, 1213 (1994).

218. H. Uehara, K. Horiai, T. Mitami and H. Suguro, Chem. Phys. Lett. **162**, 137 (1989).

219. Y. Ozaki, K. Horiai, K. Nakagawa and H. Uehera, J. Mol. Spec. **158**, 363 (1993).

220. Z. Morbi and P.F. Bernath, J. Mol. Spec. **175**, 210 (1995).

221. *Transition Metal Hydrides*, edited by A. Dedieu (VCH Publishers, New York, 1992).

222. Ö. Hauge, Astron. Astrophys. **10**, 73 (1971).

223. R.S. Wojslaw and B.F. Perry, Astrophys. J. Suppl. **31**, 75 (1976).

224. R. Frerichs, Z. Phys. **20**, 170 (1923).

225. U. Ringström, Ark. Phys. **32**, 211 (1966).

226. U. Ringström, Can. J. Phys. **98**, 2291 (1968).

227. B. Grundström, Z. Phys. **98**, 128 (1935).

228. A. Sharma, Opt. Comm. **77**, 303 (1990).

229. T. Heimer, Naturwissenschaften **23**, 372 (1935).

230. M.A. Jeppesen, Phys. Rev. **50**, 445 (1936).

231. W.T.M.L Fernando, L.C. O'Brien and P.F. Bernath, J. Mol. Spec. **139**, 461 (1990).

232. R.S. Ram, P.F. Bernath and J.W. Brault, J. Mol. Spec. **113**, 451 (1985).

233. R.S. Ram, P.F. Bernath and J.W. Brault, J. Mol. Spec. **113**, 269 (1985).

234. S.P. Beaton and K.M. Evenson, J. Mol. Spec. **142**, 336 (1990).

235. T.D. Varberg and K.M. Evenson, J. Mol. Spec. **164**, 531 (1994).

236. E. Bengtsson and E. Olsson, Z. Phys. **72**, 163 (1931).

237. H. Birk and H. Jones, Chem. Phys. Lett. **161**, 27 (1989).

238. R–D. Urban, H. Birk, P. Polomsky and H. Jones, J. Chem. Phys. **94**, 2523 (1991).

239. T. Zeigler, J.G. Snijders and E.J. Baerends, J. Chem. Phys **74**, 1271 (1981).

240. U. Ringström, Nature **198**, 981 (1963).

241. U. Ringström, Ark. Fys. **27**, 227 (1964).

242. S.K. Lee, F. Charron and P.F. Bernath (unpublished).

243. P. Pyykkö, Chem. Rev. **88**, 563 (1988).

244. P. Schwerdtfeger, M. Dolg, W.H. Eugen Schwarz, G.A. Bowmaker and P.D.W. Boyd, J. Chem. Phys. **91**, 1762 (1989).

245. P.J. Hay, W.R. Wadt, L.R. Kahn and F.W. Bobrowicz, J. Chem. Phys. **69**, 984 (1978).

246. G.J. Jansen and B.A. Hess, Chem. Phys. Lett. **160**, 507 (1989).

247. Y.S. Lee and A.D. McLean, J. Chem. Phys. **79**, 3392 (1982).

248. G. Jansen and B.A. Hess, Z. Phys. D **91**, 1762 (1989).

249. A. Pizlo, G. Jansen, B.A Hess and W. von Neissen, J. Chem. Phys **98**, 3945 (1993).

250. A. J. Sadlej, J. Chem. Phys. **95**, 2614 (1991).

251. V. Kello, A.J. Sadlej, J. Chem. Phys. **95**, 8248 (1991).

Appendix A

Line Positions of $CaNH_2$

Table A.1: Observed line positions of the $\tilde{C}^2A_1$—$\tilde{X}^2A_1$ Transition of $CaNH_2$. The observed - calculated are in column labelled Δ multiplied by 10^{-5}.

J″	Observed	Δ	J″	Observed	Δ
		$K'_a = 0 \longleftarrow K''_a = 0$			
	P_1 Branch			R_1 Branch	
0.5	17374.02970	-69	0.5	17376.44308	89
1.5	17373.47758	110	1.5	17377.08210	-243
2.5	17372.93398	175	2.5	17377.73627	-15
3.5	17372.40047	293	3.5	17378.39410	-365
4.5	17371.87715	482	4.5	17379.06999	159
5.5	17371.35887	240	5.5	17379.74826	6
6.5	17370.85221	240	6.5	17380.43476	-221
7.5	17370.35010	-206	7.5	17381.13827	377
8.5	17369.86048	-286	8.5	17381.84197	142
9.5	17369.37973	-337	9.5	17382.55360	-127
10.5	17368.91099	-20	10.5	17383.27635	-81
11.5	17368.44860	126	11.5	17384.00580	-131
12.5	17367.99426	303	12.5	17384.74627	188
13.5	17367.55042	788	13.5	17385.50174	1311
			14.5	17386.23937	-7
			15.5	17386.98361	-1279
			17.5	17388.52483	-215
			19.5	17390.07394	-261
	P_2 Branch			R_2 Branch	
0.5	17374.57371	56	0.5	17375.74734	-301
1.5	17373.97084	128	1.5	17376.34619	312
2.5	17373.37287	-280	2.5	17376.94518	-25
3.5	17372.79147	5	3.5	17377.56230	496
4.5	17372.21508	-168	4.5	17378.17497	-372
5.5	17371.65641	485	5.5	17378.80697	-239
6.5	17371.09763	191	6.5	17379.44830	-88
7.5	17370.54469	-439	7.5	17380.09059	-739
8.5	17370.01716	570	8.5	17380.74952	-601
9.5	17369.48098	-168	9.5	17381.42452	290
10.5	17368.95622	-624	10.5	17382.10117	520

Table A.1: Observed line positions of the $\tilde{C}^2A_1$—$\tilde{X}^2A_1$ Transition of $CaNH_2$. The observed - calculated are in column labelled Δ multiplied by 10^{-5}.

J″	Observed	Δ	J″	Observed	Δ
11.5	17368.44860	-199	11.5	17382.77393	-437
12.5	17367.94408	-270	12.5	17383.47264	434
13.5	17367.44875	-197	13.5	17384.17323	760
			14.5	17384.86894	-99
			15.5	17385.58920	840
			17.5	17387.01941	-118
			18.5	17387.73995	-865
			19.5	17388.48564	427

$K'_a = 1 \longleftarrow K''_a = 1$

	P^1_{11} Branch			R^1_{11} Branch	
1.5	17373.92113	-54	1.5	17376.26300	-114
2.5	17373.31766	214	2.5	17376.85547	-77
3.5	17372.73118	256	3.5	17377.46381	213
4.5	17372.15870	367	4.5	17378.07693	-159
5.5	17371.59262	-22	5.5	17378.70499	-90
6.5	17371.04054	-64	6.5	17379.34174	-152
7.5	17370.49975	21	7.5	17379.98862	-162
8.5	17369.96572	-179	8.5	17380.65224	573
9.5	17369.44346	-133	9.5	17381.31499	324
10.5	17368.92735	-370	10.5	17381.98297	-269
11.5	17368.42661	61	11.5	17382.66798	8
12.5	17367.93142	212			
13.5	17367.44875	813			
14.5	17366.97519	1558			
	P^0_{11} Branch			R^0_{11} Branch	
1.5	17373.90095	79	1.5	17376.27011	-173
2.5	17373.28580	41	2.5	17376.86896	-87
3.5	17372.69096	172	3.5	17377.47941	-123
4.5	17372.10945	355	4.5	17378.10142	-96
5.5	17371.53425	78	5.5	17378.73332	-84
6.5	17370.97069	-40	6.5	17379.36950	-597
7.5	17370.41787	-37	7.5	17380.02339	-252
8.5	17369.87367	-88	8.5	17380.68547	30
9.5	17369.34337	369			
	Q^1_{11} Branch			Q^0_{11} Branch	
1.5	17375.10168	45	4.5	17375.09063	-118
2.5	17375.08201	-257	5.5	17375.11845	199
4.5	17375.10735	424	6.5	17375.14724	-392
5.5	17375.12531	-513	7.5	17375.19948	409
6.5	17375.16460	-369	13.5	17375.63942	-221
12.5	17375.59407	74	14.5	17375.74731	419
17.5	17376.16848	-139			
	P^0_{22} Branch			R^0_{22} Branch	
1.5	17373.30921	1302	1.5	17376.94528	231
2.5	17372.76943	517	2.5	17377.60543	20
3.5	17372.23583	355	3.5	17378.26967	-350

Table A.1: Observed line positions of the $\tilde{C}^2A_1$—$\tilde{X}^2A_1$ Transition of $CaNH_2$. The observed - calculated are in column labelled Δ multiplied by 10^{-5}.

J″	Observed	Δ	J″	Observed	Δ
4.5	17371.69824	-778	4.5	17378.95855	1009
5.5	17371.20033	1319			
6.5	17370.67174	-450			
	P^1_{22} Branch			R^1_{22} Branch	
1.5	17373.31831	-658	1.5	17376.91368	-1347
2.5	17372.79171	-969	2.5	17377.57759	-574
			3.5	17378.26268	1698
			4.5	17378.91924	332
	Q^0_{22} Branch			Q^1_{22} Branch	
1.5	17375.08822	124	1.5	17375.09317	18
4.5	17375.28848	34	3.5	17375.22511	-56
8.5	17375.64878	-53	4.5	17375.30217	367

Appendix B

Line Positions of InF

All values of the lines in the following appendix is given in cm^{-1} units. The value in parenthesis are the 1σ uncertainty from the parametrized potential fit and signify the uncertainty in the last quoted digits.

Table B.1: Observed line positions of ^{115}InF in cm^{-1}.

Assignment	Observed	Assignment	Observed
	$1 \longrightarrow 0$ Band		
R(5)	533.10737(401)	R(6)	533.59988(5)
R(7)	534.09358(107)	R(8)	534.58178(38)
R(9)	535.06668(18)	R(10)	535.54868(88)
R(11)	536.02579(48)	R(12)	536.50039(140)
R(13)	536.96959(74)	R(14)	537.43189(-300)
R(15)	537.89689(-21)	R(16)	538.35520(-28)
R(17)	538.81100(99)	R(18)	539.26200(131)
R(19)	539.70640(-112)	R(20)	540.15340(291)
R(21)	540.59130(171)	R(22)	541.02491(8)
R(23)	541.45631(13)	R(24)	541.88311(-54)
R(25)	542.30731(8)	R(26)	542.72591(-100)
R(27)	543.13752(-517)	R(28)	543.55392(-64)
R(29)	543.96322(70)	R(30)	544.36632(-23)
R(31)	544.76632(-34)	R(32)	545.15992(-292)
R(33)	545.55412(-96)	R(34)	545.94483(145)
R(35)	546.32813(41)	R(36)	546.70833(22)
R(37)	547.08483(30)	R(38)	547.45923(224)
R(39)	547.82623(76)	R(40)	548.19214(216)
R(41)	548.55014(-35)	R(42)	548.90724(23)
R(43)	549.26004(51)	R(44)	549.60854(49)
R(45)	549.95234(-22)	R(46)	550.29194(-111)
R(47)	550.62795(-157)	R(48)	550.96165(-31)
R(49)	551.28625(-412)	R(50)	551.61165(-308)
R(51)	551.93545(41)	R(52)	552.25115(-16)
R(53)	552.56315(-36)	R(54)	552.87205(40)
R(55)	553.17616(43)	R(56)	553.47796(224)
R(57)	553.77196(33)	R(58)	554.06396(51)

Table B.1: Observed line positions of ^{115}InF in cm^{-1}.

Assignment	Observed	Assignment	Observed
R(59)	554.35136(19)	R(60)	554.63546(66)
R(61)	554.91386(-45)	R(62)	555.18826(-145)
R(63)	555.46207(106)	R(64)	555.73087(271)
R(65)	555.99057(-62)	R(66)	556.25507(499)
R(67)	556.50517(35)	R(68)	556.75507(-35)
R(69)	557.00377(191)	R(70)	557.24477(63)
R(71)	557.48227(2)	R(72)	557.71677(58)
R(73)	557.94758(163)	R(74)	558.17178(26)
R(75)	558.39548(258)	R(76)	558.61008(-0)
R(77)	558.82288(-18)	R(78)	559.03208(25)
R(79)	559.23628(-10)	R(80)	559.43708(37)
R(81)	559.63328(48)	R(82)	559.82508(41)
R(83)	560.01248(19)	R(84)	560.19498(-69)
R(85)	560.37559(79)	R(86)	560.55039(72)
R(87)	560.71979(-48)	R(88)	560.88719(59)
R(89)	561.04949(84)	R(90)	561.20639(-3)
R(91)	561.35969(-20)	R(92)	561.50899(-9)
R(93)	561.65409(13)	R(94)	561.79499(46)
R(95)	561.93039(-40)	R(96)	562.06309(36)
R(97)	562.19029(-5)	R(98)	562.31379(17)
R(99)	562.43239(-17)	R(100)	562.54749(33)
R(101)	562.65789(49)	R(102)	562.76370(40)
R(103)	562.86640(158)	R(104)	562.96270(72)
R(105)	563.05390(-86)	R(106)	563.14300(-16)
R(107)	563.22710(-7)	R(108)	563.30600(-78)
R(109)	563.38130(-70)	R(110)	563.45360(79)
R(111)	563.51990(69)	R(112)	563.58150(32)
R(113)	563.63910(36)	R(114)	563.69280(94)
R(115)	563.74110(56)	R(116)	563.78480(2)
R(117)	563.82560(103)	R(118)	563.86060(69)
R(119)	563.89090(12)	R(120)	563.91690(-28)
R(121)	563.93720(-191)	R(122)	563.95540(-116)
R(123)	563.96840(-112)	R(128)	563.97950(1270)
R(131)	563.90850(-242)	R(132)	563.88340(19)
R(133)	563.85290(194)	R(134)	563.81730(315)
R(135)	563.77360(83)	R(136)	563.72760(77)
R(137)	563.67670(39)	R(138)	563.62060(-61)
R(139)	563.56180(27)	R(140)	563.49870(145)
R(141)	563.42700(-137)	R(142)	563.35630(142)
R(143)	563.27720(42)	R(144)	563.19450(44)
R(145)	563.10720(49)	R(146)	563.01610(136)
R(147)	562.91940(128)	R(148)	562.81830(144)
R(149)	562.71159(65)	R(150)	562.60089(52)
R(151)	562.48569(55)	R(152)	562.36689(165)
R(153)	562.24129(63)	R(154)	562.11259(119)
R(155)	561.97709(-36)	R(156)	561.83829(-51)
R(157)	561.69569(24)	R(158)	561.54669(-71)
R(159)	561.39409(-53)	P(152)	411.31588(191)

Table B.1: Observed line positions of ^{115}InF in cm^{-1}.

Assignment	Observed	Assignment	Observed
P(149)	414.34939(-63)	P(147)	416.35790(-238)
P(146)	417.36300(176)	P(145)	418.35841(-103)
P(144)	419.35451(-32)	P(143)	420.34621(-122)
P(141)	422.32422(-1)	P(140)	423.30833(-7)
P(139)	424.29003(29)	P(138)	425.26893(68)
P(137)	426.24394(2)	P(136)	427.21614(-59)
P(135)	428.18485(-185)	P(134)	429.15465(85)
P(133)	430.11915(113)	P(131)	432.03696(-88)
P(130)	432.99427(85)	P(129)	433.94537(-72)
P(128)	434.90187(602)	P(127)	435.84258(-12)
P(126)	436.78548(-115)	P(125)	437.72729(-34)
P(124)	438.66639(70)	P(123)	439.60189(108)
P(122)	440.53220(-78)	P(121)	441.46190(-29)
P(120)	442.38830(-14)	P(119)	443.31071(-101)
P(118)	444.23481(280)	P(117)	445.14882(-51)
P(116)	446.06342(-22)	P(115)	446.97582(86)
P(114)	447.88203(-125)	P(113)	448.78893(36)
P(112)	449.69003(-82)	P(111)	450.58984(-26)
P(110)	451.48654(23)	P(109)	452.38004(55)
P(108)	453.27075(113)	P(107)	454.15555(-113)
P(106)	455.04026(-44)	P(105)	455.92226(62)
P(104)	456.79906(-44)	P(103)	457.67417(-11)
P(102)	458.54657(60)	P(101)	459.41537(80)
P(100)	460.28068(62)	P(99)	461.14298(53)
P(98)	462.00128(-43)	P(97)	462.85959(173)
P(96)	463.71029(-58)	P(95)	464.55879(-195)
P(94)	465.40780(31)	P(93)	466.25100(-7)
P(92)	467.09190(41)	P(91)	467.92971(95)
P(90)	468.76261(-24)	P(89)	469.59472(94)
P(88)	470.42372(221)	P(87)	471.24672(67)
P(86)	472.06743(2)	P(85)	472.88533(-22)
P(84)	473.70083(34)	P(83)	474.51304(83)
P(82)	475.32124(53)	P(81)	476.12644(47)
P(80)	476.92855(53)	P(79)	477.72725(45)
P(78)	478.52285(51)	P(77)	479.31475(12)
P(76)	480.10516(150)	P(75)	480.89056(114)
P(74)	481.67256(66)	P(73)	482.45067(-44)
P(72)	483.22707(5)	P(71)	484.00017(53)
P(70)	484.76938(41)	P(69)	485.53548(50)
P(68)	486.29818(50)	P(67)	487.05819(112)
P(66)	487.81259(-53)	P(65)	488.56679(95)
P(64)	489.31690(167)	P(63)	490.06030(-97)
P(62)	490.80450(54)	P(61)	491.54310(-19)
P(60)	492.28071(145)	P(59)	493.01091(-95)
P(58)	493.73961(-146)	P(57)	494.46732(40)
P(56)	495.19012(76)	P(55)	495.90912(71)
P(54)	496.62323(-84)	P(53)	497.33663(32)
P(52)	498.04333(-181)	P(51)	498.75053(-1)

Table B.1: Observed line positions of ^{115}InF in cm^{-1}.

Assignment	Observed	Assignment	Observed
P(50)	499.45174(-79)	P(49)	500.15084(-23)
P(48)	500.84664(46)	P(47)	501.53775(-10)
P(46)	502.22655(49)	P(45)	502.91105(24)
P(44)	503.59235(26)	P(43)	504.27216(224)
P(42)	504.94596(170)	P(41)	505.61556(45)
P(40)	506.28366(118)	P(39)	506.94767(131)
P(38)	507.60377(-295)	P(37)	508.26277(-82)
P(36)	508.91478(-216)	P(35)	509.56628(-49)
P(34)	510.21328(21)	P(33)	510.85568(-16)
P(32)	511.49519(11)	P(31)	512.13029(-47)
P(30)	512.76289(-1)	P(29)	513.38779(-368)
P(28)	514.01090(-560)	P(27)	514.63710(-84)
P(26)	515.25580(-1)	P(25)	515.87120(110)
P(24)	516.48161(80)	P(23)	517.08811(20)
P(22)	517.69171(29)	P(21)	518.29291(159)
P(20)	518.88772(10)	P(19)	519.47952(-77)
P(18)	520.07282(349)	P(17)	520.65522(47)
P(16)	521.23693(40)	P(15)	521.81543(76)
P(14)	522.38953(37)	P(13)	522.96113(114)
P(12)	523.52724(7)	P(11)	524.09064(-3)
P(10)	524.65074(24)	P(9)	525.20594(-72)
P(8)	525.75864(-48)	P(7)	526.30885(94)
P(6)	526.85395(96)	P(5)	527.39445(9)
P(4)	527.93245(42)	P(3)	528.46596(-3)
P(2)	528.99556(-66)		
	$2 \longrightarrow 1$ Band		
R(0)	525.28264(-920)	R(1)	525.80084(-259)
R(2)	526.30885(-244)	R(3)	526.81405(-135)
R(4)	527.31595(18)	R(5)	527.81265(27)
R(6)	528.30515(-9)	R(7)	528.79566(131)
R(8)	529.27926(-43)	R(9)	529.76136(12)
R(10)	530.23916(14)	R(11)	530.71276(-25)
R(12)	531.18257(-65)	R(13)	531.64947(-15)
R(14)	532.11027(-194)	R(15)	532.57077(-23)
R(16)	533.02607(10)	R(17)	533.47618(-95)
R(18)	533.92448(4)	R(19)	534.36408(-385)
R(20)	534.80838(81)	R(21)	535.24278(-59)
R(22)	535.67438(-93)	R(23)	536.10029(-312)
R(24)	536.52619(-144)	R(25)	536.94959(161)
R(26)	537.36479(33)	R(27)	537.77729(24)
R(28)	538.18919(344)	R(29)	538.59130(73)
R(30)	538.98880(-268)	R(31)	539.38830(-19)
R(32)	539.78170(12)	R(34)	540.55480(-120)
R(35)	540.93581(-151)	R(36)	541.31531(60)
R(37)	541.68781(-33)	R(38)	542.05571(-192)
R(39)	542.42421(104)	R(40)	542.78941(467)
R(41)	543.14762(526)	R(42)	543.49842(242)

Table B.1: Observed line positions of ^{115}InF in cm^{-1}.

Assignment	Observed	Assignment	Observed
R(43)	543.84112(-454)	R(44)	544.18622(-511)
R(45)	544.53182(-119)	R(46)	544.87032(-38)
R(47)	545.20452(14)	R(48)	545.53312(-94)
R(49)	545.85553(-420)	R(50)	546.18183(46)
R(51)	546.49863(-35)	R(52)	546.81343(86)
R(53)	547.12243(32)	R(54)	547.42773(12)
R(55)	547.72913(7)	R(56)	548.02614(-32)
R(57)	548.32034(55)	R(58)	548.61224(319)
R(59)	548.89924(501)	R(60)	549.17544(10)
R(61)	549.45194(-42)	R(62)	549.72654(126)
R(63)	549.99404(-7)	R(64)	550.25884(1)
R(65)	550.52045(99)	R(66)	550.77835(240)
R(67)	551.02885(52)	R(68)	551.27625(-32)
R(69)	551.52005(-63)	R(70)	551.76085(20)
R(71)	551.99685(38)	R(72)	552.22755(-59)
R(73)	552.45435(-130)	R(74)	552.67825(-74)
R(75)	552.89875(58)	R(76)	553.11386(68)
R(77)	553.32376(-23)	R(78)	553.53106(44)
R(79)	553.73386(81)	R(80)	553.93196(69)
R(81)	554.12606(76)	R(82)	554.31526(16)
R(83)	554.50066(-3)	R(84)	554.68186(-20)
R(85)	554.85906(-13)	R(86)	555.03176(-32)
R(87)	555.19836(-237)	R(88)	555.36586(72)
R(89)	555.52567(38)	R(90)	555.68157(39)
R(91)	555.83227(-52)	R(92)	555.98097(84)
R(93)	556.12227(-92)	R(94)	556.26277(80)
R(95)	556.39737(92)	R(96)	556.52727(63)
R(97)	556.65347(95)	R(98)	556.77397(-12)
R(99)	556.89117(-17)	R(100)	557.00377(-51)
R(101)	557.11367(79)	R(102)	557.21827(112)
R(103)	557.31727(20)	R(104)	557.41317(52)
R(105)	557.50347(-41)	R(106)	557.59097(23)
R(107)	557.67407(82)	R(108)	557.75277(139)
R(109)	557.82537(24)	R(110)	557.89538(87)
R(111)	557.95958(10)	R(112)	558.02138(131)
R(113)	558.07638(13)	R(114)	558.12818(16)
R(115)	558.17178(-359)	R(116)	558.21848(17)
R(117)	558.25748(66)	R(118)	558.29188(98)
R(119)	558.32188(135)	R(120)	558.34888(316)
R(122)	558.37278(-997)	R(131)	558.29858(-2909)
R(131)	558.33008(241)	R(133)	558.26598(10)
R(134)	558.22818(-1)	R(135)	558.18508(-88)
R(136)	558.13828(-90)	R(137)	558.08798(13)
R(138)	558.03188(-9)	R(141)	557.83828(136)
R(144)	557.60127(65)	R(145)	557.51447(181)
P(149)	409.85747(-512)	P(147)	411.85248(-670)
P(145)	413.84399(-77)	P(144)	414.83399(59)
P(143)	415.81990(62)	P(142)	416.80350(113)

Table B.1: Observed line positions of ^{115}InF in cm^{-1}.

Assignment	Observed	Assignment	Observed
P(141)	417.78020(-247)	P(140)	418.76011(-7)
P(139)	419.73401(-88)	P(138)	420.70622(-57)
P(137)	421.67552(-34)	P(136)	422.64212(1)
P(135)	423.60523(-30)	P(134)	424.56613(3)
P(133)	425.52374(-10)	P(132)	426.48004(133)
P(131)	427.43024(-48)	P(130)	428.37925(-61)
P(129)	429.32665(53)	P(128)	430.26945(-5)
P(127)	431.20806(-193)	P(126)	432.14776(18)
P(125)	433.08297(70)	P(124)	434.01447(44)
P(123)	434.94137(-151)	P(122)	435.86928(48)
P(121)	436.79248(70)	P(120)	437.71309(126)
P(119)	438.62899(7)	P(118)	439.54329(24)
P(117)	440.45420(-3)	P(116)	441.36220(-23)
P(115)	442.27010(245)	P(114)	443.16861(-129)
P(113)	444.06911(-4)	P(112)	444.96561(22)
P(111)	445.85802(-62)	P(110)	446.74852(-35)
P(109)	447.63553(-56)	P(108)	448.52013(-14)
P(107)	449.40343(201)	P(106)	450.28104(150)
P(105)	451.15454(-6)	P(104)	452.02724(63)
P(103)	452.89525(-31)	P(102)	453.76105(-39)
P(101)	454.62405(-19)	P(100)	455.48416(18)
P(99)	456.34056(-5)	P(98)	457.19826(411)
P(97)	458.04427(-33)	P(96)	458.89187(-6)
P(95)	459.73617(3)	P(94)	460.57708(-16)
P(93)	461.41538(18)	P(92)	462.24969(-35)
P(91)	463.08149(-24)	P(90)	463.91209(182)
P(89)	464.73500(-66)	P(88)	465.55730(-58)
P(87)	466.37320(-373)	P(86)	467.19261(-21)
P(85)	468.00581(30)	P(84)	468.81541(39)
P(83)	469.62272(138)	P(82)	470.42372(-72)
P(81)	471.22412(-23)	P(80)	472.01983(-121)
P(79)	472.81523(72)	P(78)	473.60463(-11)
P(77)	474.39243(68)	P(76)	475.17654(102)
P(75)	475.95594(-9)	P(74)	476.73294(-35)
P(73)	477.50695(-35)	P(72)	478.27955(151)
P(71)	479.04655(105)	P(70)	479.81036(67)
P(69)	480.57076(18)	P(68)	481.32766(-52)
P(67)	482.08357(107)	P(66)	482.83287(-63)
P(65)	483.58137(19)	P(64)	484.32578(22)
P(63)	485.06698(38)	P(62)	485.80398(-33)
P(61)	486.53768(-101)	P(60)	487.26849(-124)
P(59)	487.99899(158)	P(58)	488.72129(-45)
P(57)	489.44280(9)	P(56)	490.16140(110)
P(55)	490.87700(248)	P(54)	491.58580(44)
P(53)	492.29251(-30)	P(52)	492.99671(-16)
P(51)	493.69701(-51)	P(50)	494.39682(204)
P(49)	495.08912(51)	P(48)	495.77942(39)
P(47)	496.46722(121)	P(46)	497.14753(-205)

Table B.1: Observed line positions of ^{115}InF in cm^{-1}.

Assignment	Observed	Assignment	Observed
P(45)	497.82913(-57)	P(44)	498.50623(-14)
P(43)	499.17914(-47)	P(42)	499.84854(-83)
P(41)	500.51364(-204)	P(40)	501.17804(-47)
P(39)	501.83615(-173)	P(38)	502.49445(69)
P(37)	503.14535(-80)	P(36)	503.79285(-220)
P(35)	504.44016(-29)	P(34)	505.08136(-98)
P(33)	505.71906(-166)	P(32)	506.34967(-591)
P(31)	506.98597(-95)	P(30)	507.61467(-5)
P(29)	508.23887(-11)	P(28)	508.85938(-33)
P(27)	509.47578(-111)	P(26)	510.08858(-192)
P(25)	510.70218(162)	P(24)	511.30929(224)
P(23)	511.91009(12)	P(22)	512.50989(59)
P(21)	513.10469(-35)	P(20)	513.69599(-121)
P(19)	514.28570(-6)	P(18)	514.86970(-101)
P(17)	515.45260(55)	P(16)	516.02980(3)
P(15)	516.60371(-17)	P(14)	517.17491(55)
P(13)	517.74071(-48)	P(12)	518.30551(112)
P(11)	518.86412(18)	P(10)	519.42132(148)
P(9)	519.97172(-35)	P(8)	520.52112(48)
P(7)	521.06493(-62)	P(6)	521.60663(-14)
P(5)	522.14213(-218)		
	$3 \longrightarrow 2$ Band		
R(0)	520.07282(385)	R(1)	520.58102(415)
R(2)	521.08163(56)	R(3)	521.57753(-401)
R(4)	522.07663(-166)	R(5)	522.57063(-67)
R(6)	523.06013(-45)	R(7)	523.54474(-139)
R(8)	524.02724(-68)	R(9)	524.50544(-52)
R(10)	524.97934(-89)	R(11)	525.45074(0)
R(12)	525.91674(-73)	R(13)	526.38065(21)
R(14)	526.84005(44)	R(15)	527.29545(45)
R(16)	527.74615(-43)	R(17)	528.19225(-212)
R(18)	528.63746(-89)	R(19)	529.07766(-85)
R(20)	529.51476(-9)	R(21)	529.94776(39)
R(22)	530.37536(-69)	R(23)	530.80156(67)
R(24)	531.22057(-133)	R(25)	531.63767(-138)
R(26)	532.05287(53)	R(27)	532.46197(20)
R(28)	532.86727(-6)	R(29)	533.26937(36)
R(30)	533.66648(-35)	R(31)	534.06098(23)
R(32)	534.45008(-69)	R(33)	534.83338(-352)
R(34)	535.21838(-75)	R(35)	535.59798(54)
R(36)	535.97249(64)	R(37)	536.34209(-23)
R(38)	536.71049(162)	R(39)	537.07039(-109)
R(40)	537.43189(173)	R(41)	537.78569(81)
R(42)	538.13509(-57)	R(43)	538.48240(-8)
R(44)	538.82630(97)	R(45)	539.16350(-72)
R(46)	539.49890(-22)	R(47)	539.83230(225)
R(49)	540.48220(228)	R(50)	540.79751(-136)

Table B.1: Observed line positions of ^{115}InF in cm^{-1}.

Assignment	Observed	Assignment	Observed
R(51)	541.11481(100)	R(52)	541.42401(-72)
R(53)	541.73061(-103)	R(54)	542.03541(89)
R(55)	542.33311(-26)	R(56)	542.62811(-8)
R(57)	542.91861(-35)	R(58)	543.20552(-18)
R(59)	543.48982(145)	R(60)	543.76772(74)
R(61)	544.04072(-80)	R(62)	544.31262(62)
R(63)	544.57912(72)	R(64)	544.84002(-69)
R(65)	545.09892(-1)	R(66)	545.35262(-44)
R(67)	545.60403(94)	R(68)	545.84433(-468)
R(69)	546.09113(32)	R(70)	546.32813(-37)
R(71)	546.56163(-42)	R(72)	546.78863(-285)
R(73)	547.01673(-4)	R(74)	547.23843(52)
R(75)	547.45283(-208)	R(76)	547.66803(29)
R(77)	547.87563(-79)	R(78)	548.08034(-60)
R(80)	548.47694(-49)	R(81)	548.66884(-56)
R(82)	548.85524(-194)	R(83)	549.04124(48)
R(84)	549.21984(-29)	R(85)	549.39514(-16)
R(86)	549.56624(-1)	R(87)	549.73414(117)
R(88)	549.89594(47)	R(89)	550.05414(40)
R(90)	550.20834(57)	R(91)	550.35804(50)
R(92)	550.50365(57)	R(93)	550.64455(20)
R(94)	550.77835(-301)	R(95)	550.91445(36)
R(96)	551.04435(180)	R(97)	551.16665(-7)
R(99)	551.40215(-6)	R(100)	551.52005(655)
R(101)	551.61905(-143)	R(102)	551.72405(89)
R(103)	551.82175(24)	R(104)	551.91635(81)
R(105)	552.00615(91)	R(106)	552.09045(-15)
R(107)	552.17195(33)	R(108)	552.25115(286)
R(109)	552.32135(74)	R(110)	552.38885(29)
R(111)	552.45435(220)	R(112)	552.51165(29)
R(113)	552.57025(405)	R(114)	552.61665(0)
R(115)	552.66325(55)	R(116)	552.70435(-1)
R(117)	552.73975(-187)	R(118)	552.77285(-161)
R(119)	552.80115(-174)	R(120)	552.82545(-145)
R(121)	552.84535(-113)	R(122)	552.86225(63)
R(135)	552.65365(146)	R(136)	552.60465(4)
R(137)	552.55465(214)	R(138)	552.49595(8)
R(139)	552.43925(456)	R(140)	552.36995(98)
R(141)	552.29955(85)	R(143)	552.14475(28)
R(144)	552.06085(34)	R(145)	551.97365(168)
R(146)	551.87985(100)	R(147)	551.78265(151)
R(149)	551.57315(122)	R(150)	551.46385(344)
P(145)	409.37707(-19)	P(143)	411.33868(35)
P(141)	413.28729(-109)	P(140)	414.25879(-45)
P(139)	415.22879(147)	P(138)	416.19320(57)
P(137)	417.15560(47)	P(136)	418.11541(57)
P(135)	419.07281(108)	P(134)	420.02601(21)
P(133)	420.97802(97)	P(132)	421.92562(16)

Table B.1: Observed line positions of ^{115}InF in cm^{-1}.

Assignment	Observed	Assignment	Observed
P(131)	422.87152(48)	P(130)	423.81393(16)
P(129)	424.75353(-11)	P(128)	425.69004(-62)
P(127)	426.62574(94)	P(126)	427.56024(417)
P(125)	428.48525(79)	P(124)	429.40695(-299)
P(123)	430.33146(-108)	P(122)	431.25166(-57)
P(121)	432.16946(46)	P(120)	433.08297(11)
P(119)	433.99347(-32)	P(118)	434.90187(9)
P(117)	435.80698(14)	P(116)	436.70978(84)
P(115)	437.60818(10)	P(114)	438.50489(62)
P(113)	439.39729(-20)	P(112)	440.28870(97)
P(111)	441.17680(182)	P(110)	442.05820(-104)
P(109)	442.94141(89)	P(108)	443.81851(-27)
P(107)	444.69321(-81)	P(106)	445.56582(-44)
P(105)	446.43742(195)	P(104)	447.30172(8)
P(103)	448.16673(195)	P(102)	449.02533(47)
P(101)	449.88273(83)	P(100)	450.73654(66)
P(99)	451.58724(46)	P(98)	452.43475(12)
P(97)	453.27905(-33)	P(96)	454.12045(-59)
P(95)	454.95976(14)	P(94)	455.79556(47)
P(93)	456.62716(-29)	P(92)	457.45667(-4)
P(91)	458.28307(23)	P(90)	459.10627(43)
P(89)	459.92558(-14)	P(88)	460.74208(-36)
P(87)	461.55828(226)	P(86)	462.36509(-136)
P(85)	463.17389(18)	P(84)	463.97799(18)
P(83)	464.77860(-14)	P(81)	466.37320(217)
P(80)	467.16381(141)	P(79)	467.95061(5)
P(78)	468.73571(20)	P(77)	469.51621(-104)
P(76)	470.29522(-55)	P(75)	471.07092(-15)
P(74)	471.84372(60)	P(73)	472.60953(-242)
P(72)	473.37723(-29)	P(71)	474.13983(-1)
P(70)	474.89844(-47)	P(69)	475.65454(-17)
P(68)	476.40724(1)	P(67)	477.15635(-13)
P(66)	477.90225(-19)	P(65)	478.64575(64)
P(64)	479.38456(7)	P(63)	480.12116(61)
P(62)	480.85276(-55)	P(61)	481.58246(-29)
P(60)	482.30627(-260)	P(59)	483.03147(-19)
P(58)	483.75017(-94)	P(57)	484.46718(-4)
P(56)	485.17938(-60)	P(55)	485.88888(-51)
P(54)	486.59458(-85)	P(53)	487.29819(8)
P(52)	487.99899(158)	P(51)	488.69469(136)
P(50)	489.38750(163)	P(49)	490.07480(-21)
P(48)	490.76060(-15)	P(47)	491.44370(61)
P(46)	492.12311(109)	P(45)	492.79761(8)
P(43)	494.14122(295)	P(42)	494.80352(4)
P(41)	495.46442(-83)	P(40)	496.12432(75)
P(39)	496.77883(38)	P(38)	497.43033(48)
P(37)	498.07903(124)	P(36)	498.72263(38)
P(35)	499.36244(-81)	P(34)	500.00054(-20)

Table B.1: Observed line positions of ^{115}InF in cm^{-1}.

Assignment	Observed	Assignment	Observed
P(33)	500.63414(-60)	P(32)	501.26574(49)
P(31)	501.89175(-51)	P(30)	502.51595(21)
P(29)	503.13505(-67)	P(28)	503.75265(49)
P(27)	504.36426(-83)	P(26)	504.97366(-81)
P(25)	505.57996(-35)	P(24)	506.18226(-34)
P(23)	506.78057(-78)	P(22)	507.37657(4)
P(21)	507.96787(-27)	P(20)	508.55877(259)
P(19)	509.14078(14)	P(18)	509.72268(116)
P(17)	510.29818(-62)	P(16)	510.87298(49)
P(15)	511.44209(-49)	P(14)	512.00899(-7)
P(13)	512.57109(-83)	P(12)	513.12979(-136)
P(11)	513.68719(43)	P(10)	514.23910(35)
P(9)	514.78760(51)	P(8)	515.33140(-38)
P(7)	515.87120(-162)	P(6)	516.40681(-340)
P(5)	516.94251(-142)	P(4)	517.47641(243)
P(3)	518.00031(-4)	P(2)	518.51531(-773)
	$4 \longrightarrow 3$ Band		
R(1)	515.39900(-77)	R(2)	515.90120(88)
R(3)	516.39571(-147)	R(4)	516.89081(49)
R(5)	517.37921(-55)	R(6)	517.86251(-297)
R(7)	518.34761(14)	R(8)	518.82712(137)
R(9)	519.29972(-57)	R(10)	519.77112(4)
R(11)	520.24032(220)	R(12)	520.70122(-20)
R(13)	521.15993(-103)	R(14)	521.61683(10)
R(15)	522.06683(-190)	R(16)	522.51643(-53)
R(17)	522.96113(-27)	R(18)	523.40093(-112)
R(19)	523.83914(22)	R(20)	524.27104(-94)
R(21)	524.69814(-309)	R(22)	525.12624(-43)
R(23)	525.54724(-105)	R(24)	525.96665(56)
R(25)	526.38065(59)	R(26)	526.78965(-54)
R(27)	527.19565(-82)	R(28)	527.59845(-46)
R(29)	527.99625(-125)	R(30)	528.39175(-47)
R(31)	528.78496(187)	R(32)	529.16936(-71)
R(33)	529.55296(-22)	R(34)	529.93136(-104)
R(35)	530.30746(-27)	R(36)	530.67886(-31)
R(37)	531.04887(216)	R(38)	531.40827(-207)
R(39)	531.77007(2)	R(40)	532.12567(-17)
R(41)	532.47727(-44)	R(42)	532.82637(72)
R(43)	533.16977(13)	R(44)	533.50918(-52)
R(45)	533.84568(-13)	R(46)	534.17738(-58)
R(47)	534.50538(-76)	R(48)	534.83338(302)
R(49)	535.14848(-212)	R(50)	535.46718(31)
R(51)	535.77899(-17)	R(52)	536.08739(-6)
R(53)	536.39289(115)	R(54)	536.69199(-3)
R(55)	536.98779(-51)	R(56)	537.28119(63)
R(57)	537.56839(-41)	R(58)	537.85269(-33)
R(59)	538.13509(189)	R(60)	538.40960(25)

Table B.1: Observed line positions of ^{115}InF in cm^{-1}.

Assignment	Observed	Assignment	Observed
R(61)	538.68190(45)	R(62)	538.95160(211)
R(63)	539.21240(-108)	R(64)	539.47450(109)
R(65)	539.72920(-6)	R(66)	539.97870(-234)
R(67)	540.22910(36)	R(68)	540.47100(-136)
R(69)	540.71281(92)	R(70)	540.94501(-230)
R(71)	541.17921(58)	R(72)	541.40451(-133)
R(73)	541.62711(-182)	R(74)	541.84771(-18)
R(75)	542.06321(48)	R(76)	542.27321(-23)
R(77)	542.48021(21)	R(78)	542.68231(-11)
R(79)	542.88081(13)	R(80)	543.07481(2)
R(81)	543.26402(-72)	R(82)	543.45072(21)
R(83)	543.63202(-9)	R(84)	543.80862(-90)
R(85)	543.98222(-52)	R(86)	544.15102(-75)
R(87)	544.31262(-398)	R(88)	544.47842(120)
R(89)	544.63392(29)	R(90)	544.78532(-51)
R(91)	544.93392(12)	R(92)	545.07792(39)
R(93)	545.21972(268)	R(94)	545.35262(33)
R(95)	545.48282(-49)	R(96)	545.60403(-604)
R(97)	545.73273(16)	R(98)	545.85553(473)
R(99)	545.96563(87)	R(100)	546.07483(39)
R(101)	546.18183(200)	R(102)	546.28143(49)
R(103)	546.37773(-2)	R(104)	546.47073(48)
R(105)	546.56163(318)	R(106)	546.64173(-61)
R(107)	546.72253(63)	R(108)	546.79613(-101)
R(109)	546.86883(79)	R(110)	546.93553(92)
R(111)	546.99733(50)	R(112)	547.05443(-27)
R(113)	547.10713(-109)	R(114)	547.15803(66)
R(115)	547.20133(-82)	R(116)	547.23843(-413)
R(117)	547.27893(34)	R(118)	547.31053(30)
R(119)	547.33763(15)	R(120)	547.36163(130)
R(121)	547.37983(106)	R(130)	547.34293(-263)
R(131)	547.31943(-19)	R(132)	547.28883(-38)
R(133)	547.25393(-40)	R(134)	547.21513(18)
R(135)	547.17163(54)	R(136)	547.12243(-31)
R(137)	547.07133(145)	R(138)	547.01673(422)
R(139)	546.95153(90)	P(139)	410.76718(54)
P(138)	411.72538(2)	P(137)	412.68308(177)
P(136)	413.63509(60)	P(135)	414.58499(12)
P(134)	415.53369(123)	P(133)	416.47770(45)
P(132)	417.42140(218)	P(131)	418.35841(2)
P(130)	419.29511(39)	P(129)	420.22791(-32)
P(128)	421.15802(-88)	P(127)	422.08552(-119)
P(126)	423.01203(35)	P(125)	423.93393(15)
P(124)	424.85323(22)	P(123)	425.76824(-114)
P(122)	426.68294(9)	P(121)	427.59424(81)
P(120)	428.50105(-7)	P(119)	429.40695(105)
P(118)	430.30755(-22)	P(117)	431.20806(133)
P(116)	432.10496(221)	P(115)	432.99427(-157)

Table B.1: Observed line positions of ^{115}InF in cm^{-1}.

Assignment	Observed	Assignment	Observed
P(114)	433.88637(38)	P(113)	434.77417(98)
P(112)	435.65818(74)	P(111)	436.53898(26)
P(110)	437.41658(-46)	P(109)	438.29239(1)
P(108)	439.16489(15)	P(107)	440.03459(49)
P(106)	440.90140(92)	P(105)	441.76490(106)
P(104)	442.62371(-49)	P(103)	443.48191(37)
P(102)	444.33541(-44)	P(101)	445.18712(-2)
P(100)	446.03532(-6)	P(99)	446.88152(95)
P(98)	447.72213(-59)	P(97)	448.56163(-18)
P(96)	449.39853(70)	P(95)	450.22964(-114)
P(94)	451.05934(-131)	P(93)	451.88744(1)
P(92)	452.71165(53)	P(91)	453.53195(24)
P(90)	454.34865(-54)	P(89)	455.16406(49)
P(88)	455.97496(14)	P(87)	456.78346(52)
P(86)	457.58827(34)	P(85)	458.39027(49)
P(84)	459.19147(299)	P(83)	459.98368(-36)
P(82)	460.77628(-15)	P(81)	461.56778(213)
P(80)	462.35099(-72)	P(79)	463.13459(1)
P(78)	463.91209(-217)	P(77)	464.68760(-316)
P(76)	465.46320(-85)	P(75)	466.23410(-4)
P(74)	467.00230(129)	P(73)	467.76421(-46)
P(72)	468.52491(-19)	P(71)	469.28141(-89)
P(70)	470.03592(-34)	P(69)	470.78692(-5)
P(68)	471.53432(-11)	P(67)	472.27863(-2)
P(66)	473.01933(-25)	P(65)	473.75753(28)
P(64)	474.49134(-31)	P(63)	475.22284(8)
P(62)	475.94944(-113)	P(61)	476.67824(315)
P(60)	477.39615(-17)	P(59)	478.11325(-98)
P(58)	478.82915(33)	(57)	479.53926(-84)
P(56)	480.24836(32)	P(55)	480.95206(-58)
P(54)	481.65446(55)	P(53)	482.35177(-7)
P(52)	483.04567(-73)	P(51)	483.74087(327)
P(50)	484.42588(43)	P(49)	485.10998(7)
P(48)	485.78998(-102)	P(47)	486.46898(28)
P(46)	487.14189(-113)	P(45)	487.81259(-134)
P(44)	488.48059(-84)	P(43)	489.14479(-74)
P(42)	489.80530(-91)	P(41)	490.46380(33)
P(40)	491.11710(-20)	P(39)	491.76761(-9)
P(38)	492.41451(-14)	P(37)	493.05801(-14)
P(36)	493.69701(-118)	P(35)	494.33412(-67)
P(34)	494.96782(-9)	P(33)	495.59642(-114)
P(32)	496.22282(-91)	P(31)	496.84693(51)
P(30)	497.46533(-28)	P(29)	498.07903(-228)
P(28)	498.69293(-57)	P(27)	499.30164(-55)
P(26)	499.90654(-82)	P(25)	500.51364(464)
P(24)	501.10574(-138)	P(23)	501.70135(-36)
P(22)	502.29345(70)	P(21)	502.87955(-69)
P(20)	503.46365(-53)	P(19)	504.04416(-42)

Table B.1: Observed line positions of ^{115}InF in cm^{-1}.

Assignment	Observed	Assignment	Observed
P(18)	504.62116(-23)	P(17)	505.19356(-108)
P(16)	505.76356(-75)	P(15)	506.33106(66)
P(14)	506.89217(-73)	P(13)	507.45137(-43)
P(12)	508.00617(-93)	P(11)	508.55877(-3)
P(10)	509.10688(-0)	P(9)	509.65048(-86)
P(8)	510.19178(-40)	P(7)	510.72688(-250)
P(6)	511.26189(-106)	P(5)	511.79299(12)
P(4)	512.31869(-45)	P(3)	512.84129(-46)
	$5 \longrightarrow 4$ Band		
R(0)	509.77198(82)	R(2)	510.76758(-111)
R(3)	511.26189(-6)	R(4)	511.74719(-432)
R(5)	512.23639(-100)	R(6)	512.71969(12)
R(7)	513.19799(-5)	R(8)	513.67239(-42)
R(9)	514.14330(-57)	R(10)	514.61120(-0)
R(11)	515.07440(-41)	R(12)	515.53240(-228)
R(13)	515.99060(-21)	R(14)	516.44221(-100)
R(15)	516.89081(-104)	R(16)	517.33781(108)
R(17)	517.77741(-44)	R(18)	518.21471(-49)
R(19)	518.64822(-57)	R(20)	519.07752(-106)
R(21)	519.50602(143)	R(22)	519.92542(-139)
R(23)	520.34502(-21)	R(24)	520.75942(-42)
R(25)	521.17033(-33)	R(26)	521.57753(-11)
R(27)	521.98043(-38)	R(28)	522.38033(18)
R(29)	522.77573(8)	R(31)	523.55504(-10)
R(32)	523.93894(-16)	R(33)	524.31704(-217)
R(35)	525.06754(-29)	R(36)	525.43604(-28)
R(37)	525.80084(-10)	R(38)	526.16015(-152)
R(39)	526.51705(-146)	R(40)	526.87175(31)
R(41)	527.22035(-12)	R(42)	527.56395(-164)
R(43)	527.90585(-94)	R(44)	528.24425(19)
R(45)	528.58086(344)	R(46)	528.90766(83)
R(47)	529.23356(126)	R(48)	529.55296(-86)
R(50)	530.18526(26)	R(51)	530.49416(-49)
R(52)	530.80156(123)	R(53)	531.10347(144)
R(54)	531.39847(-128)	R(55)	531.69327(-21)
R(56)	531.98207(-114)	R(57)	532.26877(-17)
R(58)	532.55087(21)	R(59)	532.82637(-201)
R(60)	533.10037(-170)	R(61)	533.37198(23)
R(62)	533.63658(-81)	R(63)	533.89988(89)
R(64)	534.15678(22)	R(65)	534.40978(-29)
R(66)	534.65918(-35)	R(67)	534.90708(215)
R(69)	535.38358(6)	R(70)	535.61758(87)
R(71)	535.84349(-233)	R(72)	536.07049(-34)
R(73)	536.29209(34)	R(74)	536.50779(-77)
R(75)	536.72099(-28)	R(76)	536.93229(243)
R(77)	537.13459(25)	R(78)	537.33489(20)
R(79)	537.53099(9)	R(80)	537.72269(-30)

Table B.1: Observed line positions of ^{115}InF in cm^{-1}.

Assignment	Observed	Assignment	Observed
R(81)	537.90909(-183)	R(82)	538.09559(88)
R(83)	538.27390(-46)	R(84)	538.45010(27)
R(85)	538.62140(26)	R(86)	538.78890(63)
R(87)	538.95160(37)	R(88)	539.11040(40)
R(89)	539.26200(-258)	R(90)	539.41450(-47)
R(91)	539.56180(65)	R(92)	539.70640(328)
R(93)	539.84040(-48)	R(95)	540.10400(27)
R(96)	540.22910(29)	R(97)	540.35000(35)
R(99)	540.57930(70)	R(100)	540.68691(21)
R(101)	540.78861(-192)	R(102)	540.89011(2)
R(103)	540.98721(183)	R(104)	541.07721(82)
R(105)	541.16321(10)	R(106)	541.24541(-14)
R(107)	541.32601(233)	R(109)	541.46631(-72)
R(110)	541.53191(-32)	R(111)	541.59281(-30)
R(112)	541.65021(54)	R(113)	541.70111(-78)
R(115)	541.79201(-130)	R(116)	541.82971(-278)
R(117)	541.86621(-111)	R(118)	541.89681(-97)
R(119)	541.92391(3)	R(120)	541.94521(-38)
R(121)	541.96281(-12)	R(122)	541.97671(83)
P(136)	409.20097(34)	P(134)	411.08498(-68)
P(133)	412.02668(267)	P(132)	412.95968(12)
P(131)	413.89329(95)	P(130)	414.82399(169)
P(129)	415.75000(54)	P(128)	416.67310(-69)
P(127)	417.59470(-60)	P(126)	418.51451(52)
P(125)	419.43001(18)	P(124)	420.34621(339)
P(123)	421.25262(-35)	P(122)	422.16062(37)
P(121)	423.06453(-14)	P(120)	423.96593(-28)
P(119)	424.86293(-193)	P(118)	425.76094(31)
P(117)	426.65384(35)	P(116)	427.54484(139)
P(115)	428.43105(54)	P(114)	429.31505(41)
P(113)	430.19665(81)	P(112)	431.07486(73)
P(111)	431.94896(-50)	P(110)	432.82377(192)
P(109)	433.69037(-91)	P(108)	434.55777(2)
P(107)	435.42238(112)	P(106)	436.28138(-40)
P(105)	437.13858(-74)	P(104)	437.99339(-50)
P(103)	438.84559(15)	P(102)	439.69339(-61)
P(101)	440.54060(105)	P(100)	441.38130(-78)
P(99)	442.22150(-8)	P(98)	443.05661(-145)
P(97)	443.89081(-68)	P(96)	444.72231(43)
P(95)	445.54842(-81)	P(94)	446.37282(-69)
P(93)	447.19482(9)	P(92)	448.01223(-65)
P(91)	448.82783(-11)	P(90)	449.63863(-129)
P(89)	450.44754(-128)	P(88)	451.25414(-47)
P(87)	452.06064(335)	P(86)	452.85805(118)
P(85)	453.65315(-17)	P(84)	454.44675(10)
P(83)	455.23756(71)	P(82)	456.02376(-15)
P(81)	456.80636(-146)	P(80)	457.58827(-31)
P(79)	458.36627(9)	P(78)	459.14067(5)

Table B.1: Observed line positions of ^{115}InF in cm^{-1}.

Assignment	Observed	Assignment	Observed
P(77)	459.91138(-51)	P(76)	460.67968(-29)
P(75)	461.44488(2)	P(74)	462.20639(-19)
P(73)	462.96399(-109)	P(72)	463.71899(-140)
P(71)	464.47209(-39)	P(70)	465.22100(-36)
P(69)	465.96620(-81)	P(68)	466.70950(8)
P(67)	467.44861(-0)	P(66)	468.18431(-24)
P(65)	468.91731(8)	P(64)	469.64882(215)
P(63)	470.37232(-51)	P(62)	471.09442(-131)
P(61)	471.81532(-3)	P(60)	472.53223(54)
P(59)	473.24443(-31)	P(58)	473.95433(-16)
P(57)	474.66114(19)	P(56)	475.36404(-5)
P(55)	476.06414(22)	P(54)	476.76094(51)
P(53)	477.45335(-26)	P(52)	478.14275(-71)
P(51)	478.82915(-81)	P(50)	479.51166(-147)
P(49)	480.19316(22)	P(48)	480.86976(37)
P(47)	481.54266(19)	P(46)	482.21207(-12)
P(45)	482.87827(-25)	P(44)	483.54127(-20)
P(43)	484.19917(-186)	P(42)	484.85858(138)
P(41)	485.51008(12)	P(40)	486.15958(27)
P(39)	486.80539(14)	P(38)	487.44789(12)
P(37)	488.08699(14)	P(36)	488.72129(-121)
P(35)	489.35400(-72)	P(34)	489.98340(-9)
P(33)	490.60860(-20)	P(32)	491.23040(-25)
P(31)	491.84691(-214)	P(30)	492.46301(-95)
P(29)	493.07561(21)	P(28)	493.68291(-44)
P(27)	494.28852(69)	P(26)	494.88862(-18)
P(25)	495.48552(-74)	P(24)	496.07952(-70)
P(23)	496.67063(-5)	P(22)	497.25663(-97)
P(21)	497.83993(-107)	P(20)	498.42063(-23)
P(19)	498.99484(-235)	P(18)	499.56994(-3)
P(17)	500.13784(-136)	P(16)	500.70504(17)
P(15)	501.26574(-124)	P(14)	501.82395(-158)
P(13)	502.37875(-174)	P(12)	502.93195(8)
P(11)	503.47935(-32)	P(10)	504.02376(-12)
P(9)	504.56496(48)	P(8)	505.10216(69)
P(7)	505.63416(-69)	P(6)	506.16596(135)
P(4)	507.21337(10)	P(3)	507.73187(-27)
P(1)	508.76027(131)		
	$6 \longrightarrow 5$ Band		
R(1)	505.19356(108)	R(4)	506.65927(-222)
R(5)	507.14387(5)	R(7)	508.09757(12)
R(8)	508.56907(33)	R(9)	509.03438(-196)
R(11)	509.95948(-94)	R(12)	510.41658(-31)
R(14)	511.31839(-29)	R(15)	511.76369(-28)
R(16)	512.20529(-25)	R(17)	512.64339(4)
R(18)	513.07649(-93)	R(19)	513.50759(-15)
R(20)	513.93440(10)	R(21)	514.35690(-19)

Table B.1: Observed line positions of ^{115}InF in cm^{-1}.

Assignment	Observed	Assignment	Observed
R(22)	514.77490(-121)	R(23)	515.19180(45)
R(24)	515.60260(-20)	R(25)	516.01140(94)
R(26)	516.41381(-53)	R(27)	516.81471(30)
R(28)	517.21171(105)	R(29)	517.60311(0)
R(30)	517.99161(-12)	R(31)	518.37611(-42)
R(32)	518.75592(-158)	R(33)	519.13532(69)
R(34)	519.50602(-189)	R(35)	519.87772(37)
R(36)	520.24032(-261)	R(37)	520.60482(18)
R(38)	520.96342(93)	R(39)	521.31593(-55)
R(40)	521.66633(-25)	R(41)	522.01273(-6)
R(42)	522.35483(-28)	R(43)	522.69343(-10)
R(44)	523.02823(18)	R(45)	523.35813(-54)
R(46)	523.68474(-63)	R(47)	524.00884(69)
R(48)	524.32474(-226)	R(49)	524.64274(82)
R(50)	524.95264(-26)	R(51)	525.25954(-39)
R(52)	525.56344(42)	R(53)	525.86204(-10)
R(54)	526.16015(283)	R(55)	526.44845(-7)
R(56)	526.73565(-9)	R(57)	527.01905(6)
R(59)	527.57335(-16)	R(60)	527.84515(37)
R(61)	528.11185(-20)	R(62)	528.37435(-96)
R(63)	528.63746(290)	R(64)	528.89156(178)
R(65)	529.14086(-11)	R(66)	529.38826(13)
R(67)	529.63096(-29)	R(68)	529.87066(33)
R(69)	530.10546(10)	R(70)	530.33596(-37)
R(71)	530.56386(63)	R(72)	530.78716(109)
R(73)	531.00527(42)	R(74)	531.22057(104)
R(75)	531.43097(84)	R(76)	531.63767(103)
R(77)	531.83887(-18)	R(78)	532.03697(-38)
R(79)	532.23167(12)	R(80)	532.42207(44)
R(81)	532.60597(-162)	R(82)	532.78887(-55)
R(83)	532.96707(-5)	R(84)	533.14077(10)
R(85)	533.31067(58)	R(86)	533.47618(82)
R(87)	533.63658(11)	R(88)	533.79328(-13)
R(89)	533.94648(30)	R(90)	534.09358(-120)
R(91)	534.23908(-12)	R(92)	534.37538(-406)
R(93)	534.51508(-40)	R(94)	534.64678(-54)
R(95)	534.77488(-8)	R(96)	534.89948(109)
R(97)	535.01798(38)	R(98)	535.13448(189)
R(99)	535.24278(-57)	R(100)	535.35018(30)
R(101)	535.45708(491)	R(102)	535.54868(-153)
R(103)	535.64428(27)	R(104)	535.73328(-26)
R(105)	535.81849(-33)	R(106)	535.90069(86)
R(108)	536.04839(-61)	R(110)	536.18049(-54)
R(111)	536.24119(60)	R(115)	536.43609(33)
R(116)	536.47329(-45)	R(118)	536.53649(-21)
R(119)	536.56179(12)	P(130)	410.39867(261)
P(129)	411.31588(-101)	P(128)	412.23508(16)
P(127)	413.15118(103)	P(126)	414.06179(-78)

Table B.1: Observed line positions of ^{115}InF in cm^{-1}.

Assignment	Observed	Assignment	Observed
P(125)	414.97219(2)	P(124)	415.87810(-86)
P(123)	416.78320(30)	P(122)	417.68420(19)
P(121)	418.58271(43)	P(120)	419.47671(-98)
P(119)	420.37271(248)	P(118)	421.25962(-30)
P(117)	422.14732(60)	P(116)	423.03163(98)
P(115)	423.90953(-215)	P(114)	424.79143(162)
P(113)	425.66854(349)	P(112)	426.53764(27)
P(111)	427.40594(-83)	P(110)	428.27365(40)
P(109)	429.13805(126)	P(108)	429.99735(-4)
P(107)	430.85486(-20)	P(106)	431.70986(10)
P(105)	432.56126(-24)	P(104)	433.40957(-71)
P(103)	434.25527(-81)	P(102)	435.09847(-43)
P(101)	435.93798(-76)	P(100)	436.77518(-39)
P(99)	437.60818(-122)	P(98)	438.44039(16)
P(97)	439.26729(-74)	P(96)	440.09389(108)
P(95)	440.91370(-87)	P(94)	441.73340(12)
P(93)	442.54760(-135)	P(92)	443.36161(3)
P(91)	444.17111(-3)	P(90)	444.97771(7)
P(89)	445.78152(44)	P(88)	446.58142(-0)
P(87)	447.37852(-17)	P(86)	448.17293(6)
P(85)	448.96253(-141)	P(84)	449.75183(-8)
P(83)	450.53654(-24)	P(82)	451.31944(92)
P(81)	452.09754(40)	P(80)	452.87275(12)
P(79)	453.64525(27)	P(78)	454.41405(-13)
P(77)	455.18056(32)	P(76)	455.94276(-37)
P(75)	456.70306(20)	P(74)	457.45667(-275)
P(73)	458.21327(47)	P(72)	458.96287(-12)
P(71)	459.70987(-13)	P(70)	460.45378(-3)
P(69)	461.19418(-23)	P(68)	461.93218(38)
P(67)	462.66589(-10)	P(66)	463.39689(-5)
P(65)	464.12199(-267)	P(64)	464.84900(-15)
P(63)	465.57360(320)	P(62)	466.28840(1)
P(61)	467.00230(-82)	P(60)	467.71431(-30)
P(59)	468.42271(-10)	P(58)	469.12751(-23)
P(57)	469.83062(122)	P(56)	470.52652(-124)
P(55)	471.22412(129)	P(54)	471.91442(-18)
P(53)	472.59773(-534)	P(52)	473.28763(-58)
P(51)	473.96893(-111)	P(50)	474.64744(-111)
P(49)	475.32124(-247)	P(48)	475.99604(50)
P(47)	476.66294(-109)	P(46)	477.32935(18)
P(45)	477.99015(-79)	P(44)	478.64575(-360)
P(43)	479.30525(86)	P(42)	479.95586(-21)
P(41)	480.60436(1)	P(40)	481.24826(-98)
P(39)	481.89047(-27)	P(38)	482.52837(-47)
P(37)	483.16337(-16)	P(36)	483.79527(47)
P(35)	484.42588(322)	P(34)	485.04738(29)
P(33)	485.66848(40)	P(32)	486.28548(-16)
P(31)	486.89979(4)	P(30)	487.50999(-42)

Table B.1: Observed line positions of ^{115}InF in cm^{-1}.

Assignment	Observed	Assignment	Observed
P(29)	488.11769(8)	P(28)	488.72129(-6)
P(27)	489.31690(-473)	P(26)	489.91670(-172)
P(25)	490.51140(-32)	P(24)	491.10100(-54)
P(23)	491.68661(-127)	P(22)	492.27251(180)
P(21)	492.85011(9)	P(20)	493.42581(-2)
P(19)	494.00031(219)	P(18)	494.56602(-87)
P(17)	495.13212(0)	P(16)	495.69402(21)
P(15)	496.25262(66)	P(14)	496.80773(116)
P(13)	497.35673(-88)	P(12)	497.90483(-26)
P(11)	498.44933(32)	P(10)	498.99484(548)
P(9)	499.52504(-108)	P(8)	500.05974(45)
P(7)	500.58724(-163)	P(5)	501.63685(-39)
P(4)	502.15315(-286)	P(3)	502.67015(-101)
P(1)	503.69045(-15)		
	$7 \longrightarrow 6$ Band		
R(2)	500.65144(15)	R(3)	501.13724(-16)
R(5)	502.09815(-54)	R(6)	502.57325(-59)
R(7)	503.04635(101)	R(9)	503.97776(44)
R(10)	504.44016(237)	R(11)	504.89506(48)
R(12)	505.34726(-41)	R(13)	505.79556(-150)
R(14)	506.23816(-458)	R(15)	506.68447(-26)
R(16)	507.12357(58)	R(17)	507.55927(174)
R(18)	507.98957(123)	R(19)	508.41527(-14)
R(20)	508.83978(102)	R(21)	509.25778(-57)
R(22)	509.67358(-60)	R(23)	510.08858(232)
R(24)	510.49388(-69)	R(25)	510.89888(-24)
R(26)	511.30259(269)	R(27)	511.69689(1)
R(28)	512.09029(21)	R(29)	512.47959(11)
R(30)	512.86519(10)	R(31)	513.24749(60)
R(32)	513.62689(202)	R(33)	514.00020(115)
R(34)	514.36970(30)	R(35)	514.73550(-42)
R(36)	515.09810(-50)	R(38)	515.81100(-143)
R(39)	516.16381(22)	R(40)	516.51121(34)
R(41)	516.85351(-77)	R(42)	517.19391(8)
R(43)	517.52941(-9)	R(44)	517.86251(122)
R(45)	518.18911(-8)	R(46)	518.51531(212)
R(47)	518.83622(291)	R(48)	519.14952(1)
R(49)	519.46012(-167)	R(50)	519.77112(96)
R(51)	520.07282(-179)	R(52)	520.37182(-330)
R(53)	520.67192(22)	R(54)	520.96342(-92)
R(55)	521.25223(-81)	R(56)	521.53823(45)
R(57)	521.81543(-313)	R(58)	522.09593(55)
R(59)	522.36863(41)	R(60)	522.63683(-26)
R(61)	522.90203(6)	R(62)	523.16383(96)
R(63)	523.41873(-104)	R(64)	523.67264(-4)
R(65)	523.92214(56)	R(66)	524.16604(-42)
R(67)	524.40744(11)	R(69)	524.87644(-55)

Table B.1: Observed line positions of ^{115}InF in cm^{-1}.

Assignment	Observed	Assignment	Observed
R(70)	525.10774(198)	R(71)	525.33124(74)
R(72)	525.55364(245)	R(73)	525.76784(1)
R(74)	525.98015(-27)	R(75)	526.18925(32)
R(76)	526.39415(78)	R(77)	526.59315(-59)
R(78)	526.78965(-37)	R(79)	526.98295(73)
R(80)	527.16945(-87)	R(81)	527.35405(-27)
R(82)	527.53365(-57)	R(83)	527.71005(5)
R(84)	527.88235(68)	R(85)	528.04865(-56)
R(86)	528.21255(-8)	R(87)	528.37435(244)
R(88)	528.52766(61)	R(89)	528.67836(31)
R(90)	528.82386(-103)	R(91)	528.96686(-71)
R(92)	529.10536(-72)	R(94)	529.37096(36)
R(95)	529.49706(48)	R(96)	529.61886(48)
R(97)	529.73686(87)	R(98)	529.84886(-54)
R(100)	530.06446(87)	R(101)	530.16406(-30)
R(102)	530.26156(65)	R(103)	530.35356(33)
R(104)	530.44196(65)	R(105)	530.52446(-70)
R(106)	530.60436(-40)	R(107)	530.67886(-124)
R(108)	530.75196(77)	R(109)	530.82026(225)
R(110)	530.88017(-41)	R(111)	530.93877(-8)
R(112)	530.99407(122)	R(113)	531.04227(-29)
R(114)	531.09037(240)	R(115)	531.12877(-32)
R(116)	531.16597(8)	R(117)	531.19937(98)
R(119)	531.24997(-46)	R(120)	531.27057(61)
R(122)	531.29797(196)	P(126)	409.65777(77)
P(125)	410.55877(-161)	P(124)	411.46038(-59)
P(123)	412.35758(-116)	P(122)	413.25409(38)
P(121)	414.14499(-85)	P(120)	415.03329(-185)
P(119)	415.91960(-201)	P(118)	416.80350(-172)
P(117)	417.68420(-178)	P(116)	418.56441(52)
P(115)	419.43931(39)	P(114)	420.31151(43)
P(113)	421.18102(66)	P(112)	422.04772(97)
P(111)	422.91052(28)	P(110)	423.76993(-90)
P(109)	424.62813(-38)	P(108)	425.48294(-33)
P(107)	426.33474(-36)	P(106)	427.18194(-206)
P(105)	428.02955(-42)	P(104)	428.87265(-33)
P(103)	429.71235(-69)	P(102)	430.55006(-9)
P(101)	431.38476(48)	P(100)	432.21586(42)
P(99)	433.04457(94)	P(98)	433.86827(-55)
P(97)	434.69017(-84)	P(96)	435.50968(-53)
P(95)	436.32648(9)	P(94)	437.13858(-98)
P(93)	437.95029(58)	P(92)	438.75709(27)
P(91)	439.56109(19)	P(90)	440.36210(15)
P(89)	441.16100(107)	P(88)	441.95510(24)
P(87)	442.74761(88)	P(86)	443.53601(49)
P(85)	444.32011(-113)	P(84)	445.10352(-36)
P(83)	445.88352(10)	P(82)	446.65912(-75)
P(81)	447.43322(1)	P(80)	448.20353(8)

Table B.1: Observed line positions of ^{115}InF in cm^{-1}.

Assignment	Observed	Assignment	Observed
P(78)	449.73513(58)	P(77)	450.49614(72)
P(76)	451.25414(100)	P(75)	452.00724(-48)
P(74)	452.76045(130)	P(73)	453.50765(23)
P(72)	454.25685(432)	P(71)	454.99736(289)
P(70)	455.73296(-27)	P(69)	456.46846(-34)
P(68)	457.19826(-293)	P(67)	457.92997(-42)
P(66)	458.65687(50)	P(65)	459.37867(-48)
P(64)	460.09958(86)	P(63)	460.81548(42)
P(62)	461.52758(-58)	P(61)	462.23729(-76)
P(60)	462.94499(31)	P(59)	463.64799(-7)
P(58)	464.34859(40)	P(57)	465.04550(43)
P(56)	465.73880(14)	P(55)	466.42960(61)
P(54)	467.11561(-43)	P(53)	467.79911(-69)
P(52)	468.48011(-16)	P(51)	469.15791(48)
P(50)	469.83062(-68)	P(49)	470.50182(-3)
P(48)	471.16902(-6)	P(47)	471.83382(84)
P(46)	472.49303(-53)	P(45)	473.15043(-37)
P(44)	473.80443(-26)	P(43)	474.45193(-330)
P(42)	475.10224(-19)	P(41)	475.74574(-51)
P(40)	476.38644(-26)	P(39)	477.02425(46)
P(38)	477.65755(7)	P(37)	478.28985(206)
P(36)	478.91425(-46)	P(35)	479.53926(103)
P(34)	480.15856(22)	P(33)	480.77516(13)
P(32)	481.38706(-125)	P(31)	481.99817(0)
P(30)	482.60497(38)	P(29)	483.20767(10)
P(28)	483.80457(-254)	P(27)	484.40208(-112)
P(26)	484.99478(-106)	P(25)	485.58508(7)
P(24)	486.17218(147)	P(23)	486.75339(45)
P(22)	487.33179(10)	P(21)	487.90719(24)
P(20)	488.48059(188)	P(19)	489.04569(-129)
P(18)	489.61090(-85)	P(17)	490.17380(80)
P(16)	490.72980(-94)	P(15)	491.28460(-35)
P(14)	491.83831(267)	P(13)	492.38191(-87)
P(12)	492.92631(-7)	P(11)	493.46791(147)
P(9)	494.53592(3)	P(8)	495.06742(216)
P(7)	495.59642(536)	P(6)	496.11832(503)
P(5)	496.63333(140)	P(4)	497.14753(55)
P(3)	497.65773(-70)	P(2)	498.16553(-75)
	$8 \longrightarrow 7$ Band		
R(3)	496.14852(118)	R(4)	496.62323(-306)
R(5)	497.10173(13)	R(6)	497.57313(-15)
R(7)	498.04333(202)	R(8)	498.50623(54)
R(9)	498.96983(341)	R(10)	499.42294(-56)
R(11)	499.87744(54)	R(12)	500.32614(-49)
R(13)	500.77284(16)	R(14)	501.21574(69)
R(15)	501.65195(-179)	R(16)	502.08825(-47)
R(17)	502.51595(-404)	R(18)	502.94715(-41)

Table B.1: Observed line positions of ^{115}InF in cm^{-1}.

Assignment	Observed	Assignment	Observed
R(19)	503.37155(13)	R(20)	503.79285(130)
R(21)	504.20876(79)	R(22)	504.62116(51)
R(23)	505.02946(-13)	R(24)	505.43476(-2)
R(25)	505.83666(43)	R(26)	506.23816(424)
R(27)	506.62647(-138)	R(28)	507.01727(-74)
R(29)	507.40407(-33)	R(30)	507.78697(-4)
R(31)	508.16547(-36)	R(33)	508.91478(268)
R(34)	509.27858(-95)	R(35)	509.64088(-227)
R(36)	510.00198(-98)	R(37)	510.35768(-127)
R(38)	510.71208(98)	R(39)	511.05908(-35)
R(40)	511.40279(-114)	R(41)	511.74719(262)
R(42)	512.08319(182)	R(43)	512.41429(-1)
R(44)	512.74339(1)	R(45)	513.06799(-60)
R(47)	513.70620(-118)	R(48)	514.01950(-145)
R(49)	514.32880(-183)	R(50)	514.63710(69)
R(51)	514.93950(121)	R(52)	515.23360(-266)
R(53)	515.53240(209)	R(54)	515.81860(-185)
R(55)	516.10630(-35)	R(56)	516.38821(-73)
R(57)	516.66671(-56)	R(58)	516.94251(84)
R(59)	517.21171(-40)	R(60)	517.47641(-219)
R(61)	517.74071(-41)	R(62)	518.00031(63)
R(63)	518.25441(15)	R(64)	518.50621(134)
R(65)	518.75592(442)	R(66)	518.99522(109)
R(67)	519.23292(16)	R(68)	519.46662(-77)
R(69)	519.69822(20)	R(70)	519.92542(80)
R(71)	520.14712(-9)	R(72)	520.37182(604)
R(73)	520.58102(71)	R(74)	520.79152(72)
R(75)	520.99832(107)	R(76)	521.19943(-23)
R(77)	521.39813(12)	R(78)	521.59153(-76)
R(79)	521.78173(-78)	R(80)	521.96803(-63)
R(81)	522.14973(-99)	R(82)	522.32953(82)
R(83)	522.50363(103)	R(84)	522.67633(393)
R(85)	522.83853(43)	R(86)	523.00033(65)
R(88)	523.30993(-59)	R(89)	523.45983(8)
R(90)	523.60834(348)	R(91)	523.74574(-8)
R(92)	523.88304(39)	R(94)	524.14404(20)
R(96)	524.38874(35)	R(98)	524.61694(68)
R(99)	524.72474(82)	R(100)	524.82714(-25)
R(101)	524.92714(47)	R(102)	525.02214(39)
R(106)	525.35984(-10)	R(108)	525.50504(136)
R(110)	525.62964(-81)	R(111)	525.68724(-22)
R(112)	525.74244(223)	P(119)	411.51868(14)
P(117)	413.27399(313)	P(115)	415.01169(-13)
P(114)	415.87810(7)	P(113)	416.74170(33)
P(112)	417.60190(5)	P(111)	418.45901(-44)
P(110)	419.31481(64)	P(109)	420.16531(-69)
P(108)	421.01452(-42)	P(107)	421.86102(5)
P(106)	422.70432(24)	P(105)	423.54463(34)

Table B.1: Observed line positions of ^{115}InF in cm^{-1}.

Assignment	Observed	Assignment	Observed
P(104)	424.38183(26)	P(103)	425.21873(282)
P(102)	426.04804(72)	P(101)	426.87594(16)
P(100)	427.70174(46)	P(99)	428.52405(22)
P(98)	429.34345(4)	P(97)	430.16045(44)
P(96)	430.97346(-19)	P(95)	431.78406(-22)
P(94)	432.59246(54)	P(93)	433.39497(-160)
P(92)	434.19757(-63)	P(91)	434.99347(-334)
P(90)	435.79098(-143)	P(89)	436.58678(181)
P(88)	437.37288(-162)	P(87)	438.16029(-70)
P(86)	438.94489(46)	P(85)	439.72129(-352)
P(84)	440.49970(-243)	P(83)	441.27650(12)
P(82)	442.04700(-55)	P(81)	442.81581(17)
P(80)	443.58071(7)	P(79)	444.34371(117)
P(78)	445.10352(218)	P(77)	445.85802(99)
P(76)	446.60982(22)	P(75)	447.35972(68)
P(74)	448.10463(-74)	P(73)	448.84943(88)
P(72)	449.58973(115)	P(71)	450.32504(-44)
P(70)	451.05934(13)	P(69)	451.79004(26)
P(68)	452.51855(136)	P(67)	453.24115(-26)
P(66)	453.96295(50)	P(65)	454.67955(-75)
P(64)	455.39656(160)	P(63)	456.10666(24)
P(62)	456.81596(130)	P(61)	457.51867(-103)
P(60)	458.22167(16)	P(59)	458.91797(-212)
P(58)	459.61537(-6)	P(57)	460.30758(4)
P(56)	460.99308(-332)	P(55)	461.68048(-152)
P(54)	462.36509(73)	P(53)	463.04329(-14)
P(52)	463.71899(-25)	P(51)	464.39209(33)
P(50)	465.06120(19)	P(49)	465.72790(94)
P(48)	466.38630(-330)	P(47)	467.04820(-75)
P(46)	467.70481(-18)	P(45)	468.35751(-19)
P(44)	469.00731(21)	P(43)	469.64882(-435)
P(42)	470.29522(-67)	P(41)	470.93482(-45)
P(40)	471.57132(1)	P(39)	472.20423(24)
P(38)	472.83393(62)	P(37)	473.45883(-43)
P(36)	474.08113(-70)	P(35)	474.70024(-80)
P(34)	475.32124(439)	P(33)	475.92914(-12)
P(32)	476.53744(-84)	P(31)	477.14425(35)
P(30)	477.74575(-35)	P(29)	478.34545(57)
P(28)	478.93995(-29)	P(27)	479.52866(-352)
P(25)	480.70556(-16)	P(24)	481.28816(84)
P(23)	481.86537(-11)	P(21)	483.01187(48)
P(20)	483.58137(224)	P(19)	484.14247(-93)
P(18)	484.70268(-151)	P(17)	485.26088(-60)
P(16)	485.81768(240)	P(15)	486.36488(-69)
P(14)	486.91379(143)	P(13)	487.45699(137)
P(12)	487.99019(-517)	P(11)	488.52849(-309)
P(10)	489.06289(-137)	P(9)	489.59310(-31)
P(8)	490.11920(20)	P(7)	490.63980(-124)

Table B.1: Observed line positions of ^{115}InF in cm^{-1}.

Assignment	Observed	Assignment	Observed
P(6)	491.15950(-2)	P(5)	491.67711(266)
P(4)	492.18561(-19)	P(1)	493.69701(-135)
	9 $\longrightarrow$ 8 Band		
R(1)	490.24610(291)	R(5)	492.15281(64)
R(6)	492.62021(-18)	R(8)	493.54691(97)
R(10)	494.45632(-65)	R(11)	494.90492(-209)
R(12)	495.35282(-58)	R(13)	495.79922(309)
R(14)	496.24002(482)	R(15)	496.67063(3)
R(16)	497.10173(-59)	R(17)	497.53063(27)
R(18)	497.95423(-48)	R(19)	498.37603(66)
R(20)	498.79553(321)	R(21)	499.20554(-4)
R(22)	499.61434(-78)	R(23)	500.02064(-30)
R(24)	500.42454(150)	R(25)	500.82214(74)
R(26)	501.21574(-29)	R(27)	501.60855(162)
R(28)	501.99565(157)	R(29)	502.37875(128)
R(30)	502.75595(-115)	R(31)	503.13505(209)
R(32)	503.50645(140)	R(33)	503.87265(-72)
R(34)	504.23766(-26)	R(35)	504.59986(120)
R(37)	505.30906(30)	R(38)	505.65766(-45)
R(39)	506.00316(-48)	R(43)	507.34697(-58)
R(44)	507.67437(44)	R(45)	507.99757(110)
R(46)	508.31577(62)	R(47)	508.63197(199)
R(48)	508.94108(13)	R(49)	509.24848(44)
R(50)	509.55098(-27)	R(51)	509.84988(-70)
R(52)	510.14398(-204)	R(53)	510.43708(-49)
R(54)	510.72688(166)	R(55)	511.00878(-19)
R(56)	511.29149(268)	R(57)	511.56389(-83)
R(58)	511.83599(-73)	R(59)	512.10419(-59)
R(60)	512.36889(-2)	R(61)	512.62969(60)
R(62)	512.88579(46)	R(63)	513.13789(27)
R(64)	513.38779(184)	R(65)	513.62689(-343)
R(66)	513.87050(-23)	R(67)	514.10650(-65)
R(68)	514.33890(-69)	R(69)	514.56830(26)
R(71)	515.01430(133)	R(74)	515.65070(40)
R(75)	515.85510(39)	R(76)	516.05570(61)
R(77)	516.25181(36)	R(78)	516.44221(-155)
R(79)	516.63171(-31)	R(80)	516.81471(-152)
R(81)	516.99621(-18)	R(82)	517.16901(-347)
R(84)	517.51411(165)	R(85)	517.67791(158)
R(86)	517.83631(20)	R(87)	517.99161(-20)
R(88)	518.14351(11)	R(89)	518.29291(201)
R(90)	518.43471(43)	R(91)	518.57251(-104)
R(92)	518.70952(81)	R(94)	518.96672(9)
R(96)	519.20782(-17)	R(97)	519.32192(-53)
R(100)	519.64052(-37)	R(101)	519.73902(33)
R(102)	519.83332(100)	(103)	519.92542(366)
R(104)	520.00702(0)	R(106)	520.16432(-62)

Table B.1: Observed line positions of ^{115}InF in cm^{-1}.

Assignment	Observed	Assignment	Observed
R(108)	520.30622(19)	R(110)	520.43102(78)
R(111)	520.48522(-79)	R(112)	520.53912(159)
P(116)	409.76627(-56)	P(115)	410.62967(-26)
P(114)	411.49158(137)	P(113)	412.34618(-146)
P(112)	413.20209(-14)	P(110)	414.90199(-85)
P(109)	415.75000(115)	P(108)	416.59200(2)
P(107)	417.43150(-72)	P(106)	418.27001(42)
P(104)	419.93541(-20)	P(103)	420.76382(-44)
P(102)	421.58992(-7)	P(101)	422.41292(13)
P(100)	423.23253(-14)	P(99)	424.05043(82)
P(98)	424.86293(-66)	P(96)	426.48004(-267)
P(95)	427.28764(-18)	P(94)	428.08945(-51)
P(93)	428.88875(-36)	P(92)	429.68325(-203)
P(91)	430.47846(0)	P(90)	431.26886(23)
P(89)	432.05526(-53)	P(88)	432.83977(-18)
P(87)	433.62177(70)	P(86)	434.39877(-40)
P(85)	435.17457(34)	P(84)	435.94598(-28)
P(83)	436.71938(415)	P(82)	437.48058(-56)
P(81)	438.24249(-151)	P(80)	439.00349(-29)
P(79)	439.75669(-380)	(78)	440.51210(-202)
P(77)	441.26410(-55)	P(76)	442.01100(-109)
P(74)	443.49701(-65)	P(73)	444.23481(-96)
P(71)	445.70282(19)	P(70)	446.43162(27)
P(69)	447.15782(89)	P(68)	447.88203(266)
P(67)	448.59853(-12)	P(64)	450.73654(-95)
P(63)	451.44454(47)	P(62)	452.14744(-3)
P(61)	452.84715(-54)	P(60)	453.54565(96)
P(59)	454.23865(16)	P(58)	454.92886(-22)
P(57)	455.61696(52)	P(56)	456.30066(9)
P(55)	456.98236(88)	P(54)	457.65857(-58)
P(53)	458.33377(21)	P(52)	459.00437(-35)
P(51)	459.67247(-15)	P(50)	460.33728(1)
P(49)	460.99958(94)	P(48)	461.65808(136)
P(47)	462.31149(-5)	P(46)	462.96399(94)
P(45)	463.61139(13)	P(44)	464.25579(-38)
P(43)	464.89770(-8)	P(42)	465.53690(83)
P(41)	466.17070(-33)	P(40)	466.80220(-46)
P(39)	467.43071(-26)	P(38)	468.05531(-62)
P(37)	468.67771(17)	P(36)	469.29431(-148)
P(35)	469.91052(-17)	P(33)	471.13012(-26)
P(32)	471.73492(-24)	P(31)	472.33743(87)
P(30)	472.93463(7)	P(29)	473.52863(-53)
P(28)	474.12023(-13)	P(27)	474.70894(78)
P(26)	475.29364(111)	P(25)	475.87494(146)
P(24)	476.45034(-66)	P(22)	477.59615(40)
P(21)	478.16285(-10)	P(20)	478.72715(46)
P(19)	479.28735(37)	P(18)	479.84566(185)
P(17)	480.39666(-50)	P(15)	481.49306(-37)

Table B.1: Observed line positions of ^{115}InF in cm^{-1}.

Assignment	Observed	Assignment	Observed
P(14)	482.03537(-97)	P(13)	482.57577(3)
P(12)	483.11167(3)	P(11)	483.64387(-17)
P(10)	484.17297(5)	P(8)	485.21928(-84)
P(7)	485.73618(-224)	P(6)	486.25468(150)
P(2)	488.27359(-315)	P(1)	488.77519(147)
	10 $\longrightarrow$ 9 Band		
R(6)	487.71629(151)	R(7)	488.17739(144)
R(8)	488.63619(267)	R(10)	489.53740(-40)
R(11)	489.98340(-110)	R(12)	490.42580(-177)
R(14)	491.30200(-79)	R(15)	491.73391(-103)
R(16)	492.16311(-31)	R(17)	492.58851(27)
R(18)	493.01091(152)	R(19)	493.42581(-105)
R(20)	493.84101(35)	R(21)	494.25192(114)
R(22)	494.65452(-268)	R(23)	495.06032(40)
R(24)	495.46442(548)	R(25)	495.85482(57)
R(27)	496.63333(-39)	R(28)	497.01683(-104)
R(29)	497.39793(-35)	R(30)	497.77533(37)
R(31)	498.14753(-35)	R(32)	498.51823(117)
R(32)	498.51903(197)	R(33)	498.88333(85)
R(34)	499.24514(99)	R(35)	499.60244(40)
R(36)	499.95614(-2)	R(37)	500.30734(84)
R(38)	500.65144(-161)	R(39)	500.99574(-7)
R(40)	501.33564(87)	R(41)	501.67015(21)
R(43)	502.32835(-48)	R(44)	502.65265(11)
R(45)	502.97255(12)	R(46)	503.28975(126)
R(47)	503.60585(515)	R(48)	503.90996(87)
R(50)	504.51406(-22)	R(51)	504.81176(68)
R(52)	505.10216(-186)	R(53)	505.39386(78)
R(54)	505.67956(129)	R(55)	505.95816(-141)
R(56)	506.23816(118)	R(57)	506.51107(56)
R(58)	506.78057(45)	R(59)	507.04587(5)
R(60)	507.30807(46)	R(62)	507.81917(-26)
R(63)	508.06897(-47)	R(64)	508.31577(25)
R(65)	508.55877(112)	R(66)	508.79708(123)
R(67)	509.03438(430)	R(69)	509.49368(702)
R(70)	509.71528(629)	R(72)	510.14398(226)
R(74)	510.55898(48)	R(75)	510.76098(9)
R(76)	510.96068(141)	R(77)	511.15228(-136)
R(78)	511.34409(9)	R(79)	511.53069(36)
R(81)	511.89119(29)	R(82)	512.06579(67)
R(83)	512.23639(109)	R(84)	512.40269(127)
R(86)	512.71969(-180)	R(88)	513.02539(10)
R(89)	513.17149(43)	R(90)	513.31239(-36)
R(91)	513.45159(124)	R(92)	513.58409(24)
R(93)	513.71960(634)	R(94)	513.83830(-24)
R(95)	513.96010(39)	R(96)	514.07730(54)
R(97)	514.18840(-128)	R(99)	514.40400(88)

Table B.1: Observed line positions of ^{115}InF in cm^{-1}.

Assignment	Observed	Assignment	Observed
R(100)	514.50320(-43)	P(111)	409.69317(-18)
P(109)	411.37698(37)	P(108)	412.21448(52)
P(107)	413.05238(394)	P(106)	413.88129(122)
P(105)	414.70749(-132)	P(104)	415.53369(-99)
P(103)	416.35790(24)	P(101)	417.99570(80)
P(100)	418.80941(24)	P(99)	419.62351(299)
P(98)	420.43021(128)	P(97)	421.23412(-31)
P(96)	422.03642(-56)	P(95)	422.83642(-16)
P(94)	423.63373(49)	P(93)	424.42863(170)
P(92)	425.21873(108)	P(91)	426.00434(-107)
P(90)	426.78934(-84)	P(89)	427.57034(-162)
P(88)	428.35105(29)	P(87)	429.12925(271)
P(86)	429.89895(-37)	P(85)	430.67016(106)
P(84)	431.43636(52)	P(83)	432.19996(41)
P(82)	432.95707(-317)	P(81)	433.71787(-1)
P(80)	434.47187(-60)	P(79)	435.22337(-63)
P(78)	435.97078(-170)	P(76)	437.46108(87)
P(75)	438.20149(202)	P(74)	438.93619(56)
P(73)	439.66939(70)	P(72)	440.39850(-16)
P(71)	441.12580(29)	P(70)	441.84860(-64)
P(69)	442.57030(45)	P(68)	443.28731(-4)
P(67)	444.00091(-79)	P(66)	444.71071(-220)
P(62)	447.52513(-108)	P(61)	448.22053(-108)
P(60)	448.91393(10)	P(59)	449.60373(87)
P(58)	450.28104(-767)	P(57)	450.97044(-91)
P(56)	451.65004(-74)	P(55)	452.32704(4)
P(54)	453.00105(104)	P(53)	453.66995(17)
P(52)	454.33705(73)	P(51)	454.99736(-227)
P(50)	455.65826(-143)	P(49)	456.31586(-63)
P(48)	456.97096(92)	P(47)	457.62017(-16)
P(46)	458.26857(123)	P(45)	458.90947(-160)
P(44)	459.55057(-95)	P(43)	460.18878(9)
P(42)	460.82348(92)	P(41)	461.45498(186)
P(40)	462.07948(-89)	P(39)	462.70399(-33)
P(38)	463.32599(106)	P(37)	463.94219(-3)
P(36)	464.55879(261)	P(35)	465.16810(130)
P(34)	465.77480(73)	P(32)	466.98060(206)
P(31)	467.57471(-103)	P(30)	468.17021(65)
P(29)	468.76261(260)	P(28)	469.34691(-16)
P(27)	469.93062(-12)	P(24)	471.66102(-33)
P(23)	472.23123(-18)	P(22)	472.79973(170)
P(20)	473.92113(13)	P(19)	474.47794(60)
P(18)	475.02874(-148)	P(17)	475.58024(59)
P(15)	476.67044(231)	P(14)	477.20545(-173)
P(13)	477.74575(300)	P(12)	478.27955(472)
P(11)	478.81165(823)		

$11 \longrightarrow 10$ Band

Table B.1: Observed line positions of ^{115}InF in cm^{-1}.

Assignment	Observed	Assignment	Observed
R(14)	486.41698(-45)	R(15)	486.84569(-65)
R(16)	487.26849(-311)	R(17)	487.69259(-63)
R(18)	488.10869(-250)	R(20)	488.93619(2)
R(21)	489.34440(123)	R(22)	489.74910(261)
R(23)	490.15160(547)	R(24)	490.54220(11)
R(25)	490.93400(-36)	R(26)	491.31900(-394)
R(28)	492.08781(-118)	R(29)	492.46301(-344)
R(30)	492.83851(-168)	R(31)	493.20921(-99)
R(32)	493.57391(-257)	R(33)	493.93951(48)
R(35)	494.65452(162)	R(36)	495.00472(52)
R(37)	495.37132(1957)	R(38)	495.69402(-151)
R(39)	496.03502(-51)	R(40)	496.37182(6)
R(41)	496.70383(-39)	R(42)	497.03383(95)
R(44)	497.67923(42)	R(45)	497.99603(-4)
R(46)	498.31083(131)	R(47)	498.61863(-52)
R(48)	498.92603(108)	R(49)	499.22774(80)
R(50)	499.52504(-4)	R(51)	499.81814(-124)
R(52)	500.11074(90)	R(53)	500.39574(-70)
R(54)	500.67924(6)	R(55)	500.95874(68)
R(56)	501.23434(127)	R(57)	501.50395(-26)
R(58)	501.77125(-22)	R(59)	502.03545(62)
R(60)	502.29345(-86)	R(61)	502.54925(-63)
R(62)	502.80375(220)	R(63)	503.04635(-296)
R(64)	503.28975(-341)	R(65)	503.53375(67)
R(66)	503.77145(238)	R(67)	504.00216(101)
R(68)	504.22876(-51)	R(70)	504.67396(28)
R(71)	504.88786(-209)	R(74)	505.51506(9)
R(76)	505.91196(19)	R(77)	506.10396(-22)
R(79)	506.47627(-76)	R(81)	506.83507(124)
R(83)	507.17577(121)	R(85)	507.49687(-229)
R(86)	507.65787(247)	R(91)	508.37507(-72)
R(95)	508.87558(-318)	R(96)	508.99388(-39)
R(98)	509.21238(-59)	R(99)	509.31678(64)
R(100)	509.41548(28)	P(106)	409.52477(-1033)
P(105)	410.35067(-748)	P(103)	411.99588(21)
P(102)	412.81198(187)	P(101)	413.62179(10)
P(100)	414.43119(83)	P(98)	416.03910(8)
P(97)	416.83960(62)	P(95)	418.42901(-114)
P(94)	419.22131(-3)	P(93)	420.00861(-97)
P(92)	420.79402(-88)	P(91)	421.57762(37)
P(90)	422.35552(-112)	P(89)	423.13353(46)
P(88)	423.90953(301)	P(87)	424.67513(-186)
P(86)	425.44484(36)	P(85)	426.20894(-3)
P(84)	426.97034(-12)	P(83)	427.72914(20)
P(82)	428.48525(83)	P(81)	429.23715(29)
P(80)	429.98395(-233)	P(79)	430.73306(39)
P(78)	431.47476(-125)	P(77)	432.21586(-45)
P(75)	433.69037(264)	P(74)	434.41707(-177)

Table B.1: Observed line positions of ^{115}InF in cm^{-1}.

Assignment	Observed	Assignment	Observed
P(73)	435.14337(-350)	P(72)	435.86928(-255)
P(70)	437.31408(161)	P(69)	438.02799(-15)
P(68)	438.74349(279)	P(67)	439.44979(-35)
P(65)	440.85870(-97)	P(64)	441.55850(-123)
P(63)	442.26130(465)	P(61)	443.64171(66)
P(60)	444.32741(-110)	P(59)	445.01321(41)
P(57)	446.37282(96)	P(56)	447.04772(111)
P(55)	447.72213(396)	P(54)	448.39163(510)
P(53)	449.05133(-35)	P(52)	449.71473(111)
P(51)	450.37214(-21)	P(50)	451.02664(-120)
P(49)	451.68144(133)	P(48)	452.32704(-209)
P(47)	452.97275(-217)	P(46)	453.61745(-0)
P(45)	454.25685(12)	P(44)	454.89386(111)
P(43)	455.52666(118)	P(42)	456.15506(11)
P(41)	456.78346(233)	P(40)	457.40277(-126)
P(38)	458.64047(54)	P(37)	459.25377(85)
P(36)	459.86188(-72)	P(35)	460.46898(3)
P(34)	461.07288(90)	P(33)	461.66988(-180)
P(32)	462.26709(-96)	P(31)	462.85959(-147)
P(30)	463.45059(-13)	P(29)	464.03709(7)
P(28)	464.62039(43)	P(27)	465.20060(106)
P(26)	465.77480(-93)	P(25)	466.34730(-124)
P(24)	466.91680(-116)	P(23)	467.48431(31)
P(21)	468.60641(56)	P(19)	469.71462(57)
P(18)	470.26292(-9)	P(17)	470.80882(28)
P(16)	471.35072(8)	(15)	471.88982(54)
P(14)	472.42373(-76)	P(13)	472.95563(-61)
P(12)	473.48463(11)	P(11)	474.01133(200)
P(10)	474.53384(316)	P(8)	475.56344(53)
P(6)	476.58264(147)	P(4)	477.58405(-138)
	12 $\longrightarrow$ 11 Band		
R(10)	479.83656(-340)	R(11)	480.27886(-118)
R(13)	481.14996(54)	R(16)	482.43597(951)
R(18)	483.25977(6)	R(19)	483.67267(178)
R(20)	484.07797(-46)	R(21)	484.48268(35)
R(22)	484.88278(20)	R(25)	486.05938(-196)
R(27)	486.83139(256)	R(28)	487.20759(55)
R(29)	487.58199(43)	R(30)	487.95189(-49)
R(31)	488.31939(-11)	R(32)	488.68609(319)
R(36)	490.09930(-3)	R(37)	490.44310(-100)
R(40)	491.45560(-32)	R(41)	491.78651(82)
R(42)	492.11391(223)	R(43)	492.43301(-88)
R(46)	493.37771(-12)	R(48)	493.98871(55)
R(50)	494.58162(-163)	R(51)	494.87332(-175)
R(52)	495.16302(-4)	R(53)	495.44872(150)
R(54)	495.72762(8)	R(55)	496.00362(-40)
R(56)	496.27442(-223)	R(57)	496.54553(10)

Table B.1: Observed line positions of ^{115}InF in cm^{-1}.

Assignment	Observed	Assignment	Observed
R(59)	497.07043(-96)	R(61)	497.58123(-64)
R(64)	498.31993(149)	R(65)	498.55773(156)
R(66)	498.78893(-107)	R(67)	499.01804(-188)
R(69)	499.46664(-135)	R(70)	499.68494(-119)
R(76)	500.91134(-82)	R(78)	501.28804(-110)
R(79)	501.46965(-203)	R(83)	502.15995(-190)
R(85)	502.48135(-156)	R(87)	502.78585(-204)
R(90)	503.21385(-126)	R(91)	503.34975(33)
R(94)	503.73085(283)	R(95)	503.84595(-14)
P(101)	409.29307(38)	P(97)	412.48578(-207)
P(92)	416.41680(23)	P(90)	417.96510(-247)
P(89)	418.73861(-6)	P(88)	419.50791(110)
P(85)	421.79292(-52)	P(83)	423.30193(-104)
P(81)	424.80193(141)	P(80)	425.54574(94)
P(79)	426.28594(-11)	P(78)	427.02434(5)
P(77)	427.75644(-305)	P(75)	429.22055(-25)
P(74)	429.94675(-13)	P(70)	432.81747(-314)
P(69)	433.53127(-8)	P(68)	434.23877(-24)
P(67)	434.94137(-220)	P(66)	435.64598(94)
P(65)	436.34338(-1)	P(63)	437.73219(144)
P(62)	438.42069(95)	P(61)	439.10569(10)
P(60)	439.78699(-132)	P(58)	441.14370(-60)
P(57)	441.81960(205)	P(56)	442.48890(126)
P(53)	444.47731(-154)	P(45)	449.64733(-48)
P(43)	450.90824(49)	P(42)	451.53294(10)
P(41)	452.15374(-92)	P(39)	453.38735(-115)
P(38)	454.00015(-35)	P(37)	454.60865(-55)
P(36)	455.21816(353)	P(35)	455.81736(62)
P(34)	456.41506(-49)	P(33)	457.00866(-239)
P(30)	458.77787(26)	P(29)	459.35977(-2)
P(27)	460.51418(5)	P(25)	461.65148(-355)
P(23)	462.78219(-28)	P(17)	466.08500(156)
P(15)	467.15651(2)	P(10)	469.78132(235)
P(8)	470.80162(-216)		

Table B.2: Observed line positions of ^{113}InF in cm^{-1}. Lines marked with ‡ are taken from ref. [219]

Assignment	Observed	Assignment	Observed
	$1 \longrightarrow 0$ Band		
		R(7)	534.75708(-437)
R(8)	535.25438(285)	R(11)	536.70289(400)
R(12)	537.17259(-111)	R(15)	538.57800(289)
R(20)	540.83451(81)	R(21)	541.27381(2)
R(23)	542.14101(-131)	R(24)	542.57141(67)
R(25)	542.99521(-4)	R(26)	543.41372(-214)
R(28)	544.24562(32)	R(29)	544.65302(-111)
R(30)	545.05552(-351)	R(32)	545.85553(-147)
R(33)	546.25093(88)	R(34)	546.64173(258)
R(36)	547.40613(70)	R(37)	547.78243(-18)
R(39)	548.52524(22)	R(40)	548.89024(1)
R(41)	549.24914(-230)	R(42)	549.60854(-9)
R(43)	549.96074(-108)	R(44)	550.30424(-675)
R(45)	550.64845(-768)	R(46)	550.99785(61)
R(47)	551.33455(24)	R(48)	551.66865(132)
R(49)	551.99685(54)	R(50)	552.32135(13)
R(51)	552.64235(27)	R(52)	552.95816(-72)
R(53)	553.27146(-13)	R(54)	553.57856(-166)
R(55)	553.88496(20)	R(56)	554.18506(-16)
R(57)	554.47996(-161)	R(58)	554.77506(124)
R(59)	555.06276(81)	R(60)	555.34896(299)
R(61)	555.62637(49)	R(62)	555.90147(-18)
R(63)	556.17207(-121)	R(64)	556.44037(-40)
R(65)	556.70317(-94)	R(66)	556.96337(7)
R(67)	557.21827(-6)	R(68)	557.46957(37)
R(69)	557.71677(88)	R(70)	557.95958(116)
R(71)	558.20018(343)	R(72)	558.43148(59)
R(73)	558.65958(-125)	R(74)	558.88748(91)
R(75)	559.10788(-23)	R(76)	559.32488(-55)
R(77)	559.54048(195)	R(78)	559.74788(48)
R(79)	559.95248(44)	R(80)	560.15168(-76)
R(81)	560.34979(119)	R(82)	560.54429(378)
R(83)	560.72649(-166)	R(84)	560.91049(-105)
R(85)	561.09159(94)	R(86)	561.26579(30)
R(87)	561.43469(-135)	R(88)	561.59999(-232)
R(89)	561.76259(-169)	R(90)	561.93039(843)
R(91)	562.07789(256)	R(92)	562.22559(121)
R(93)	562.36689(-223)	R(94)	562.50959(6)
R(95)	562.64629(68)	R(96)	562.77930(194)
R(97)	562.90410(-66)	R(99)	563.14390(-260)
R(100)	563.25990(-93)	R(101)	563.36990(-90)
R(102)	563.47110(-529)	R(104)	563.66720(-722)
R(105)	563.76360(-325)	P(83)‡	475.01670(-65)
P(82)‡	475.82710(-111)	P(80)‡	477.44090(71)
P(76)‡	480.62500(-8)	P(71)‡	484.53220(-14)

Table B.2: Observed line positions of ^{113}InF in cm^{-1}.

Assignment	Observed	Assignment	Observed
P(67)‡	487.59680(-177)	P(66)‡	488.35610(-70)
P(52)‡	498.61810(15)	P(50)‡	500.02930(-0)
P(49)‡	500.73040(58)	P(46)‡	502.81070(9)
P(43)‡	504.86010(-7)	P(32)‡	512.10440(-85)
P(31)‡	512.74210(-57)	P(30)‡	513.37610(-43)
P(27)‡	515.25660(-5)	P(21)‡	518.92000(17)
P(15)‡	522.45350(101)	P(14)‡	523.02880(31)
P(12)‡	524.16970(23)	P(8)‡	526.40800(80)
P(3)‡	529.12090(-7)		
	2 ⟶ 1 Band		
R(10)	530.89832(14)	R(14)	532.77415(-164)
R(17)	534.14251(-136)	R(19)	535.03591(-80)
R(20)	535.47585(-150)	R(21)	535.91374(-40)
R(24)	537.20192(67)	R(25)	537.62168(-85)
R(26)	538.04015(24)	R(28)	538.86341(42)
R(30)	539.67088(45)	R(31)	540.06805(-21)
R(32)	540.45837(-380)	R(33)	540.85076(-140)
R(37)	542.37289(28)	R(39)	543.10929(21)
R(44)	544.88186(127)	R(47)	545.89428(-119)
R(48)	546.22540(-33)	R(52)	547.51126(488)
R(53)	547.81867(225)	R(54)	548.12336(95)
R(55)	548.42583(150)	R(56)	548.72293(76)
R(57)	549.01569(-24)	R(58)	549.30535(-27)
R(60)	549.86876(-394)	R(61)	550.15049(40)
R(62)	550.42215(-123)	R(63)	550.69195(-61)
R(64)	550.96169(408)	R(65)	551.21971(118)
R(66)	551.47603(71)	R(67)	551.72405(-392)
R(68)	551.97361(-286)	R(70)	552.46255(152)
R(74)	553.37972(-42)	R(75)	553.59750(-196)
R(76)	553.81430(-29)	R(77)	554.02469(-83)
R(78)	554.23131(-94)	R(79)	554.43508(32)
R(80)	554.63545(239)	R(81)	554.82721(8)
R(82)	555.01690(-7)	R(84)	555.38825(430)
R(85)	555.56231(124)	R(88)	556.06610(-77)
R(90)	556.38704(432)	R(92)	556.68122(-21)
R(93)	556.82442(8)	R(95)	557.09679(-46)
P(76)‡	475.68380(-134)	P(74)‡	477.24550(-193)
P(64)‡	484.86210(61)	P(40)‡	501.76140(-46)
P(35)‡	505.03180(-95)	P(28)‡	509.46490(88)
P(23)‡	512.52240(-6)	P(22)‡	513.12310(-29)
P(18)‡	515.48990(-116)	P(12)‡	518.93350(-22)
P(6)‡	522.24480(21)		
	3 ⟶ 2 Band		
R(17)	528.84736(-56)	R(23)	531.45627(-405)

Table B.2: Observed line positions of ^{113}InF in cm^{-1}.

Assignment	Observed	Assignment	Observed
R(24)	531.88297(73)	R(26)	532.71707(258)
R(30)	534.33018(-225)	R(31)	534.72658(-59)
R(32)	535.11998(197)	R(33)	535.50428(-65)
R(34)	535.88739(-55)	R(35)	536.26729(27)
R(36)	536.64269(52)	R(38)	537.38189(125)
R(43)	539.15190(-573)	R(46)	540.17220(-391)
R(47)	540.50420(-341)	R(52)	542.10471(-28)
R(53)	542.41701(463)	R(55)	543.01391(-114)
R(56)	543.31122(90)	R(57)	543.60222(70)
R(58)	543.88902(36)	R(59)	544.16932(-241)
R(60)	544.45112(40)	R(61)	544.72422(-141)
R(62)	544.99492(-154)	R(63)	545.26172(-147)
R(65)	545.78393(-42)	R(66)	546.03913(37)
R(67)	546.28493(-413)	R(69)	546.77773(46)
R(72)	547.47743(-113)	R(73)	547.70443(41)
R(74)	547.92603(70)	R(76)	548.35724(180)
R(78)	548.76854(-29)	R(79)	548.96894(-30)
R(80)	549.16154(-392)	R(81)	549.35734(-13)
R(84)	549.90884(60)	R(86)	550.25044(-386)
R(87)	550.42214(117)	R(88)	550.58365(24)
R(90)	550.89525(-26)	P(70)	475.41020(3)
P(63)‡	480.64710(37)	P(58)‡	484.28800(42)
P(52)‡	488.54490(-94)	P(42)‡	495.36900(-186)
P(37)‡	498.65900(483)	P(35)‡	499.94270(-44)
P(32)‡	501.84980(-52)	P(27)‡	504.95750(-102)
P(20)‡	509.16210(133)	P(15)‡	512.05300(-174)
P(14)‡	512.62200(-69)	P(13)‡	513.18570(-131)
P(9)‡	515.40640(-149)		
	4 ⟶ 3 Band		
R(14)‡	522.25250(-168)	R(15)‡	522.70720(-3)
R(16)‡	523.15770(122)	R(24)‡	526.61420(86)
R(27)‡	527.84730(91)	R(30)‡	529.04350(-117)
R(31)‡	529.43550(-84)	R(32)‡	529.82370(-43)
R(33)‡	530.20780(-22)	R(50)‡	536.13290(15)
R(52)‡	536.75390(-43)	R(65)‡	540.40110(-11)
R(67)‡	540.90250(126)	R(72)‡	542.07980(39)
R(76)‡	542.94660(-99)	R(79)‡	543.55450(-60)
P(64)‡	475.02900(2496)	P(63)‡	475.73590(-133)
P(61)‡	477.19200(-168)	P(60)‡	477.91580(-114)
P(51)‡	484.27620(15)	P(50)‡	484.96530(-51)
P(45)‡	488.36310(-60)	P(35)‡	494.90370(125)
P(34)‡	495.53510(-220)	P(22)‡	502.87990(-187)
P(18)‡	505.21550(-104)	P(11)‡	509.16210(-206)

Appendix C

Line Positions of CuH and CuD

All values of the lines in the following appendix is given in cm^{-1} units. The value in parenthesis are the 1σ uncertainty from the parametrized potential fit and signify the uncertainty in the last quoted digits.

Table C.1: Observed line positions of CuH in cm^{-1}.

Assignment	Observed	Assignment	Observed
	Lines for ^{63}CuH		
	$v = 0$ Pure Rotational Lines		
R(1)	31.25245896(805)	R(2)	46.84704270(-62)
R(3)	62.40372505(47)	R(4)	77.90993471(-360)
R(5)	93.35319690(-6)	R(6)	108.72109931(142)
R(7)	124.00134262(172)	R(9)	154.25025469(-56)
R(10)	169.19497188(-80)		
	$1 \longrightarrow 0$ Band		
P(28)	1285.47010(15)		
P(27)	1309.81163(-544)	P(26)	1334.00394(110)
P(25)	1358.01530(-121)	P(24)	1381.84660(-43)
P(23)	1405.48262(-41)	P(22)	1428.91315(29)
P(21)	1452.12582(119)	P(20)	1475.10677(58)
P(19)	1497.84578(62)	P(18)	1520.33017(116)
P(17)	1542.54530(32)	P(16)	1564.48086(68)
P(15)	1586.12205(50)	P(14)	1607.45612(18)
P(13)	1628.47070(63)	P(12)	1649.15079(17)
P(11)	1669.48470(56)	P(10)	1689.45718(-1)
P(9)	1709.05636(8)	P(8)	1728.26789(-6)
P(7)	1747.06942(-927)	P(6)	1765.47514(4)
P(5)	1783.44388(9)	P(4)	1800.97146(3)
P(3)	1818.04522(39)	P(2)	1834.65093(6)
P(1)	1850.77524(-134)	R(0)	1881.53471(-116)
R(1)	1896.14433(1)	R(2)	1910.22361(141)
R(3)	1923.75696(-49)	R(4)	1936.73822(-1)
R(5)	1949.15299(0)	R(6)	1960.99042(4)
R(7)	1972.23910(-27)	R(8)	1982.88956(38)

Table C.1: Observed line positions of CuH in cm^{-1}.

Assignment	Observed	Assignment	Observed
R(9)	1992.92971(35)	R(10)	2002.35004(29)
R(11)	2011.14063(15)	R(12)	2019.29263(57)
R(13)	2026.79615(87)	R(14)	2033.64226(101)
R(15)	2039.82173(26)	R(16)	2045.32833(61)
R(17)	2050.15363(147)	R(18)	2054.28660(-65)
R(19)	2057.72651(73)	R(20)	2060.45495(-592)
R(21)	2062.48387(-208)	R(22)	2063.79259(-216)
	$2 \longrightarrow 1$ Band		
P(24)	1320.28342(12)	P(23)	1343.39215(-6)
P(22)	1366.28960(-126)	P(21)	1388.96745(-52)
P(20)	1411.41199(-2)	P(19)	1433.61164(48)
P(18)	1455.55390(47)	P(17)	1477.22699(42)
P(16)	1498.61757(-60)	P(15)	1519.71576(10)
P(14)	1540.50591(-38)	P(13)	1560.97737(14)
P(12)	1581.11511(-42)	P(11)	1600.90749(-67)
P(10)	1620.34219(17)	P(9)	1639.40377(-20)
P(8)	1658.08020(-66)	P(7)	1676.35976(21)
P(6)	1694.22656(-31)	P(5)	1711.67037(64)
P(4)	1728.67498(-13)	P(3)	1745.23052(52)
P(2)	1761.32098(-58)	P(1)	1776.93647(-55)
R(0)	1806.69120(190)	R(1)	1820.80113(-20)
R(2)	1834.38776(4)	R(3)	1847.43630(-24)
R(4)	1859.93512(-96)	R(5)	1871.87479(-3)
R(6)	1883.24163(9)	R(7)	1894.02449(-72)
R(8)	1904.21529(20)	R(9)	1913.80052(-20)
R(10)	1922.77093(-96)	R(11)	1931.11837(-30)
R(12)	1938.83134(-14)	R(13)	1945.90099(3)
R(14)	1952.31744(-66)	R(15)	1958.07374(-39)
R(16)	1963.16062(0)	R(18)	1971.29304(43)
R(19)	1974.31409(-857)		
	$3 \longrightarrow 2$ Band		
P(21)	1326.08210(-1135)	P(20)	1348.03300(82)
P(19)	1369.72296(94)	P(18)	1391.15499(343)
P(17)	1412.31121(210)	P(16)	1433.18162(-120)
P(15)	1453.76086(25)	P(14)	1474.03133(110)
P(13)	1493.97961(30)	P(12)	1513.59469(-64)
P(11)	1532.86693(126)	P(10)	1551.77662(-99)
P(9)	1570.31790(-51)	P(8)	1588.47542(19)
P(7)	1606.23588(61)	P(5)	1640.51414(50)
P(4)	1657.00766(127)	P(3)	1673.05326(206)
R(3)	1771.77263(-198)	R(4)	1783.79009(-68)
R(9)	1835.29672(118)		
	$4 \longrightarrow 3$ Band		
P(18)	1326.86577(-193)	P(17)	1347.54009(119)

Table C.1: Observed line positions of CuH in cm^{-1}.

Assignment	Observed	Assignment	Observed
P(15)	1388.00818(212)	P(14)	1407.77748(-134)
P(13)	1427.22386(-471)	P(12)	1446.34229(-97)
P(11)	1465.11135(63)	P(10)	1483.51746(-120)
P(9)	1501.55441(-31)	P(8)	1519.20465(-177)
P(6)	1553.30752(67)		
	Lines for ^{65}CuH		
	$v = 0$ Pure Rotational Lines		
R(1)	31.23744250(594)	R(3)	62.37379334(34)
R(4)	77.87261369(-248)	R(5)	93.30854271(-149)
R(6)	108.66918670(64)	R(7)	123.94225861(184)
R(9)	154.17712530(337)	R(10)	169.11498137(-715)
	$1 \longrightarrow 0$ Band		
P(27)	1309.66917(-526)	P(26)	1333.85051(303)
P(25)	1357.84958(108)	P(24)	1381.66726(82)
P(23)	1405.28856(-137)	P(22)	1428.70824(91)
P(21)	1451.90537(-141)	P(20)	1474.87598(-14)
P(19)	1497.60304(4)	P(18)	1520.07521(33)
P(17)	1542.27959(57)	P(16)	1564.20433(179)
P(15)	1585.83246(6)	P(14)	1607.15624(78)
P(13)	1628.15897(52)	P(12)	1648.82804(-1)
P(11)	1669.14802(-282)	P(10)	1689.11421(82)
P(9)	1708.70226(3)	P(8)	1727.90410(22)
P(7)	1746.70541(52)	P(6)	1765.09154(-30)
P(5)	1783.05131(-5)	P(4)	1800.57023(9)
P(3)	1817.63463(-36)	P(2)	1834.23279(-4)
P(1)	1850.35137(70)	R(1)	1895.69875(177)
R(2)	1909.76832(-17)	R(4)	1936.27257(-43)
R(5)	1948.68420(157)	R(6)	1960.51624(92)
R(7)	1971.76021(15)	R(8)	1982.40598(-12)
R(9)	1992.44254(-41)	R(10)	2001.86075(26)
R(11)	2010.64868(-18)	R(12)	2018.79879(22)
R(13)	2026.30134(94)	R(15)	2039.32642(102)
R(16)	2044.83109(-74)	R(17)	2049.65890(193)
R(18)	2053.79320(-10)	R(19)	2057.23157(-204)
	$2 \longrightarrow 1$ Band		
P(24)	1320.13353(414)	P(23)	1343.22486(-127)
P(22)	1366.11367(95)	P(21)	1388.77660(-126)
P(20)	1411.21075(70)	P(19)	1433.39747(-1)
P(18)	1455.32495(-321)	P(17)	1476.99075(90)
P(16)	1498.36869(-147)	P(15)	1519.45578(-75)
P(14)	1540.23386(-236)	P(13)	1560.69617(-23)
P(12)	1580.82291(-124)	P(11)	1600.60597(-48)
P(10)	1620.02929(-91)	P(9)	1639.08251(22)
P(8)	1657.74941(-15)	P(7)	1676.01794(-95)

Table C.1: Observed line positions of CuH in cm^{-1}.

Assignment	Observed	Assignment	Observed
P(6)	1693.87598(-117)	P(5)	1711.31089(-34)
P(4)	1728.30506(-306)	P(3)	1744.85407(-78)
R(1)	1820.38724(-327)	R(2)	1833.97087(-2)
R(3)	1847.01521(113)	R(4)	1859.50877(36)
R(5)	1871.44289(52)	R(6)	1882.80518(44)
R(7)	1893.58308(-142)	R(8)	1903.77006(-86)
R(10)	1922.31883(-335)	R(11)	1930.66574(-118)
R(12)	1938.37632(-185)	R(13)	1945.44466(-193)
R(14)	1951.86141(-175)	R(15)	1957.61872(-43)
R(16)	1962.70336(-276)	R(17)	1967.11396(-195)
R(18)	1970.83792(-273)		
	$3 \longrightarrow 2$ Band		
P(21)	1325.93214(98)	P(19)	1369.53398(-285)
P(18)	1390.95564(52)	P(17)	1412.10247(90)
P(16)	1432.96702(268)	P(15)	1453.53304(167)
P(14)	1473.79182(141)	P(13)	1493.73089(178)
P(12)	1513.33490(-4)	P(11)	1532.59678(147)
P(10)	1551.49930(178)	P(9)	1570.03106(224)
P(8)	1588.17607(-33)	P(7)	1605.92820(74)
P(6)	1623.26936(20)	P(5)	1640.18774(-98)
P(4)	1656.67231(-105)	R(3)	1771.39653(751)
	Lines for ^{63}CuD $v = 0$ Pure Rotational Lines		
R(2)	23.94036747(317)	R(4)	39.85692409(12)
R(5)	47.79230537(82)	R(7)	63.60104136(-22)
R(8)	71.46795030(27)	R(9)	79.30561495(-161)
R(10)	87.11086218(58)	R(11)	94.88053132(138)
R(13)	110.30063531(-115)	R(15)	125.54121025(64)
R(16)	133.08657194(-187)	R(18)	148.01255170(106)
	$1 \longrightarrow 0$ Band		
P(33)	1006.06640(-319)	P(31)	1030.11937(61)
P(30)	1042.02890(150)	P(29)	1053.85629(177)
P(28)	1065.59668(-25)	P(27)	1077.25280(141)
P(26)	1088.81477(16)	P(25)	1100.28300(-28)
P(24)	1111.65411(5)	P(23)	1122.92409(50)
P(22)	1134.08894(47)	P(21)	1145.14464(-65)
P(20)	1156.08968(-92)	P(19)	1166.92055(-39)
P(18)	1177.63198(-88)	P(17)	1188.22202(-84)
P(16)	1198.68738(-7)	P(15)	1209.02257(-57)
P(14)	1219.22563(-78)	P(13)	1229.29316(-60)
P(12)	1239.22098(-70)	P(11)	1249.00633(-32)
P(10)	1258.64432(-86)	P(9)	1268.13416(37)
P(8)	1277.46862(-35)	P(7)	1286.64758(31)
P(6)	1295.66373(-149)	P(5)	1304.51893(-46)

Table C.1: Observed line positions of CuH in cm^{-1}.

Assignment	Observed	Assignment	Observed
P(4)	1313.20525(-111)	P(3)	1321.72002(-272)
P(1)	1338.22262(-764)	R(3)	1376.28093(-58)
R(4)	1383.31316(-129)	R(5)	1390.14632(-134)
R(7)	1403.20253(-25)	R(8)	1409.41917(42)
R(9)	1415.42331(18)	R(10)	1421.21315(8)
R(11)	1426.78543(-35)	R(12)	1432.13712(-142)
R(13)	1437.26786(-81)	R(14)	1442.17518(162)
R(15)	1446.85128(63)	R(16)	1451.29376(-367)
R(17)	1455.55347(4198)	R(18)	1459.49344(299)
R(19)	1463.23099(-101)		
	$2 \longrightarrow 1$ Band		
P(30)	1009.92261(-132)	P(29)	1021.55195(10)
P(28)	1033.09382(-74)	P(27)	1044.54867(-22)
P(26)	1055.91301(134)	P(25)	1067.18030(61)
P(24)	1078.35077(108)	P(23)	1089.41795(-43)
P(22)	1100.38252(7)	P(21)	1111.23877(21)
P(20)	1121.98302(-34)	P(19)	1132.61342(-4)
P(18)	1143.12650(104)	P(17)	1153.51642(45)
P(16)	1163.78100(-53)	P(15)	1173.91880(8)
P(14)	1183.92573(163)	P(13)	1193.79484(62)
P(12)	1203.52746(183)	P(11)	1213.11623(135)
P(10)	1222.55973(121)	P(9)	1231.85287(-25)
P(8)	1240.99691(167)	P(7)	1249.98298(152)
P(6)	1258.80671(-167)	P(5)	1267.48232(971)
P(4)	1275.97221(145)	R(2)	1330.56499(3547)
R(3)	1337.58334(265)	R(4)	1344.43938(273)
R(5)	1351.09826(391)	R(6)	1357.55517(442)
R(7)	1363.80561(271)	R(8)	1369.84901(115)
R(9)	1375.68078(-198)	R(10)	1381.30710(235)
R(11)	1386.71195(86)	R(12)	1391.89945(44)
R(13)	1396.86670(84)	R(14)	1401.60616(-287)
R(15)	1406.12150(-444)	R(16)	1410.41659(248)
R(17)	1414.47378(272)	R(18)	1418.29439(-3)
	$3 \longrightarrow 2$ Band		
P(27)	1012.01964(-72)	P(25)	1034.26702(269)
P(24)	1045.24161(136)	P(23)	1056.11401(-53)
P(22)	1066.88456(57)	P(21)	1077.54376(-159)
P(20)	1088.09388(-145)	P(19)	1098.52950(-113)
P(18)	1108.84733(-61)	P(17)	1119.04347(-43)
P(16)	1129.11427(-91)	P(15)	1139.05644(-196)
P(14)	1148.87209(190)	P(13)	1158.54722(7)
P(12)	1168.08589(-3)	P(11)	1177.48190(-118)
P(10)	1186.73854(328)	P(9)	1195.83903(-5)
P(8)	1204.78862(-253)	P(7)	1213.58870(60)
P(6)	1222.22743(86)	R(7)	1324.68997(-173)
R(8)	1330.56499(9)	R(10)	1341.68333(121)

Table C.1: Observed line positions of CuH in cm^{-1}.

Assignment	Observed	Assignment	Observed
R(14)	1361.32156(-84)	R(16)	1369.79883(-419)
	Lines for ^{65}CuD		
	$v = 0$ Pure Rotational Lines		
R(2)	23.91767721(551)	R(3)	31.87497145(724)
R(4)	39.81918711(76)	R(5)	47.74708785(24)
R(8)	71.40054581(154)	R(9)	79.23091544(-120)
R(10)	87.02892849(-97)	R(11)	94.79143398(111)
R(13)	110.19743398(129)	R(14)	117.83475810(-374)
R(15)	125.42424259(143)		
	$1 \longrightarrow 0$ Band		
P(27)	1076.90171(-163)		
P(26)	1088.45544(101)	P(25)	1099.91244(136)
P(24)	1111.26946(-47)	P(23)	1122.52842(79)
P(22)	1133.68046(-35)	P(21)	1144.72543(-60)
P(20)	1155.66034(46)	P(19)	1166.47997(109)
P(18)	1177.17976(15)	P(17)	1187.75908(52)
P(16)	1198.21172(-54)	P(15)	1208.53635(-86)
P(14)	1218.72688(-302)	P(13)	1228.78710(25)
P(12)	1238.70367(-86)	P(11)	1248.47970(23)
P(10)	1258.10691(-124)	P(9)	1267.58495(-216)
P(8)	1276.90916(-368)	P(7)	1286.08484(294)
P(6)	1295.09129(45)	P(5)	1303.92248(-1374)
R(3)	1375.68078(5041)	R(8)	1408.73940(-22)
R(9)	1414.73785(-147)	R(10)	1420.52453(-37)
R(11)	1426.09301(-56)	R(13)	1436.57100(160)
R(14)	1441.47700(574)	R(15)	1446.14581(14)
R(16)	1450.58728(-284)	R(17)	1454.80083(-137)
R(18)	1458.78381(428)	R(19)	1462.55976(3995)
	$2 \longrightarrow 1$ Band		
P(28)	1032.78744(51)	P(25)	1066.84001(348)
P(24)	1077.99309(-179)	P(23)	1089.05491(288)
P(22)	1100.00585(118)	P(21)	1110.84854(-94)
P(20)	1121.58222(-88)	P(19)	1132.20151(-65)
P(18)	1142.70629(304)	P(17)	1153.08333(34)
P(16)	1163.33643(-150)	P(15)	1173.46379(-88)
P(14)	1183.46025(48)	P(13)	1193.31983(7)
P(12)	1203.04099(-23)	P(11)	1212.62162(90)
P(10)	1222.05082(-397)	P(9)	1231.34228(226)
P(8)	1240.47159(-139)	P(7)	1249.45156(132)
P(6)	1258.26935(94)	P(5)	1266.92558(147)
R(2)	1329.96735(4568)		
	$3 \longrightarrow 2$ Band		
P(21)	1077.19003(378)	P(20)	1087.73063(532)

Table C.1: Observed line positions of CuH in cm^{-1}.

Assignment	Observed	Assignment	Observed
P(18)	1108.45737(85)	P(17)	1118.64411(211)
P(15)	1138.63241(-357)	P(12)	1167.62990(-407)
P(11)	1177.02033(-132)	P(8)	1204.29838(-405)
P(6)	1221.71872(-197)		

Appendix D

Line Positions of AgH and AgD

All values of the lines in the following appendix is given in cm^{-1} units. The value in parenthesis are the 1σ uncertainty from the parametrized potential fit and signify the uncertainty in the last quoted digits.

Table D.1: Observed line positions of AgH in cm^{-1}.

Assignment	Observed	Assignment	Observed
	Lines for ^{107}AgH		
	$1 \longrightarrow 0$ Band		
P(28)	1215.25629(20)	P(27)	1235.61352(-457)
P(26)	1255.79873(-158)	P(25)	1275.79593(8)
P(24)	1295.59327(-431)	P(23)	1315.19802(-16)
P(22)	1334.59051(38)	P(21)	1353.76565(-9)
P(20)	1372.71645(-71)	P(19)	1391.43610(-31)
P(18)	1409.91576(40)	P(17)	1428.14526(-55)
P(16)	1446.11991(50)	P(15)	1463.82825(52)
P(14)	1481.26637(407)	P(13)	1498.41466(9)
P(12)	1515.27666(73)	P(11)	1531.83796(23)
P(10)	1548.09267(134)	P(9)	1564.02866(63)
P(8)	1579.63906(-9)	P(7)	1594.91623(21)
P(6)	1609.84972(-25)	P(5)	1624.43261(22)
P(4)	1638.65421(-47)	P(2)	1665.98269(-205)
P(1)	1679.06156(-1404)	R(1)	1715.94815(-351)
R(2)	1727.41838(79)	R(3)	1738.45353(-357)
R(4)	1749.06118(-114)	R(5)	1759.22458(-92)
R(6)	1768.93959(60)	R(7)	1778.19480(-51)
R(8)	1786.98824(117)	R(9)	1795.30815(113)
R(10)	1803.14606(-197)	R(11)	1810.50345(32)
R(12)	1817.36657(111)	R(13)	1823.72873(40)
R(14)	1829.58546(33)	R(15)	1834.92961(16)
R(16)	1839.75624(130)		
	$2 \longrightarrow 1$ Band		
P(23)	1256.30007(-8)	P(22)	1275.32095(-208)

Table D.1: Observed line positions of AgH in cm^{-1}.

Assignment	Observed	Assignment	Observed
P(21)	1294.12400(-56)	P(20)	1312.69796(61)
P(19)	1331.03368(-21)	P(18)	1349.12671(22)
P(17)	1366.96678(-52)	P(16)	1384.54835(-5)
P(15)	1401.86196(25)	P(14)	1418.88963(-946)
P(12)	1452.11486(187)	P(11)	1468.27234(-53)
P(10)	1484.13387(1036)	P(9)	1499.65863(215)
P(8)	1514.86290(-43)	P(7)	1529.73630(70)
P(6)	1544.26505(23)	P(4)	1572.26016(-22)
P(3)	1585.70848(-142)	R(4)	1679.06156(364)
R(5)	1688.82347(-115)	R(6)	1698.14169(-94)
R(7)	1707.00555(114)	R(8)	1715.40437(187)
R(9)	1723.33045(88)	R(10)	1730.77407(-431)
	$3 \longrightarrow 2$ Band		
P(19)	1270.36509(-228)	P(16)	1322.77922(-356)
P(15)	1339.71975(-140)	P(14)	1356.37960(-35)
P(12)	1388.82831(105)	P(11)	1404.60106(131)
P(9)	1435.20052(-136)	P(8)	1450.01413(-102)
P(7)	1464.49041(-184)	P(6)	1478.61761(-735)
	Lines for ^{109}AgH $1 \longrightarrow 0$ Band		
P(27)	1235.56574(174)	P(26)	1255.74408(170)
P(25)	1275.73312(-98)	P(24)	1295.52907(-299)
P(23)	1315.12816(-75)	P(22)	1334.51517(-199)
P(21)	1353.68882(-28)	P(20)	1372.63724(33)
P(19)	1391.35307(48)	P(18)	1409.82668(-134)
P(17)	1428.05498(-1)	P(16)	1446.02569(53)
P(15)	1463.73071(57)	P(14)	1481.16092(-49)
P(13)	1498.31102(58)	P(12)	1515.16921(59)
P(11)	1531.72851(119)	P(10)	1547.97726(-63)
P(9)	1563.91177(14)	P(8)	1579.52043(56)
P(7)	1594.79373(-19)	P(6)	1609.72564(48)
P(5)	1624.30496(1)	P(4)	1638.52473(4)
P(2)	1665.85038(44)	P(1)	1678.92463(-1392)
R(1)	1715.80606(-238)	R(2)	1727.27286(33)
R(3)	1738.31048(17)	R(4)	1748.91332(-59)
R(5)	1759.07413(-145)	R(6)	1768.78919(148)
R(7)	1778.04212(-65)	R(8)	1786.83225(-115)
R(9)	1795.15137(-97)	R(11)	1810.34609(-74)
R(12)	1817.20901(46)	R(13)	1823.56988(-106)
R(14)	1829.42886(145)	R(15)	1834.77180(28)
R(16)	1839.59777(81)		
	$2 \longrightarrow 1$ Band		
P(25)	1217.56773(144)	P(23)	1256.23965(-64)
P(22)	1275.26009(53)	P(21)	1294.05595(-156)

Table D.1: Observed line positions of AgH in cm^{-1}.

Assignment	Observed	Assignment	Observed
P(20)	1312.62786(109)	P(19)	1330.95995(12)
P(18)	1349.04938(39)	P(17)	1366.88559(-84)
P(16)	1384.46257(-163)	P(15)	1401.77211(-213)
P(14)	1418.80757(-85)	P(12)	1452.01601(-10)
P(11)	1468.17289(-10)	P(10)	1484.02012(-58)
P(9)	1499.55143(62)	P(8)	1514.75503(15)
P(7)	1529.62420(-24)	P(6)	1544.15180(75)
P(4)	1572.14353(190)	P(3)	1585.58856(-25)
R(2)	1658.07863(253)	R(4)	1678.92463(295)
R(5)	1688.68594(-104)	R(6)	1698.00053(-319)
R(7)	1706.86421(-13)	R(8)	1715.26868(728)
R(9)	1723.18420(-337)	R(10)	1730.62919(-642)

$3 \longrightarrow 2$ Band

P(19)	1270.30545(224)	P(16)	1322.70598(-276)
P(15)	1339.64182(-210)	P(14)	1356.29856(-106)
P(13)	1372.66799(7)	P(12)	1388.74194(105)
P(11)	1404.51226(179)	P(9)	1435.10925(225)
P(7)	1464.39358(148)	P(6)	1478.52306(77)

Lines for ^{107}AgD

$1 \longrightarrow 0$ Band

P(30)	970.10558(-24)	P(29)	979.78969(15)
P(28)	989.39599(398)	P(27)	998.90889(-227)
P(26)	1008.34151(-337)	P(25)	1017.69223(118)
P(24)	1026.94995(242)	P(23)	1036.11432(215)
P(22)	1045.18259(-22)	P(21)	1054.15696(-29)
P(20)	1063.03194(-137)	P(19)	1071.80874(-4)
P(18)	1080.48177(32)	P(17)	1089.04861(-48)
P(16)	1097.50970(20)	P(15)	1105.85908(-135)
P(14)	1114.09996(31)	P(13)	1122.22422(-73)
P(12)	1130.23346(-60)	P(11)	1138.12449(-29)
P(10)	1145.89564(76)	P(9)	1153.54129(-83)
P(8)	1161.06367(-62)	P(7)	1168.45908(-11)
P(6)	1175.72229(-232)	P(5)	1182.86096(260)
P(4)	1189.85247(-579)	P(3)	1196.72221(7)
P(1)	1210.03088(-233)	R(3)	1240.78131(-3)
R(4)	1246.48592(523)	R(5)	1252.02783(264)
R(6)	1257.40899(-385)	R(7)	1262.64333(165)
R(8)	1267.71008(33)	R(9)	1272.61182(-330)
R(10)	1277.35630(43)	R(11)	1281.93031(15)
R(12)	1286.33404(-205)	R(13)	1290.57354(168)
R(14)	1294.63637(71)	R(15)	1298.52472(-98)
R(16)	1302.24016(-6)	R(17)	1305.77764(12)
R(18)	1309.13921(334)	R(19)	1312.31382(22)
R(20)	1315.30780(-127)	R(22)	1320.74596(-78)

$2 \longrightarrow 1$ Band

Table D.1: Observed line positions of AgH in cm^{-1}.

Assignment	Observed	Assignment	Observed
P(27)	968.46039(306)	P(26)	977.74572(-341)
P(25)	986.95236(-30)	P(24)	996.07301(716)
P(23)	1005.08548(-114)	P(22)	1014.01425(139)
P(21)	1022.84205(-39)	P(20)	1031.57433(111)
P(19)	1040.20074(-232)	P(18)	1048.72836(-144)
P(17)	1057.14784(-343)	P(16)	1065.46302(-226)
P(15)	1073.67104(136)	P(14)	1081.76397(172)
P(13)	1089.74105(23)	P(12)	1097.60061(-258)
P(11)	1105.34754(37)	P(10)	1112.96983(-75)
P(9)	1120.46827(-294)	P(8)	1127.84617(-73)
P(7)	1135.09473(-73)	P(6)	1142.21475(3)
P(5)	1149.20234(-18)	P(4)	1156.05859(191)
P(2)	1169.35589(28)	R(3)	1205.82663(169)
R(5)	1216.77962(-407)	R(6)	1222.02752(-187)
R(7)	1227.11732(66)	R(8)	1232.04169(-188)
R(9)	1236.80768(-49)	R(10)	1241.40869(13)
R(11)	1245.85017(732)	R(12)	1250.10911(-6)
R(13)	1254.20812(245)	R(14)	1258.12793(-262)
R(15)	1261.88880(681)	R(16)	1265.46162(340)
R(17)	1268.86090(343)	R(18)	1272.08318(514)
R(19)	1275.11927(107)	R(20)	1277.97192(-434)
	$3 \longrightarrow 2$ Band		
P(23)	974.04225(353)	P(20)	1000.10597(96)
P(18)	1016.97577(-259)	P(17)	1025.25746(-0)
P(16)	1033.43284(413)	P(15)	1041.48893(-102)
P(14)	1049.44274(369)	P(13)	1057.26849(-537)
P(12)	1064.99186(-38)	P(11)	1072.59032(-172)
P(9)	1087.42528(-200)	P(8)	1094.66056(214)
P(7)	1101.76189(-50)	R(4)	1176.32042(221)
R(5)	1181.57461(-245)	R(6)	1186.68690(727)
R(7)	1191.62339(-57)	R(8)	1196.40870(63)
R(11)	1209.77759(-225)	R(12)	1213.90374(-16)
R(14)	1221.64424(323)	R(16)	1228.68558(102)
	Lines for ^{109}AgD $1 \longrightarrow 0$ Band		
P(29)	979.67332(-247)	P(28)	989.27729(266)
P(27)	998.79017(-1)	P(26)	1008.21902(-131)
P(25)	1017.56244(-52)	P(24)	1026.81702(107)
P(23)	1035.97918(204)	P(22)	1045.04506(71)
P(21)	1054.01650(108)	P(20)	1062.88799(-15)
P(19)	1071.66020(-12)	P(18)	1080.32913(-62)
P(17)	1088.89522(103)	P(16)	1097.35052(-93)
P(15)	1105.69980(52)	P(14)	1113.93336(-209)
P(13)	1122.05706(-68)	P(12)	1130.06295(-96)
P(11)	1137.94942(-232)	P(10)	1145.71949(48)

Table D.1: Observed line positions of AgH in cm^{-1}.

Assignment	Observed	Assignment	Observed
P(9)	1153.36266(-82)	P(8)	1160.88434(139)
P(7)	1168.27409(-111)	P(6)	1175.53884(81)
P(5)	1182.67042(116)	P(4)	1189.66704(33)
P(3)	1196.52826(6)	R(4)	1246.27075(49)
R(5)	1251.81335(31)	R(6)	1257.20015(108)
R(7)	1262.42752(116)	R(8)	1267.49370(74)
R(9)	1272.39480(-214)	R(10)	1277.13665(23)
R(11)	1281.71030(80)	R(12)	1286.11305(-127)
R(13)	1290.34821(-86)	R(14)	1294.41286(92)
R(15)	1298.30109(-4)	R(16)	1302.01324(-168)
R(18)	1308.90826(-110)	R(19)	1312.08473(-191)
	$2 \longrightarrow 1$ Band		
P(27)	968.34484(-121)	P(26)	977.63273(-161)
P(25)	986.83462(21)	P(24)	995.94556(138)
P(23)	1004.96029(-127)	P(22)	1013.88274(-170)
P(21)	1022.71049(-23)	P(20)	1031.43944(120)
P(19)	1040.06412(-73)	P(18)	1048.58511(-331)
P(17)	1057.00802(125)	P(16)	1065.31309(-461)
P(15)	1073.51826(-81)	P(14)	1081.60890(24)
P(13)	1089.58265(-166)	P(12)	1097.44520(139)
P(11)	1105.18129(-369)	P(10)	1112.80306(-256)
P(9)	1120.30284(-73)	P(8)	1127.67410(-252)
P(7)	1134.92258(-2)	P(6)	1142.03820(-115)
P(5)	1149.02677(208)	P(4)	1155.87435(-214)
R(5)	1216.58485(121)	R(7)	1226.91479(122)
R(8)	1231.83981(72)	R(9)	1236.59900(-339)
R(10)	1241.19856(-300)	R(11)	1245.63547(75)
R(12)	1249.89847(-152)	R(13)	1253.99470(-85)
R(14)	1257.91977(21)	R(15)	1261.67351(327)
R(16)	1265.24885(307)	R(17)	1268.64170(-277)
R(18)	1271.87085(630)	R(19)	1274.89920(-513)
R(20)	1277.76060(-150)	R(21)	1280.43595(-26)
R(24)	1287.33477(-546)		
	$3 \longrightarrow 2$ Band		
P(20)	999.97973(-52)	P(17)	1025.12390(51)
P(16)	1033.29586(423)	P(15)	1041.34795(-196)
P(14)	1049.29361(-249)	P(12)	1064.84324(-41)
P(11)	1072.44703(632)	P(10)	1079.91751(43)
P(9)	1087.27671(607)	P(8)	1094.49865(-57)
P(7)	1101.60041(-27)	R(4)	1176.12594(-589)
R(6)	1186.49650(630)	R(8)	1196.21978(387)
R(11)	1209.58133(-292)	R(12)	1213.70793(58)

Appendix E

Line Positions of AuH and AuD

All values of the lines in the following appendix is given in cm^{-1} units. The value in parenthesis are the 1σ uncertainty from the parametrized potential fit and signify the uncertainty in the last quoted digits.

Table E.1: Observed line positions of AuH in cm^{-1}.

Assignment	Observed	Assignment	Observed
	Lines for ^{197}AuH		
	$1 \longrightarrow 0$ Band		
P(22)	1818.67532(139)	P(20)	1861.62373(174)
P(19)	1882.66998(171)	P(18)	1903.42248(206)
P(17)	1923.87284(120)	P(16)	1944.01653(145)
P(15)	1963.84413(29)	P(14)	1983.35140(44)
P(13)	2002.52915(-33)	P(12)	2021.37077(-163)
P(11)	2039.87266(-2)	P(10)	2058.02303(-28)
P(9)	2075.81625(-97)	P(8)	2093.24616(-123)
P(7)	2110.30525(-153)	P(6)	2126.98757(-78)
P(5)	2143.28364(-145)	P(4)	2159.18947(-55)
P(3)	2174.69397(-220)	P(2)	2189.79825(166)
P(1)	2204.48548(110)	R(0)	2232.59339(-128)
R(1)	2246.00363(8)	R(2)	2258.97181(-79)
R(3)	2271.49483(-31)	R(4)	2283.56357(-95)
R(5)	2295.17467(48)	R(6)	2306.31778(17)
R(7)	2316.98827(-7)	R(8)	2327.18057(61)
R(9)	2336.88665(50)	R(10)	2346.10195(133)
R(11)	2354.81852(137)	R(12)	2363.03032(73)
R(13)	2370.73287(104)	R(14)	2377.91891(107)
R(15)	2384.58121(-42)	R(16)	2390.71799(73)
R(17)	2396.31846(-40)	R(18)	2401.37948(-110)
R(19)	2405.89384(-280)	R(20)	2409.85875(-251)
R(21)	2413.26625(-247)	R(22)	2416.11063(-269)
	$2 \longrightarrow 1$ Band		
P(18)	1824.22909(-280)	P(17)	1844.27316(-29)
P(16)	1864.00264(-197)	P(15)	1883.41907(31)

Table E.1: Observed line positions of AuH in cm^{-1}.

Assignment	Observed	Assignment	Observed
P(14)	1902.50758(-164)	P(13)	1921.26938(13)
P(12)	1939.69197(-12)	P(11)	1957.77016(-77)
P(10)	1975.49891(-3)	P(9)	1992.86943(16)
P(8)	2009.87422(-83)	P(7)	2026.50874(-65)
P(5)	2058.63649(24)	P(4)	2074.11370(-130)
P(2)	2103.86981(96)	R(2)	2170.91590(193)
R(4)	2194.65529(78)	R(6)	2216.55770(109)
R(7)	2226.80174(-10)	R(9)	2245.85169(345)
R(11)	2262.92685(42)	R(12)	2270.71373(217)
R(13)	2277.98578(14)	R(14)	2284.74403(163)
R(15)	2290.97405(-157)		

Lines for ^{197}AuD
$1 \longrightarrow 0$ Band

P(35)	1261.40701(-284)	P(34)	1272.73754(-214)
P(33)	1283.97548(-151)	P(31)	1306.16585(-161)
P(29)	1327.96732(-65)	P(28)	1338.71766(-10)
P(27)	1349.36455(-40)	P(26)	1359.90818(35)
P(25)	1370.34476(10)	P(24)	1380.67334(-34)
P(23)	1390.89358(42)	P(22)	1401.00210(79)
P(21)	1410.99596(-41)	P(20)	1420.87659(2)
P(19)	1430.63994(-18)	P(18)	1440.28476(-48)
P(17)	1449.80981(-33)	P(16)	1459.21321(18)
P(15)	1468.49212(0)	P(14)	1477.64589(29)
P(13)	1486.67183(13)	P(12)	1495.56858(-3)
P(11)	1504.33478(23)	P(10)	1512.96746(-26)
P(9)	1521.46624(-9)	P(8)	1529.82867(6)
P(7)	1538.05233(-43)	P(6)	1546.13658(-44)
P(5)	1554.08012(51)	P(4)	1561.87910(33)
P(3)	1569.53282(7)	P(2)	1577.04021(44)
R(1)	1605.56411(42)	R(2)	1612.31348(349)
R(3)	1618.90002(101)	R(4)	1625.32955(49)
R(5)	1631.59928(84)	R(6)	1637.70602(53)
R(7)	1643.64970(116)	R(8)	1649.42670(74)
R(9)	1655.03654(45)	R(10)	1660.47757(25)
R(11)	1665.74782(-20)	R(12)	1670.84685(25)
R(13)	1675.77166(20)	R(14)	1680.52043(-59)
R(15)	1685.09320(-51)	R(16)	1689.48785(-13)
R(17)	1693.70139(-88)	R(18)	1697.73456(-51)
R(19)	1701.58400(-84)	R(20)	1705.24957(-51)
R(21)	1708.72900(-28)	R(22)	1712.02145(48)
R(25)	1720.75950(334)		

$2 \longrightarrow 1$ Band

P(32)	1256.29100(56)	P(31)	1267.19410(16)
P(30)	1277.99996(96)	P(29)	1288.70510(109)
P(28)	1299.30703(-29)	P(27)	1309.80804(75)
P(26)	1320.20218(-6)	P(25)	1330.49078(28)

Table E.1: Observed line positions of AuH in cm^{-1}.

Assignment	Observed	Assignment	Observed
P(24)	1340.67133(96)	P(23)	1350.74075(60)
P(22)	1360.69905(92)	P(21)	1370.54200(-57)
P(20)	1380.27224(48)	P(19)	1389.88480(85)
P(18)	1399.37748(8)	P(17)	1408.74978(-58)
P(16)	1418.00025(-83)	P(15)	1427.12778(-1)
P(14)	1436.12791(-84)	P(13)	1445.00096(-123)
P(12)	1453.74549(-86)	P(11)	1462.35965(20)
P(10)	1470.84008(33)	P(9)	1479.18550(2)
P(8)	1487.39406(-82)	P(7)	1495.46635(16)
P(6)	1503.39752(-13)	P(5)	1511.18731(-21)
P(4)	1518.83530(126)	P(3)	1526.33389(-158)
R(2)	1568.19822(-209)	R(4)	1580.91800(153)
R(5)	1587.03514(49)	R(6)	1592.99150(84)
R(7)	1598.78337(53)	R(8)	1604.40959(7)
R(9)	1609.86889(-17)	R(10)	1615.15907(-75)
R(11)	1620.28025(7)	R(12)	1625.22756(-95)
R(13)	1630.00184(-137)	R(14)	1634.60137(-130)
R(15)	1639.02480(-51)	R(16)	1643.26573(-380)
R(17)	1647.33308(-70)	R(18)	1651.21532(-116)
R(19)	1654.91508(-101)	R(20)	1658.43152(48)
R(21)	1661.76056(74)		
	$3 \longrightarrow 2$ Band		
P(27)	1270.16074(-367)	P(26)	1280.41208(-472)
P(25)	1290.55840(-325)	P(24)	1300.59578(-152)
P(23)	1310.51675(-537)	P(22)	1320.33225(-218)
P(21)	1330.03121(-136)	P(20)	1339.61275(-211)
P(19)	1349.07871(-88)	P(18)	1358.42300(-207)
P(17)	1367.64766(-194)	P(16)	1376.75152(7)
P(15)	1385.72825(-65)	P(13)	1403.30425(51)
P(12)	1411.89699(-67)	P(11)	1420.36088(61)
P(10)	1428.69016(33)	P(9)	1436.88548(87)
P(8)	1444.94346(59)	P(7)	1452.86483(196)
P(6)	1460.64336(47)	P(5)	1468.28248(130)
P(4)	1475.77579(-22)	P(3)	1483.12826(260)
R(5)	1542.45798(210)	R(6)	1548.26063(112)
R(7)	1553.89973(49)	R(8)	1559.37350(10)
R(9)	1564.68220(187)	R(10)	1569.81890(52)
R(11)	1574.78531(-60)	R(12)	1579.58119(-7)
R(13)	1584.20348(66)	R(14)	1588.64976(80)
R(15)	1592.91556(-249)	R(16)	1597.00828(-21)
R(17)	1600.91209(-658)	R(19)	1608.19011(-175)